



**Fabrication and Characterization of Silicon Nanowire  
Scanning Probes**

**DISSERTATION**

zur Erlangung des akademischen Grades eines

**DOKTOR-INGENIEURS**

**(DR.-ING.)**

der Fakultät für Ingenieurwissenschaften,  
Informatik und Psychologie der Universität Ulm

von

**Arezo Behroudj**

**aus Teheran**

Gutachter:

Prof. Dr.-Ing. Steffen Strehle  
Prof. Dr.-Ing. Julia Körner

Amtierende/r Dekan/in:

Prof. Dr.-Ing. Maurits Ortmanns

Ulm, 03.03.2020 (Datum des Promotionskolloquiums)

# Acknowledgement

The contents of this page have been removed for data privacy protection reasons.

Some parts of the dissertation include materials and results which were published in the following paper:

A. Behroudj, D. Geiger, and S. Strehle, “Epitaxial Bottom-up Growth of Silicon Nanowires on Oxidized Silicon by Alloy-Catalyzed Gas-Phase Synthesis,” *Nano Lett.*, vol. 19, no. 11, pp. 7895–7900, Nov. 2019. DOI: [10.1021/acs.nanolett.9b02950](https://doi.org/10.1021/acs.nanolett.9b02950);[1]

Adapted with permission from [1]. Copyright (2019) American Chemical Society.

# Table of Contents

<b>Introduction .....</b>	<b>1</b>
<b>Thesis Objectives .....</b>	<b>3</b>
<b>1. State of the Art.....</b>	<b>5</b>
1.1 Silicon Nanowires .....	5
1.1.1 Silicon Nanowire Synthesis.....	5
I. Top-Down Fabrication.....	5
II. Bottom-Up Synthesis Method .....	6
(a) Metal-Catalyzed Synthesis of Silicon Nanowires .....	10
(b) Alloy-Catalyzed Synthesis of Silicon Nanowires.....	12
(c) Metal-Free Catalyst Synthesis of Silicon Nanowires .....	12
1.1.2 Silicon Nanowire Integration .....	14
I. Localized Growth of Silicon Nanowires .....	14
II. Silicon Nanowire Transfer.....	15
1.2 Atomic Force Microscopy (AFM).....	17
1.2.1 AFM Measurement Modes.....	17
1.2.2 AFM Applications .....	22
1.2.3 High Aspect Ratio Scanning Tips Using Nanowires and Nanotubes .....	23
<b>2. Experimental Methods.....</b>	<b>25</b>
2.1 Silicon Nanowire Synthesis and Characterization Methods.....	25
2.1.1 Growth Substrate Preparation .....	25
2.1.2 Nanowire Chemical Vapor Deposition (NWCVD) Reactor .....	25
2.1.3 Electrical Characterization of Silicon Nanowires .....	27
2.2 Silicon Nanowire Integration via Surface-Controlled Contact Printing.....	29
2.3 Microfabrication Methods .....	31
2.3.1 Photolithography .....	31
2.3.2 Reactive Ion Etching (RIE) .....	31
2.4 Characterizing Silicon Nanowire Probes in AFM .....	31



<b>3. Silicon Nanowire Probe Fabrication and Analysis .....</b>	<b>33</b>
3.1 Si <sub>3</sub> N <sub>4</sub> -Cantilever Fabrication Using Si <sub>3</sub> N <sub>4</sub> -Membranes .....	34
3.1.1 Investigating Young's Elastic Modulus of Si <sub>3</sub> N <sub>4</sub> -Films .....	39
3.1.2 Estimation of Cantilever Spring Constant and Resonance Frequency .....	42
3.2 Silicon Nanowire Regrowth .....	49
3.2.1 Silicon Nanowire Contact Printing on Si <sub>3</sub> N <sub>4</sub> -Membranes and -Cantilevers.....	49
3.2.2 Silicon Nanowire Regrowth via VLS .....	54
3.3 Silicon Nanowire Probe Fabrication .....	60
3.3.1 Confining the Catalyst Area on Cantilevers .....	60
3.3.2 Silicon Nanowire Regrowth on Membranes and Cantilevers with or without a Tip .....	62
3.4 Analysis of Fabricated Probes in AFM .....	65
3.5 Analysis of Silicon Nanowire Tip Mechanical Behaviors for AFM Applications ..	76
3.5.1 Softness of a Silicon Nanowire Tip .....	76
I. Analytical Investigations for Silicon Nanowire Softness.....	77
II. Simulation Investigations for Silicon Nanowire Softness.....	80
3.5.2 Cantilever and Silicon Nanowire Oscillations.....	86
I. Analytical Investigation for Silicon Nanowire Oscillations .....	86
II. Simulation Investigations for Silicon Nanowire Oscillations .....	88
<b>4. Synthesis of Highly Ordered Silicon Nanowires .....</b>	<b>103</b>
4.1. Epitaxial Synthesis of Silicon Nanowires Using Alloy Catalysts .....	104
4.1.1. Synthesis of Al/Au-catalyzed Silicon Nanowires on Different Substrate Materials.....	110
4.1.2. TEM/EDX Analysis of Al/Au-catalyzed Silicon Nanowires .....	111
4.1.3. Network Formation .....	113
4.2.1. Time Between Metal Deposition and Synthesis .....	114
4.2.2. Temperature and Pressure Effects on Silicon Nanowire Epitaxial Synthesis Using Al/Au-Catalyst.....	115
4.2.3. Al and Au Thickness and Ratio Effects on Silicon Nanowire Epitaxial Synthesis .....	116

4.3. Nucleation Time, Growth Rate and Activation Energy.....	119
4.3. Electrical Properties of Al/Au-catalyzed Silicon Nanowires .....	122
4.4. Growth of a Single Al/Au-catalyzed Silicon Nanowire .....	124
<b>Summary .....</b>	<b>127</b>
<b>Outlook .....</b>	<b>129</b>
<b>Appendix .....</b>	<b>131</b>
A. Devices and Machines .....	131
B. Software .....	132
C. Chemicals and Substrates .....	133
D. Process Recipes.....	134
E. Cleaning Procedure.....	137
F. Si <sub>3</sub> N <sub>4</sub> -Membrane Fabrication.....	138
G. Si <sub>3</sub> N <sub>4</sub> -Cantilever Fabrication .....	139
H. Silicon Nanowire Growth .....	140
I. Silicon Nanowire Contact Printing .....	141
J. Fabricating Metal Pads for Silicon Nanowires (Electrical Measurements).....	142
K. TEM Investigations and Sample Preparations .....	143
L. Lift-off Process on Si <sub>3</sub> N <sub>4</sub> -Membranes and Fabricating Metal Structures on Si <sub>3</sub> N <sub>4</sub> - Cantilevers .....	144
M. Fabricating Diamond Coated Si <sub>3</sub> N <sub>4</sub> -Membranes and Cantilevers .....	146
M.1. Diamond Synthesis on Si <sub>3</sub> N <sub>4</sub> -Membranes .....	146
M.2. Cantilever Fabrication on Diamond Coated Si <sub>3</sub> N <sub>4</sub> -Membranes .....	147
M.3. Diamond Cantilever Fabrication.....	148
M.4. Raman Investigations.....	149
N. Etching Silicon Nanowires .....	151
O. Simulation Parameters and Conditions .....	153

<b>Table of Abbreviations .....</b>	<b>155</b>
<b>References .....</b>	<b>157</b>
<b>Author Publications .....</b>	<b>177</b>
<b>Curriculum Vitae .....</b>	<b>179</b>

# Introduction

Many researchers hold the view of silicon nanowires as a potential constituent for future nano-sensors and devices, owing to their electrical, mechanical and optical properties and inherent small diameters. [2] In the 1960s, silicon nanowires were first synthesized via a metal-catalyzed chemical vapor deposition process. [3] Since then, many approaches have been employed to integrate silicon nanowires into devices. Therefore, a wide range of applications is reported, either for silicon nanowire arrays, for instance, in antireflection coatings [4], [5], solar cells and photovoltaic devices [6]–[8], or for single-silicon nanowires namely in fabricating nanoscaled probes [9], [10] and nano-electronic devices such as field effect transistors [11].

In general, to fabricate silicon nanowire-based devices, nanowires are either synthesized directly in regions of interest or transferred to a device substrate. [12] Silicon nanowire localization on the device substrate can be realized either by narrowing down the fabrication region for top-down fabrication [13] of silicon nanowires or by confining the catalyst region for the bottom-up synthesis. [14] Alternatively, bottom-up synthesized silicon nanowires can be transferred using assembly techniques such as surface-controlled contact printing. [15] These techniques and methods were realized with the aim of yielding efficient and reproducible silicon nanowire integrations. However, fabricating a single silicon nanowire-based device using bottom-up grown silicon nanowires is still challenging and elaborate, as it is currently realized by applying advanced and sophisticated techniques such as focused-ion-beam deposition for confining the growth area. [16] Current silicon nanowire integration techniques require still further development towards large-scale production and industrialization, as the main criteria including reproducibility, cost-effectiveness and control over the nanowire position and orientation were not met.

Within the scope of potential silicon nanowire applications, bottom-up grown silicon nanowires can be applied in scanning atomic force microscopy (AFM). AFM belongs undoubtedly to one of the most common tools for studying material surface properties. [17] Properties and characteristics of a scanning tip have a significant impact on scanning qualities. Here, nanowires and nanotubes are the ones meeting the main criteria for scanning high aspect ratio features on a sample surface, owing to their high aspect ratio characteristics. [16], [18], [19] Not only silicon nanowires have a similar geometry feature, but also as Engstrom et al. reported, [10] can rival and even outperform carbon nanotubes. Furthermore, silicon nanowires were assumed to be soft scanning tips. [16] Nevertheless, efficient integration strategies are required to fabricate such scanning probes on a larger scale.



# Thesis Objectives

The main goal of the thesis is a realization of a low-cost and facile approach for silicon nanowire integration based on both, growth and assembly strategies. Unlike the reported techniques and methods, advanced and sophisticated approaches shall be avoided. In this work, silicon nanowires are aimed to be applied in atomic force microscopy (AFM) probes as a scanning tip. In this regard, this work pursues the following sub-objectives:

- a. Bottom-up growth of vertically aligned single silicon nanowires using gold catalysts.
- b. Fabrication of probes composed of a micro-sized  $\text{Si}_3\text{N}_4$ -cantilever.
- c. Combining “a” and “b” in order to synthesize a single silicon nanowire on an AFM cantilever.

In order to realize a single silicon nanowire via the bottom-up growth, a new strategy is proposed by applying the contact printing method and regrowing silicon nanowires from the gold particles at the tip of the contact printed nanowires. In principle, by contact printing silicon nanowires into a region of interest (here on the tip region of cantilevers), the gold particles at the tip of the nanowires can be employed again as catalyst to yield silicon nanowire scanning tips.

Beside the fabrication, characterization of the fabricated probes is also one of the thesis goals. The characterizations are targeted by testing the fabricated probes in AFM and comparing it to a pyramidal silicon tip. Furthermore, the mechanical behaviors of silicon nanowire tips on micro-cantilevers, including the silicon nanowire softness and oscillation behavior, are aimed to be studied.



# 1. State of the Art

## 1.1 Silicon Nanowires

Silicon nanowires are one of the most well-known nanomaterials that have vastly advanced silicon nanotechnology. Silicon nanowires are defined as nanorod structures with properties that are not often seen in bulk or three-dimensional materials such as high surface-to-volume ratio and its potential for making nano-electronic devices [16], [20]–[22]. In the last decades, many fabrication techniques were developed to prepare silicon nanowires [23], [24]. In this section, an introduction is given for synthetic methods in detail and briefly on properties and applications of silicon nanowires.

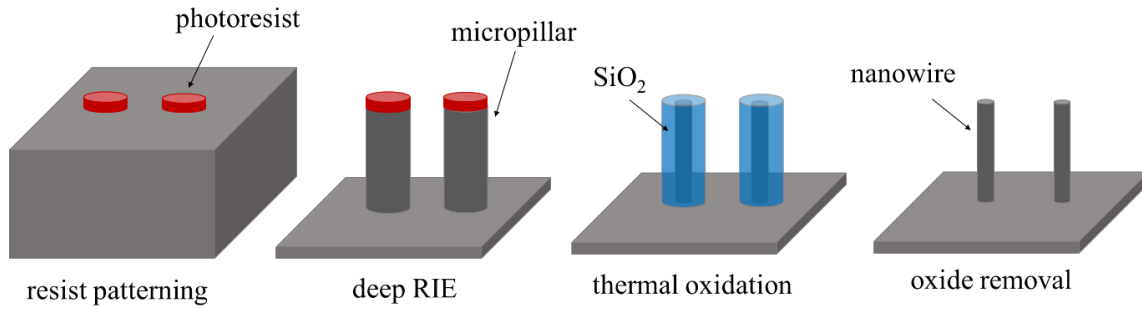
### 1.1.1 Silicon Nanowire Synthesis

The top-down and bottom-up synthesis methods are the main classic synthesis methods for silicon nanowires, which are introduced and compared in the following sections.

#### I. Top-Down Fabrication

The main principle of the top-down fabrication method is to start with a bulk silicon material and remove the material to yield nanowires. This approach relies mainly on etching techniques, for instance, metal-assisted wet chemical etching or reactive ion etching (RIE) [25], [26]. With this method, the fabrication of highly ordered silicon nanowires is feasible both in horizontal or vertical configurations with respect to the substrate surface [27], [28]. In principle, a hard mask is employed for etching and defining nanowire geometries. For this purpose, photo- and electron beam lithography are consistently superior approaches in the nanometer size definition and position of nanowires [29]. For instance, **Figure 1** illustrates schematically a top-down etching method for fabricating silicon nanowires, as Nakamura et al. [30] reported. In this method, at first silicon micropillars are fabricated by etching a silicon substrate with a patterned resist using deep RIE technique. Afterward, the micropillars were thermally oxidized and later, the oxide layer was removed to form silicon nanowires. The main advantage of the top-down approach is the fabrication of horizontal silicon nanowires, the uniformity in silicon nanowire size and the possibility for large-scale fabrication [29], [23]. However, with this method, fabrication of nanotubes and more complex core/shell structures is hardly feasible, and the characteristics of the nanowires are the same as substrates and can not be tuned during the synthesis. Therefore, an alternative method was introduced, known as the bottom-up synthesis technique.





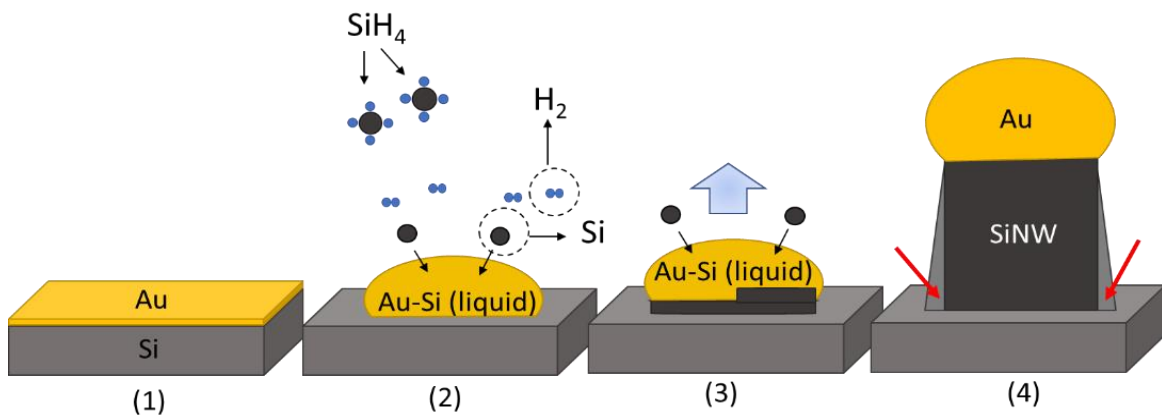
**Figure 1** Schematic illustration of a top-down fabrication process for vertical silicon nanowire formation (based on [30]).

## II. Bottom-Up Synthesis Method

In contrast to top-down techniques which are based on material removal, the bottom-up synthesis represents an anisotropic growth of nanowires using catalysts and gas-phase precursors. One of the most established techniques is based on the vapor-liquid-solid (VLS) synthesis mechanism [3]. Based on this mechanism, thin metal films or nanoparticles act as a catalyst for nanowire growth by forming liquid droplets of an alloy (silicon/metal) from a silicon vapor source. In principle, the silicon atoms are transported through the liquid droplet to the crystalizing interface. Consequently, by a continuous silicon supply, silicon is precipitated beneath the catalyst droplet. During the growth, the catalyst part remains at the tip of the nanowires. There are many techniques for bottom-up synthesis of silicon nanowires, for instance, chemical vapor deposition (CVD) either at high or low growth temperature (below 700 °C) [31]–[34], molecular beam epitaxy [35]–[39] and laser ablation [40].

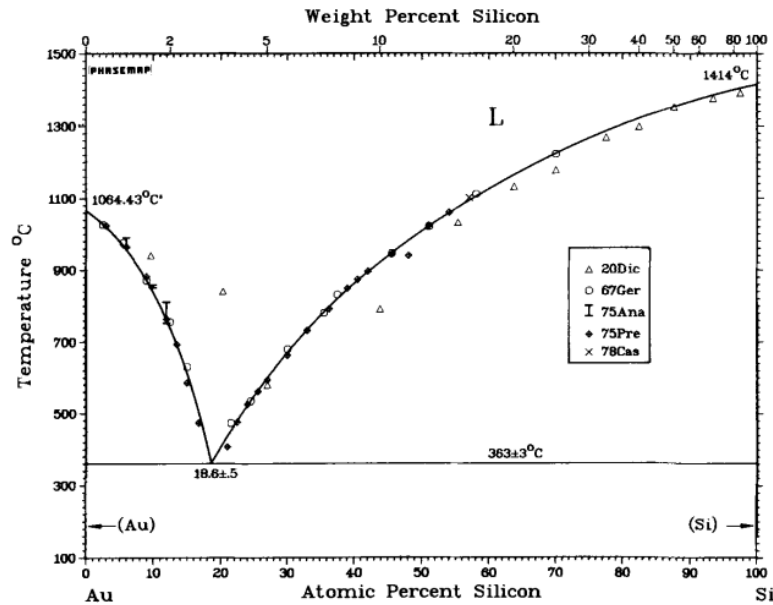
Synthesis of silicon nanowires using a CVD technique was first realized by Wagner and Ellis in 1964 [3]. This approach is still one of the most common techniques for silicon nanowire synthesis. As mentioned earlier, VLS is a realized mechanism for Au-catalyzed silicon nanowires. For a better understanding, silicon nanowire synthesis on pristine Si (111) substrates via VLS mechanism are schematically illustrated in **Figure 2**. The synthesis is basically composed of four main steps. The first step shows the preparation of a pristine Si (111) substrate, on which a thin gold layer is deposited. The second step shows a condition, where the sample is placed in a reactor and at the growth temperature. As the precursor gases like silane ( $\text{SiH}_4$ ) are introduced, a liquid Au-Si eutectic alloy is formed. The formation of an alloy is due to the fact that the growth temperature is higher than the eutectic temperature (about 363 °C based on the Au-Si phase diagram, shown in **Figure 3**) and by thermal cracking of silane [41]. Silicon from the gas phase dissolves in the gold catalyst forming the aforementioned Au-Si alloy by releasing hydrogen [3]. At equilibrium, only a limited amount of silicon can be dissolved in the Au-Si droplets. The additional supply of silicon from  $\text{SiH}_4$  causes the droplets to release the excess silicon by precipitating it beneath the alloy droplet [23]. Consequently, silicon atoms crystallize at the liquid-solid interface, as shown in **Figure 2** step three [42]. In this approach, the silicon nanowire growth continues with the Au-Si droplet at their tip, as silicon atoms crystallize beneath the

alloy droplet. After cooling down to room temperature, the pure Au-catalyst remains at the tip of the nanowire [23] as shown in step four of **Figure 2**. The tapering of silicon nanowires, indicated by the red arrows in **Figure 2** step four, can happen because of silicon deposition from thermally cracked gas molecules, which is a vapor-solid mechanism. Tapering indicates that the radial growth is slow compared to the axial growth, as the activation energy of the radial growth is larger than the axial growth. [43] Furthermore, Au surface diffusion along silicon nanowire sidewalls within the growth process causes tapering as well, which is more observed in UHV systems and at low pressures. [42] The silicon nanowire growth rate is dependent on the  $\text{SiH}_4$  decomposition at the surface, the diffusion of silicon into the alloy droplet, and the precipitation of silicon beneath the droplet. [42]



**Figure 2** Schematic illustration of the silicon nanowire synthesis based on the VLS growth mechanism. (1) growth substrate preparation: deposition of thin a gold layer on a pristine Si (111) substrate. (2) Liquid Au-Si alloy droplets are formed by introducing  $\text{SiH}_4$  at a growth temperature and after alloy oversaturation, silicon begins to precipitate beneath the droplet. (3) The blue arrow indicates the growth direction. (4) Synthesized silicon nanowire after cooling back to room temperature. The red arrows indicate silicon deposition from thermally cracked gas molecules, which results in the silicon nanowire tapering (based on [23], [42]).

One of the reasons why gold as a catalyst is favored, is due to its chemical stability. However, a significant advantage of using gold as a catalyst is a simple eutectic binary phase diagram with silicon (shown in **Figure 3**) [3], [23], [44]. As it was mentioned earlier, at the growth temperature (above the eutectic temperature),  $\text{SiH}_4$  cracks at the surface of Au-Si alloy droplets. As silicon concentration in the alloy droplet continuously rises, the silicon concentration reaches the boundary of the pure silicon phase. At this point, the silicon starts precipitating beneath the catalysts, which with time results in the growth of a wire. [45]



**Figure 3** Au-Si phase diagram (source: [44]). Reprinted by permission from, Springer Nature, *Bulletin of alloy phase diagrams*, [44], copyright (1983).

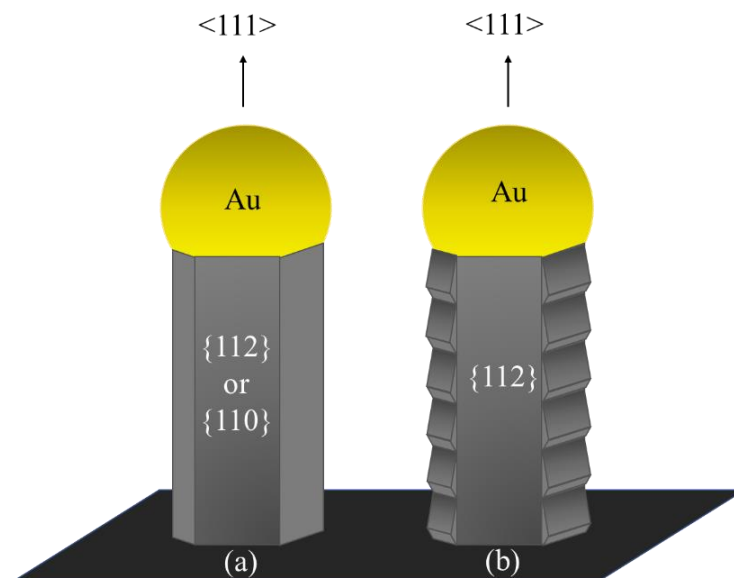
Basically, the name vapor-liquid-solid represents the path of silicon in the growth process, which starts with a vapor phase. Then, it diffuses in liquid droplets and at last, crystallizes in the wire in the solid phase. [23] What makes the VLS mechanism very remarkable, is its universality, as it works for a large number of catalysts and nanowire materials [46]–[48]. A great advantage of bottom-up synthesis by a CVD technique is that the doping of silicon nanowires is possible directly from the vapor phase. For instance, for n-doping phosphine ( $\text{PH}_3$ ) [14], [49] or arsine ( $\text{AsH}_3$ ) [14] and for p-doping, trimethyl borane (TMB) [50] or diborane ( $\text{B}_2\text{H}_6$ ) [51] were employed in the precursor gas.

The growth rate of the nanowires greatly depends on the partial pressure of  $\text{SiH}_4$  and the growth temperature. As it was reported by Lew et al. [52], the growth rate has an approximately linear relationship with the partial pressure of  $\text{SiH}_4$ . The growth rate also shows an exponential dependence on inverse growth temperature based on the Arrhenius relation ( $\propto \exp(-E_a/kT)$ ). [14]

VLS grown silicon nanowires are often single-crystalline (diamond-type). Silicon nanowires with this growth fashion can be synthesized epitaxially on a pristine single-crystalline silicon substrate. There are three families of growth direction reported for epitaxial grown silicon nanowires:  $\langle 110 \rangle$ ,  $\langle 112 \rangle$  and  $\langle 111 \rangle$  [53]–[57]. The crystal orientation of silicon nanowires is reported to depend on the nanowire diameter. [53], [54] Silicon nanowires with a diameter smaller than 20 nm grow in  $\langle 110 \rangle$  directions and silicon nanowires with a diameter in the range of 20–50 nm grow preferably in  $\langle 112 \rangle$  direction. [53], [54] Subsequently, the  $\langle 111 \rangle$  growth directions are mainly observed for silicon nanowires with a diameter larger than 50 nm [53], [54]. In the growth process, the sidewalls, the liquid-solid interface and silicon volume have their own energetic contributions. [53], [54] With regard to the aforementioned energetic contributions, for

thinner silicon nanowires (less than 20 nm in diameter), the contribution of sidewall energy plays an important role. On the other hand, the thicker silicon nanowires (with a diameter greater than 50 nm) show a tendency to grow with an orientation, which minimizes the energetic contribution of the solid nanowire interface with the catalyst. [53], [54] For instance, in a case of epitaxial synthesis, silicon nanowires with a growth direction of  $\langle 111 \rangle$  on a single-crystalline silicon substrate with (111) crystal orientation may appear perpendicular or inclined with an angle of  $70.5^\circ$ . There are more members, which belong to the family of  $\langle 111 \rangle$  direction [14][23]. It is reported by Schmid et al. [14] that silicon nanowires with larger diameters have a higher tendency to grow normal to the (111) substrate surface. In principle, if a nanowire changes the growth direction, the catalyst droplet must be tilted in the early stages of the growth. Therefore, this process for silicon nanowires with a larger diameter and consequently, larger catalyst droplet requires higher energy, which makes it less energetically favored.

Silicon nanowires with  $\langle 111 \rangle$  crystal orientation have a hexagonal cross-section with surface facets of either  $\{110\}$  or  $\{112\}$ , as it is depicted in **Figure 4** (a). [3], [58] Besides this, as it was reported by Ross et al. [59], silicon nanowires appeared with so-called saw-tooth faceting. This observation was made by growing silicon nanowires in a transmission electron microscopy. As reported,  $\langle 111 \rangle$  oriented silicon nanowires are still hexagonal in shape, but instead of being bound to six facets of  $\{112\}$ , they are bound to three flat  $\{112\}$  facets and three side surfaces with a regular rough structure (so-called saw-tooth shaped), as it is depicted in **Figure 4** (b). The saw-tooth facets were speculated to have the  $(\bar{1}\bar{1}1)$ ,  $(1\bar{1}\bar{1})$ , and  $(\bar{1}\bar{1}\bar{1})$  planes in the upward-facing facets and the downward-facing facets are the  $(3\bar{1}\bar{1})$ ,  $(\bar{1}3\bar{1})$ , and  $(\bar{1}\bar{1}3)$  planes. [23]

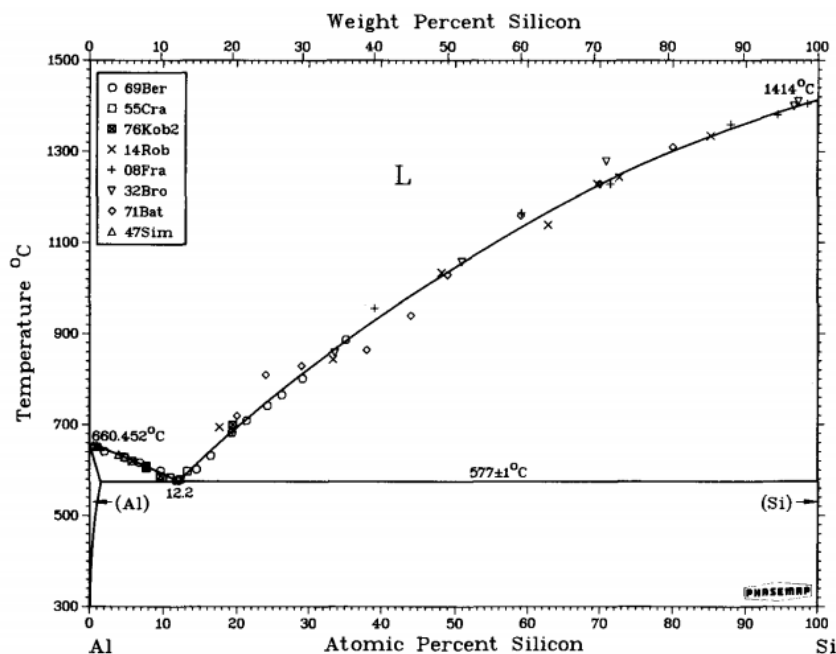


**Figure 4** (a) A hexagonal  $\langle 111 \rangle$  oriented silicon nanowire with  $\{111\}$  or  $\{112\}$  side facets. (b) A hexagonal  $\langle 111 \rangle$  oriented silicon nanowire with saw-tooth facet structures (based on [59]).

There are different types of bottom-up synthesis that are classified here into three categories by considering catalysts used for synthesis: metal-catalyzed synthesis, synthesis using alloy catalysts and using metal-free catalysts. They are further discussed in the following sections.

### (a) Metal-Catalyzed Synthesis of Silicon Nanowires

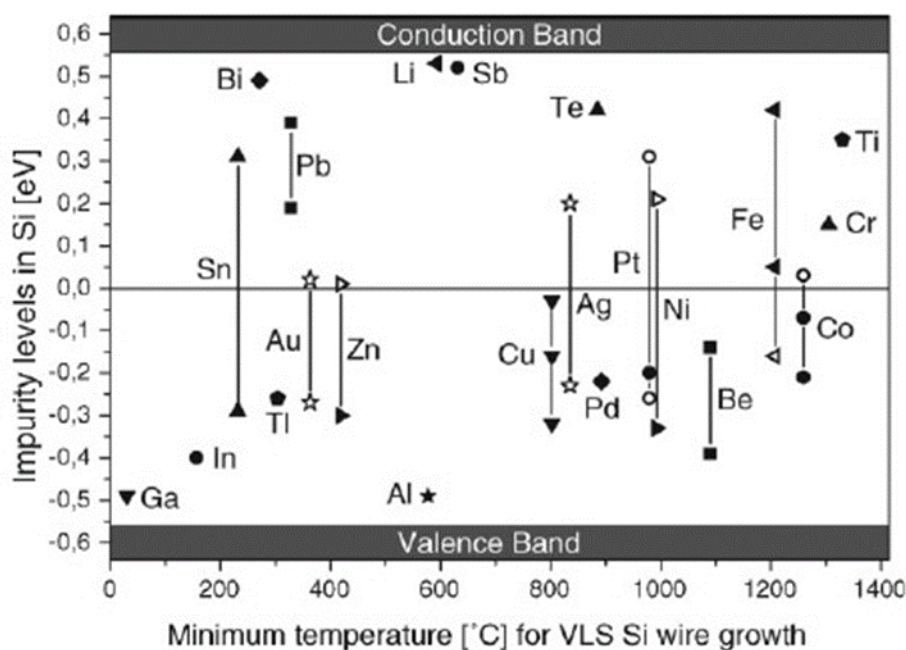
The main requirement to choose the right metal catalyst is based on their binary phase diagram with silicon. A pure silicon solid phase in the phase diagram is the most important prerequisite for the silicon nanowire growth. The growth mechanism can be understood by the phase diagram. For instance, for the VLS growth mechanism, the phase boundary is a liquidus line. However, the VLS mechanism is not the only approach to grow silicon nanowires. For instance, vapor-solid-solid (VSS) silicon nanowire growth, is also reported for some other metal catalysts like Al (the corresponding phase diagram is shown in **Figure 5**). Again, even for VSS synthesis, the phase boundary is required to be adjacent to the pure silicon side. Besides the Au-catalysts, a large variety of metal materials is reported to be applied as a catalyst for growing silicon nanowires, such as Ag [3], [34], [60], Al [32], [61]–[63], Cu [3], [54], [64], [65], Ga [66], [67], Pt [3], [9], [68], [69] and many more. It should be noted that the nanowire characteristics and the required growth conditions are not necessarily the same. In the article on silicon nanowire synthesis, reported by Bootsma et al. [70], there is an interesting classification for metal catalysts. They are categorized into three types: “type A”, “type B” and “type C”. This classification is developed more in detail in the review article by Schmidt et al. [23]



**Figure 5** Al-Si phase diagram (source: [71]). Reprinted by permission from, Springer Nature, *Bulletin of alloy phase diagrams*, [71], copyright (1984).

- “Type A” catalysts are very similar to Au. Their phase diagram is a simple eutectic phase diagram and silicon composition at the eutectic point is larger than 10 atomic %. These catalysts, like Au, apparently tend to mix with silicon. [23] Consequently, lower precursor pressures are required for silicon nanowire synthesis using metal catalysts with high silicon solubility, compared to the catalysts with low silicon solubility. [23] Additionally, for the “type A” catalysts, there is no metal-silicide phase. Al, Au and Ag are classified into “type A” catalysts. [23], [70] Based on the fact that the Al-Si phase diagram is very similar to the Au-Si phase diagram, the VLS growth mechanism can also be realized for the synthesis of Al-catalyzed silicon nanowires. VLS synthesis of single-crystalline silicon nanowires was reported using  $\text{SiH}_4$  gases at above eutectic temperature (580-700 °C). [62] On the other hand, there are reports on the synthesis of silicon nanowires based on VSS mechanism using Al-catalyst at a temperature below the eutectic point of the Al-Si system (430-490 °C). [62]
- “Type B” catalysts are the metals with low silicon solubility. Unlike “type A”, they do not have the simple eutectic phase diagrams and the silicon composition at the eutectic point is smaller than 1 atomic %. However, there is no silicide phase formation. Typical catalysts of this type are In, Ga, or Zn. [23]
- “Type C” catalysts are distinct metal catalysts due to the silicide formation. Very commonly, they have eutectic points at high temperatures compared to the other catalyst types and there can be even more than one silicide phase in their phase diagrams. Examples of this catalyst type are Cu, Pt, or Ti. [23]

Metal catalysts for silicon nanowire synthesis might incorporate in silicon nanowires as an impurity. [4] It was reported that each catalyst has an impurity energy level in the bandgap of silicon, which affects the electrical properties of silicon nanowires [23], [24], [72]. Although the synthesis of silicon nanowires using Au-catalyst is the most established synthesis mechanism, using Au-catalyst has a decisive disadvantage for the semiconductor industry. This is due to the fact that Au impurities create deep level defects in the silicon bandgap, resulting in increasing carrier recombination. [73], [74] On the other hand, using Al as a catalyst, does not create deep level defects and according to the graph depicted in **Figure 6**, the position of the respective impurity level is a shallow p-dopant.[75]



**Figure 6** Minimum growth temperature for VLS synthesis of silicon nanowires plotted versus their impurity level energies in silicon bandgap. Reprinted with permission from [23] © 2009 WILEY-VCH Verlag GmbH & Co. KGaA, Weinheim.

### (b) Alloy-Catalyzed Synthesis of Silicon Nanowires

Silicon nanowire synthesis using alloy catalysts was introduced in the last decade. Therefore, there is a handful of reports on this matter. One of the earliest reports is about the synthesis of silicon nanowires using Au and Ga as a catalyst [76]. As Lugstein et al. reported [76] that epitaxial growth of single-crystalline silicon nanowires ( $\langle 111 \rangle$  oriented) was obtained on Si (100) and Si (111) substrates by Au/Ga-catalyzed chemical vapor deposition using  $\text{SiH}_4$  precursor. Energy dispersive x-ray investigations on the catalytic part of the nanowires have shown that these particles are composed of about 25% Ga and 75% Au and form a crystalline intermetallic phase [76]. Later, the main motivation of using alloy catalysts was to create abrupt axial Si-Ge and Si-SiGe heterojunctions in nanowires via vapor-solid-solid synthesis, for instance, using Au/Ga [77], Ag/Au [78] and Al/Au [79] alloy catalysts. Besides the synthesis of heterostructures, Bi/Sn alloys were, for instance, employed to achieve so-called catalyst-doping [80].

### (c) Metal-Free Catalyst Synthesis of Silicon Nanowires

Silicon nanowires can be synthesized using catalysts other than metals and alloys via the CVD technique. Silicon nanowires using metal-free catalysts are reported to be based on various growth approaches such as oxygen-assisted growth [81], [82], carbothermal growth [83], [84] and sulfur-assisted growth approaches [85]. For instance, Ishiyama et al. reported [85] that the epitaxial silicon nanowires can be synthesized on single-crystalline silicon substrates by a thermal treatment using silicon sulfide at 1200 °C. Basically, instead of the metal-silicon alloys, the silicon sulfide in the liquid phase assists the nucleation and

nanowire growth [85]. Similar to metal catalysts, sulfur contamination in silicon nanowires are inevitable. [85] As catalyst impurities in the silicon nanowires are unavoidable [74], the non-catalytic growth approach became very intriguing in the last decade. Some progress has been made for the growth of silicon nanowires without using catalysts. For instance, Kim et al. reported a successful approach for a catalyst-free CVD growth of single-crystalline silicon nanowires, for which the diameter and doping level of the nanowires were well controlled during the growth [86]. Basically, nanocrystalline seeds on the reactive oxide surface induce nucleation instead of metal catalysts. [86]



### 1.1.2 Silicon Nanowire Integration

One of the major challenges to fabricate nanowire-based devices based on the bottom-up growth of silicon nanowires is the precise and accurate positioning of the nanowires. In this regard, many approaches were reported to integrate silicon nanowires into devices. In general, the approaches are categorized into two classes: “growth in place” and “growth and place”. [12] In the first approach, silicon nanowires are synthesized directly in areas of interest, either arrays of nanowires or a single one depending on their applications. [12] In the case of a single silicon nanowire, growth in place is a relatively challenging issue. Sometimes, direct synthesis on devices and target substrates is not feasible, as for instance substrates might not be compatible with the growth conditions. Therefore, transferring silicon nanowires became a very practical strategy, which is developing over the last decade. [12] The aforementioned strategies for silicon nanowire integrations will be discussed more in detail in the following sections.

#### I. Localized Growth of Silicon Nanowires

The most straightforward strategy for the localized growth of silicon nanowires can be to pattern catalysts. Basically, this localizes the catalyst available for silicon nanowire synthesis and as a result, silicon nanowires are grown only locally. One of the most common techniques for catalyst confinement is lithography. This is known as one of the standard strategies for micro- and nano-fabrications. [87] There are many different lithography approaches, including photolithography (for microfabrication), electron-beam lithography (for micro- and nano-fabrication), nanoimprint lithography, etc. [87] Photo- and electron beam-lithography are carried out using polymers in liquid form or dry sheets [88], known as resists. [87] Depending on the approach, resists are either photo- or electron-beam sensitive. The resists can be spin-coated or evaporated on the substrate surface. In case of the dry resist sheet, they are simply laminated to the surface. Similarly, in nanoimprint lithography, a stamp is used to pattern a layer on a substrate surface. [89] With regard to this, highly ordered nanowire arrays are reported to be grown from catalysts patterned by nanoimprint lithography, in combination with an etching step. [89], [90]

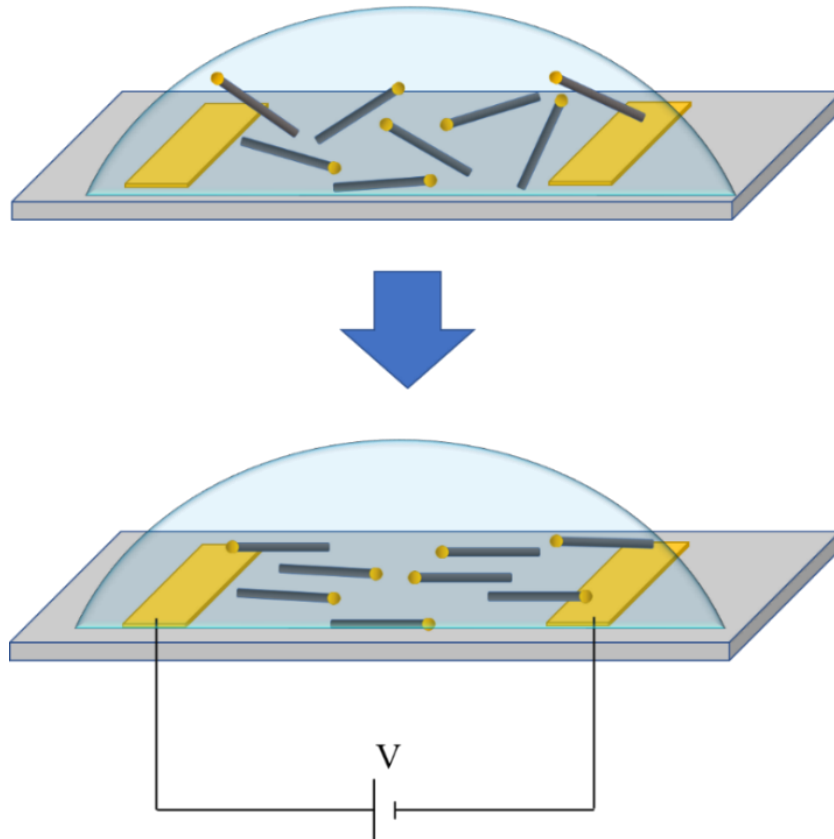
Another strategy is nanosphere lithography, which is based on assembly-free or growth in place approaches. In this technique, an ordered monolayer of silica or polystyrene particles are used as a shadow mask. [90] Using other types of shadow masks such as porous layer of alumina [91], [92] or nano-stencil masks [93] yield patterned metal deposition. Furthermore, another more advanced method for rearrangement of catalyst particles is reported by using atomic force microscopy (AFM). [94]

Other assembly-free approaches focused on localizing one of the growth parameters, for instance, temperature, by heating in a certain area. As Cao et al. reported [95], the metallic catalysts were locally and rapidly heated using a focused light beam, which resulted in the growth of semiconductor nanowires in predefined locations. Growing silicon nanowires on a resistor structure was also reported to yield localized silicon nanowire synthesis at room

temperature. [96] Furthermore, highly localized silicon nanowires are grown using an electrical biased AFM, as Ryu et al. reported. [97] With this technique, a strong electric field is created between the tip and the substrate, which causes the dissociation of the precursor gas and initiate the nanowire growth locally. [97] The aforementioned techniques are quite sophisticated and despite the successful synthesis, they can not be targeted for large-scale fabrications. This is one of the reasons why the assembly-based strategies became significantly noticed.

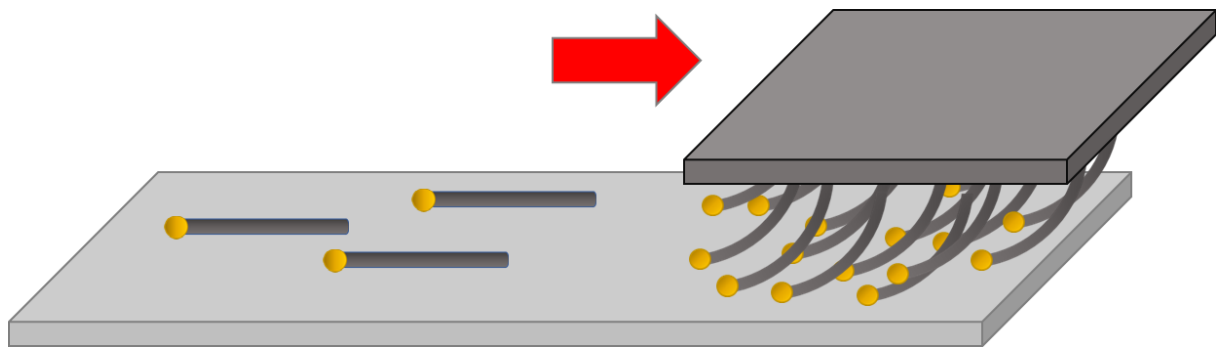
## II. Silicon Nanowire Transfer

Silicon nanowires are grown typically randomly oriented as a non-ordered arrangement on the growth substrates. In order to integrate nanowires into devices and sensors, there are many approaches reported for transferring nanowires from their initial substrates to target samples. One of the transferring methods is known as electric field-based assembly strategies [98], [99]. In this method, nanowire breakage from initial substrates is performed in a liquid (e.g., isopropyl alcohol or water), forming nanowire suspension. The suspended nanowires are then transferred on a substrate with electrical pads, enabling them to apply an electrical potential in order to align nanowires between the electrical pads by dielectrophoresis. This is accordingly depicted in **Figure 7**. At last, the solvents are evaporated.



**Figure 7** Electric field-based assembly strategy. After applying an electrical potential between the electrical pads, nanowires get aligned between the pads (based on [12]).

As electrical pads are the main prerequisites for dielectrophoresis, this strategy might not be compatible with many applications. [12] Another transfer method is the mechanical printing-based approach. For instance, a roll printing strategy was developed for large-scale assembly of silicon nanowires, as Yerushalmi et al. reported [100]. Another transfer method is the so-called contact printing, by which high uniformity and reproducibility can be achieved. [101]–[103] Silicon nanowires are mechanically sheared on the receiving substrates and break off growth substrates due to the friction between nanowires and target substrates and subsequently, are transferred, as schematically illustrated in **Figure 8**. [101], [102] The contact printing approach can be further enhanced by fabricating so-called catcher structures [15] or applying patterned photoresists [104]. These techniques improve the localization of contact printed silicon nanowires. The contact printing device is still under development and progress. The other advantage of contact printing is that integration of silicon nanowires on a flexible and non-common substrate such as flexible polyimide substrates becomes feasible. [105]



**Figure 8** Silicon nanowire contact printing. Silicon nanowires break off a growth substrate by shearing motion and friction between nanowires and a target substrate (based on [15]). The red arrow indicates the direction of contact printing.

## 1.2 Atomic Force Microscopy (AFM)

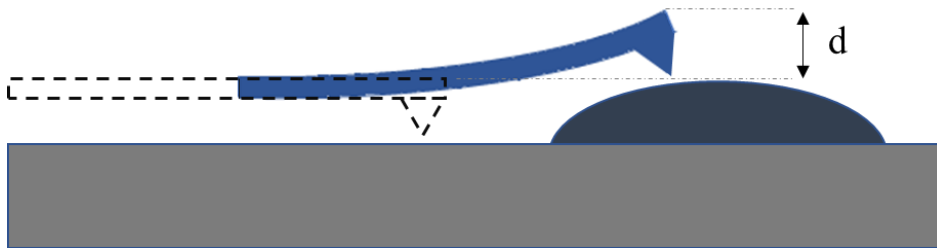
The invention of AFM opened up a lot of possibilities for research and studies in the field of nanoscale science and technology. AFM was first invented in 1986 by Binnig. [106], [107] Since then, AFM was developed and employed for a variety of research fields and applications. The main application of AFM is for measuring surface topography with a nanometer scale. [107] This is carried out by applying a probe composed of a micro-sized cantilever with a sharp tip. The cantilevers are conventionally made of either Si or Si<sub>3</sub>N<sub>4</sub>. Measuring the interacting force between a tip and a sample surface is possible, as long as the distance of the tip from the sample surface is 0.1-100 nm. In principle, a tip scans over a surface and the motion or deflection of the cantilever, which is based on the interacting force between the tip and sample is recorded and translated to a height change of the sample surface. [108]–[110] There are various methods for measuring the cantilever deflection, such as optical deflection technique [111], tunneling current measurements [107], fiber interferometry [112] and piezoresistive [113].

### 1.2.1 AFM Measurement Modes

AFM measurements, in general, can be operated in two modes, either static (known as contact mode) or dynamic modes (e.g., tapping mode). In static mode, the cantilever remains static and simply scans over a surface. On the other hand, in dynamic mode, the cantilever resonates while scanning over a surface. In static mode, the cantilever bending can be measured and subsequently, the bending force can be estimated by knowing the spring constant and employing the following relation, which is known as Hook's law: [110]

$$F = kd \quad (1-1)$$

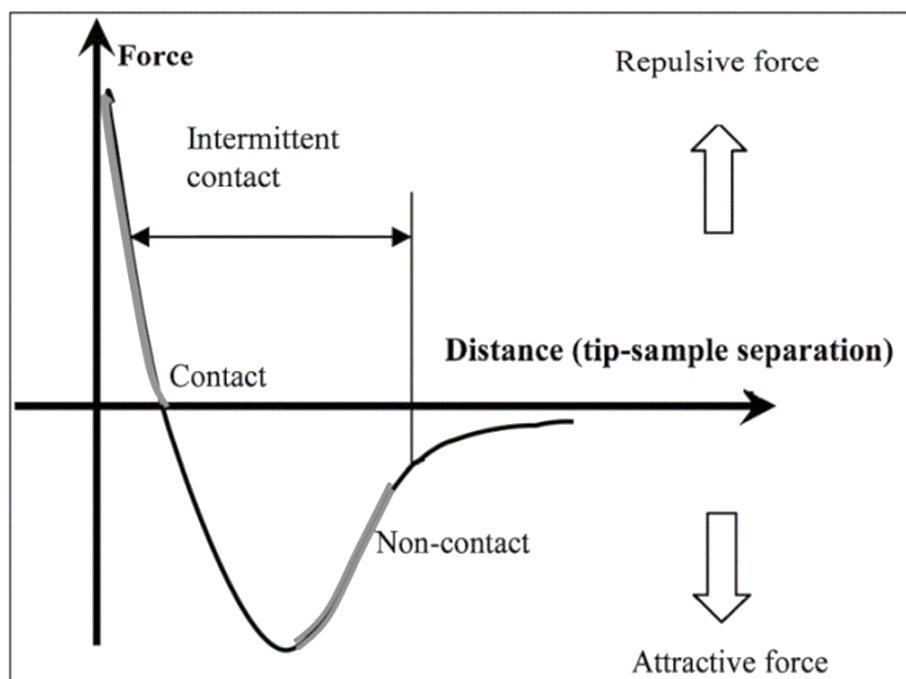
Here,  $F$ ,  $d$  and  $k$  stand for the elastic force of the cantilever, bending displacement and spring constant, respectively. The distance  $d$  is accordingly demonstrated in **Figure 9**. Usually, the spring constant of a cantilever is between 0.01-100 N/m.



**Figure 9** AFM static (contact) mode. Here,  $d$  is the vertical displacement of the bent cantilever from its initial position (based on [110]).

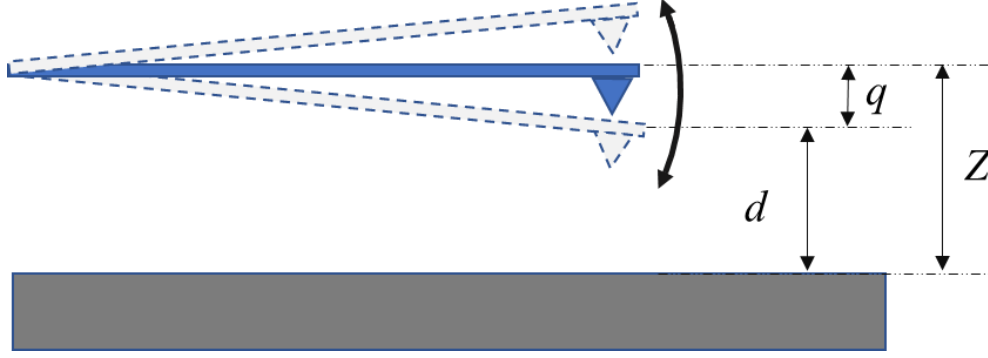
The AFM force-distance curve is depicted in **Figure 10**. As it is shown in the graph, the interaction forces are mainly categorized as attractive (for larger interatomic distance) and repulsive forces (for shorter interatomic distance). Van der Waals interactions, electrostatic and chemical forces are classes of the attractive force.[114] Examples of repulsive forces are Pauli-exclusion interaction and electron-electron Coulomb interactions. [114] In fact,

the attractive force diminishes, when the atoms of the tip are very close to the surface atoms, in a way that electron clouds start repelling each other electrostatically. Besides the repulsive forces, there is a capillary force present due to the contamination or a water layer over the sample surface. These forces are dominant in contact mode, although they are attractive. In static mode, the tip is in contact with the sample, as it scans the surface. In this case, the interaction forces are mainly repulsive. In contact mode, the aim is to keep either cantilever height or force constant during measurements. So, any deflection is compared to the set value and any deviation from the set value is compensated by raising or lowering the cantilever position. Therefore, the topography image is constructed based on the signal required to keep the cantilever at a constant height or the force value constant. [17]



**Figure 10** Interaction force between AFM tip and sample versus their distance (source: [17]). Reprinted from [17], copyright (2004) with permission from Elsevier.

In dynamic mode (also known as a non-contact mode), AFM measurements can be done either with amplitude modulation (AM) or frequency modulation (FM). For AM-AFM, the measurement is operated with a very small amplitude of the cantilever and its vibration amplitude is monitored and served as a feedback signal in order to construct the topography image. [115] The FM-AFM is based on the resonance frequency shift. This mode is also known as a tapping mode. [115]



**Figure 11** Tip–sample distance parameters for dynamic AFM.  $Z$  is defined as an average distance between the tip and the sample,  $d$  is the minimum distance and  $q$  is the instant displacement from  $z$  of the cantilever when the cantilever is oscillated by an external force (based on [110]).

By employing piezoelectric devices such as PZT actuator or bimorphs, the cantilever is vibrationally excited. [110] The resonance parameters for a cantilever are the resonance frequency, amplitude and phase. The external perturbation, produced in the PZT actuator with a frequency close to the resonance frequency of the cantilever, affects the resonance response of the cantilever. The cantilever motion can be approximated and defined with the following equation: [110]

$$m\ddot{q} + kq + \frac{m\omega_0}{Q}\dot{q} = F_{ts} + F_0 \cos(\omega t) \quad (1-2)$$

Basically, this equation is for a one-dimensional point mass ( $m$ ) attached at a spring. In this equation,  $F_0$  and  $\omega$  are the amplitude and the angular frequency of the sinusoidal driving force produced by the actuator, respectively.  $Q$ ,  $k$  and  $\omega_0$  stand respectively for the quality factor, spring constant and the angular resonance frequency of the cantilever.  $F_{ts}$  represents the interaction force between the tip and the sample.  $F_{ts}$  is zero, when the tip is away from the sample surface. By considering the harmonic perturbation for the cantilever, the model can be described by the following equation: [110]

$$q = A \cos(\omega t - \phi) + B e^{-\alpha t} \cos(\omega_r t + \beta) \quad (1-3)$$

Here,  $\phi$  stands for the phase difference between the driving force and the cantilever motion and  $\omega_r$  represents the resonance angular frequency of the cantilever by considering the damping effect [116]. The resonance angular frequency with damping ( $\omega_r$ ) can be defined based on the following relation: [110]

$$\omega_r = \omega_0 \sqrt{1 - \frac{1}{2Q^2}} \quad (1-4)$$

Here,  $\omega_0$  is the angular frequency without damping and  $Q$  represents the quality factor.

By considering the tip-sample interaction as parabolic potential ( $\propto q^2$ ), the force is proportional to  $q$  and is defined by the following relation: [110]

$$F_{ts} = \left( \frac{dF_{ts}}{dz} \right) q + \text{const.} \quad (1-5)$$

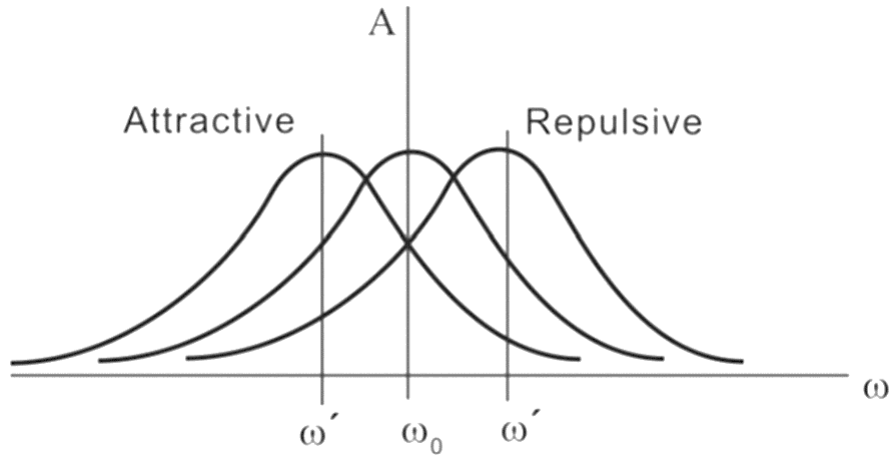
Here,  $dF_{ts}/dq$  as a force gradient is a constant value and by considering the equations (1-2) and (1-5), the effective spring constant ( $k_e$ ) can be obtained by the following relation: [110]

$$k_e = k - \frac{dF_{ts}}{dz} \quad (1-6)$$

Consequently, the modified resonance frequency by considering the tip-sample interaction force can be determined as: [110]

$$\omega' = \sqrt{\frac{k_e}{m}} = \sqrt{\frac{k - (dF_{ts}/dz)}{m}} \quad (1-7)$$

In this case, instead of force, the gradient of the force causes the resonance frequency shift. [110] For a better understanding, the relation between the interacting force and the frequency shift is illustrated in **Figure 12**. Accordingly, the attractive or repulsive forces affect the polarity of the resonance frequency shift. The horizontal axis is the angular frequency and the vertical axis is the amplitude of the cantilever displacement.



**Figure 12** The frequency shift due to the interacting force. The horizontal axis is the angular frequency and the vertical axis is the amplitude of the cantilever displacement. The repulsive force increases the resonance frequency, while the attractive interacting force decreases it (source: [110]). Republished with permission of IOP Publishing, from [110], permission conveyed through Copyright Clearance Center, Inc.

There has been progress in designing different measurement modes such as pulsed-force mode [117] and force-volume imaging [118], [119]. The recently developed AFM measurement mode known as peak force tapping mode, operates very similarly to tapping mode, but not in resonance mode. [120] Tapping oscillation is carried out at frequencies below the resonance frequency of the cantilever. [120] Basically, the system is based on combining the advantages of both contact (force control) and tapping modes (less damage

caused by lateral force). [120] This mode is basically enabled to extract a force curve at each pixel.



### 1.2.2 AFM Applications

One of the biggest advantages of using AFM is that performing measurements is feasible in nearly all environments, including vacuum, solutions such as biological buffers or at ambient atmospheric conditions. [17] This is one of the reasons why AFM is still one of the most active tools in the research field of nanoscale science and technology for a broad range of applications. One of the most highlighted applications is to study biological-relevant topics. AFM has the ability to measure forces in the nano-Newton range in physiological conditions, drug-protein interactions, protein-protein interaction, cell-cell or cell-protein interactions and many other intermolecular forces. [17] As AFM enables to extract topography features, it is upgraded to probe even a single molecule with a high lateral resolution and simultaneously measuring small interaction forces, or adhesions. [17] For instance, many experiments are conducted on DNA [121]–[125], polysaccharides [126]–[129] and proteins [122], [128]. In addition, AFM is utilized to provide quantitative chemical and mechanical information. [127], [130] This technique has been used extensively for the characterization of mechanical properties of a sample such as elasticity [131] or hardness [132] using the nanoindentation technique [133]. Besides, AFM became extensively noticed for investigating electrical characteristics of nanostructures such as carbon nanotube [134] or silicon nanowires [135]. This type of measurement is commonly conducted using the conductive-AFM technique, scanning tunneling microscopy or Kelvin force scanning probe microscopy.[136] The scanning probes applied for the aforementioned applications should be compatible with the measurement setup and environment. [136] For instance, using the conductive-AFM technique demands a highly conductive scanning probe. [136] Furthermore, the electrochemical scanning probe microscopy was introduced to explore surface processes or liquid-liquid interfaces. [137] This has led to many applications in various research fields such as material science, biomedical research, corrosion, catalysis, fuel cells, and battery research. [138], [139] Moreover, AFM is applied for the fabrication of nanostructures. One of the first applications was the oxidation process on silicon surfaces using scanning probe microscopy. [140] Later, it was shown that using a conductive AFM tip under electrical bias can oxidize silicon [141], [142], metal films such as Ti [143], Al [144] and Nb [140]. This technique has also been applied to fabricate compound semiconductor nanostructures [145], or metal-based electronic devices [146], [147]. Last but not least, AFM utilized with tip-enhanced Raman spectroscopy techniques, enables chemical analysis and topography measurements with a high resolution.[148], [149] As AFM measurements can be operated in a liquid environment, this technique has enabled to study biological samples. [150], [151]

### 1.2.3 High Aspect Ratio Scanning Tips Using Nanowires and Nanotubes

AFM probes with high lateral resolution and high aspect ratio characteristics are highly required for constructing high-resolution topography images of samples with high aspect ratio features. [152] Among the various types of realized scanning tips [152]–[157], nanowires and nanotubes became extensively noticed for the application of high aspect ratio scanning probes. [154] One of the most common high aspect ratio tips are carbon nanotube scanning probes, which have been recently commercialized. [154] One of the first fabrication methodologies for carbon nanotube tips is demonstrated by Dai et al. [158] These probes were fabricated by attaching individual tubes to the conventional silicon AFM probes. In this method, micromanipulators were used to position a nanotube on a cantilever tip, while everything can be visually observed in an optical microscope. As Dai et al. reported [158], the main advantage of using carbon nanotube scanning probes is their slenderness and flexibility, which prevents damage from the tip crash. [159] At first, the assembly of nanotubes was carried out in an optical light microscope, which only worked for nanotubes with large diameters due to the low resolution of the light microscopes. Therefore, the assembly was carried out later in scanning electron microscopy (SEM) [160]. The assembly quality was further enhanced by a so-called welding process, using carbonaceous contaminants on the sample surfaces and a focused electron beam in SEM. [161] As the advantages of using carbon nanotubes became more elucidated, the interest in the mass fabrication of such scanning probes was rising as well. However, the aforementioned methods are quite elaborate and time-consuming due to the individual customization and assembly of each probe. In this regard, Nguyen *et al.* [162] introduced a method for mass fabrication of such probes, involving electron-beam patterning of metal catalysts and subsequent PECVD process for the bottom-up growth of free-standing carbon nanotubes on microfabricated cantilevers.

Besides carbon nanotubes, using other material nanowire structures as a scanning tip became intriguing, for instance, using copper [154], silver [163], tungsten [19] and silicon nanowires [10], [16]. Due to the high wear in metallic nanowires, silicon nanowires and carbon nanotubes are the competing counterparts. Engstrom et al. [10] reported a method for the fabrication of both silicon nanowire and carbon tube probes using the nanostencil lithography technique. The main principle in this technique is to use a thin  $\text{Si}_3\text{N}_4$ -membrane with small apertures to deposit metals with desired patterns. [10] Individual vertical silicon nanowires are synthesized epitaxially on the silicon cantilever with crystal orientation of  $\langle 111 \rangle$  via the VLS process. The multiwall carbon nanotubes were grown by a plasma-enhanced chemical vapor process on the AFM probes. The high aspect ratio characteristics were subsequently analyzed by scanning micrometer-deep trenches in AFM. Fabricated silicon nanowire tips were reported to show superior performance compared to carbon nanotubes, as they show more consistency in resolving high aspect ratio geometries. It is also further argued that carbon nanotube Young's modulus is notably diminished because of defects, interlayer sliding and hollow internal structures. On the other hand, silicon nanowires are crystalline structures with less defects and buckling. Therefore, they show consistent performance [10]. Before this, the first introduction of silicon nanowire probes was given by Christiansen *et al.* [164] In their approach, a VLS gold-catalyzed silicon

nanowire is assembled to an AFM tip by a similar method as pick and place via a nanomanipulator using electron beam induced contamination deposition. The fabricated silicon nanowire scanning tips were employed for nano-Raman spectroscopy, as the gold cap enhances the Raman signals significantly. [164] Later, in 2017, Knittel et al. [16] reported another method using a focused ion beam for the fabrication of high aspect ratio silicon nanowire scanning probes. They described the nanowire tips as a soft scanning probe, applicable for sensitive and delicate samples such as biological analytes. [16] Furthermore, it is mentioned that silicon nanowire probes can be modified with well-established chemistry, which can be, for instance, used for chemical force microscopy. [16] Additionally, silicon nanowire electrical properties can be tuned during the synthesis and growth of highly doped silicon nanowires can provide a high aspect ratio probe for operating conductive-AFM measurements. [16]

## 2. Experimental Methods

### 2.1 Silicon Nanowire Synthesis and Characterization Methods

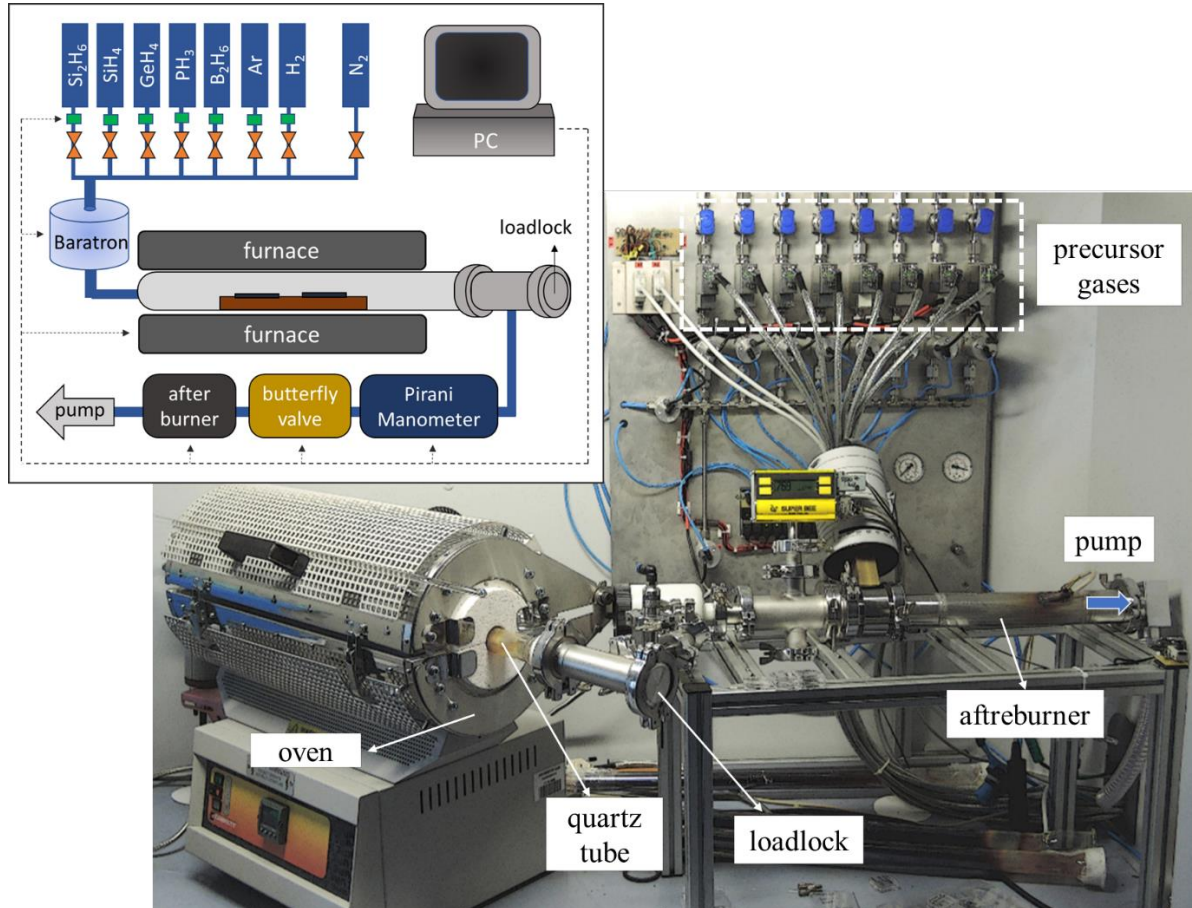
#### 2.1.1 Growth Substrate Preparation

In this work, different types of substrates and materials, including single crystalline silicon substrates with crystal orientations of (100), (110) and (111), silicon substrates covered by  $\text{SiO}_2$ - and  $\text{Si}_3\text{N}_4$ -films, silicon and  $\text{Si}_3\text{N}_4$ -cantilevers were employed as growth substrates for silicon nanowire syntheses. The detailed information about the substrates can be found in Appendix section C, **Table-A 4**. It should be noted that all these materials can withstand silicon nanowire growth conditions. Due to the variation in growth substrate types, different sample sizes were used. However, the sample sizes were compatible with the sample-holder size (not larger than 2 cm in width) in the nanowire chemical vapor deposition (NWCVD) reactor. Prior to synthesis and metal evaporation, the standard cleaning procedure was applied to the growth substrates (for more details see Appendix section E and H). After a cleaning step, a thin layer (in the range of 2-20 nm) of Au- or Al-films or both films were evaporated on the substrates, using an electron evaporation beam under a high vacuum. The metal layers were used basically as catalysts for the bottom-up synthesis of silicon nanowires [3].

#### 2.1.2 Nanowire Chemical Vapor Deposition (NWCVD) Reactor

Silicon nanowire syntheses in this work were carried via a bottom-up approach in a CVD reactor. The reactor except for the pump and the computer is stored inside a laboratory fume-hood. A photo and schematic of the device are depicted in **Figure 13**. The main reaction chamber is basically a quartz tube, which is surrounded by a furnace tube, as it is shown in **Figure 13**. Different process gases can be employed in the chamber, including disilane  $\text{Si}_2\text{H}_6$ , monosilane  $\text{SiH}_4$  2% in helium (He), monogermane  $\text{GeH}_4$  2% in He (for germanium nanowire synthesis), dopant gases such as phosphine  $\text{PH}_3$  200 ppm in He and diborane  $\text{B}_2\text{H}_6$  100 ppm in He, Ar for dilution or cooling step and  $\text{H}_2$  for side-wall passivation. The nitrogen gas ( $\text{N}_2$ ) is used for venting the chamber. The gas flows are adjusted by mass-flow controllers. They can be mixed, except for  $\text{N}_2$  and forwarded to the quartz tube or the main reactor chamber. Within the nanowire synthesis process, the total pressure inside the tube can be adjusted by a butterfly valve and a pressure controller. A capacitive manometer (type Baratron) is used to control the working pressure during the synthesis, as it is illustrated in **Figure 13**. Growth substrates are placed on a quartz boat and subsequently, inserted into the tube through the load lock. During the stand-by states or at evacuated condition, the base pressure (less than 0.08 mbar) is controlled by a Pirani manometer. The process gases might cause damages to the rotary pump. Therefore, a hot-filament afterburner was installed, which operates at 600 °C to crack residual process gasses prior to pumping. Silicon nanowire growth conditions, including temperature,

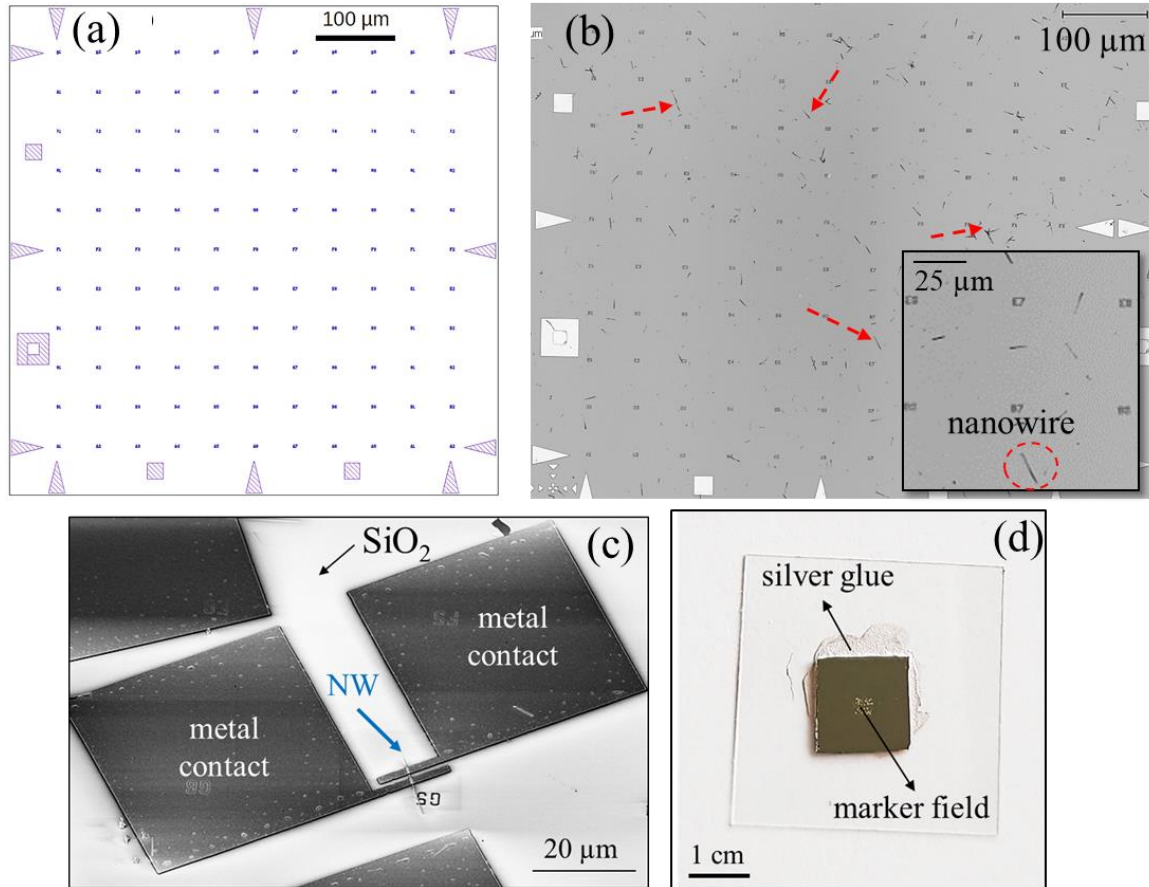
working pressure and gas flows, can be controlled and monitored by a computer. The detailed synthesis conditions are provided in Appendix section **D**, **Table-A 8**. This is quite advantageous in the reproducibility of complex growth processes. The details of the NWCVD components can be found in Appendix in section **A**, **Table-A 2**. The NWCVD reactor was constructed at the Institute of Electron Devices and Circuits Ulm University, and optimized by S.T. Jäger, within his doctoral research work. More detailed information about the NWCVD reactor can be found in his dissertation [165].



**Figure 13** A photo and schematic illustration of NWCVD components.

### 2.1.3 Electrical Characterization of Silicon Nanowires

In this work, the electrical characteristics of synthesized silicon nanowires were individually investigated. In order to fabricate a single silicon nanowire-based device, the as-grown silicon nanowires were released from the growth substrate and transferred by using the drop-casting method. Silicon nanowires were released in ethanol solution in an ultrasonication bath. Then, the suspended silicon nanowires in ethanol were drop-casted on a silicon substrate covered by an insulating film such as  $\text{SiO}_2$  and subsequently, the ethanol was evaporated. As silicon nanowires are randomly positioned via the drop-casting method, alignment-markers were structured on the receiving substrates before drop-casting the nanowires. The markers as a coordinate system assisted in nanowire position registration on the surface and subsequently fabricating metal pads for electrical connections. These marker fields consisted of four identical parts and were prepared by electron beam lithography. The markers consisted of electron beam evaporated 5 nm Ti and 45 nm Au. A schematic illustration of a marker field is correspondingly shown in **Figure 14** (a). The drop-casting method was employed to transfer the nanowires on the substrates (**Figure 14** (b)). Afterward, metal pads for electrical connections on silicon nanowires were patterned by lithography using an electron beam technique and a resist lift-off process. The metal stacks were composed of Ti/Al/Au layers. The total thickness of the metal stack was chosen to be about double the nanowire diameter for ensuring proper electrical contacts. The details of the fabrication procedures can be found in Appendix, section J. One example of fabricated metal pads on silicon nanowire is shown in the SEM image of **Figure 14** (c). In order to apply a back-gate potential on a silicon nanowire with field-effect transistor configuration, the sample with marker field was glued to a glass substrate using electrically conductive silver glue (**Figure 14** (d)). Individual electrical analysis for silicon nanowires was later conducted in a probe station device. The probe station utilized manipulators, allowing precise positioning of thin needles on the surface and recorded the electrical signals in a computer.

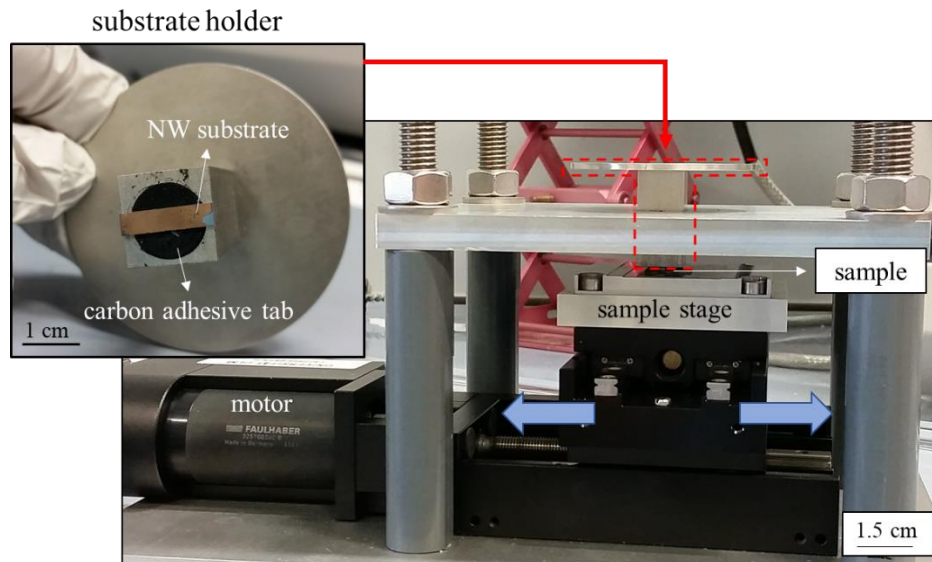


**Figure 14** (a) Schematic illustration of a quadrant of the marker field. (b) Confocal microscope image of drop-casted silicon nanowires (indicated by the red arrows) on a marker field. The inset image shows a magnified view of the nanowires on the marker field area. The red dashed circle indicates a nanowire. (c) SEM image of a fabricated single silicon nanowire-based device on a SiO<sub>2</sub> surface. (d) A sample with marker fields, glued on a glass substrate using a silver glue.



## 2.2 Silicon Nanowire Integration via Surface-Controlled Contact Printing

As silicon nanowires are integrated into probes and cantilevers for fabrication of silicon nanowire scanning probes, in this work, instead of the drop-casting method, they were transferred from their growth substrates to a target substrate using surface-controlled contact printing [15]. The initially used version of the contact printing device is shown in **Figure 15**. In principle, this device is composed of a motorized sample stage that hosted the target substrate, enabling controlled and reproducible velocity. Basically, one direction of movement was designed for the sample stage, while the nanowire substrate is glued to the holder at a constant position, but in contact with the receiving substrate on the sample stage. The translational movement of the substrate and the friction between the nanowires and surface caused nanowire breakage from the growth substrate and the nanowire transfer to the target sample. A normal pressure between the growth and target substrates was provided by a static weight.

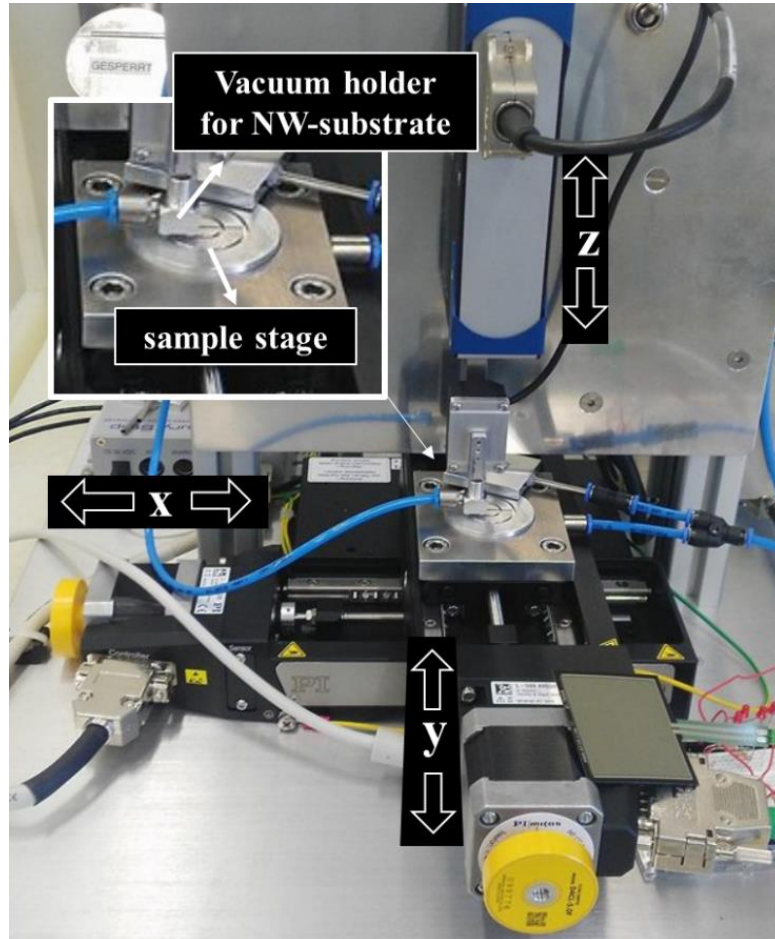


**Figure 15** The initially used version of the contact printing device. The blue arrows indicate the movement direction for the sample stage.

The more advanced version of the surface-controlled contact printing device was developed in 2018, by P. Salimitari (Ulm university) within her master thesis. This device is also in-house built and shown in **Figure 16**. The main principle is nevertheless the same as the initial version, but the sample stage motion is not limited to one direction, and it can move in both x- and y-directions, as depicted in **Figure 16** (a). Furthermore, the nanowire substrate (NW-substrate) is held by vacuum to the holder rather than using glues, which might create instability and irreproducibility in contact printing. In addition, the nanowire substrate motion in the z-direction is controlled by a different stage. A load can be defined and precisely applied on the substrate during contact printing, instead of using static weights. All in all, the advancement was made to create more accuracy and reproducibility in silicon nanowire contact printing on various types of substrates, for instance, fragile samples like



cantilevers and membranes. The stage motions (in terms of velocity and distance) and the applied forces are software-controlled and can be tuned. However, prior to contact printing, it is required to perform a force calibration step using a sample with the same thickness as the receiving substrates. The detailed contact printing approach is demonstrated in Appendix section I.



**Figure 16** *Advanced version of the contact printing device.*

## 2.3 Microfabrication Methods

### 2.3.1 Photolithography

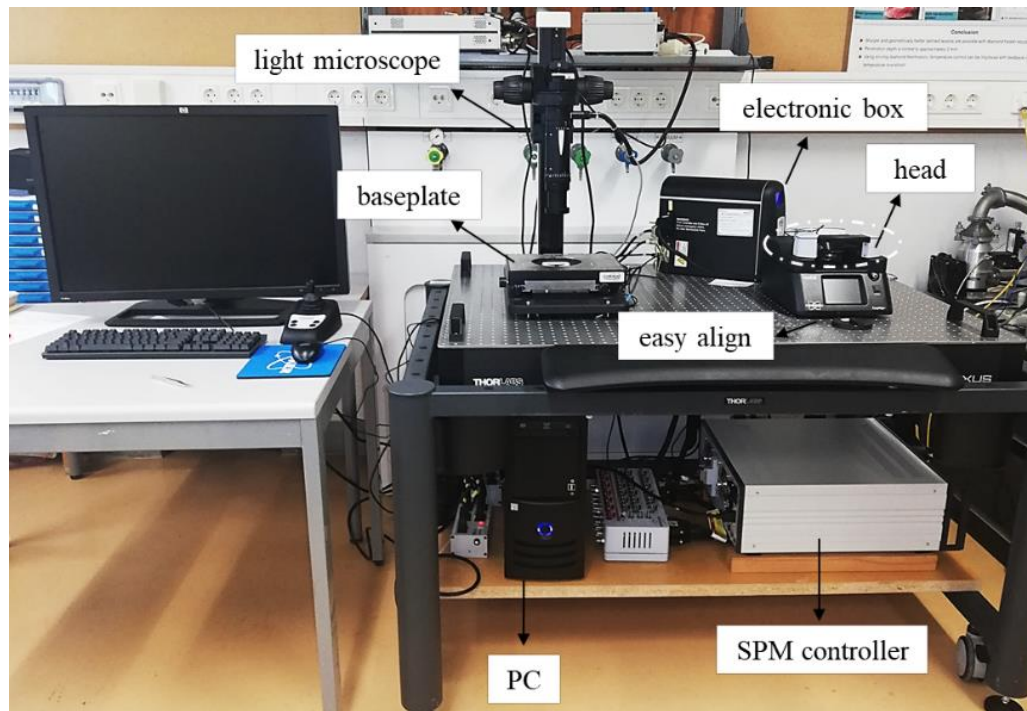
Silicon nanowires are integrated into cantilevers in order to fabricate silicon nanowire scanning probes. For the fabrication of micro-cantilevers, silicon substrates with crystal orientation of (100), with 1  $\mu\text{m}$  thick  $\text{Si}_3\text{N}_4$ -films coated on both sides were employed (see Appendix **Table-A 4**). After cutting wafers into a designed sample size (e.g. 2 cm  $\times$  2 cm), they were cleaned via the standard cleaning procedure (see Appendix section **E**). Micro-patterns were fabricated on the samples via the photolithography technique. At first, the liquid photoresist (AZ5214E) was spin-coated homogenously on substrates. Then, they were exposed to UV light using a mask aligner (Karl Suss MJB-3 and SUSS MicroTec MJB4) and a photomask. Later, the exposed photoresist was developed in a developer solution. The details of the fabrication procedure can be found in Appendix section **D**, **Table-A 9** and **Table-A 10**.

### 2.3.2 Reactive Ion Etching (RIE)

For etching  $\text{Si}_3\text{N}_4$ , reactive ion etching was chosen using  $\text{CF}_4$  gas and plasma. The RIE system consists of a cylindrical vacuum chamber, with graphite plate holders in the bottom portion of the chamber. The wafer plate is electrically isolated from the rest of the chamber. The reactor gases,  $\text{CF}_4$ ,  $\text{O}_2$  and Ar enter via small inlets into the chamber and pumped using a vacuum system. Gas enters through small inlets in the top of the chamber and exits to the vacuum pump system through the bottom. Gas pressure is typically maintained by adjusting the gas flow rate. The etching conditions, including pressure, gas flows, plasma power and etching time, are controlled by a user interface in a computer (for more details, see Appendix, section D, **Table-A 6**).

## 2.4 Characterizing Silicon Nanowire Probes in AFM

Silicon nanowire scanning probes were analyzed in a commercial AFM (Bruker Bioscope catalyst). The corresponding AFM device is shown in **Figure 17**. The main components of the device are the scanning probe microscope (SPM) controller, the base plate (stage for scanning samples), electronic box (to produce laser beam and monitoring the laser adjustment on the photodiode), head (holder for AFM probes), easy align (to adjust the laser beam on the backside of cantilevers and its reflection on the photodiode), light microscope (to monitor the scanning surface) and a computer. All measurements were controlled via software. At first, for the laser alignment on the cantilever, the head is placed on the so-called easy-align and after alignment, it is transferred on top of the baseplate. This device enables the peak force tapping mode [166].



**Figure 17** Atomic force microscopy (AFM) device.

# 3. Silicon Nanowire Probe

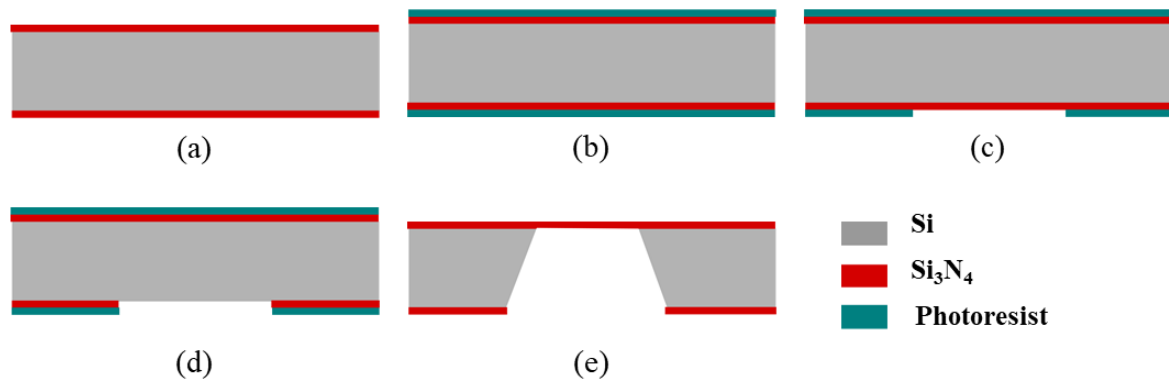
## Fabrication and Analysis

In the last decades, several attempts were made to produce an ideal scanning tip for AFM applications. Among the reported methodologies, nanowire and nanotube tips are known to outperform conventional pyramid-shaped tips for high aspect ratio topography measurements [10], [16], [154], [167], [168]. Moreover, nanowires and nanotubes are claimed to provide a soft scanning capability compared to silicon pyramid-shaped structures, meaning that they can be elastically bent in a case of a high interaction force between the tip and a sample surface. This consequently prevents crash and damages concerning sample surface and the tip itself [16], [158]. This is advantageous particularly for delicate samples such as biological specimens, where performing non-invasive topography and scanning measurements are highly required [167], [169], [170]. The major reported methodologies for fabrication and characterization of nanowire and nanotube scanning tips can be found in the state of the art (section 1.2.3) in more detail. Among the aforementioned probes, silicon nanowire tips not only promised higher accuracy in high aspect ratio measurements, but also they showed higher consistency in the measurements compared to carbon nanotubes [10]. Despite the fact that carbon nanotubes can potentially have a higher Young's modulus compared to silicon nanowires, it can also be strongly diminished by defects, interlayer sliding and hollow structures in carbon nanotubes [171], leading to low mechanical stability and less consistency in measurements. On the other hand, bottom-up synthesized silicon nanowires are single-crystalline structures with the least amount of defects, leading to their mechanical behavior enhancement [171]. The main reason why such probes are not commercialized yet is due to the fact that the fabrication procedures reported so far are elaborate, costly and also not compatible with mass production due to the required individual customizations for each probe. The latter issue can be found more pronounced in approaches such as assembly of the nanowires by using micromanipulators or using FIB techniques (for more details see state of the art, section 1.2.3). With this in mind, the focus of the work here is to establish a fundamental fabrication approach, of which cost-effectiveness, reproducibility and feasibility are the main features. In this work, the basis of the fabrication methodology of silicon nanowire probes consists of nano- (silicon nanowire synthesis) and micro-fabrication (cantilevers), which are discussed in two separate sections. The third section subsequently focuses on the integration of silicon nanowires into the fabricated cantilevers by combining the two previous methods. At last, the fabricated probes were characterized in the AFM apparatus and compared to commonly used probes. Further characterization of silicon nanowire probes was performed via finite element analysis, aiming to find an optimum geometry for nanowires and cantilevers to avoid malfunctions of scanning probes to the utmost extent possible.

### 3.1 Si<sub>3</sub>N<sub>4</sub>-Cantilever Fabrication Using Si<sub>3</sub>N<sub>4</sub>-Membranes

In this work, the fabrication of silicon nanowire scanning probes is composed of two main steps; microfabrication (cantilever) and nanofabrication (silicon nanowire tip). In this section, the cantilever fabrication procedure is demonstrated. So far, the realized methods for AFM cantilever fabrications consist of several microfabrication steps, including lithography, coating and etching processes [172], [173]. Here, an approach is introduced for tipless Si<sub>3</sub>N<sub>4</sub>-cantilever fabrication simply by using Si<sub>3</sub>N<sub>4</sub>-membranes. Producing Si<sub>3</sub>N<sub>4</sub>-membranes is one of the most conventional microfabrication procedures and they are commercially available. They are used for several applications, e.g., as TEM membrane grids and samples for X-ray related studies. However, in this work, instead of using available and commercial Si<sub>3</sub>N<sub>4</sub>-membranes, in-house fabricated and customized membranes are used. Here, a single-crystalline silicon wafer (100), with Si<sub>3</sub>N<sub>4</sub>-films coated on both sides are used as a primary substrate. For this work, low-stress LPCVD (low-pressure chemical vapor deposition) Si<sub>3</sub>N<sub>4</sub>-films were selected for membrane fabrications, which were purchased from Microchemical GmbH. Low-stress fabricated membranes provide a nearly flat surface, which is suitable for patterning micro-sized structures via photolithography. Furthermore, the transparency of fabricated membranes creates an optical contrast, which greatly assists alignment during the photolithography process. For instance, defining cantilever areas with respect to the membrane position becomes quite simple, as membrane areas are optically distinguishable.

In order to fabricate the membranes, at first, photolithography is performed on one side of the substrate, as it is schematically illustrated in **Figure 18** (b) and (c) in order to define the membrane area. Subsequently, the Si<sub>3</sub>N<sub>4</sub>-film is etched using CF<sub>4</sub> and plasma in the areas where the photoresist is removed after the development. Afterward, the photoresist is removed, and the silicon substrate is entirely etched only in the area that silicon is exposed and Si<sub>3</sub>N<sub>4</sub> is removed, using in 20% wt KOH solution at 80 °C (for more details see Appendix, section F). As it is shown in **Figure 18** (e), a Si<sub>3</sub>N<sub>4</sub>-membrane supported by the silicon frame is thus fabricated.

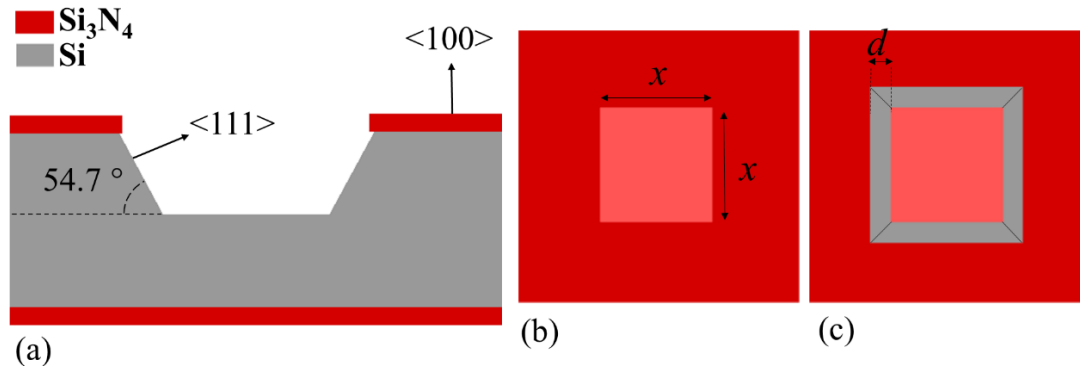


**Figure 18** (a) A silicon wafer sandwiched between two Si<sub>3</sub>N<sub>4</sub>-films. (b) Spin-coated photoresists on both sides of the wafer. (c) Lithography performed on one side of the wafer. (d) Etching Si<sub>3</sub>N<sub>4</sub> in the opening area of the photoresist. (e) Removing the photoresist and etching Si in KOH.

Defining the membrane areas on the backside of the wafer is not so straightforward, as the membrane area on the back of the substrate is not size-wise identical as the membrane areas on the top of the substrate. The reason is that etching silicon in KOH solution takes place anisotropically. The  $\langle 111 \rangle$  planes act as "stop planes" for anisotropic etchants, as the etching rate in the direction of  $\langle 111 \rangle$  planes is considerably lower than other two  $\langle 100 \rangle$  and  $\langle 110 \rangle$  planes [174]–[176]. Furthermore, due to the crystal structure and anisotropic etching process, designing membrane areas such as circular patterns are hardly doable. Therefore, it is important to design membrane areas with sharp edges and sides such as a rectangle, on the backside of the silicon (100) wafer. Moreover, the sides should be parallel or perpendicular with respect to crystal plane  $\langle 110 \rangle$  or the cut edge of the wafers. Last but not least, as it is depicted in **Figure 19** (a), the crystal plane  $\langle 111 \rangle$  has an angle of  $54.7^\circ$  with respect to the crystal plane  $\langle 100 \rangle$ . Therefore, for fabricating a simple square-shaped membrane with the size of  $x^2$  (shown in **Figure 19** (b)), it is required to design a square-shaped structure on the backside of the wafer with a size of  $(x+d)^2$  (shown in **Figure 19** (c)). Here  $d$  is defined as below:

$$d = t / \tan 54.7^\circ = t / 1.412 \quad (3-1)$$

In the above-mentioned relation,  $t$  stands for the thickness of the wafers. Since the used wafers are  $380 \mu\text{m}$  thick,  $d$  is  $269.05 \mu\text{m}$ .

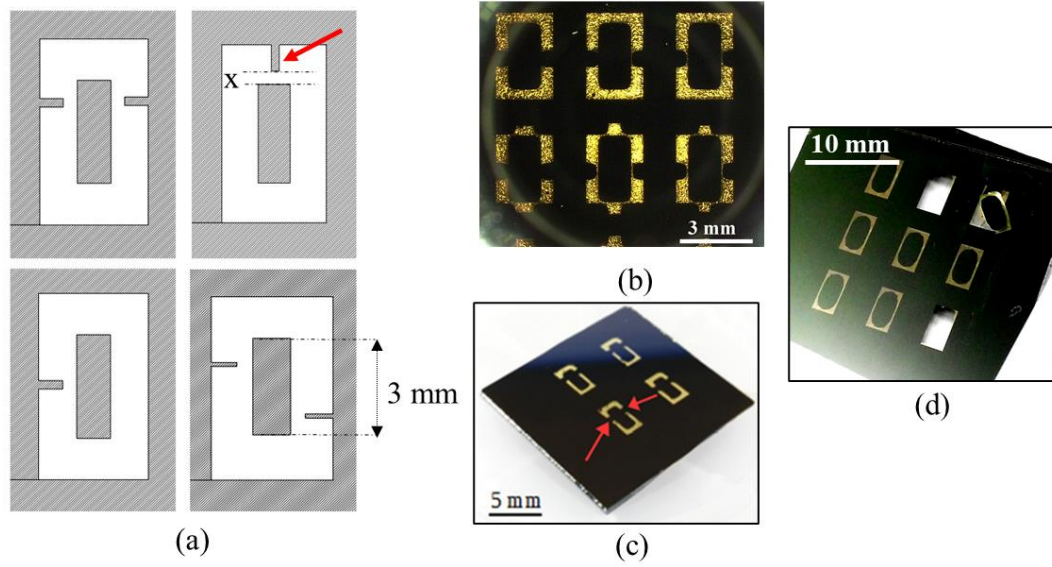


**Figure 19** (a) Schematic illustration of a silicon wafer etched partially in KOH. (b) Schematic illustration of a membrane on the front-side. (c) Schematic illustration of a membrane on the backside.

As the idea of using  $\text{Si}_3\text{N}_4$ -membranes is to fabricate  $\text{Si}_3\text{N}_4$ -cantilevers for AFM applications, the design of the membranes can be further enhanced into the shape of the probes, which would later fit the AFM probe holder. In order to secure the mechanical stability of the membranes, supporting arms were introduced beside the probes, which are indicated by the red arrows in **Figure 20** (c). Due to the fragility in the membranes, the membranes can easily break and get damaged without the supporting arms (**Figure 20** (d)). The supporting arms, indicated by the red arrows in **Figure 20** (c), can be simply broken in order to release the probes after the fabrication process. For this purpose, besides different membrane designs, the variable  $x$  (indicated by the red arrow in **Figure 20** (a))

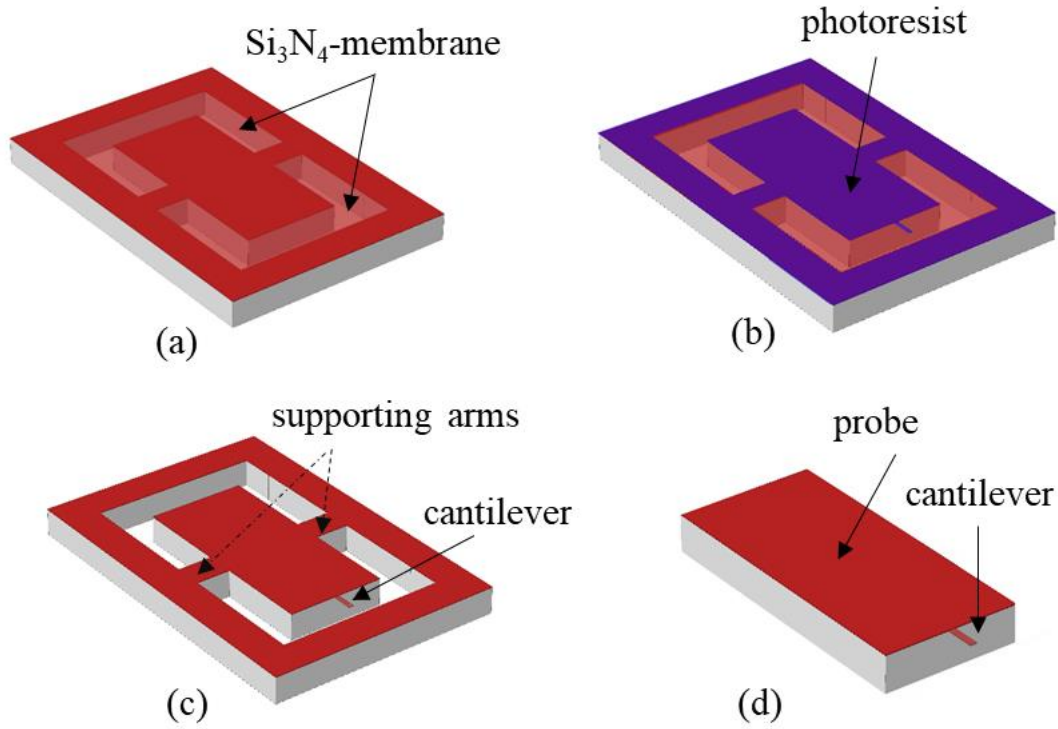


was studied. For instance, for 380  $\mu\text{m}$  silicon wafers, 400  $\mu\text{m}$  is an optimum value for  $x$ , serving the purpose.



**Figure 20** (a) Schematic designs of membranes and supporting arms with the distance of  $x$  from the probe area on the backside of the sample. (b) Fabricated  $\text{Si}_3\text{N}_4$ -membranes with different designs and supporting arms. (c) Fabricated  $\text{Si}_3\text{N}_4$ -membranes. The red arrow indicates the supporting arms. (d) Fabricated  $\text{Si}_3\text{N}_4$ -membranes without supporting arms.

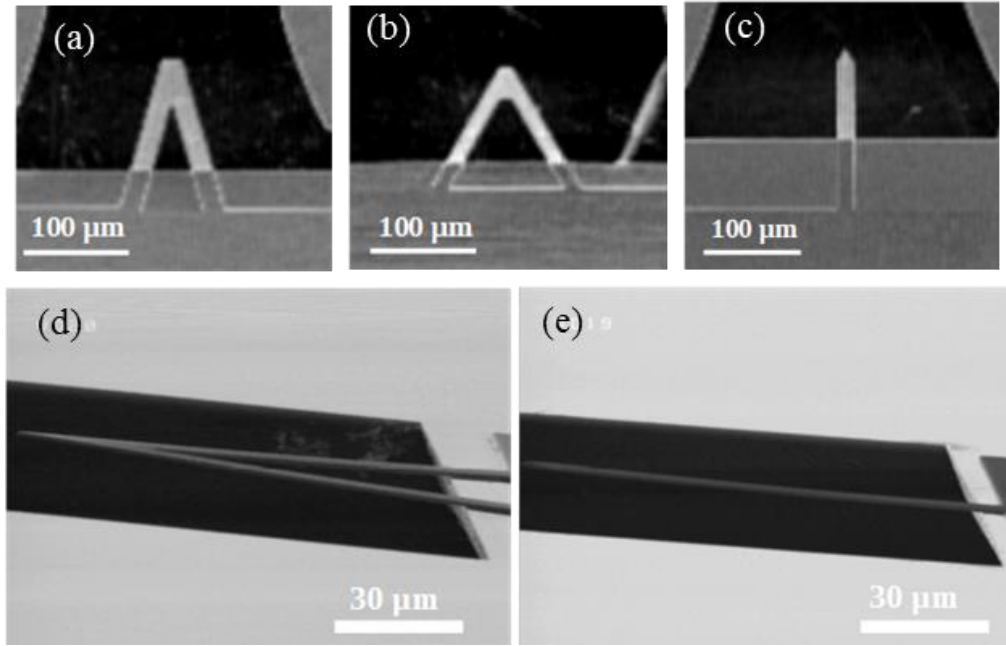
The cantilever fabrication using  $\text{Si}_3\text{N}_4$ -membranes is a relatively simple approach. A schematic illustration of the  $\text{Si}_3\text{N}_4$ -cantilever fabrication procedure is accordingly presented in **Figure 21**. The cantilever areas were simply defined on membranes via one photolithography step. Afterward, the open areas on the developed photoresist were etched using  $\text{CF}_4$  and plasma. After the photoresist removal,  $\text{Si}_3\text{N}_4$ -cantilevers are fabricated. Finally, the probes can be released by breaking the supporting arms. The details of the fabrication procedure can be found in Appendix, section G.



**Figure 21** (a) Schematic illustration of a fabricated  $\text{Si}_3\text{N}_4$ -membrane. (b) Schematic illustration of a developed and patterned photoresist with a cantilever shape on the  $\text{Si}_3\text{N}_4$ -membrane after photolithography. (c) Schematic illustration of the fabricated  $\text{Si}_3\text{N}_4$ -cantilever after etching  $\text{Si}_3\text{N}_4$  and removing the photoresist. (d) Released probe after breaking the supporting arms.

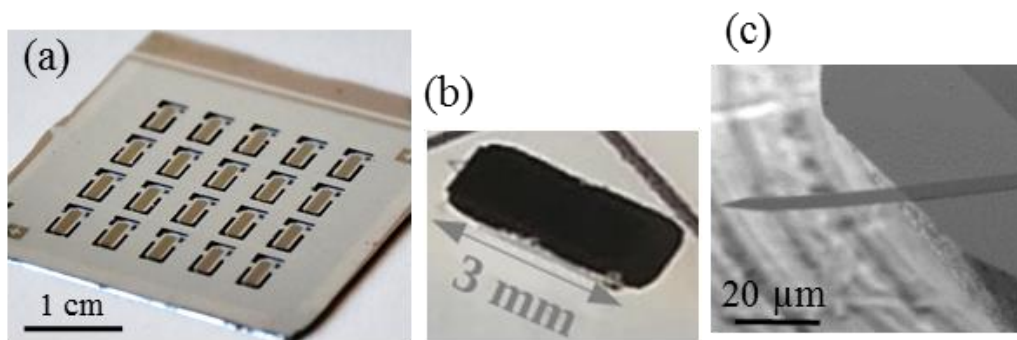
It is simple to define different geometries through photolithography using a lithography mask with different shape and pattern designs (**Figure 22** (a), (b) and (c)). Altering the micro-cantilever geometries results in different spring constants and resonance frequencies [177]. Furthermore, AFM cantilevers are required to be straight and with no bending. The SEM images of fabricated cantilevers are shown in **Figure 22** (d) and (e) for a simple beam and a V-shaped cantilever, respectively. As depicted from the images, the fabricated cantilevers are almost without bending. Besides fabricating a simple cantilever, the fabrication of cantilevers with customized structures is of interest, for instance, for fabricating actuators on cantilevers [178], [179]. Fabrication of customized metal structures on  $\text{Si}_3\text{N}_4$ -membranes is also found to be feasible by a lithography step within the aforementioned fabrication procedure. The corresponding fabrication steps are described in Appendix section **L**. Furthermore, using  $\text{Si}_3\text{N}_4$ -membranes provides a suitable platform for fabrication of nanocrystalline diamond coated cantilevers (see Appendix sections **M** for more details). Diamond coated cantilevers can provide a higher spring constant and alternative material for the fabrication of resonant sensors because of their higher Young's elastic modulus value [180].





**Figure 22** (a) and (b) Light microscope images of top-views of two different fabricated V-shaped  $\text{Si}_3\text{N}_4$ -cantilevers. (c) Light microscope images of a top-view of a rectangular-shaped cantilever beam. (e) and (d) SEM images of side-views of fabricated cantilevers.

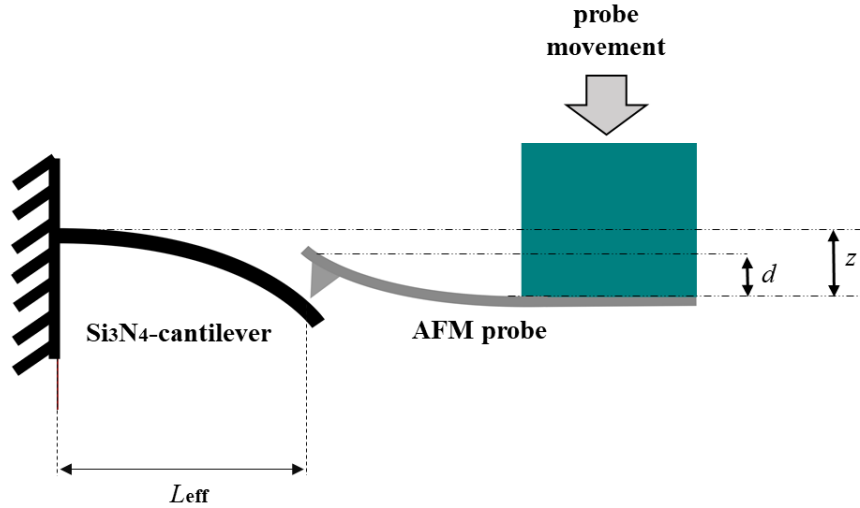
It is possible to fabricate 20 probes composed of tip-less  $\text{Si}_3\text{N}_4$ -cantilevers only on a  $3\text{ cm} \times 3\text{ cm}$  area of a  $\text{Si}_3\text{N}_4$ -Si wafer (see **Figure 23** (a)). The final fabricated probes can be later used in AFM, as they fit size-wise to the AFM probe holder. As mentioned before, cantilevers with different geometries and shapes have different mechanical behaviors, including their spring constant and resonance frequency. In order to investigate and manipulate the mechanical behaviors of the fabricated cantilevers, it is required at first to investigate the Young's elastic modulus of the LPCVD  $\text{Si}_3\text{N}_4$ -film, which is elaborated in the next section.



**Figure 23** (a) Fabricated  $\text{Si}_3\text{N}_4$ -cantilever on 20 in 1 chip. (b) A fabricated probe size-wise compatible with the AFM probe holder. (c) A magnified image of a fabricated  $\text{Si}_3\text{N}_4$ -cantilever.

### 3.1.1 Investigating Young's Elastic Modulus of Si<sub>3</sub>N<sub>4</sub>-Films

There are different values found in the literature for Si<sub>3</sub>N<sub>4</sub>-film Young's elastic modulus [181]. The values are reported ranging from 95 GPa [182] to 370 GPa [183], [184]. The reason for the variation is that Si<sub>3</sub>N<sub>4</sub>-films can be synthesized via different methods and under different synthesis conditions. Therefore, each synthesized film has its own mechanical properties. Here, a method is applied, which is first established by Serre et al. in order to investigate Young's elastic modulus of films [185], [186]. In this method, the micro-mechanical properties are measured by beam bending using AFM in contact mode.

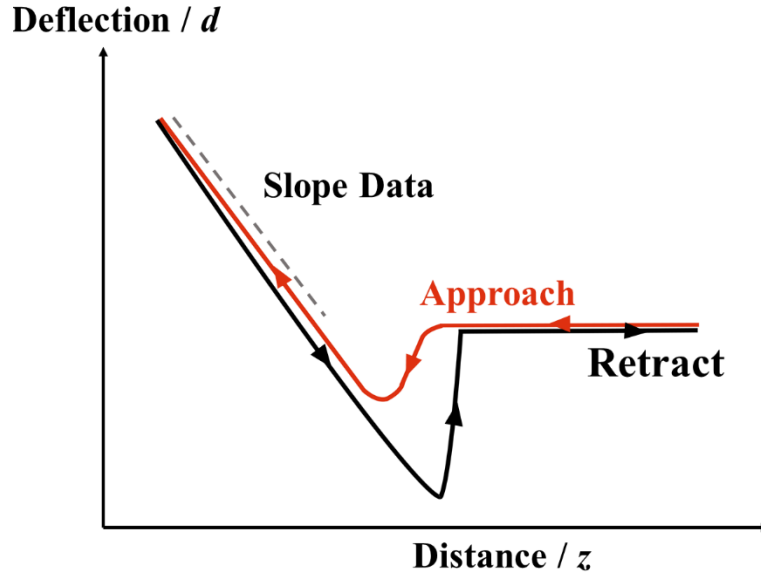


**Figure 24** Beam bending analysis using AFM – A load is applied by AFM probe on the beam, by lowering the probe position (the probe movement is indicated by the grey arrow). The probe deflection is measured by the reflection of the laser light from the back of the AFM cantilever on a photodiode. Here,  $d$  and  $z$  stand for probe deflection and displacement, respectively (based on [185], [186]).

The fabricated beam is bent by a force applied by the AFM probe, as shown in **Figure 24**. The AFM probe movement is precisely controllable by using a piezoelectric stage and the deflection can be accurately measured by the laser reflection from the backside of the cantilever on a photodetector. The probe deflection versus the displacement in  $z$ -direction gives the so-called force graph shown in **Figure 25**. The total displacement is the sum of the AFM cantilever deflection and the cantilever bending. Cantilevers that are elastically bent, follow in principle Hook's law. The equal spring constant ( $K_{eq}$ ) which is a result of two springs in series, can be expressed as followed [185], [186]:

$$\frac{1}{K_{eq}} = \frac{1}{K_{AFM}} + \frac{1}{K_{Cant}} \quad (3-2)$$

Here,  $K_{AFM}$  and  $K_{Cant}$  stand for the spring constant of the AFM cantilever and fabricated Si<sub>3</sub>N<sub>4</sub>-cantilever, respectively.



**Figure 25** Schematic graphic representation of an approach AFM curve. The red and black graph represent respectively the approach and retract behavior of the AFM probe toward and from the beam. The slope of the linear part gives information about Young's elastic modulus (based on [185], [186]).

The spring constant of the fabricated  $\text{Si}_3\text{N}_4$ -cantilever is given then by: [187]

$$K_{cant} = 3EI / (L_{eff}^3(1 - \nu^2)) \quad (3-3)$$

Here,  $L_{eff}$  stands for the length between the base of the fabricated cantilever and the point where the AFM tip contacts the cantilever (**Figure 24**).  $E$  and  $\nu$  represent the Young's elastic modulus and poison ratio of the  $\text{Si}_3\text{N}_4$ -film, respectively.  $I$  is the moment of inertia of the cantilever beam. For a beam with a rectangular cross-section,  $I$  in different axis direction is defined by: [188]

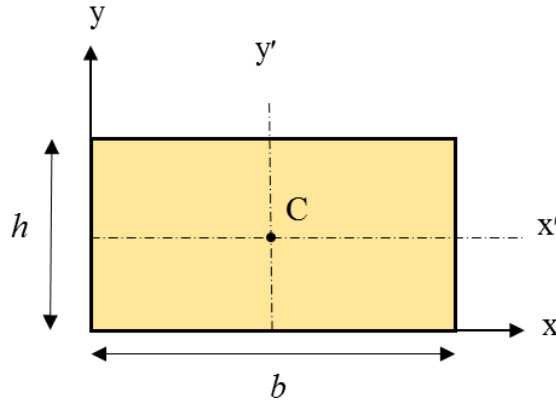
$$I_x = \frac{bh^3}{3}, \quad I_y = \frac{hb^3}{3}, \quad I_{x'} = \frac{bh^3}{12}, \quad I_{y'} = \frac{hb^3}{12} \quad (3-4)$$

Where  $h$  and  $b$  stand for the thickness and the width of the cantilever (see **Figure 26**). What here is applied is the following relation: [188]

$$I_{x'} = \frac{bh^3}{12} \quad (3-5)$$

Then, the spring constant of the cantilever is followed as:

$$K_{cant} = Ebh^3 / 4(L_{eff}^3(1 - \nu^2)) \quad (3-6)$$



**Figure 26** Cross-section of a rectangular beam with a width of  $b$  and thickness of  $h$ . Point  $C$  represents the center of the cross-section.

According to Hook's law, the applied force ( $F$ ) is given below: [184]

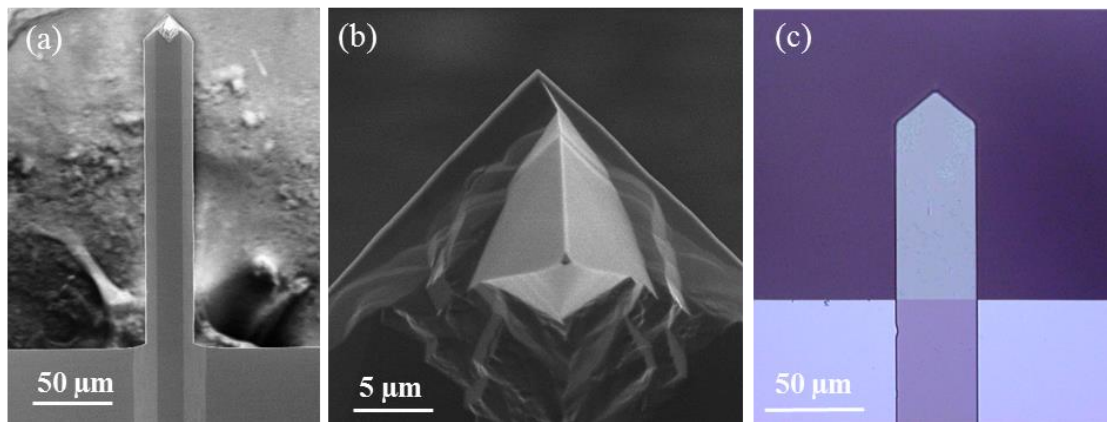
$$F = K_{eq}z = K_{AFM}d \quad (3-7)$$

Where  $d$  and  $z$  stand for the deflection and displacement of the AFM cantilever, respectively. Therefore, the slop in **Figure 25** is given by: [184]

$$\frac{\partial d}{\partial z} = \frac{K_{eq}}{K_{AFM}} \quad (3-8)$$

If the spring constant of the AFM probe is known, the Young's elastic modulus of the cantilever can be readily calculated by considering the aforementioned relations.

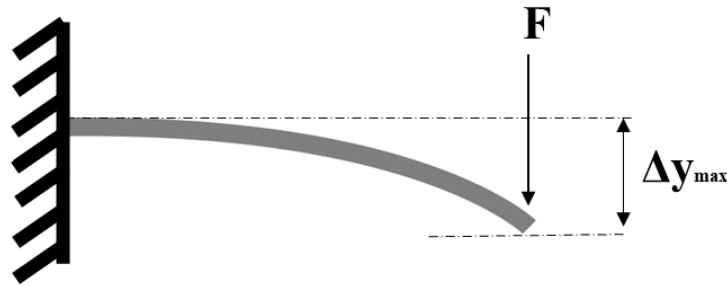
Based on this, an investigation was carried out on three  $\text{Si}_3\text{N}_4$ -cantilevers with a similar shape, as shown in **Figure 27** (c). A silicon AFM probe is used to perform the measurements in AFM (**Figure 27** (a) and (b)). The geometries of the cantilever and the AFM cantilever and tip were measured in SEM. By considering 0.2 value for poisons ratio of  $\text{Si}_3\text{N}_4$  [189], the estimated Young's elastic modulus, according to the mentioned method, is  $204 \pm 18$  GPa. This value is similar to the one reported for LPCVD  $\text{Si}_3\text{N}_4$ -films by Guo et al. [190] and Zhang et al. [191]



**Figure 27** (a) and (b) Top-view images of the AFM cantilever with tip. (c) A  $\text{Si}_3\text{N}_4$ -cantilever used for the Young's elastic modulus investigation of the  $\text{Si}_3\text{N}_4$ -film.

### 3.1.2 Estimation of Cantilever Spring Constant and Resonance Frequency

The determination of the cantilever spring constant is of great importance for AFM applications. In the previous section, it was described how the Young's elastic modulus of  $\text{Si}_3\text{N}_4$ -films could be estimated, which is required for spring constant and resonance frequency estimation. In principle, cantilever geometries affect their spring constants and consequently, their resonance frequencies. By knowing the basic mechanical information, it is possible to estimate these parameters of the fabricated cantilevers. Here, at first, the theoretical models were applied to estimate the aforementioned parameters for the fabricated  $\text{Si}_3\text{N}_4$ -cantilevers. Also, the resonance frequency of cantilevers was simulated via finite element method analysis in COMSOL Multiphysics 5.3 a software. In order to verify the simulated results, they were compared to the analytical solution. Here, for the theoretical and simulation analysis, the fabricated cantilever is considered as a beam with one fixed-end and one free end, as schematically illustrated in **Figure 28**. A load, denoted as  $F$ , is applied on the free end of the beam.



**Figure 28** Beam bending with end-load ( $F$ ) and deflection of  $\Delta y_{\max}$

There is a linear relationship between the applied force and the cantilever deflection, as long as the deformation is in the elastic region [192], [193]. The spring constant of the cantilever is defined as follows: [187]

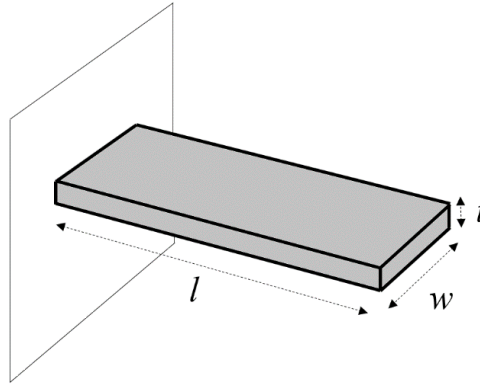
$$K = \frac{F}{\Delta y_{\max}} = \frac{3EI}{l^3} \quad (3-9)$$

Where  $E$ ,  $I$  and  $l$  stand for Young's elastic modulus, second moment of inertia and cantilever length, respectively. By considering a cantilever with a simple rectangular shape and by taking the moment of inertia of a rectangular cross-section into account, the previous relation can be simplified into the following relation:

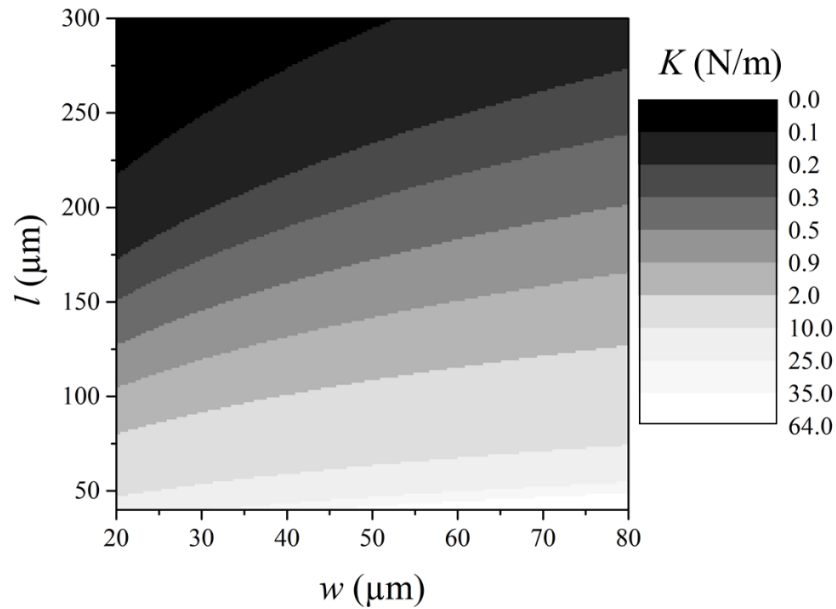
$$K = \frac{Ewt^3}{4l^3} \quad (3-10)$$

Here,  $t$  and  $w$  stand for the thickness and width of a cantilever, respectively (as it is shown in **Figure 29**). In order to have a better overview of this relation, a contour plot of the spring constant is plotted in **Figure 30**, while the cantilever width and length vary in a range of 20-80  $\mu\text{m}$  and 40-300  $\mu\text{m}$ , respectively. As cantilevers, fabricated by the aforementioned fabrication procedure in this work, are almost 1  $\mu\text{m}$  thick  $\text{Si}_3\text{N}_4$  films, for the spring constant estimation, the cantilever thickness is considered to be 1  $\mu\text{m}$ . From the relation

and plot, it can be figured that a wider and shorter cantilever has a higher spring constant or representing a stiffer cantilever compared to a longer cantilever with a smaller width.



**Figure 29** Schematic illustration of a rectangular-shaped cantilever beam.



**Figure 30** Contour plot of spring constant of a rectangular-shaped ( $1 \mu\text{m}$  thick)  $\text{Si}_3\text{N}_4$ -cantilever beam with different lengths ( $l$ ) and widths ( $w$ ).

Natural frequency of cantilevers is composed of different orders ( $n$ ). The natural frequency of a cantilever with a rectangular shape is given by the following relation: [177]

$$f_n = \frac{a_n}{2\pi} \sqrt{\frac{EI}{dwtl^4}} \quad (3-11)$$

Here, the density of the cantilever material, width and thickness of the cantilever beam are denoted as  $d$ ,  $w$  and  $t$ , respectively. The cantilever schematic is accordingly shown in **Figure 29**. As  $1 \mu\text{m}$  thick  $\text{Si}_3\text{N}_4$ -membranes were applied for the cantilever fabrications, the thickness ( $t$ ) of the cantilever is considered to be  $1 \mu\text{m}$ . By considering a cantilever with a simple rectangular shape and by taking the moment of inertia of a rectangular cross-section into account, the previous relation can be simplified to the following relation:

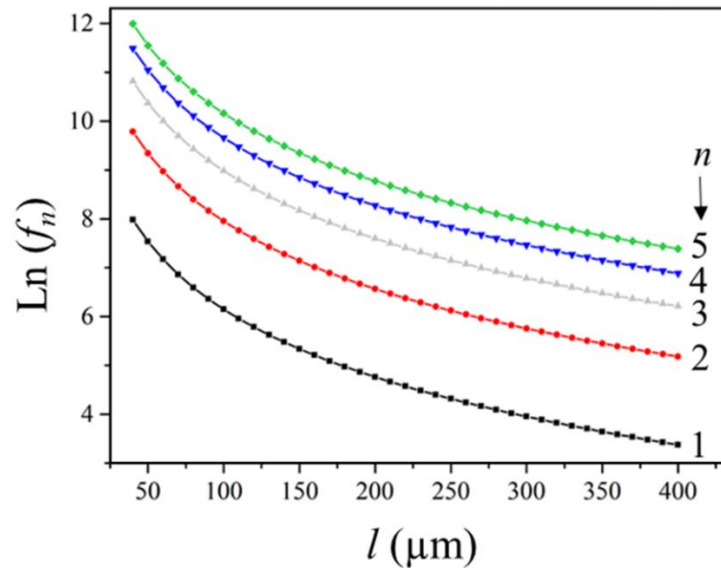
$$f_n = \frac{a_n}{2\pi} \sqrt{\frac{E(\frac{1}{12}wt^3)}{dwtl^4}} = \frac{a_n t}{4\pi l^2} \sqrt{\frac{E}{3d}} \quad (3-12)$$

According to the give relation (3- 12), the resonance frequency variation is mainly affected by changing the cantilever length, as the thickness is a constant value. Here,  $E$  is 204.4 GPa. The parameter  $d$  stands for the mass density, which can vary depending on the synthesis conditions. Here, for the sake of simplicity, this value is considered to be 3100 kg/m<sup>3</sup>, which is close to the density of the bulk silicon nitride material [194], [195]. The  $a_n$  value for the first five orders are given in **Table 1**.

**Table 1**  $a_n$  values for different orders ( $n$ ) of resonance (source: [177]).

order ( $n$ )	$a_n$
1	3.52
2	22.0
3	61.7
4	121
5	200

Based on the theory and the defined relations, the first five orders of resonance frequencies of 1  $\mu\text{m}$  thick  $\text{Si}_3\text{N}_4$ -cantilevers with a rectangular geometry were estimated and plotted in the graph shown in **Figure 31**. The higher the order ( $n$ ) is, the higher the resonance frequency becomes. The longer cantilever has a lower resonance frequency according to the relation and the plotted graph.



**Figure 31** First five orders of resonance frequencies calculated by the analytical solution for a rectangular-shaped 1  $\mu\text{m}$  thick  $\text{Si}_3\text{N}_4$ -cantilever with a width of 40  $\mu\text{m}$ . Here,  $l$  stands for the cantilever length and  $f_n$  represents the resonance frequency of the cantilever with order of  $n$ .

Investigating resonance frequency and spring constant of a rectangular-shaped beam was so far feasible based on the theory and given relations. However, investigating similar parameters for a V-shaped cantilever or more complex geometry is relatively complicated. The main reason is due to the second moment of inertia estimation, as it is more complex



in geometries other than a rectangle. The moment of inertia and the geometry, in general, have a significant impact on the mechanical properties of the beam in terms of resonance frequency and spring constant. Therefore, further analysis of resonance frequency and vibrational mode shapes with different cantilever geometries was carried out by utilizing the finite element method (COMSOL multiphysics 5.3a, in eigenfrequency mode). Prior to simulating the complex structures, a simple rectangular-shaped beam was simulated. Later, they were compared to the analytical solution in order to verify the simulated results. The analysis was performed on a rectangular-shaped 1  $\mu\text{m}$  thick  $\text{Si}_3\text{N}_4$ -cantilever with different lengths and widths and the corresponding results are presented in **Table 2** and **Table 3**. In **Table 2**, the investigated resonance frequencies (first order) of a rectangular-shaped 1  $\mu\text{m}$  thick  $\text{Si}_3\text{N}_4$ -cantilever with a width of 40  $\mu\text{m}$  are given for different cantilever lengths (60, 100, 140, 180 and 220  $\mu\text{m}$ ). They were calculated by both analytical solutions and COMSOL simulations. The final values were compared to each other and the relative errors (%) with respect to the theoretical value are presented as well. The errors are less than 1 %. It should be noted that for shorter cantilevers, the simulated results have a slightly higher deviation from theoretical results. In **Table 3**, the first order of resonance frequency of a rectangular-shaped 1  $\mu\text{m}$  thick  $\text{Si}_3\text{N}_4$ -cantilever with a length of 140  $\mu\text{m}$  is given for different cantilever widths (20, 40, 60, 80 and 100  $\mu\text{m}$ ). Similarly, the analytical results are compared to simulation results. The analytical results suggest that the first order of resonance frequency, which is investigated based on the theory, is independent of the width of the cantilever, unlike the values from simulations. The error is nevertheless less than 2 %. This shows the simulation method can also be applied for the rough estimation of resonance frequencies of a cantilever with different and complex geometries.

**Table 2** *The first order of the resonance frequencies investigated via the analytical solution and COMSOL simulation and the estimated error for a rectangular 1  $\mu\text{m}$  thick  $\text{Si}_3\text{N}_4$ -cantilever with a width of 40  $\mu\text{m}$  and different lengths.*

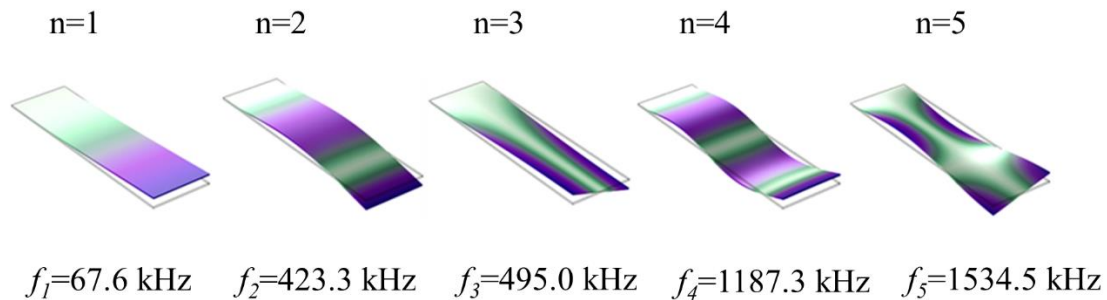
Length	60 $\mu\text{m}$	100 $\mu\text{m}$	140 $\mu\text{m}$	180 $\mu\text{m}$	220 $\mu\text{m}$
Resonance freq. (from analytical solution)	364.96 kHz	131.39 kHz	67.03 kHz	40.55 kHz	27.15 kHz
Resonance freq. (from COMSOL simulation)	370.93 kHz	132.93 kHz	67.63 kHz	40.84 kHz	27.31 kHz
Error (%)	1.64	1.17	0.90	0.72	0.59



**Table 3** The first order of the resonance frequencies investigated via the analytical solution and COMSOL simulation and the estimated error for a rectangular 1  $\mu\text{m}$  thick  $\text{Si}_3\text{N}_4$ -cantilever with a length of 140  $\mu\text{m}$  and different widths.

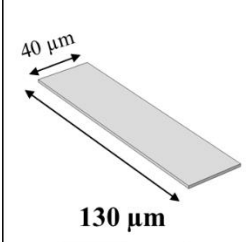
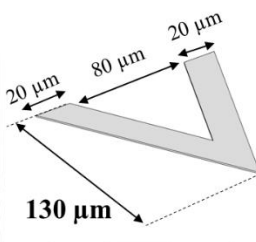
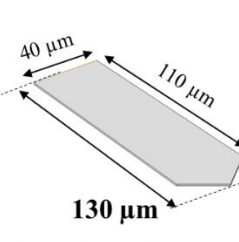
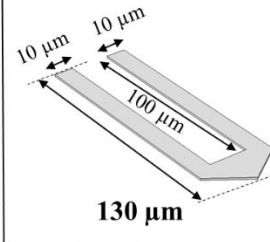
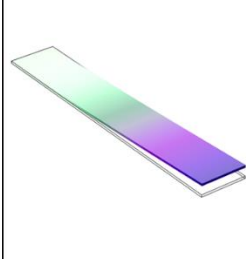
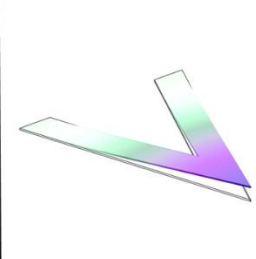
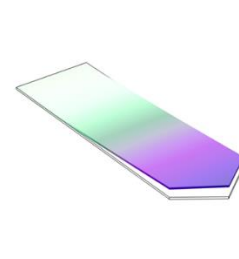
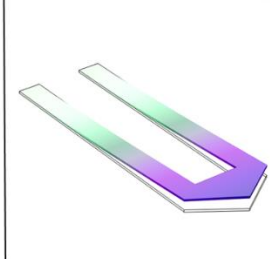
Width	20 $\mu\text{m}$	40 $\mu\text{m}$	60 $\mu\text{m}$	80 $\mu\text{m}$	100 $\mu\text{m}$
Resonance freq. (from analytical solution)	67.03 kHz	67.03 kHz	67.03 kHz	67.03 kHz	67.03 kHz
Resonance freq. (from COMSOL simulation)	67.33 kHz	67.63 kHz	67.86 kHz	68.03 kHz	68.15 kHz
Error (%)	0.45	0.90	1.24	1.49	1.67

Besides the resonance frequency estimation for complex cantilever geometries, the simulation method can provide the vibrational shape modes at each order of resonance frequency. For instance, the first five orders of the resonance frequencies of a  $\text{Si}_3\text{N}_4$ -cantilever, simulated in COMSOL in eigenfrequency mode are shown in **Figure 32**. The rectangular  $\text{Si}_3\text{N}_4$ -cantilever with a thickness of 1  $\mu\text{m}$  is considered for the simulation. The beam width and length are 40  $\mu\text{m}$  and 140  $\mu\text{m}$ , respectively. Here, a resonance order represents the sequence of the resonance frequencies, so that the first order corresponds to the lowest resonance frequency.



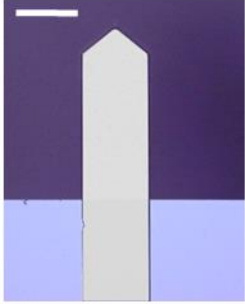
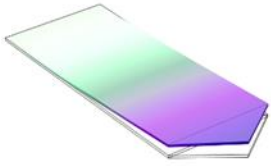

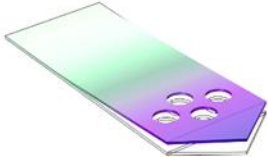

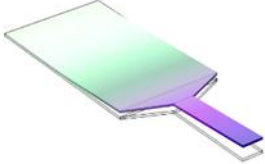

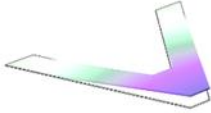

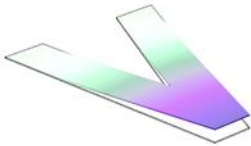
**Figure 32** Simulated first five orders of resonance frequencies of a rectangular 1  $\mu\text{m}$  thick  $\text{Si}_3\text{N}_4$ -cantilever (with a length of 140  $\mu\text{m}$  and width of 40  $\mu\text{m}$ ) and their mode shapes.

After verification of the simulation results, the resonance frequency of the cantilevers with different geometries was simulated. The four cantilevers with different geometries were used, which are shown in **Figure 33**. These cantilevers have the same length of 130  $\mu\text{m}$ , but different shapes. The results depict that the resonance frequencies vary by changing the geometries.

1	2	3	4
			
			
f: 78.5 kHz	f: 99.6 kHz	f: 91.6 kHz	f: 73.3 kHz

**Figure 33** First order of resonance frequencies of 1  $\mu\text{m}$  thick  $\text{Si}_3\text{N}_4$ -cantilevers with four different geometries.

As it was mentioned before, the purpose of the simulation and its verification was to investigate the spring constant and resonance frequencies based on the designed geometries before the fabrication procedure. The most important point here is how the investigated values are close to the actual values by measurements. In **Figure 34**, five fabricated  $\text{Si}_3\text{N}_4$ -cantilevers with different geometries and a thickness of 1  $\mu\text{m}$  are shown. Their resonance frequencies were measured simply by testing it in AFM and also simulated in COMSOL. Their simulated vibrational mode shapes are accordingly shown in **Figure 34**. This shows that simulations and measurements yield similar values for the first order of resonance frequencies. For a better comparison, the relative error with respect to the measured values are calculated. The estimated errors are between 0.76 % to 2.89 %. The deviation of the simulated values can be explained by the fact that the thickness of  $\text{Si}_3\text{N}_4$ -cantilevers changes during the fabrication process and might be lessened within etching  $\text{Si}_3\text{N}_4$  to fabricate the cantilevers. The other point that can be addressed to this issue is that some of the fabricated cantilevers are slightly bent due to the stress in the film. Although the bending is not sever, this may have an impact on the accuracy of the investigated resonance frequency of cantilevers via simulation.

fabricated cantilevers	simulated cantilevers	resonance frequency
		$f_{\text{simulated}}$ : 136.08 kHz $f_{\text{measured}}$ : 137.12 kHz error: 0.76 %
		$f_{\text{simulated}}$ : 134.21 kHz $f_{\text{measured}}$ : 138.20 kHz error: 2.89 %
		$f_{\text{simulated}}$ : 148.25 kHz $f_{\text{measured}}$ : 150.50 kHz error: 1.49 %
		$f_{\text{simulated}}$ : 50.37 kHz $f_{\text{measured}}$ : 51.52 kHz error: 2.23 %
		$f_{\text{simulated}}$ : 37.66 kHz $f_{\text{measured}}$ : 38.15 kHz error: 1.28 %

**Figure 34** Simulated and measured resonance frequency of five fabricated  $\text{Si}_3\text{N}_4$ -cantilevers , their light microscope images (the scale bar is 50  $\mu\text{m}$ ) and mode shapes.

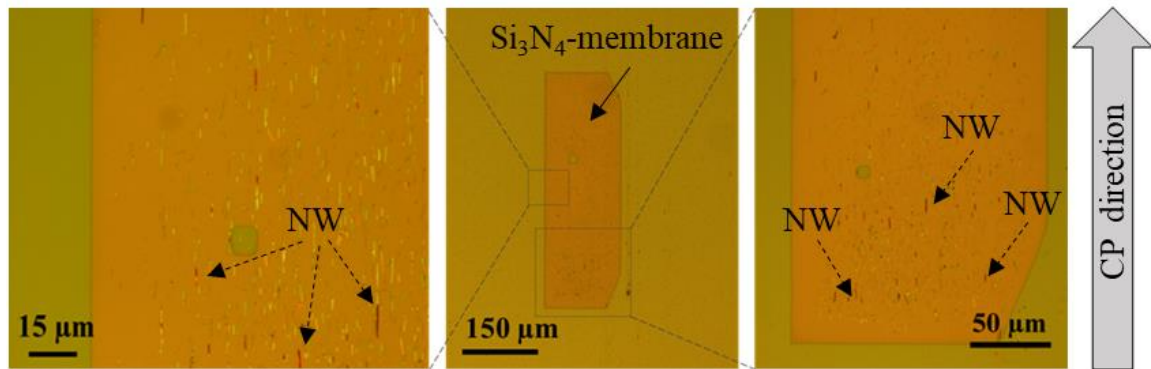
## 3.2 Silicon Nanowire Regrowth

As discussed earlier, silicon nanowire scanning probe fabrication is composed of two main steps; micro- (cantilever and probe) and nano-fabrication (silicon nanowire synthesis). In the previous section, it was described how cantilever and probes can be fabricated and, in this section, only nanowire synthesis for the purpose of fabricating a single silicon nanowire tip will be discussed. The main goal here is to synthesize a single silicon nanowire in a predefined location, which can be utilized for a 3D nano-scale probe or an AFM scanning tip. So far, synthesis of a localized single silicon nanowire is reported by either using a shadow mask [10] or using electron beam lithography for catalyst confinement or using focused ion beam technique [16]. These high-cost techniques are relatively complex and therefore, in this work, using these techniques is not targeted. Instead, a new facile and low-cost approach is explored, which is based on transferring silicon nanowires into a region of interest on a target substrate and so-called regrowth of silicon nanowires using the confined gold catalysts at the tip of the transferred silicon nanowires. Silicon nanowires are here transferred via surface controlled contact printing technique, which is based on dry friction between a nanowire and a target surface [15]. Au-catalyzed silicon nanowires have catalytic parts at their tips [24]. The catalytic part at the tip of silicon nanowires simply provides the confined catalyst area for growing a single silicon nanowire. Therefore, combining the surface-controlled contact printing technique and silicon nanowire regrowth can yield a localized single silicon nanowire. In order to perform the regrowth process, the feasibility of silicon nanowire contact printing on cantilevers and  $\text{Si}_3\text{N}_4$ -membranes should be verified. In this section, surface-controlled contact printing applied on cantilevers and membranes is demonstrated and then further insight into the regrowth process will be indicated.

### 3.2.1 Silicon Nanowire Contact Printing on $\text{Si}_3\text{N}_4$ -Membranes and -Cantilevers

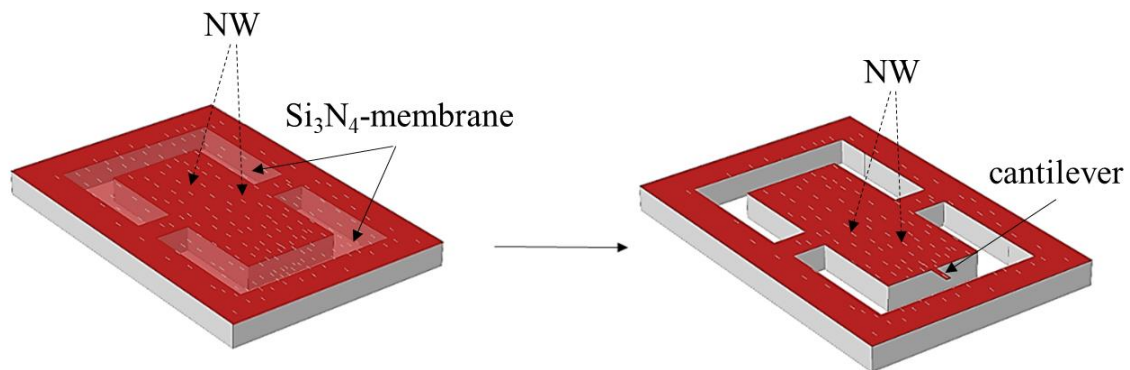
Silicon nanowire contact printing is one of the nanowire assembly techniques, enabling the controlled transfer of nanowires from the growth substrate to pre-defined locations on a target substrate. The fundamental concept of contact printing is based on friction between the nanowires and the receiving substrates. If the frictional force exceeds a critical value, the nanowires will break off the growth substrate and remain on the target surface. As mentioned earlier,  $\text{Si}_3\text{N}_4$ -membranes are used to fabricate cantilevers. Since the intention of the work is to integrate silicon nanowires into cantilevers, the silicon nanowire contact printing technique was applied to  $\text{Si}_3\text{N}_4$ -membranes and cantilevers. The contact printing parameters are presented in Appendix section I. In **Figure 35**, optical microscope images of contact printed silicon nanowires on a 1  $\mu\text{m}$  thick  $\text{Si}_3\text{N}_4$ -membrane are shown. Silicon nanowires, applied for contact printing, were synthesized using 5 nm gold catalyst film on a silicon substrate at a growth temperature of 485 °C, in an atmosphere of  $\text{SiH}_4/\text{He}$  (2%

SiH<sub>4</sub> in He) and H<sub>2</sub> flowing with 100 sccm and 20 sccm, respectively, at a working pressure of 75 mbar for 20 minutes. The synthesized silicon nanowires have an average length of almost 20  $\mu\text{m}$ . As it is shown in the images of **Figure 35**, the membrane was not damaged after contact printing. This technique was applied to more Si<sub>3</sub>N<sub>4</sub>-membranes with different shapes and geometries and it appeared that despite the fragility of membranes compared to bulk substrates, surface-controlled contact printing with a pure shearing motion does not cause damages to membranes with even and flat surfaces.



**Figure 35** Optical light microscope images of contact printed silicon nanowires on a Si<sub>3</sub>N<sub>4</sub>-membrane. The left and right images show closer views of the contact printed areas on the membrane. Here, NW stands for nanowire. The grey arrow on the right side indicates the direction of contact printing (CP).

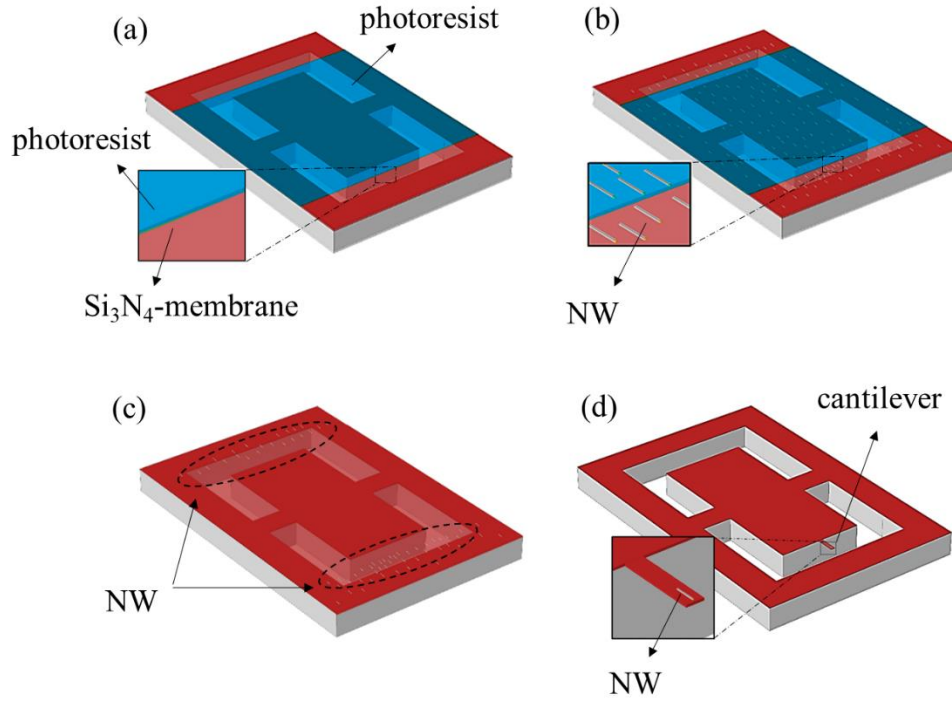
Contact printing silicon nanowires are applicable for fabricating Si<sub>3</sub>N<sub>4</sub>-cantilevers with integrated silicon nanowires. In **Figure 36**, a schematic illustration of contact printed silicon nanowires on a Si<sub>3</sub>N<sub>4</sub>-membrane and subsequently fabricated Si<sub>3</sub>N<sub>4</sub>-cantilevers is given. The fabrication procedure is based on the approach mentioned in section 3.1.



**Figure 36** Schematic illustrations of contact printed silicon nanowires on a Si<sub>3</sub>N<sub>4</sub>-membrane and subsequent fabrication of a Si<sub>3</sub>N<sub>4</sub>-cantilever with contact printed silicon nanowires.

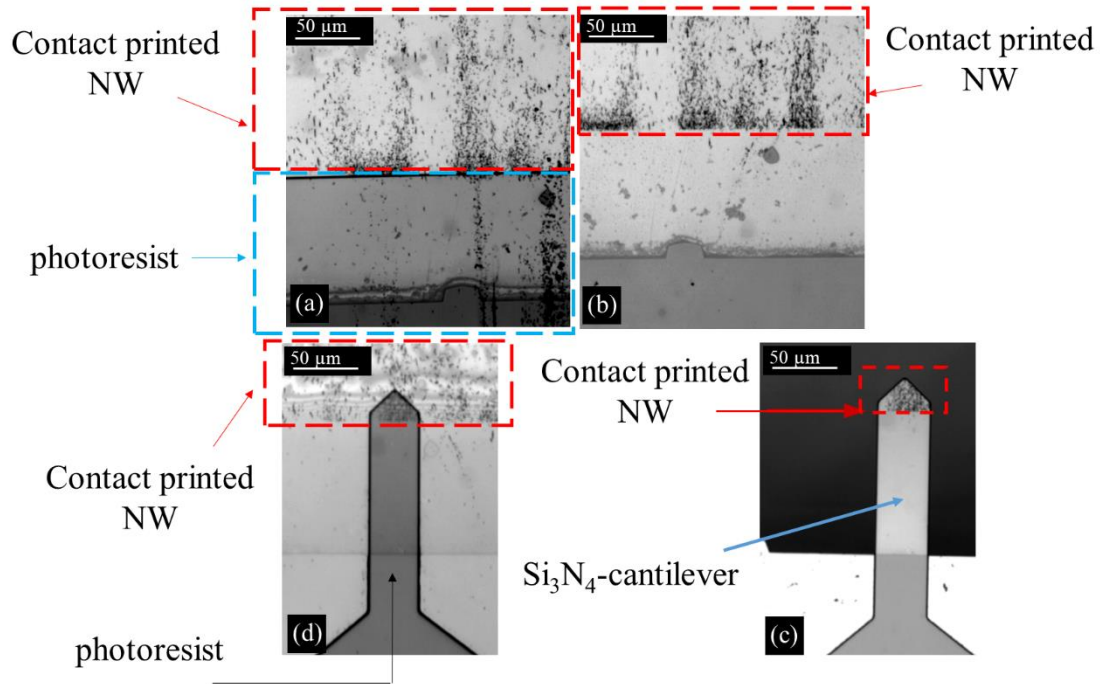
Silicon nanowire contact printing on membranes can be further enhanced by applying a photoresist, which is developed and covering partially membrane surface areas. **Figure 37** (a) shows a schematic of a membrane, partly covered by a developed photoresist. Silicon nanowires are then contact printed on the membrane (b) and after photoresist removal, silicon nanowires remain only on the region, which was not covered by the resist. The rest of the nanowires will be then removed within the resist removal (c) similar to a lift-off

process [87]. At last, cantilevers are fabricated via the mentioned approach in section 3.1 (**Figure 37** (d)). Correspondingly, optical microscope images exemplifying this method, are shown in **Figure 38**. Image (a) indicates the contact printed silicon nanowires on a 1  $\mu\text{m}$  thick  $\text{Si}_3\text{N}_4$ -membrane, partly covered by a photoresist. It can be clearly seen that silicon nanowires on the photoresist area were removed after the photoresist removal. The subsequent cantilever fabrication resulted in the cantilever with silicon nanowires contact printed only on the tip region.



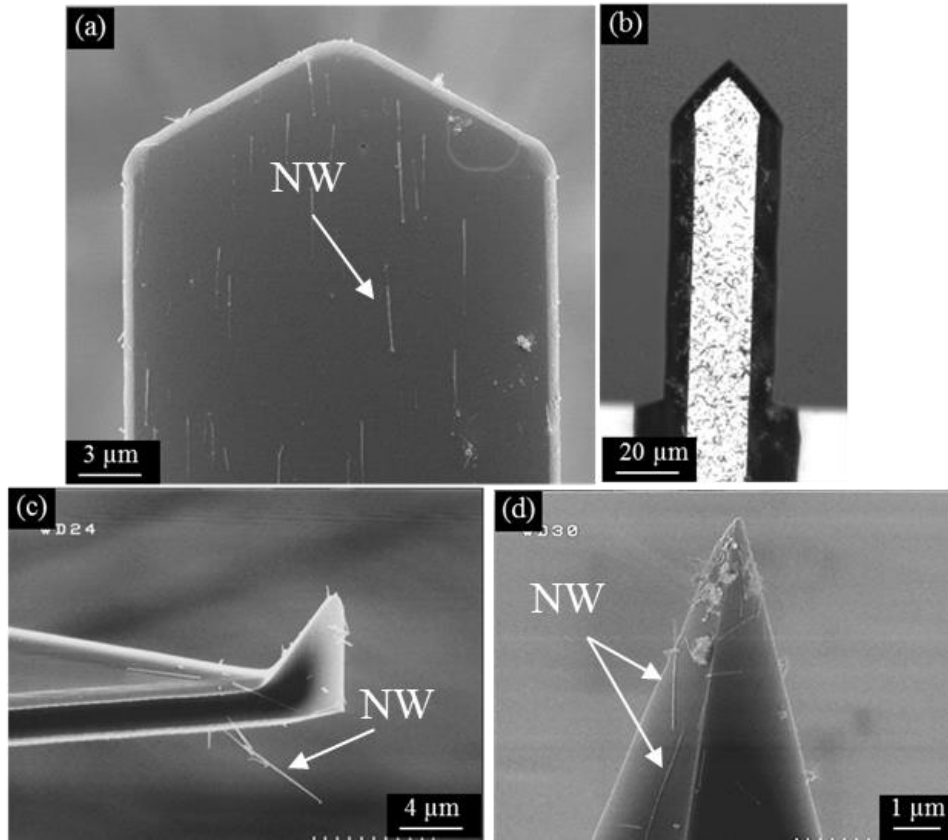
**Figure 37** Schematic illustration of silicon nanowire contact printing on a  $\text{Si}_3\text{N}_4$ -membrane and subsequent cantilever fabrication. (a) Performing one step lithography to pattern a photoresist and remove the resist partially on the  $\text{Si}_3\text{N}_4$ -membrane area. (b) Performing silicon nanowire contact printing. (c) Removing the photoresist after the lithography step. (d) Fabrication of a  $\text{Si}_3\text{N}_4$ -cantilever.





**Figure 38** (a) Optical light microscope images of the contact printed silicon nanowires on a  $\text{Si}_3\text{N}_4$ -membrane with a developed photoresist. The dashed red and blue squares indicate the location of the contact printed silicon nanowires (NW) and the patterned photoresist, respectively. (b) Contact printed silicon nanowires (NW) after the photoresist removal. The nanowire location is indicated by the red dashed square. (c) Patterning photoresist into a cantilever area on the  $\text{Si}_3\text{N}_4$ -membrane via the photolithography process. (d) Cantilever fabrication after etching  $\text{Si}_3\text{N}_4$  in  $\text{CF}_4$  and plasma and removing the photoresist. The red dashed square indicates the region on the cantilever where the contact printed silicon nanowires remained after the photoresist removal. The blue arrow indicates the fabricated cantilever.

Silicon nanowire contact printing can be performed not only on membranes but also directly on cantilevers. The contact printing parameters are presented in Appendix section I. Pure shearing motion of the nanowire substrate over the membrane within contact printing does not cause breakage or damage for cantilevers with or without a tip. The main advantage of silicon nanowire contact printing directly on cantilevers is to apply it on cantilevers with tips and cantilevers made of different materials, for instance, silicon (with a higher spring constant) and not only on the fabricated  $\text{Si}_3\text{N}_4$ -cantilevers from membranes. Some examples of contact printed silicon nanowires on cantilevers are shown in **Figure 39**. The main drawback of this method is that selective contact printing cannot be achieved directly on cantilevers, as performing a microfabrication process is quite challenging. Due to the small area on cantilevers, spin-coating photoresists homogeneously is indeed demanding. So far, dry resist-sheets were reported for performing photolithography directly on cantilevers. [88] However, they can not be applied as a catcher, as in this case, the resist removal after silicon nanowire contact printing is challenging. Therefore, further developments are required to define the removable catchers on the cantilever and with the available technologies, the fabrication of the catchers is not yet possible.



**Figure 39** SEM images of contact printed silicon nanowires directly on a pre-fabricated  $\text{Si}_3\text{N}_4$ -cantilever (a), a tipless Si-cantilever (b), Si-cantilevers with pyramidal tips (c and d). Here, the nanowires are indicated with the white arrows and NW stand for nanowire.

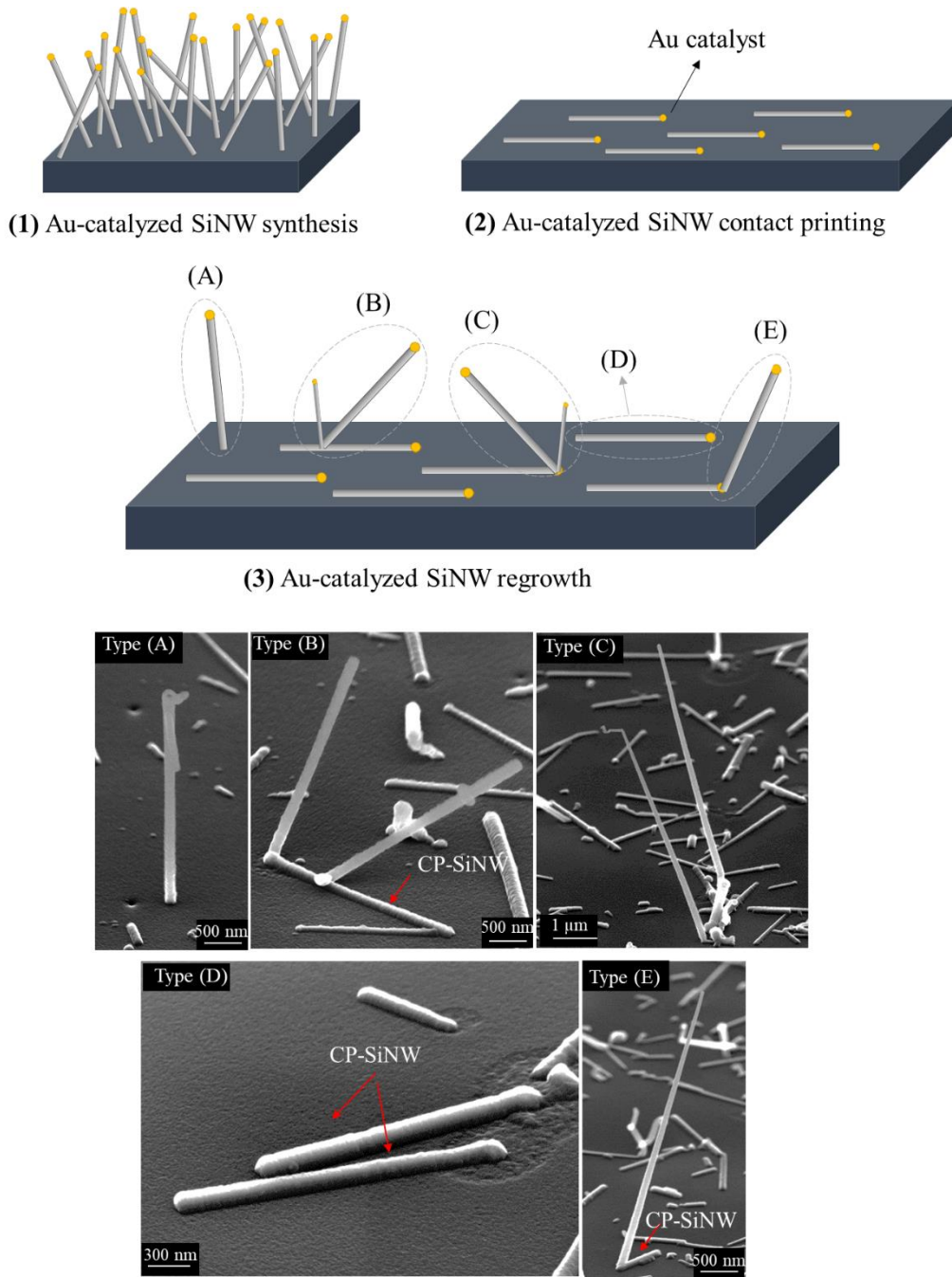


### 3.2.2 Silicon Nanowire Regrowth via VLS

As it was mentioned before, the regrowth process is based on the contact printing method and using the catalyst particles at the tip of the contact printed silicon nanowires for the silicon nanowire synthesis. The regrowth strategy is employed in this work for the fabrication of silicon nanowire scanning probes. The regrowth process is composed of three steps, as schematically illustrated in **Figure 40**:

- (1) Silicon nanowire synthesis using gold catalyst.
- (2) Silicon nanowire contact printing onto a target substrate.
- (3) Silicon nanowire regrowth.

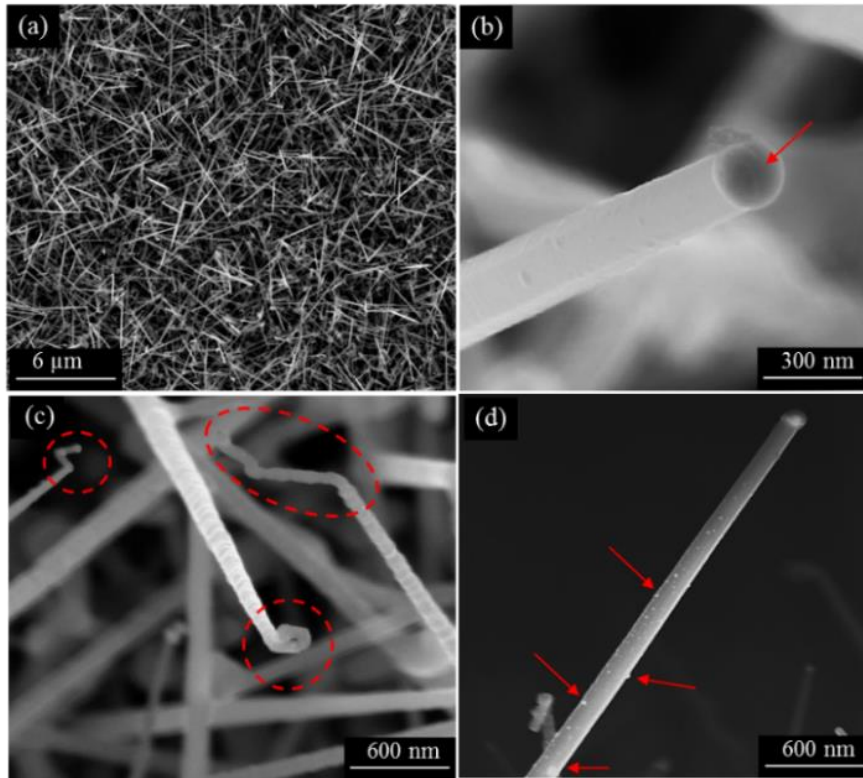
Silicon nanowires are mainly synthesized via a VLS bottom-up approach using gold catalysts [24]. After silicon nanowire contact printing, the gold catalysts at their tips are reused for another VLS synthesis of nanowires. Synthesized silicon nanowires possess a thin oxide layer that encapsulates the catalyst tip too. The oxide formation on the catalyst can be due to oxygen residues in the non-high vacuum reactor utilized for silicon nanowire synthesis. Furthermore, the catalyst is not pure gold anymore but a eutectic gold-silicon alloy. [44] Therefore, the formation of a native oxide layer around the catalyst particle is inevitable. The oxide layer must be removed using 2 % buffered hydrofluoric acid. Afterward, the silicon nanowire regrowth is followed. At the end, the different regrowth modes appear, which are schematically shown and categorized from (A) to (E) in **Figure 40**. Besides, the SEM images, exemplifying the regrowth modes, are accordingly shown. The silicon nanowire synthesis and regrowth were carried out at a growth temperature of 550 °C, in an atmosphere of SiH<sub>4</sub>/He (2% SiH<sub>4</sub> in He) and H<sub>2</sub> flowing with 20 sccm and 80 sccm, respectively at a working pressure of 10 mbar for 1 hour. The SEM image of the primarily used silicon nanowires for the regrowth is shown in **Figure 41** (a).



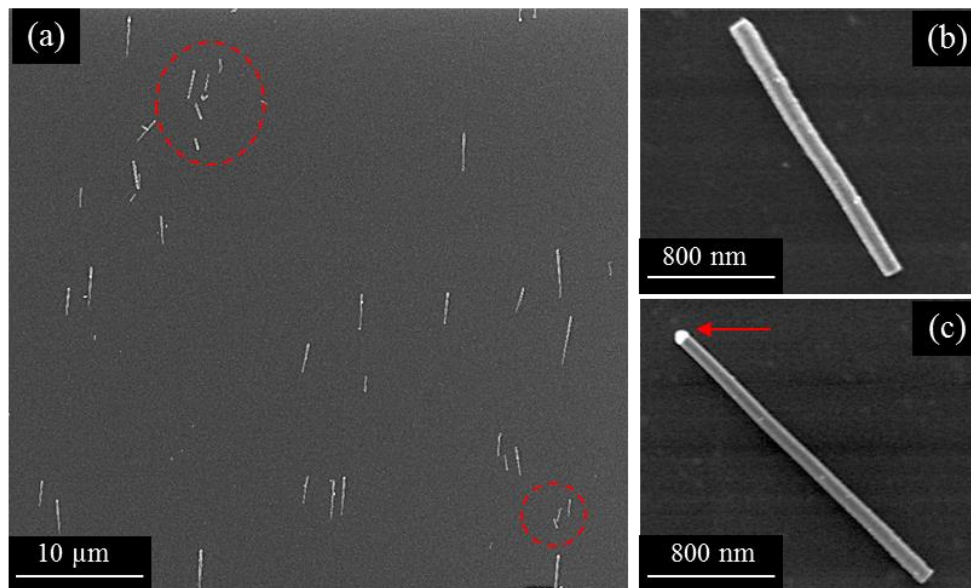
**Figure 40** Schematic illustrations of the regrowth process; (1) Synthesis of silicon nanowires (SiNW) using gold catalyst. (2) Contact printing silicon nanowires (SiNW) on a planar surface. (3) Performing a second synthesis process (regrowth). This ends up with five modes from (A) to (E). For the fabrication of a single silicon nanowire scanning tip, type (E) is the favored one. In the SEM images, CP-SiNW stands for contact printed silicon nanowires.

Type (A) shows a mode, in which a silicon nanowire is synthesized on a target surface, but not from a tip of contact printed nanowires, as it was expected. This can be due to the fact that at high temperatures, the Au/Si-droplets can migrate on the surface [196]. Consequently, nanowire synthesis takes place not exactly on the tip of nanowires. Type (B) and (C) show the synthesis of more than one silicon nanowire, which can be attributed to a larger catalyst area or migration of droplets and its merging can provide a larger catalyst

particle for nanowire synthesis. According to SEM images of Au-catalyzed silicon nanowires shown in **Figure 41** (d), the gold particles can also be observed on the silicon nanowire stem. This is most likely due to the migration of Au/Si-droplets, which is enhanced at high temperatures. These gold particles can give rise to the probability of the regrowth type (C). Silicon nanowires also appear with different tip formations. Correspondingly, **Figure 41** (b) shows a nanowire with a gold catalyst particle at the tip, indicated by the red arrow, while **Figure 41** (c) shows a nanowire with a different tip formation, on which a gold particle cannot be distinguished. Such nanowires cannot probably contribute to the regrowth process. Therefore, they remain inactive for the regrowth process. The other reason for the creation of the type (D) is that, within the contact printing steps, silicon nanowires can break from more than just one point on their stems. As a result, silicon nanowires can remain on a target surface with different lengths. This means that not all the contact printed nanowires on a target surface have a catalytic part. Therefore, not all silicon nanowires are involved in the regrowth process due to the lack of a catalyst. In **Figure 42** (a), SEM images of contact printed silicon nanowires are shown on a silicon surface and the red dashed circle areas show silicon nanowires with shorter lengths, which can correspond to silicon nanowire breakage at different points at their stems. Correspondingly, the magnified images of two nanowires after contact printing are shown without a catalyst tip in **Figure 42** (b) and with Au-catalyst at the tip in **Figure 42** (c), indicated by the red arrow. Finally, the type (E) is the most favored mode for the fabrication of a silicon nanowire scanning tip. This is the type that the regrowth is designed for. For the type (E), two scenarios can be considered. In one case, the liquid catalyst migrates on the surface of nanowires and substrates, which leads to the random orientation of regrown silicon nanowires. In the second case, the liquid catalyst droplet remains at the initial position at the silicon nanowire tip. The regrowth, in this case, is very similar to a crystal kink [197], [198]. Kinking is reported to form different angles depending on the growth direction. [199] For instance, one of the reported angles is  $90^\circ$ , which can be an ideal angle for the regrown silicon nanowire scanning tip.

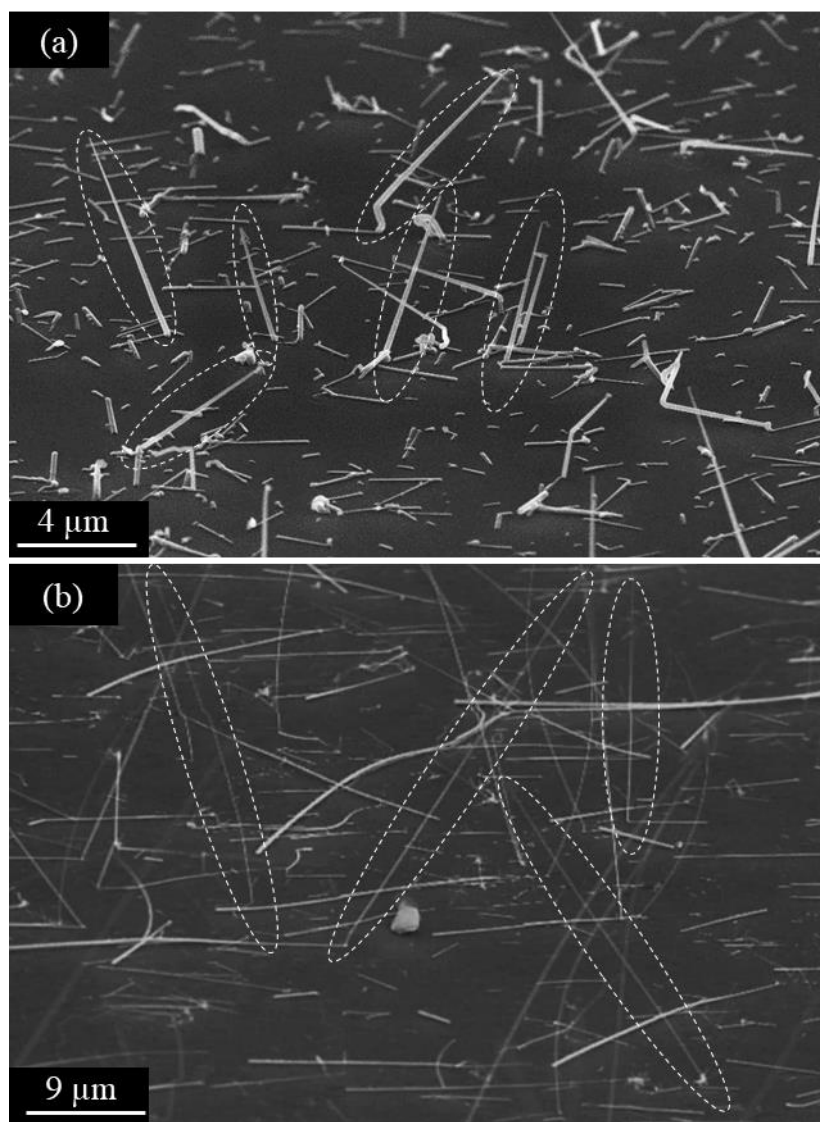


**Figure 41** (a) Synthesized Au-catalyzed silicon nanowires (b) A silicon nanowire from (a) with Au-catalyst at the tip (indicated by the red arrow). (c) Silicon nanowires from (a) without a catalyst tip. The silicon nanowire tips are indicated by the dashed red circles. (d) Au-particles on the nanowire stem (indicated by the red arrows).



**Figure 42** (a) Contact printed Au-catalyzed silicon nanowires on a silicon surface. The red dashed circles indicate nanowires with shorter lengths. These nanowires are probably broken into a few pieces during the contact printing process. (b) and (c) show two contact printed silicon nanowires without catalyst and with Au-catalyst (indicated by the red arrow), respectively.

All mentioned regrowth types can take place within the regrowth process, and the synthesis conditions and contact printing have presumably a significant impact on the domination of one of the regrowth modes. For instance, two growth conditions are employed in this work, which are demonstrated in Appendix in section **D**, **Table-A 8**. Basically, contact printed silicon nanowires provide the main catalyst particles for the regrowth process. Therefore, any improvements in selectivity in contact printing leads to a more enhanced localized regrowth process. Furthermore, modifying the regrowth conditions, including the gas pressure and temperature, is one of the most critical factors for the domination of one of the regrowth modes. Presumably, the main differences in the regrowth modes are initiated by the gold particle migration on the surface. For instance, the higher the temperature, the higher the migration of gold particles. Correspondingly, **Figure 43** shows examples of two regrowth processes. Experiments were carried out under two different synthesis conditions. Image (a) depicts contact printed and regrown Au-catalyzed silicon nanowires on a silicon surface. The primary and regrown silicon nanowires were synthesized at a growth temperature of 550 °C, in an atmosphere of SiH<sub>4</sub>/He (2% SiH<sub>4</sub> in He) and H<sub>2</sub> flowing with 20 sccm and 80 sccm, respectively at a working pressure of 10 mbar for 1 hour. Image (b) shows contact printed and regrown Au-catalyzed silicon nanowires on a silicon surface. The primary and regrown silicon nanowires were synthesized at a growth temperature of 485 °C, in an atmosphere of SiH<sub>4</sub>/He (2% SiH<sub>4</sub> in He) and H<sub>2</sub> flowing with 100 sccm and 20 sccm, respectively at a working pressure of 75 mbar for 20 minutes. For instance, it was observed that in comparison with the primary growth conditions, a lower growth temperature at 485 °C, an increased working pressure of 75 mbar, and a higher SiH<sub>4</sub> partial pressure (100 sccm SiH<sub>4</sub>/He, 20 sccm H<sub>2</sub>) apparently increase the probability of initiating the ideal regrowth mode (type (E)). According to the SEM images, the regrowth process in terms of density and modes are quite different in these two conditions. Therefore, understanding the role of parameters in dominating the regrowth mode is very important. However, this scope of study demands a higher amount of experiments, which was not carried out in this work and requires further study and investigation in the future.



**Figure 43** (a) Contact printed Au-catalyzed silicon nanowires on a silicon surface. The primary and regrown silicon nanowires were synthesized at a growth temperature of 550 °C, in an atmosphere of  $\text{SiH}_4/\text{He}$  (2%  $\text{SiH}_4$  in He) and  $\text{H}_2$  flowing with 20 sccm and 80 sccm, respectively at a working pressure of 10 mbar for 1 hour. (b) Contact printed Au-catalyzed silicon nanowires on a silicon surface. The primary and regrown silicon nanowires were synthesized at a growth temperature of 485 °C, in an atmosphere of  $\text{SiH}_4/\text{He}$  (2%  $\text{SiH}_4$  in He) and  $\text{H}_2$  flowing with 100 sccm and 20 sccm, respectively at a working pressure of 75 mbar for 20 minutes. In both SEM images, the white dashed circles indicate the regrown silicon nanowires.

### 3.3 Silicon Nanowire Probe Fabrication

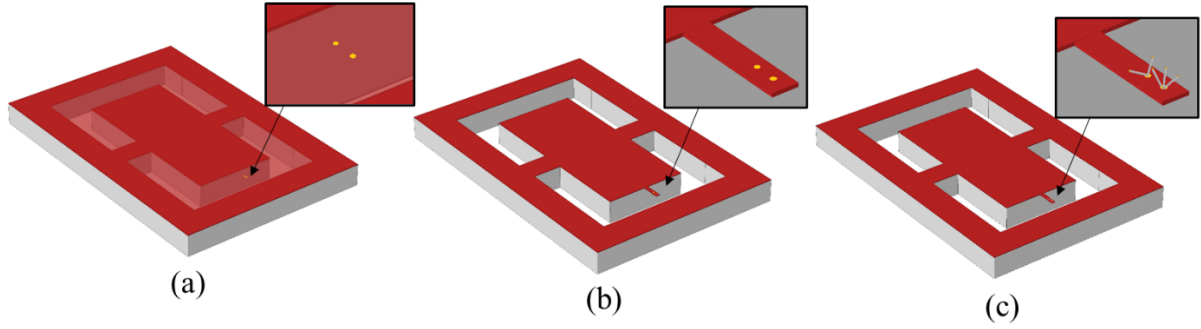
This section focuses mainly on the integration of silicon nanowires into fabricated AFM probes and it is first reported and discussed by confining the catalyst area on the cantilever by applying photolithography for micro patterning and a lift-off process [200]. Afterward, the fabrication of silicon nanowire probes using the regrowth approach is described. Further analysis and characterization of the fabricated probes by AFM and via simulations are discussed.

#### 3.3.1 Confining the Catalyst Area on Cantilevers

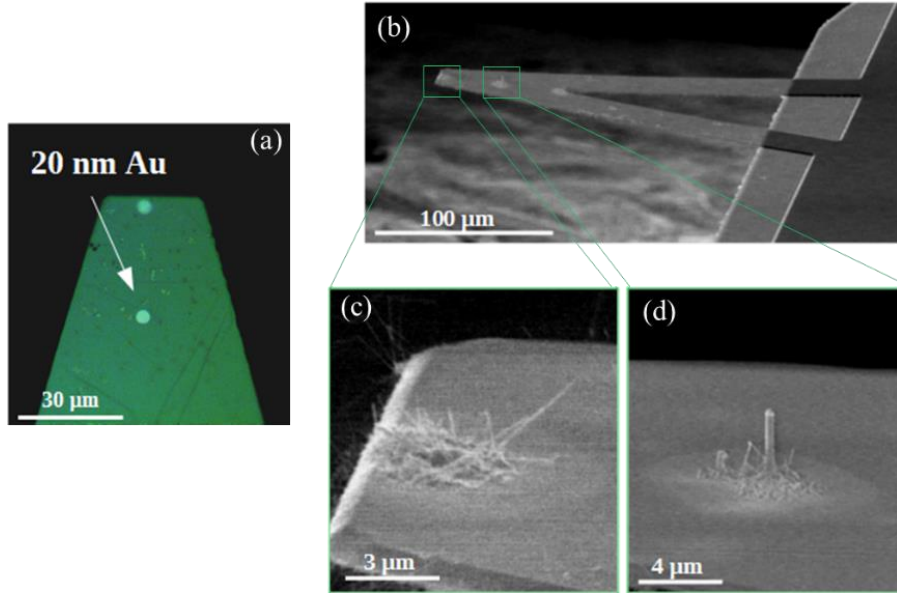
Lift-off processes are a well-known strategy in microfabrication to create micro-sized patterned metal layers on a planar surface. In the case of growing a single silicon nanowire via VLS synthesis, it is of interest to confine the catalyst areas (mainly gold) down to 1-2  $\mu\text{m}$  and even smaller depending on the growth conditions and the thickness of the catalyst layer [201]. As a matter of fact, the resolution of confined areas depends mainly on the type of applied lithography techniques. One of these types known as electron beam lithography (EBL) is a technique by which resolutions down to a few hundred nanometers can be achieved. However, it can only be applied to electrically conductive samples [202]. Since  $\text{Si}_3\text{N}_4$ -membranes are electrically insulating substrates [203], using EBL is a hardly compatible fabrication technique. Additionally, using EBL is rather an upscale fabrication procedure for mass production, while the motivation of the fabrication process here is to avoid any costly and complex approaches. Therefore, UV photolithography was chosen to pattern photoresists on  $\text{Si}_3\text{N}_4$ -membranes. After the membrane fabrication (described in section 3.1), a photoresist was spin-coated on membranes and subsequently, after lithography and development, a 20 nm thick Au-layer was thermally evaporated. After a lift-off process, circular gold areas were structured with diameters of 5  $\mu\text{m}$  on the surface of the membranes, as schematically shown in **Figure 44** (a). The optimum and possibly smallest areas to achieve are around 5  $\mu\text{m}$  with a thickness of 20 nm. Notably, the poor adhesion of the gold layer on the  $\text{Si}_3\text{N}_4$  surface [204] creates challenges for the lift-off process and specifically within the cantilever fabrication, thinner gold layers can simply fall off the surface. As a pure gold catalyst was required for the silicon nanowire synthesis, using adhesion promoters were avoided. However, the gold layer with the mentioned dimension remained nearly intact after the cantilever fabrication process, shown in **Figure 44** (b) and **Figure 45** (a). The as-fabricated cantilever was then inserted into the nanowire CVD tube, in order to synthesize silicon nanowires. Under the growth condition (growth temperature: 550 °C, pressure: 10 mbar,  $\text{SiH}_4/\text{He}$  (2% dilution): 20 sccm,  $\text{H}_2$ : 80 sccm, time: 1 h) more than one silicon nanowire was grown in each area. The schematic illustration of the fabrication procedure is shown in **Figure 44** (c) and SEM images of a readily fabricated cantilever with synthesized silicon nanowires are presented in **Figure 45** (b), (c) and (d). This shows that seemingly the confinement via photolithography does not suffice for a single silicon nanowire growth. Therefore, an alternative technique is required to provide the sufficiently small gold areas or particles for the growth of a single silicon



nanowire tip. This alternative technique, which is based on the silicon nanowire regrowth, is described fully in the next section.



**Figure 44** Schematic illustrations of the silicon nanowire probe fabrication by confining catalyst areas. (a) Confined catalyst areas on a  $\text{Si}_3\text{N}_4$ -membrane after lithography and lift-off processes. (b) Fabrication of cantilevers on membranes after a lithography step and photoresist removal. (c) Silicon nanowire growth on the cantilever.

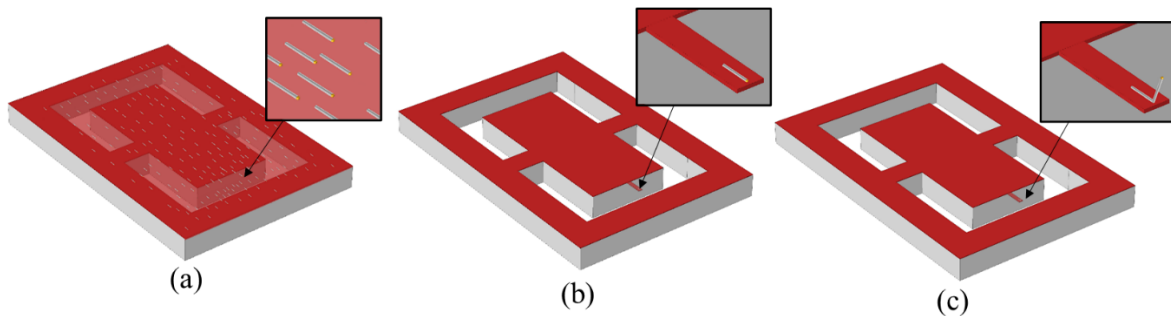


**Figure 45** (a) Optical light microscope image of confined catalyst areas (20 nm thick Au-film) on a fabricated  $\text{Si}_3\text{N}_4$ -cantilever. (b) SEM image of synthesized silicon nanowires on the  $\text{Si}_3\text{N}_4$ -cantilever. (c) and (d) SEM images of magnified views on synthesized silicon nanowires in two locations on the cantilever.



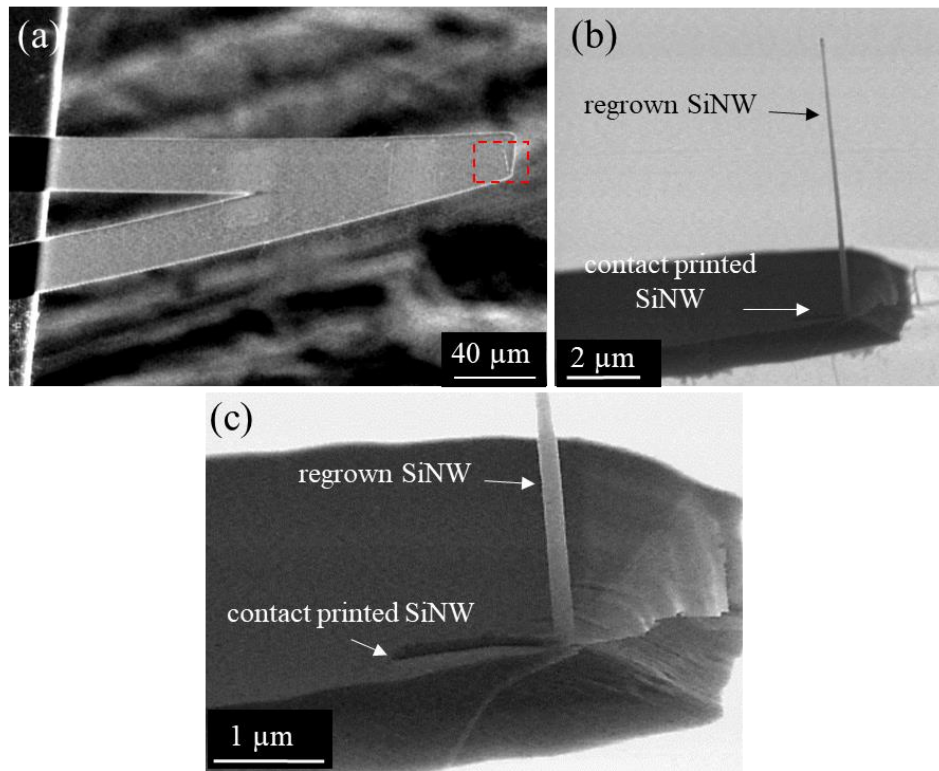
### 3.3.2 Silicon Nanowire Regrowth on Membranes and Cantilevers with or without a Tip

Silicon nanowire regrowth is a strategy to grow a single silicon nanowire. This technique was applied for the fabrication of silicon nanowire AFM probes, in this work. The schematic illustrations of the corresponding fabrication procedure are shown in **Figure 46**. At first, Au-catalyzed silicon nanowires were contact printed on  $\text{Si}_3\text{N}_4$ -membranes, as discussed in section 3.2. Afterward, cantilevers were fabricated. At last, after the photoresist removal, the fabricated cantilevers were inserted in 2% buffered hydrofluoric acid to remove the oxide layers around the silicon nanowire catalyst. Subsequently, the fabricated cantilevers were transferred to the NWCVD tube for the VLS growth.



**Figure 46** Schematic illustrations of the silicon nanowire probe fabrication using the contact printing and regrowth methods. (a) Contact printed silicon nanowires on a  $\text{Si}_3\text{N}_4$ -membrane. (b) Fabrication of a cantilever on the membrane after a lithography step and the subsequent photoresist removal. (c) Silicon nanowire regrowth on the cantilever.

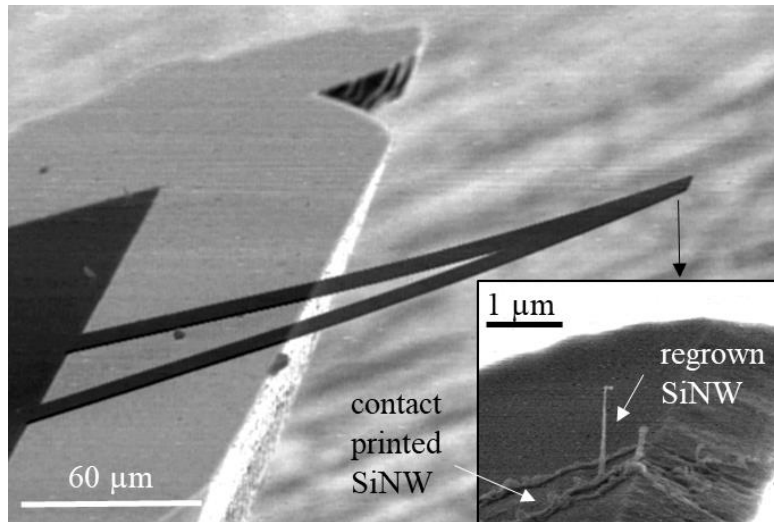
**Figure 47** shows SEM images of a V-shaped cantilever, on top of which a nanowire is synthesized via the regrowth strategy. At first, nanowires were contact printed on a  $\text{Si}_3\text{N}_4$ -membrane. Then, a V-shaped cantilever was fabricated. The V-shaped cantilever fabrication procedure is the same as the one for the fabrication of rectangular cantilevers, as mentioned in section 3.1. **Figure 47** (c) clearly shows how the nanowire tip was grown from the tip of a contact printed silicon nanowire. The regrown silicon nanowire is oriented nearly perpendicular with respect to the surface of the cantilever.



**Figure 47** (a) SEM images of a fabricated silicon nanowire AFM probe via contact printing on a membrane and regrowth on a cantilever. (b) Magnified SEM image of a regrown silicon nanowire on the cantilever forming an angle of almost 90° with respect to the cantilever surface. (c) Magnified SEM image of the contact printed silicon nanowire and the regrown one on the cantilever.

Another alternative method for growing silicon nanowires via regrowth is simply contact printing silicon nanowires directly on cantilevers. This method is not limited to tipless  $\text{Si}_3\text{N}_4$ -cantilevers, but also silicon cantilevers and even cantilevers with a tip can be used for the regrowth of silicon nanowires. Performing contact printing as it was demonstrated in the section 3.2.1 is quite simple. The SEM image in **Figure 48** shows a pre-fabricated V-shaped  $\text{Si}_3\text{N}_4$ -cantilever on which a silicon nanowire is regrown from contact printed silicon nanowires directly on the cantilever. The only drawback addressed to this method is that it is very challenging to have selectivity in contact printing directly on cantilevers, because defining nanowire catchers on the cantilevers are elaborate and intricate. In fact, cantilever areas are not large enough in order to spin-coat photoresists homogeneously, perform lithography and consequently, fabricate catcher structures. Although employing dry resist sheets are reported for performing microfabrication on cantilevers [88], the dry resist sheets are not easily removable and should not be present within silicon nanowire synthesis in the NWCVD reactor. In contrast, fabricating catchers on  $\text{Si}_3\text{N}_4$ -membranes are feasible, as they have large enough and nearly flat surfaces. Therefore, contact printing on  $\text{Si}_3\text{N}_4$ -membranes has an advantage due to the possibility of selectivity during contact printing. Regarding this, one of the relevant examples is discussed in section 3.2.1. Nevertheless, the advantage of contact printing on different types of cantilevers with tip and without tip gives this approach pronounced worthiness. This is particularly intriguing when cantilevers with higher spring constants (more than 1 N/m) are required, as  $\text{Si}_3\text{N}_4$ -

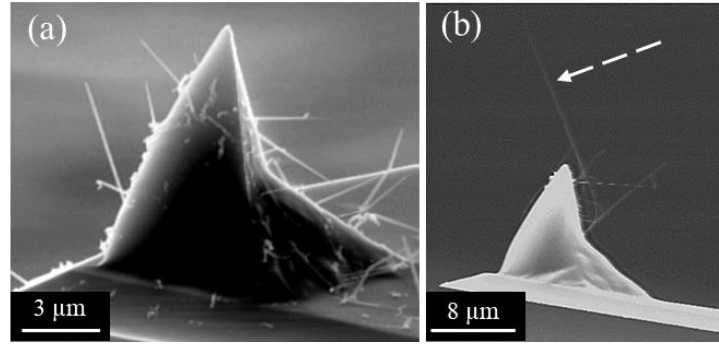
cantilevers are often soft cantilevers with relatively low spring constants, as discussed in section 3.1.2 (less than 1 N/m).



**Figure 48** SEM image of a fabricated silicon nanowire probe after contact printing silicon nanowires and regrowth on the cantilever.

As mentioned before,  $\text{Si}_3\text{N}_4$ -cantilevers have relatively low spring constants. If a cantilever with a higher spring constant is required, then contact printing and regrowth of silicon nanowires on silicon cantilevers with a higher spring constant will be beneficial. The silicon nanowire contact printing can be performed directly on silicon cantilevers with and without a tip. For instance, this approach was applied to commercial silicon cantilevers with tips, which is discussed in section 3.2.1. In principle, using a pyramidal tip provides an area for elevating some of the contact printed silicon nanowires on the tip region and in other words, it enables selectivity for the regrown silicon nanowires to be used as a tip in this area.

**Figure 49** shows the SEM images of the regrown silicon nanowires with two different regrowth conditions. For instance, growing nanowires with a shorter length ranging from 6 to 8 μm (growth temperature: 550 °C, pressure: 10 mbar,  $\text{SiH}_4/\text{He}$ : 20 sccm,  $\text{H}_2$ : 80 sccm, time: 1 h) may not lead to a functional nanowire probe due to the nanowire orientations and locations on the tip. Under this growth condition, it is less likely to be able to synthesize silicon nanowires, whose tips are higher than the apex of the pyramidal tip. On the other hand, by growing silicon nanowires with a greater length ranging from 20 to 22 μm under a different growth condition (growth temperature: 485 °C, pressure: 75 mbar,  $\text{SiH}_4/\text{He}$ : 100 sccm,  $\text{H}_2$ : 20 sccm, time: 20 min) the nanowire tip is located well above the apex of the pyramidal silicon tip.

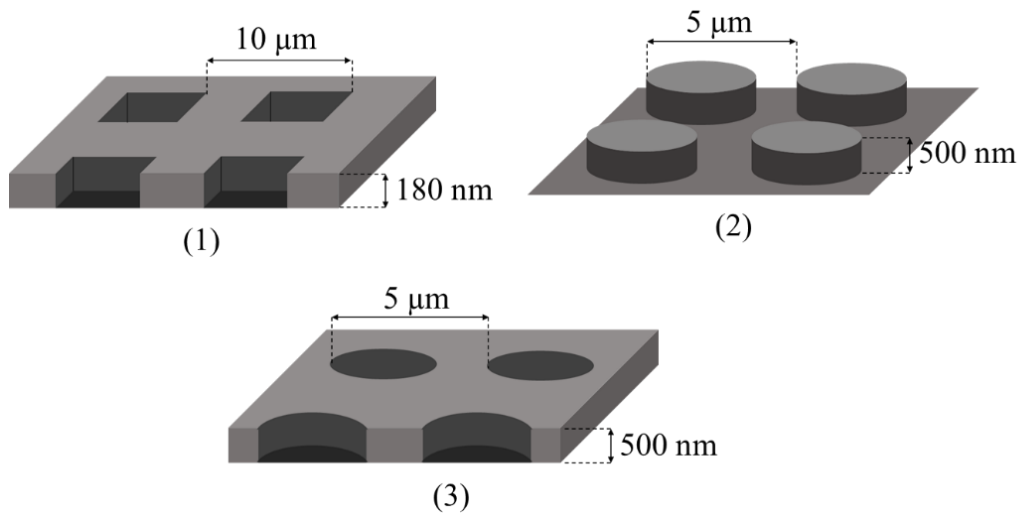


**Figure 49** (a) SEM images of regrown silicon nanowires on a silicon AFM tip under the following regrowth conditions: growth temperature: 550 °C, pressure: 10 mbar, SiH<sub>4</sub>/He (2% dilution): 20 sccm, H<sub>2</sub>: 80 sccm, time: 1 h. (b) SEM images of regrown silicon nanowires on a silicon AFM tip under the following regrowth conditions: growth temperature: 485 °C, pressure: 75 mbar, SiH<sub>4</sub>/He (2% dilution): 100 sccm, H<sub>2</sub>: 20 sccm, time: 20 min.

Compared to the previous method, including the photolithography and lift-off processes and any other established and realized methods (as mentioned in state of the art, section 1.2.3), the regrowth process is a relatively low-cost strategy. However, the number of functioning probes were a few per 30-40 fabricated probes, as further enhancement in contact printing and regrowth process is still required. By further improvements, this strategy can have the potential to be compatible with mass production.

### 3.4 Analysis of Fabricated Probes in AFM

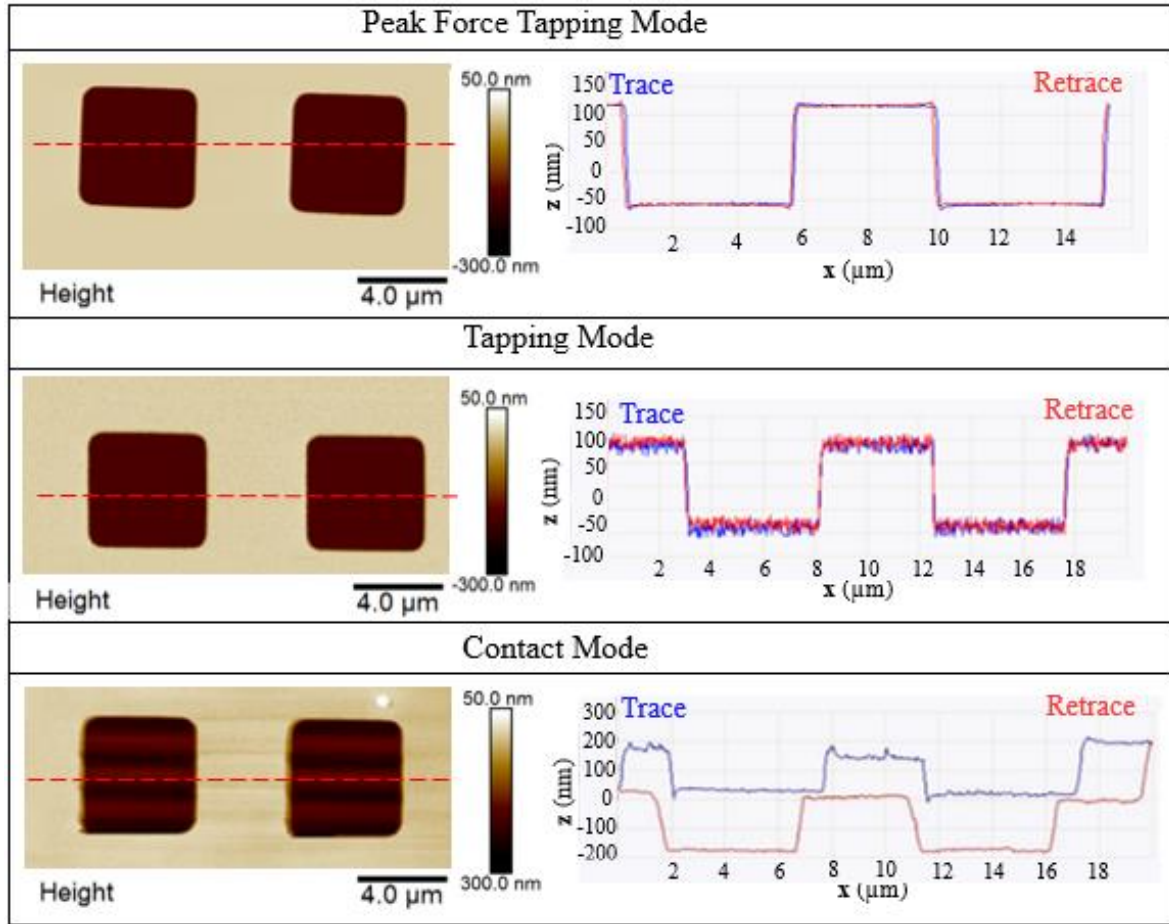
After silicon nanowire probe fabrication, they were tested in AFM by scanning a reference sample. Three different reference samples were employed for testing the functionality of the fabricated probes, as shown in **Figure 50**.



**Figure 50** Three types of the AFM reference samples utilized in this work.

The first investigation was carried out for the fabricated probe shown in **Figure 48**, whose resonance frequency is around 255 kHz. This probe was used to scan the reference sample (1), shown in **Figure 50**, by applying different measurement modes: contact, tapping and peak force tapping modes. As depicted in **Figure 50**, this reference sample is composed of

square-shaped trenches with a pitch size of  $10\text{ }\mu\text{m}$  and a height of  $180\text{ nm}$ . Here, the purpose of the measurements was to see how well the fabricated probe resolves the surface features and whether the obtained topography image reveals features with the expected dimension. Plus, how the scanning quality differs in each scanning mode. The topography images of the reference sample with three different modes are shown in **Figure 51**. These topography images are constructed by trace scans. According to the results, the pitch size and the height in the scanning images are in good accordance with the real size of the structure in the sample with only 5 % error in lateral resolution and 1.6 % error in height. Besides the topography images, the trace and retrace of a similar scan line from each mode are also displayed in **Figure 51**. In fact, the scan quality can be simply judged by a trace and retrace of a scan line. Therefore, for a better comparison, the scan lines are selected from nearly the same position on the topography images. In principle, the trace and retrace of scan lines are required to be matched in order to provide an accurate and reliable scanning topography image of a sample surface. When tracking is poor, the trace and retrace of height no longer overlap. According to the results shown in **Figure 51**, the best quality of the scanning image is found in the peak force tapping mode as the trace and retrace scan lines fit each other. In tapping mode, despite the trace and retrace overlap, the measurement is quite noisy, and the scanning quality is consequently deteriorated. The noise can be attributed to cantilever oscillations. In tapping mode, cantilevers are required to oscillate at their resonance frequency, while in peak force tapping mode, the cantilever oscillations take place at frequencies far below their resonance frequencies. [152] As expected, the lower the frequency of oscillation, the less noise is produced in the measurements, which subsequently results in an improved quality of scanning images. In contact mode, the trace and retrace do not overlap and form a hysteresis. All piezoelectric ceramics display a hysteretic behavior. When a probe scans back and forth cyclically and slowly, the same driving signal may not always represent the same position in the two scanning directions. [205] AFM measurement accuracy is frequently compromised by severe hysteresis caused by the scanning piezo, and by nonlinearities in measurements. Proper calibration can be a solution to overcome this issue. [152], [206] However, it is not simple for every case. Furthermore, the change in adhesion force and lateral forces produce changes in cantilever deflections comparable to those arising from surface height variations. [207]

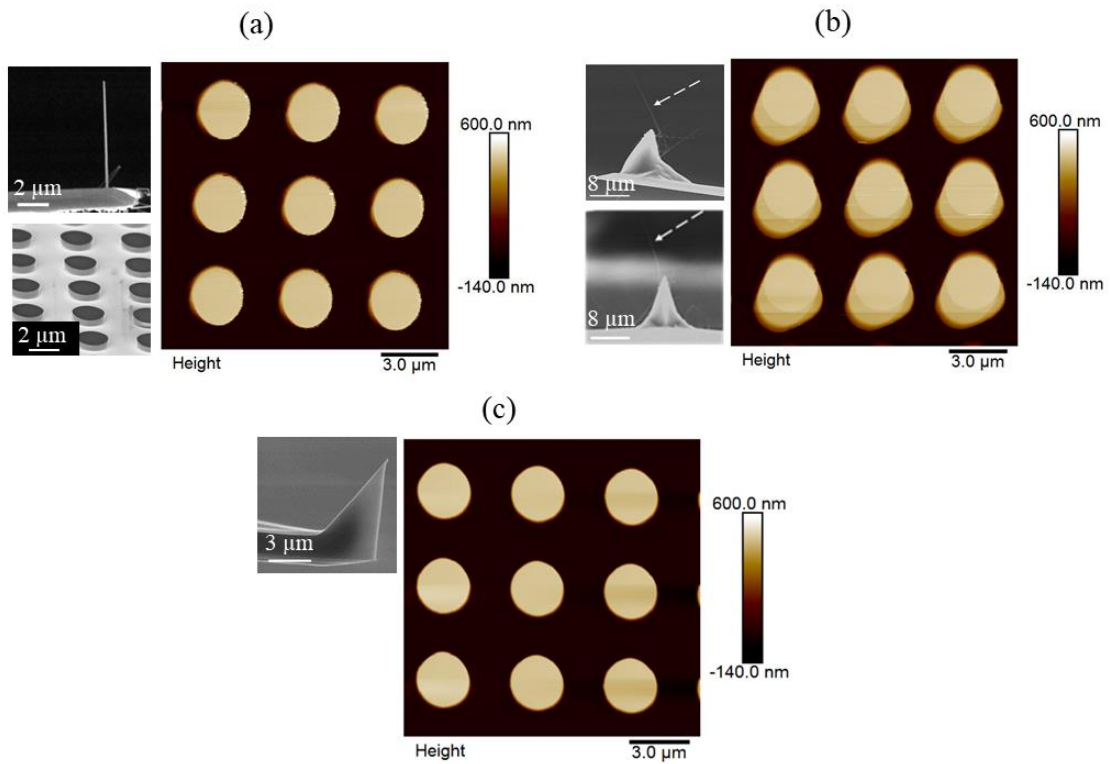


**Figure 51** AFM topography images by using the silicon nanowire probe on a reference sample (1) shown in **Figure 50** (with a pitch size of 10 μm and a step height of 180 nm) in three modes: peak force tapping, tapping and contact mode. The images on the left side show the topography images. The red dashed lines represent a scanning line and the following trace and retrace of the scanning line are shown in the graphs on the right side.

The next investigation was carried out on the probes shown in **Figure 47** and **Figure 49**. The main difference between these two probes is the tip geometry and their angles with respect to the cantilever surface. These two probes were used in AFM to scan the reference sample (2), as shown in **Figure 50** and SEM image, lower left in **Figure 52** (a). The reference sample here is composed of circular pillars with a pitch size of 5 μm and a height of 500 nm. The main advantage of using circular structures is to understand the effect of the angle of the silicon nanowire tip on the scanning quality. The silicon nanowire tip (shown in **Figure 52** (a)) is 8 μm long with a diameter of 120 nm and a cantilever spring constant of 0.6 N/m, while the nanowire in the probe (b) is 20 μm long and has a diameter and a cantilever spring constant of 80 nm and 0.3 N/m, respectively. The measurement for probe (a) in **Figure 52** was carried out in peak force tapping mode, whereas for the probe (b), the measurement was feasible only in contact mode. The long nanowires with smaller diameters are assumed to be more prone to vibration whilst the cantilever oscillates, consequently leading to measurement disturbance. The more detailed discussion on this matter can be found in section 3.5.2. According to the topography images shown in **Figure 52**, the probe (a) could resolve the pillars more accurately compared to the probe (b) with



the longer nanowire tip. The pitch size and the height values are in accordance with the dimension of the reference sample, though. The nanowire tip in the probe (b) has an angle of around  $61^\circ$  with respect to the cantilever surface along the cantilever length and an angle of around  $73^\circ$  with respect to the cantilever surface along with the width of the cantilever, while the nanowire from the probe (a) is perpendicularly located with respect to the cantilever surface. This could fairly portend the failure of the probe (b) in tracking the circular pillars accurately. Nevertheless, for the best performance, the angular orientation of the nanowire should be considered by the angle that the probe itself is located with respect to the sample surface. In the applied apparatus, this angle is  $12^\circ$ . All in all, the topography image of the probe (a) is very similar to the topography image of the pyramidal silicon tip (c).

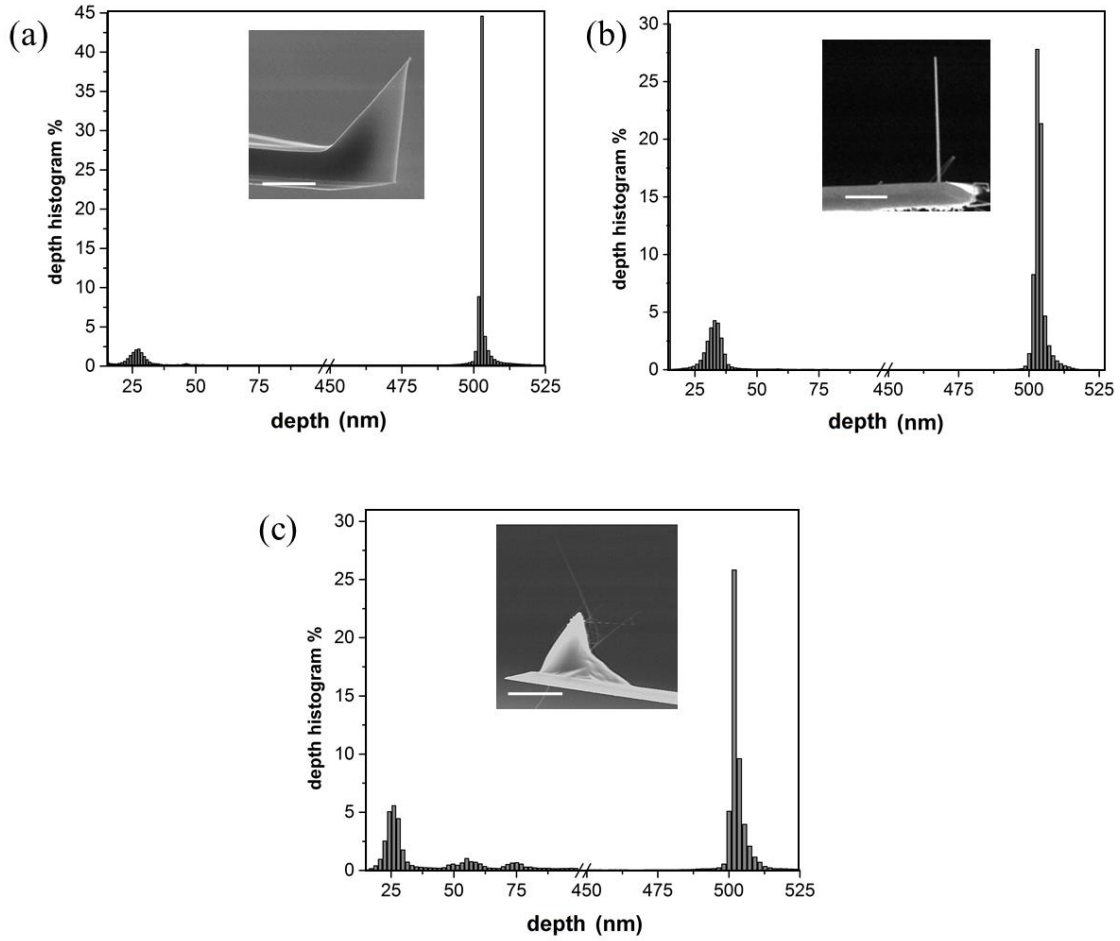


**Figure 52** (a) The left hand-side images are SEM images of a silicon nanowire probe with a length of 8 μm and an AFM reference sample composed of circular pillars with a pitch size of 5 μm and a height of 500 nm. The right hand-side image shows the AFM topography image of the reference sample by using the silicon nanowire probe. (b) The left hand-side images are SEM images of a silicon nanowire tip with a length of 20 μm shown along the length of the cantilever (image on the top) and along the width of the cantilever (image below). The right hand-side image shows the AFM topography image of the reference sample by using the silicon nanowire probe. (c) The left hand-side image is SEM image of the pyramidal silicon probe. The right hand-side image shows the AFM topography image of the reference sample using the pyramidal silicon probe.

The silicon nanowire tips shown in **Figure 52** were compared to a conventional AFM probe (Bruker-OTESPA) with a spring constant of 14 N/m and a resonance frequency 210 kHz using the reference samples (2), shown in **Figure 50**, in peak force tapping mode. The height histograms of the topographical images are shown in **Figure 53**. Therefore, for a

better comparison, depth histograms of such measurements for these three probes are evaluated and shown in **Figure 53** (a), (b) and (c) using the commercial silicon AFM tip, the silicon nanowire tip on a  $\text{Si}_3\text{N}_4$ -cantilever and the silicon nanowire on a silicon AFM tip, respectively. The AFM images (shown in **Figure 52**) and histograms were acquired with the same scanning parameters (except from the probe (b), for which the scanning was carried out in contact mode) and modification frameworks in the analysis software. As it can be depicted from the depth histogram, the obtained graphs for each measurement are composed of two main histograms in two depth ranges and the difference between depths of the main peaks represents the height of the circular pillars in the reference sample (500 nm). For AFM measurements using the silicon nanowire on an AFM tip (**Figure 53** (b)), the graph is composed of three peaks in the depth range lower than 80 nm, confirming the distorted measurements shown in **Figure 52** (c). To accurately measure the pillar heights from the histograms, the height difference of the main two peaks by investigating the mean value of the histogram data in lower and higher depth ranges is calculated and subsequently subtracted, only for **Figure 53** (a) and (b). For the commercial AFM tip, the height is investigated as 476 nm with 4.87% error, while for the nanowire tip on the  $\text{Si}_3\text{N}_4$ -cantilever, this value is 468 nm with a slightly higher error 6.34%. In the depth range of 475-525 nm of the histograms, the peak value for the conventional AFM probe is almost 45%, which is higher than the one for the silicon nanowire tip (almost 28%). Moreover, in this range, the data distribution is observed to be higher for the silicon nanowire tip compared to the one from the common silicon AFM tip. Silicon nanowires are assumed to have different mechanical behaviors as an AFM tip compared to a pyramidal silicon tip, although the material for both types is the same. As a result, the nanowire bending behavior is presumably different and a required load for nanowire bending might not necessarily suffice to cause bending or deformation in pyramidal tips due to their greater mass and different geometry. This feature makes nanowires a softer tip, for which a slight change in the interaction load between the tip and the sample, might cause the nanowire bending and affect the scanning quality. Therefore, scanning with silicon nanowires requires precise control of the applied force, particularly for scanning at the edge of the pillars, where the applied load on the tip can drastically change. Hence, this can be a reason that a higher distribution range for the silicon nanowire tip is observed in their histograms. It is also important to note that the bending behavior or the softness of the nanowires depend considerably on their geometries, including their length and diameter. Therefore, studying their mechanical behaviors is quite demanding throughout tracing topography features of different materials. Regarding this matter, the softness of silicon nanowire probes was investigated and is fully discussed in section **3.5.1**.

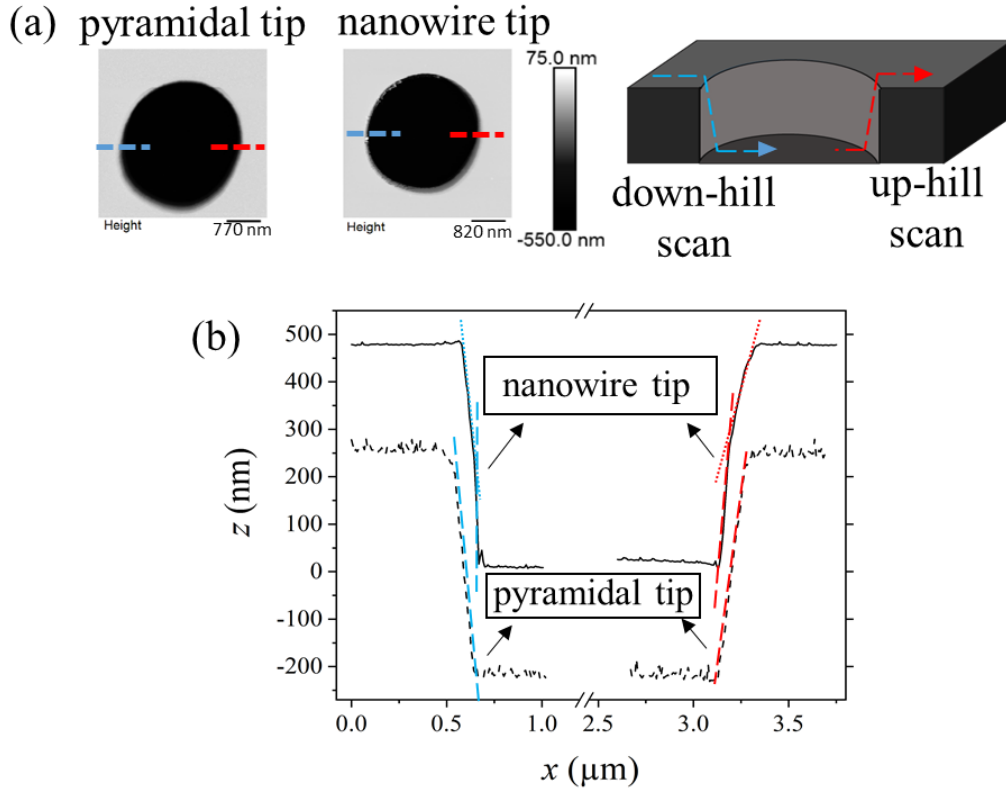




**Figure 53** (a) Histograms of measured depth by a conventional silicon AFM tip scanning the reference sample (2) shown in **Figure 50**. The scale bar of the inset image is 6  $\mu\text{m}$ . (b) Histograms of measured depth by the silicon nanowire tip on a  $\text{Si}_3\text{N}_4$ -cantilever scanning the reference sample. The scale bar of the inset image is 2  $\mu\text{m}$ . (c) Histograms of measured depth by the silicon nanowire tip on a silicon pyramidal tip scanning the reference sample. The scale bar of the inset image is 8  $\mu\text{m}$ .

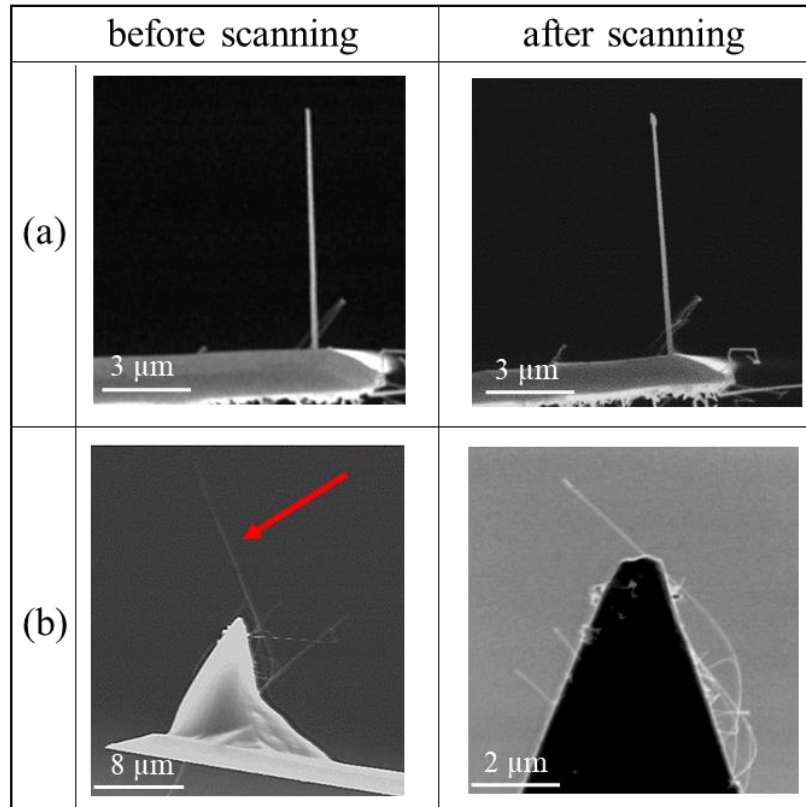
For further investigation of the fabricated silicon nanowire tips, they were examined in AFM by scanning the reference sample (3) with circular pit structures, as shown in **Figure 50**. Then, they were compared to the pyramidal silicon tip. The overall topography scan seems similar for both types of probes. In both topography images, as shown in **Figure 54** (a), there is an asymmetry artifact. For further investigations, a scan line from a similar position is chosen on both topography images. Then, the sidewall slopes were compared to each other. As shown in **Figure 54** (b), the slope of down- and up-hills are  $-3.9 \pm 0.1$  and  $3.1 \pm 0.1$ , respectively for the pyramidal silicon tip. The scanned sidewalls by the silicon nanowire tip for both up- and down-hill scans are defined with two regions. The reason for the different transition behavior from the lower part to the upper part (also vice versa) can probably be due to the nanowire alignment and also the large tip radius of the silicon nanowire, while the lower part is indicating the high aspect ratio feature. By considering a linear behavior for the lower and upper parts of each sidewall transitions, a slope for the upper part of about  $-3.8 \pm 0.8$  and  $1.8 \pm 0.1$ , and for the lower part of about  $-9.3 \pm 0.1$  and  $4.7 \pm 0.3$  always for down- and up-hills scanning, respectively is obtained. The results

indicate that the silicon nanowire is more suitable for resolving high aspect ratio structure, as the lower parts of the down- and up-hill slopes for the silicon nanowire probe is lower than the one for the pyramidal tip.



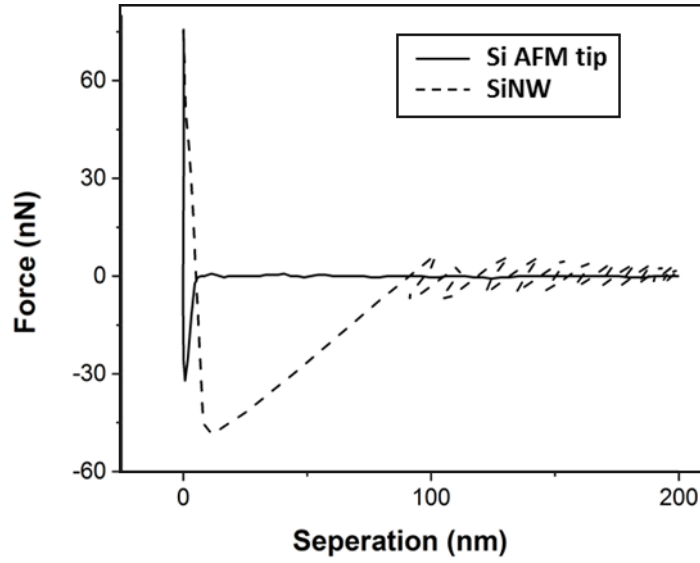
**Figure 54** (a) AFM topography images of the reference sample using the silicon nanowire and pyramidal silicon tips and schematic illustration of the scan lines on the reference sample. (b) Line profiles, as indicated in (a) for evaluating the high aspect ratio properties of the scanning tips based on the slope values of the red and blue dashed lines.

Silicon nanowires are reported to have relatively high mechanical stability and consistency in measurements even compared to carbon nanotubes. [10], [16] In order to qualify the mechanical stability of the fabricated probes in **Figure 52**, they were inspected in SEM before and after scanning. According to the SEM images shown in **Figure 55**, the silicon nanowire from probe (a) remained nearly intact after several scans, even under relatively high scanning loads (nearly 500 nN). On the other hand, the silicon nanowire from probe (b) suffered from poor mechanical stability, as deformation and footage of breakage can be clearly seen. As a result, the nanowire mechanical stability depends greatly on their geometries, despite the high Young's elastic modulus. The longer nanowires with smaller diameters are more prone to damage and breakage during scanning.



**Figure 55** (a) SEM images of a silicon nanowire tip with a length of  $8\ \mu\text{m}$  before and after several AFM scans. (b) SEM images of a silicon nanowire tip with a length of  $20\ \mu\text{m}$  on a silicon AFM tip before and after AFM scanning. The silicon nanowire is indicated by the red arrow.

The PFT (peak force tapping) mode has the advantage that the physical properties of the sample can be obtained while imaging the sample. This information and investigation can be acquired from the force graph that the PFT is enabled to record for each scanned point. [166] The force graphs represent the force applied to the tip against the tip separation from the sample surface. [152] The plot shows two behaviors for approaching the tip to the sample and retracting it from the surface. Most of the mechanical properties and information are characterized by the retract plot. The minimum force observed in the retract graph indicates the adhesion force between the tip and the sample. [120] Accordingly, the retract plots of the silicon nanowire tip on the  $\text{Si}_3\text{N}_4$ -cantilever is compared to a common silicon AFM tip while scanning on a sapphire sample shown in **Figure 56**. The dashed line represents the retract graph for the silicon nanowire tip and the full solid line stands for the retract plot of the conventional AFM probe. The peak force value was kept constant for both probes during the measurements as  $75\ \text{nN}$ . The adhesion force of the nanowire tip is estimated to be  $50\ \text{nN}$ , while this value for the conventional AFM probe is around  $36\ \text{nN}$ . The adhesion force variation can be due to the presence of the gold catalyst at the tip whose adhesion might differ from the silicon material, as they both scan the sapphire surface.



**Figure 56** The retract force graphs plotted for the silicon nanowire tip (dashed line) and the conventional AFM probe (solid line) while scanning a sapphire surface.

For the next investigation, the roughness of a silicon surface was measured using the silicon nanowire probe, as shown in **Figure 52** (a). The measurement was compared to the roughness value measured using a pyramidal silicon AFM probe. For the roughness value, the root mean square roughness is calculated based on the following relation, where  $M$  and  $N$  are the numbers of the values in  $x$ - and  $y$ -directions, respectively and  $h(x_k, y_l)$  stands for a height value [208]:

$$\text{RMS} = \sqrt{\frac{1}{MN} \sum_{k=0}^{M-1} \sum_{l=0}^{N-1} (h(x_k, y_l))^2} \quad (3-13)$$

The value of RMS can be directly obtained from surface topography images shown in **Figure 57** (a) and (b) by using the analysis software. The RMS values measured by the silicon nanowire probe and silicon pyramidal tip are  $1.8 \pm 0.0$  nm and  $8.4 \pm 0.4$  nm, respectively, by scanning four similar regions on the silicon surface between the pillars in the reference sample using each probe type. In principle, the smaller the tip radius, the higher the resolution can be achieved for tracing small features, which can lead to a higher RMS value. The silicon AFM pyramidal probe has a smaller tip radius (nearly 10 nm, based on the provided information from the manufacturer) compared to the silicon nanowire with a tip radius of about 60 nm. Therefore, smaller features on the silicon surface can be better resolved by the pyramidal silicon probe. Consequently, the higher variation in the height values measured by the pyramidal silicon tip leads to a higher value for RMS. Furthermore, the silicon nanowire scanning tip is more prone to smoothing. Nevertheless, the silicon nanowire tip can also be sharpened by post-processing, for instance, as discussed briefly in Appendix section N. Based on the topography images shown in **Figure 57** (a) and (b), the higher contrast in topography images with more texture can be observed in the topography image acquired by the pyramidal silicon AFM probe (**Figure 57** (b)), on the same region, where the silicon nanowire probe shows a lower lateral resolution (**Figure 57** (a)). It should

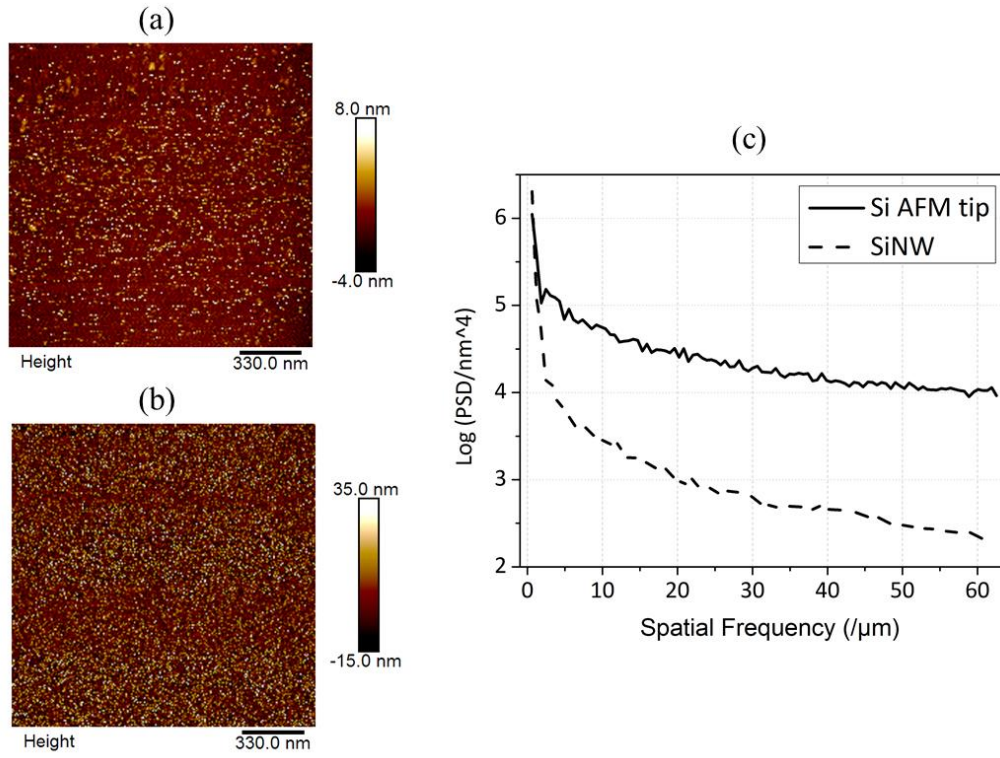
be noted that the measurement conditions were set the same and performed in peak force tapping mode. The RMS is only sensitive to the vertical signals and not depending on the horizontal structures. The power spectral density (PSD) function instead analyzes the surface roughness based on the height variations and also the lateral distribution, over which the height values vary. [209] By considering roughness features having waveforms, the inverse of the corresponding wavelength is called spatial frequency. The PSD function provides surface roughness features with their amplitudes with respect to spatial frequencies. [210] Mathematically, the PSD is defined as a squared fast Fourier transformation (FFT) of the surface and is given by the relation below [211]:

$$PSD_{2D}(f_x, f_y) = \frac{1}{L^2} \left\{ \sum_{m=1}^N \sum_{n=1}^N h_{mn} e^{-2\pi i \Delta L (f_x m + f_y n)} (\Delta L)^2 \right\}^2 \quad (3-14)$$

Here,  $L^2$  is the scanned surface area,  $N$  is the number of data points per line and row,  $h_{mn}$  is the profile height at a position of  $(m, n)$ ,  $f_x$  and  $f_y$  are the spatial frequency in the  $x$ - and  $y$ -directions.  $\Delta L$  stands for the sampling distance ( $\Delta L = L/N$ ). PSD (power spectral density) plots were obtained from the same measurements for the nanowire tip and the conventional silicon AFM tip. In **Figure 57** (c), the logarithmic value of the power is displayed against frequency ( $1/\mu\text{m}$ ). In this plot, the solid line and the dashed line represent the PSD behavior of the conventional silicon AFM tip and the silicon nanowire tip, respectively. RMS values using the PSD function can be subsequently calculated using the following relation [211]:

$$RMS = \sqrt{\int_{f_1}^{f_2} PSD(f) df} \quad (3-15)$$

RMS values were calculated in the software analysis and are 1.3 nm and 7.4 nm for the silicon nanowire probe and pyramidal silicon tip, respectively. These values are very close to the RMS value calculated by considering only the height variations (relation (3-13)). However, as it can be depicted from the graph shown in **Figure 57** (c) the PSD values of the pyramidal silicon tip is quite higher than the silicon nanowire tip for the nearly entire spatial frequency range, as the silicon nanowire tip has lower lateral resolution and less height deviation for spatial frequency cursors.



**Figure 57** (a) AFM topography image of a silicon surface using the silicon nanowire probe. (b) AFM topography image of a silicon surface using the pyramidal silicon AFM probe. (c) Power spectral density (PSD) graph, plotted based on the AFM topography images (a) and (b). In the graph, SiNW and Si AFM tip stand for the silicon nanowire probe and conventional pyramidal silicon tip, respectively.

### 3.5 Analysis of Silicon Nanowire Tip Mechanical Behaviors for AFM Applications

According to the measurement results discussed in the previous section, the mechanical stability of the silicon nanowire scanning probes and their scanning qualities depend on the geometry and dimension of the nanowires, mainly length and diameters. For instance, performing measurements using the fabricated probe with a longer silicon nanowire shown in **Figure 52** (b) was quite challenging, particularly in vibrational modes. Furthermore, it also suffered from poor mechanical stability. Therefore, for fabricating the silicon nanowire probe with a desired functionality and performance quality, it is important to know the mechanical behaviors of silicon nanowires as a scanning tip. So far, the main focus was given on the realization of a method for the nanowire or nanotube probe fabrication mainly for the sake of high aspect ratio measurements. However, there was never a survey solely on how the mechanical characteristics of silicon nanowires affect the topography measurements. Many of these characteristics or behaviors are very difficult to be investigated via measurements and only theoretical analysis and simulations can provide a better insight into their mechanical characteristics. Furthermore, due to the relatively low reproducibility in the fabrication procedure, a few numbers of the probes were fabricated in this work. Therefore, the analysis of the mechanical behaviors of silicon nanowire probes was not experimentally doable. Here, in order to predict the mechanical behaviors of a silicon nanowire probe, they were analyzed by the theoretical methods and simulated in COMSOL multiphysics software. By means of the mentioned analyses, it is easier to design a silicon nanowire probe with desired features. The two characteristics which mainly concern the functionality of a scanning tip, are their softness and the vibrational behavior. In the following section, these two properties are discussed separately, at first, via analytical solutions and later by simulations.

#### 3.5.1 Softness of a Silicon Nanowire Tip

Besides the high aspect ratio characteristics, silicon nanowires were discussed to be a soft scanning tip [16]. In other words, a small interaction load between the tip and the sample surface might lead to elastically bending and buckling of the nanowires. This feature can effectively protect sample surfaces and the tip itself from damages caused by the tip crash onto a sample surface. The tip softness is favored, especially for scanning very soft and delicate samples such as living cells, whose stiffness and Young's modulus are quite low. On the other hand, this feature can lead to a lower imaging resolution, as some surface features might not be accurately traced due to the nanowire deflections. As cantilever bending is used for tracking the height changes on a scanned surface, silicon nanowire deformations prevent the cantilever bending and consequently, height changes can not be recorded. In principle, the nanowire bending behavior depends significantly on the length and diameter of the nanowires. Hence, the nanowire softness can be tuned by merely controlling the length and diameter of nanowires during the synthesis. Not only silicon nanowire softness but also cantilever spring constants can have an impact on the overall softness of a scanning tip. Basically, depending on the softness of nanowire tips and the

spring constant of the corresponding cantilever, one of them might be prone to elastic deformation. For instance, a very stiff cantilever with a high spring constant requires a higher load for bending than a quite long silicon nanowire and only a small interaction force is enough for the nanowire deflection. Therefore, understanding the correlation between the cantilever spring constant and nanowire softness is important in order to estimate probe properties and fabricate a probe with a desired characteristic, either a very stiff scanning probe or a very soft one depending on the required applications. In this section, the first step toward defining the softness of the nanowire scanning probe is taken by applying analytical solutions. Later, the simulation results are compared and discussed in detail, in order to see how cantilevers and nanowires mechanically behave, when a probe is displaced toward a scanning sample at a static point.

### I. Analytical Investigations for Silicon Nanowire Softness

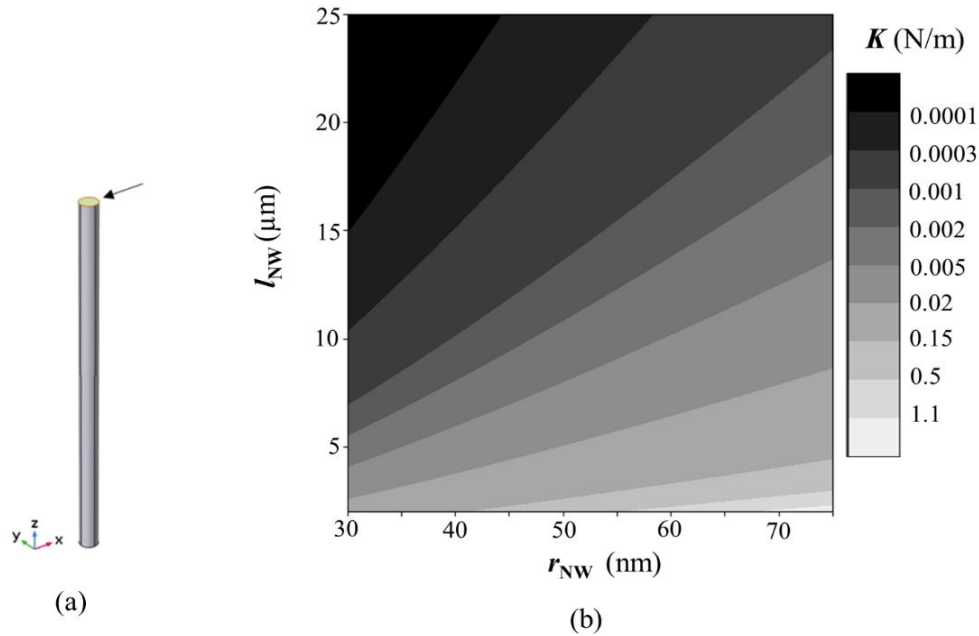
The fact that the elastic deformation of silicon nanowires and defining the interaction force between a nanowire tip and a sample is very complex in three-dimension, defining the softness of nanowires in this sense, is also a very challenging task. Therefore, the simplest approach to investigate the softness of silicon nanowires is to compare the spring constant or stiffness of cantilevers to those of nanowires. Defining and investigating cantilever spring constants based on the theories mentioned in section 3.1.2 is straightforward. However, the deflection of silicon nanowires under the interaction force is very intricate. It can be in the form of bending or buckling or even a more complex deformation. In a case of simple bending, estimation of nanowire spring constant is relatively simple, by considering a circular cross-section for nanowires, whose diameter is homogeneous throughout the entire length (**Figure 58**). The bending behavior, in this case, is the bending of a beam fixed at one end. According to the theories mentioned in section 3.1.2, it is possible to investigate the nanowire spring constant based on the following relation:

$$K = \frac{3E\pi r^4}{4l^3} \quad (3-16)$$

Here  $E$ ,  $r$  and  $l$  stand for Young's elastic modulus, radius and length of a silicon nanowire, respectively. For nearly a decade, there were studies to understand the mechanical properties of silicon nanowires and one of the most debatable topics is Young's elastic modulus of silicon nanowires. The Young's modulus of silicon nanowires is reported to differ slightly from bulk silicon material and both are reported strongly to be dependent on crystal orientations. [212], [213] Some experimentally obtained results show that Young's modulus of silicon nanowires are size-dependent up to 100 nm in diameter [214], [215], whereas theoretical analysis and computational studies show that Young's elastic modulus of silicon nanowires with diameter less than 10 nm is size-dependent [216]. One of the reasons for the difference between theoretical and experimental is that the influence of the surface effect, passivation, defects and surface contour are not considered for analytical solution and simulation modeling. Theoretical analysis suggests that internal stress has an impact on Young's elastic modulus of nanowires leading to a non-linear force-deflection behavior. [217] Gordon et al. reported the Young's modulus of VLS synthesized silicon [111] nanowires with a diameter of about 100 nm is about 160-180 GPa. [218] In their work, the Young's elastic modulus was investigated experimentally in AFM using the



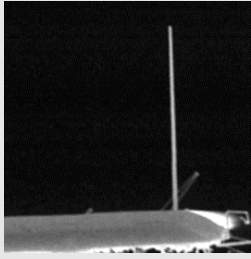
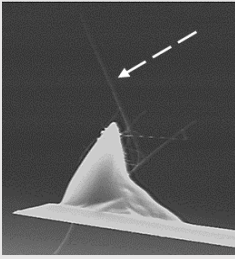
multipoint bending method. [218] In this thesis, the Young's modulus of silicon nanowires is approximated to be 170 GPa, based on the experimental investigations carried out by Gordon et al. [218] and Heidelberg et al. [219]. This value is also considered for the simulation in this work. Nevertheless, based on the mentioned relation for the spring constant of silicon nanowires, the spring constant depends significantly on the length and diameter of the silicon nanowire. Correspondingly, the contour map of the investigated spring constant ( $K$ ), based on the mentioned relation, is shown in **Figure 58** (b) for different values of  $r$  and  $l$  for the silicon nanowire radius and length, respectively.



**Figure 58** (a) Schematic of a silicon nanowire geometry with a circular cross-section applied for analytical solutions. The top surface is considered to be a fixed end (indicated by the black arrow). (b) Contour map of spring constant ( $K$ ) for different length ( $l$ ) and radius ( $r$ ) of silicon nanowires.

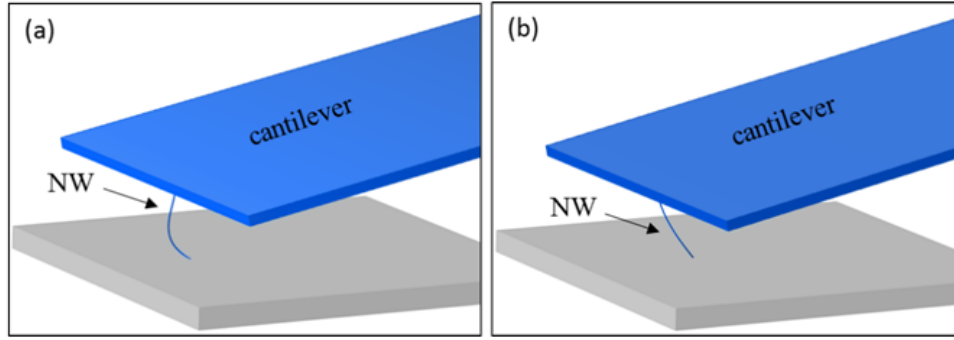
As mentioned before, silicon nanowires are reported to resemble a soft scanning probe. However, so far, a very clear definition of a soft tip is not provided. Based on this, a comparison is made here between the spring constant of cantilevers and nanowires for the fabricated probes shown in **Figure 52** and a fabricated silicon nanowire probe from a comparative study. This silicon nanowire probe, fabricated by the FIB technique, is taken from a study conducted by P. Knittel et al. [16]. In this study, the fabricated probe is claimed to be a soft tip and suitable for scanning biological samples. However, no experimental proof or quantitative analysis is provided. The three probes with the geometrical parameters and spring constants are given in **Table 4**. The spring constant of nanowires is estimated based on the geometry and aforementioned theoretical relations. Comparing the spring constant of cantilevers and nanowires provides the first overview of how soft a tip can be. Accordingly, the nanowires from probe 1 and 2 have lower spring constants compared to the spring constant of the corresponding cantilevers, which might pronounce the tip softness. However, the nanowire from probe 3 reveals a relatively high spring constant around 4.8 N/m, which cannot confirm that the silicon nanowire is a soft scanning tip.

**Table 4** Geometrical parameters and spring constants of nanowires and cantilevers of probe 1, 2 and 3. Probe 1 and 2 are previously shown in **Figure 52** and probe 3 is taken from a report by P. Knittel et al. [16]. Here,  $K_{Cl}$ ,  $K_{NW}$ ,  $L_{NW}$  and  $D_{NW}$  stand for the cantilever spring constant, nanowire spring constant, nanowire length and nanowire diameter.

	“Probe 1”	“Probe 2”	“Probe 3”
			fabricated silicon nanowire probe by FIB, taken from a comparative study by P. Knittel et al. [16]
$K_{Cl}$ (N/m)	0.6	0.3	$\approx 0.1$
$K_{NW}$ (N/m)	$< 0.1$	$< 0.1$	$\approx 4.8$
$L_{NW}$ ( $\mu\text{m}$ )	8	20	1.5
$D_{NW}$ (nm)	120	80	160

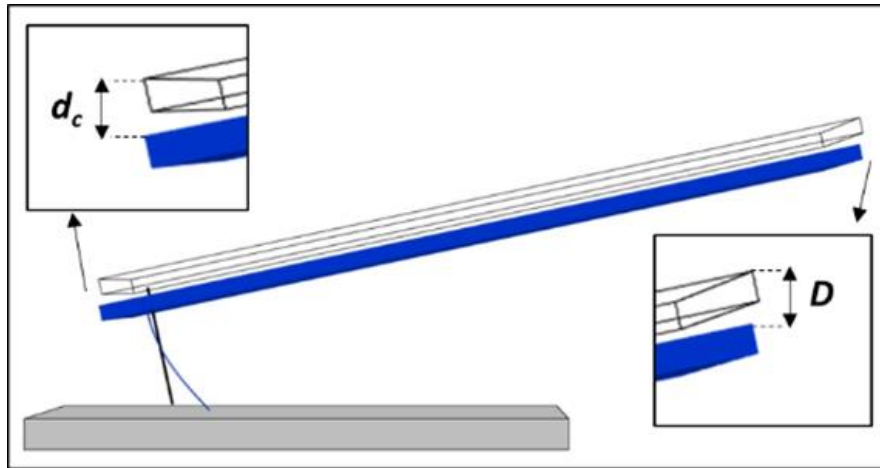
## II. Simulation Investigations for Silicon Nanowire Softness

The previous investigation based on the analytical solution was used to compare the spring constants of cantilevers and nanowires. However, this approach could not provide a full insight into the softness or the mechanical behaviors of a nanowire tip. The point is, a nanowire tip, which is in contact with a sample surface or in the vicinity of it, is under a relatively complex interaction force, which may result in a complex deformation in the nanowire rather than simple bending or buckling. Therefore, for the next study, the aim was to simulate the mechanical behaviors of a nanowire tip. The simulation was carried out in a three-dimensional configuration by a finite element method (FEM) based simulation (COMSOL Multiphysics 5.3a, supported by P. Salimitari). The details of simulation conditions and parameters are presented in Appendix, section O. This study was carried out before the Young's modulus investigation for the  $\text{Si}_3\text{N}_4$ -film in this work. Therefore, the Young's modulus of the  $\text{Si}_3\text{N}_4$ -film was considered to be approximately 250 GPa [220], instead of 204.4 GPa. The silicon nanowire was modeled as a cylindrical object aligned to the surface normal of the microcantilever surface with respect to a non-deformable sample surface. The silicon nanowire has a gold particle at the tip, with a hemisphere shape. The simulated probe was, furthermore, tilted by about  $12^\circ$  to account for a typical AFM probe tilt and brought into mechanical contact to the sample surface. As a result, either the nanowire or the cantilever experiences a deflection within this displacement. Expectedly, a soft tip deforms before the cantilever deflects. Since the friction coefficients between the tip (here gold catalyst at the tip of the nanowire) and scanning samples vary, for the sake of simplicity, the conditions of simulations were set at first without considering friction between the tip and the sample. The simulation was conducted then by considering friction between the tip and the sample surface. In principle, the coefficient value varies depending on the substrate and tip material. In the scenario, where the nanowire bends on the surface, depending on the nanowire bending behavior, not only the friction of the gold-sample but also the silicon-sample is assumed to play an important role. Therefore, assigning a certain value for the friction coefficient is hardly possible. Here, for the sake of simplicity and in order to only differentiate this analysis from the one without friction, a friction coefficient value of 0.5 is considered, regardless of the tip and sample material. The silicon nanowire deformations are accordingly shown in **Figure 59** under two conditions; with friction (a) and without friction (b). As illustrated in **Figure 59** (a), the nanowire tends to buckle instead of sliding on the surface, when there is friction between the tip and the sample. On the other hand, in a case of no friction, the silicon nanowire tip tends to bend and slip on the sample surface (**Figure 59** (b)).

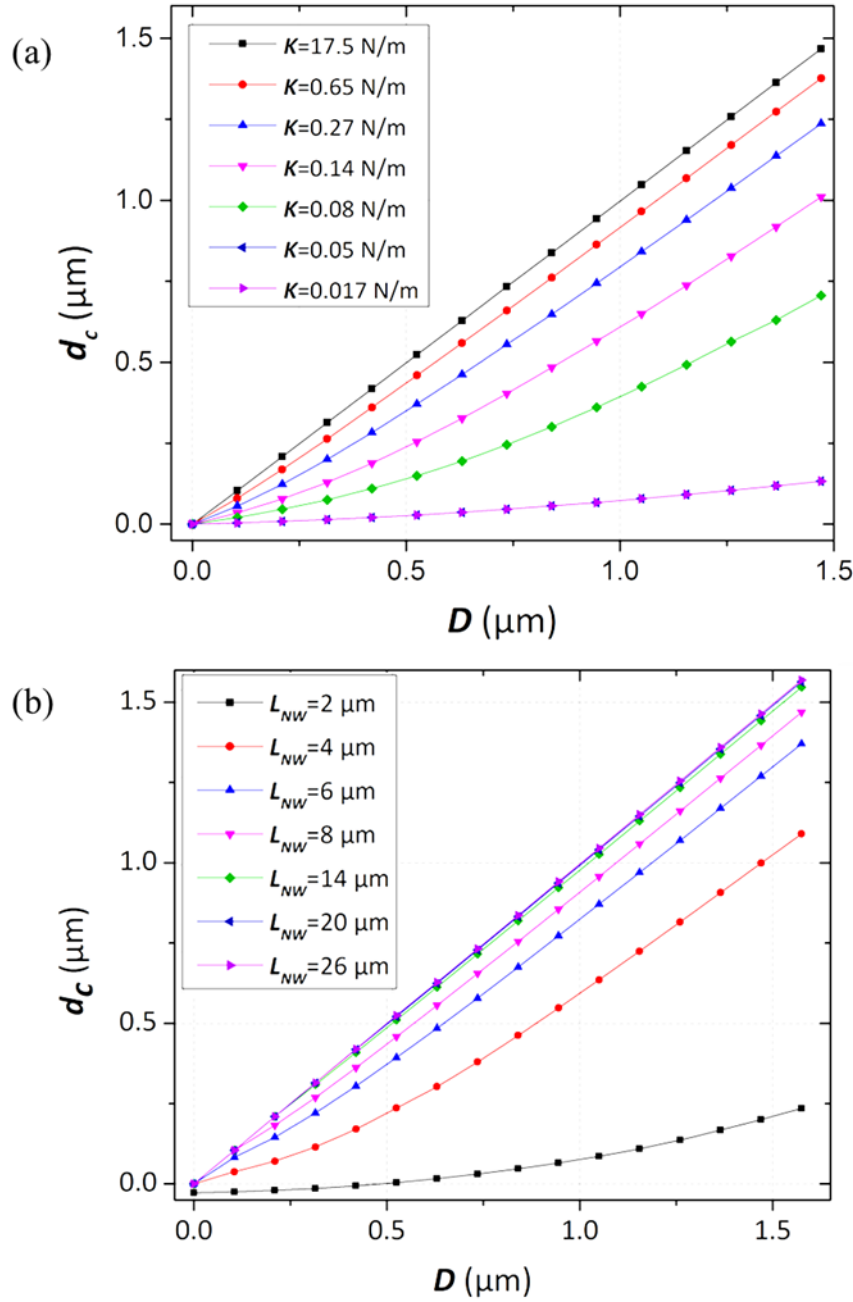


**Figure 59** (a) Schematic illustration of the silicon nanowire shape after lowering the cantilever toward the sample surface by considering friction between the tip and the sample (with a friction coefficient of 0.5 between for the tip and the sample). (b) Schematic illustration of the silicon nanowire shape after lowering the cantilever toward the sample surface without any friction between the tip and the sample.

As mentioned before, at first, the simulations were conducted without considering any friction between the tip and the sample. The nanowire geometry was considered as a cylindrical geometry and the probe is slightly tilted by about  $12^\circ$  with respect to the sample surface (**Figure 60**). Here, the main purpose is to see how the cantilever spring constant and nanowire geometry affect the softness of a scanning probe. Therefore, two conditions were set for the analysis. Under one condition, the nanowire geometry was kept constant (with a diameter of 120 nm and a length of 8  $\mu\text{m}$ ) and the spring constant of the cantilever changed between 0.017 and 17.5 N/m. For the latter condition, the cantilever length varied between 2 and 26  $\mu\text{m}$ , whereas the cantilever spring constant was kept constant at 0.6 N/m. As mentioned earlier, in the simulation, a nanowire tip on a cantilever is in contact with a sample surface and displaced further toward a sample surface. For a better analysis, as illustrated in **Figure 60**, the displacement of the probe ( $D$ ) was compared to the displacement of the cantilever mainly at the edge, where the tip is near ( $d_c$ ). The maximum displacement of the probe ( $D$ ) is about 1.5  $\mu\text{m}$ . The acquired data from the simulations are plotted in the graphs shown in **Figure 61** (a) and (b). As it can be depicted from the graph (a) by keeping the nanowire geometry constant and increasing the cantilever spring constants, the displacement at the edge of the cantilever (denoted as  $d_c$ ) is nearly the same as the main displacement of the probe ( $D$ ). This shows that the stiffer the cantilever, the less it deflects, as the nanowire is prone to deformation. On the other hand, the cantilever spring constant is kept constant and by increasing the nanowire length from 2 to 26  $\mu\text{m}$ , the cantilever displacement increases up to the nearly same value as the main displacement ( $D$ ). For nanowires longer than 14  $\mu\text{m}$ , the cantilever displacement at the edge of the cantilever ( $d_c$ ) has a linear trend with the main displacement of the probe ( $D$ ), with nearly the same value as  $D$ . Basically, the longer the nanowire, the less deflection is observed in the cantilever, as the nanowire is soft enough to be deformed.



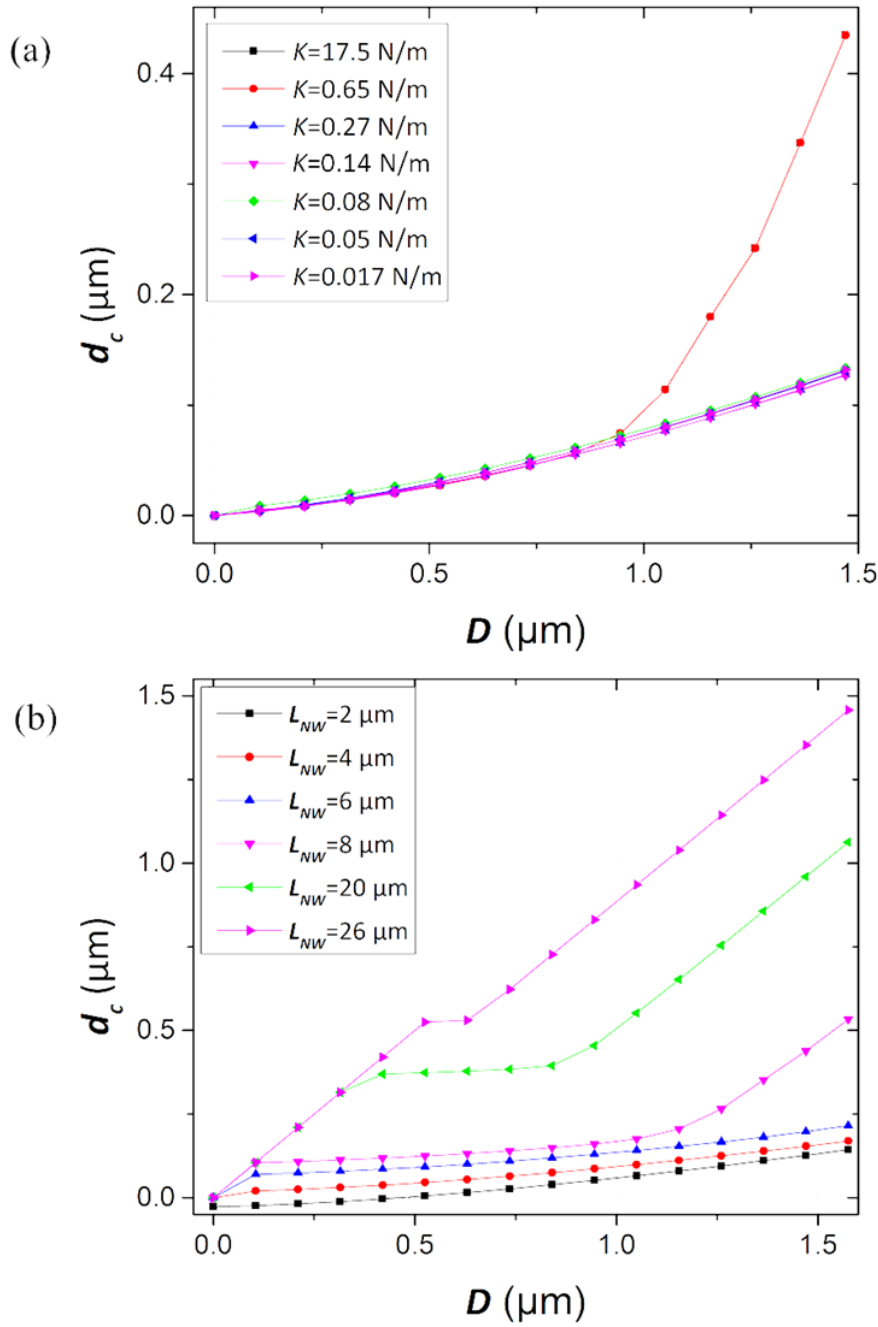
**Figure 60** A schematic illustration of a probe displacement toward a sample surface. The probe displacement is denoted as  $D$  and the cantilever displacement at the edge, close to the tip location, is denoted as  $d_c$ .



**Figure 61** Plotted graphs from simulated data showing the main displacement of the probe ( $D$ ) versus the cantilever displacement at the edge ( $d_c$ ) with no friction between the tip and the sample for two conditions; (a) the nanowire geometry is kept constant (length of  $8 \mu\text{m}$  and diameter of  $120 \text{ nm}$ ) and the spring constant of cantilever varies between  $0.017$  to  $17.5 \text{ N/m}$ . The corresponding trend of  $K=0.017 \text{ N/m}$  and  $K=0.05 \text{ N/m}$  are nearly the same and they overlap. Here,  $K$  indicates the spring constant of the cantilever. (b) For the condition, where the cantilever spring constant is kept constant at  $0.6 \text{ N/m}$  and the nanowire length varies between  $2$  to  $26 \mu\text{m}$ . The corresponding trend of  $L_{NW}=20 \mu\text{m}$  and  $L_{NW}=26 \mu\text{m}$  are nearly the same and they overlap. The nanowire length is denoted as  $L_{NW}$ .

The simulation was also conducted by considering a friction coefficient of  $0.5$  between the tip and the sample, similar to the case with no friction. All the conditions were set the same as in the aforementioned simulations. The plots of acquired data are shown in **Figure 62**,

which show the displacement of the probe ( $D$ ) against the displacement of the cantilever at the edge ( $d_c$ ). The graph (a) shows a condition where the cantilever spring constant varies between 0.017 to 17.5 N/m, while the nanowire geometry is constant (diameter of 120 nm and length of 8  $\mu\text{m}$ ). The cantilevers with the spring constants of 17.5 and 0.65 N/m have a similar trend. Accordingly, cantilevers with any spring constant values deflect when  $D$  increases up to 0.9  $\mu\text{m}$  and a further increase of  $D$  causes nanowires to slip on the surface as a result of overcoming their friction interaction. This happens only for cantilevers with spring constants of 0.65 N/m, 17.5 N/m and most likely any values between. Therefore, the cantilever displacement is compensated approximately within 0.9  $\mu\text{m}$  to 1.5  $\mu\text{m}$ , where the displacement of the cantilever ( $d_c$ ) is nearly the same as the main displacement of the probe ( $D$ ). On the other hand, for cantilevers with a spring constant of 0.27 N/m and lower, the cantilever tends to deflect within the entire displacement range shown in the graph (a). The graph (b) in **Figure 62** shows a condition where the nanowire length varies between 2 and 26  $\mu\text{m}$ , while the spring constant of the cantilever is constant at 0.6 N/m. For the nanowire length ranging from 2 to 6  $\mu\text{m}$ , the cantilever deflects, as the cantilever displacement ( $d_c$ ) is noticeably lower than the main displacement ( $D$ ). For the nanowires with the length of 8  $\mu\text{m}$  and longer, the trend is quite linear. However,  $d_c$  reaches a plateau within the probe displacements ( $D$ ) and the plateau range is different for each nanowire length. Accordingly, the cantilever does not deflect, as the nanowire is presumably deformed and the cantilever displacement ( $d_c$ ) increases nearly as much as  $D$  increases, except from the plateau ranges. For lower  $D$  values than the plateau ranges, silicon nanowires deflect, as shown in **Figure 59** (a). Within the plateau range, the cantilever deflects and seemingly, the silicon nanowire does not deform. In the displacement range higher than plateau range, the silicon nanowire most likely overcomes the friction and slips on the surface as shown in **Figure 59** (b) and the cantilever does not deflect. The plateau range is smaller for the longer nanowires. All in all, the conducted simulations show that the softness of a probe depends not only on the mechanical characteristics of a nanowire tip but also the cantilever spring constant. Therefore, using nanowires as a scanning tip does not necessarily provide a soft scanning probe.



**Figure 62** Plotted graphs from simulated data showing the main displacement of the probe ( $D$ ) versus the cantilever displacement at the edge ( $d_c$ ) by considering a friction coefficient of 0.5 between the tip and the sample for two conditions; (a) the nanowire geometry is kept constant (length of 8  $\mu\text{m}$  and diameter of 120 nm) and the spring constant of cantilever varies between 0.017 to 17.5 N/m. The corresponding trend of  $K=0.65$  N/m and  $K=17.5$  N/m are nearly the same and they overlap. Likewise, a similar trend is observed for the other values of  $K$ . Here,  $K$  indicates the spring constant of the cantilever. (b) For the condition, where the cantilever spring constant is kept constant at 0.6 N/m and the nanowire length varies between 2 to 26  $\mu\text{m}$ . Here, the nanowire length is denoted as  $L_{NW}$ .



### 3.5.2 Cantilever and Silicon Nanowire Oscillations

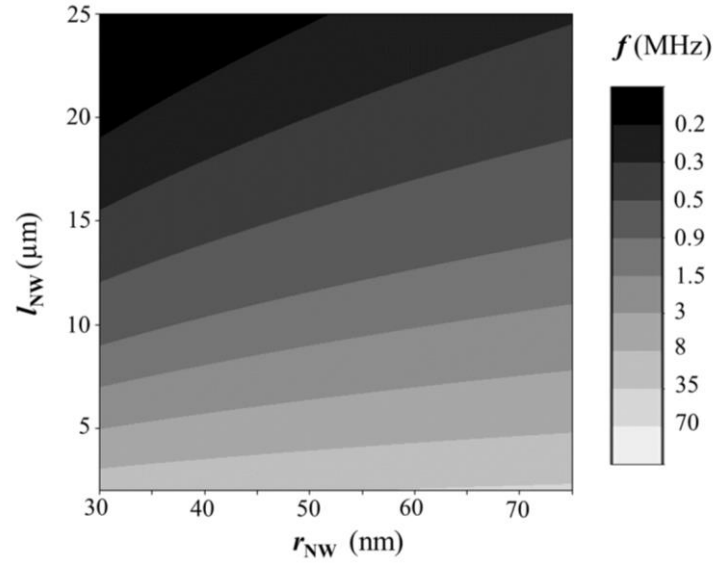
AFM measurements are carried out in two modes; contact and non-contact modes. In the latter case, AFM probes are tapping in the vicinity of the sample surface and the oscillation takes place at the resonance frequency of the cantilever. [221] This mode is known as a tapping mode. The tapping mode overcomes some of the limitations of contact mode by eliminating lateral forces that can distort or damage samples. [152] During measurements in tapping mode, keeping the amplitude of the oscillation constant is a key factor. In principle, due to height changes on a surface, which leads to a change in the interaction force between a tip and sample surface, the oscillation amplitude shifts to a lower value. [152] A required signal to keep the oscillation amplitude constant is recorded as the height change in the surface topography. [222] Conventional AFM probes are composed of a pyramid-shaped tip on silicon or silicon nitride cantilevers. As the resonance frequency of the tip is higher than the resonance frequency of the cantilever itself, it is very unlikely for the tip to oscillate at the frequency, at which the cantilever resonates. However, the cantilever oscillations might cause silicon nanowire vibrations, as the resonance frequency of the tip might coincide with the resonance frequency of the cantilever. This is a critical issue as the oscillation of the tip makes scanning results inaccurate and it is not feasible for the tip to trace topography features on scanned surfaces. Although the cantilever does not necessarily oscillate at its resonance frequency in peak force tapping mode [223], the silicon nanowire oscillation has to be taken into account, not only for tapping mode but also for peak force tapping mode. Here, the aim is to understand the oscillation behavior of a silicon nanowire on a cantilever, particularly when a cantilever resonates at its resonance frequency. The oscillation is not only an important subject for AFM topography applications, but also for dynamic-mode cantilever sensors. [224] So far, in section 3.1.2, it was mentioned how cantilever resonance frequencies could be investigated by the analytical methods and COMSOL simulation. Here, a theoretical study is provided for the investigations of silicon nanowire resonance frequencies. Afterward, the vibrational behavior of a silicon nanowire tip on a cantilever, including resonance frequencies and amplitudes of vibrations based on COMSOL simulations will be discussed.

#### I. Analytical Investigation for Silicon Nanowire Oscillations

As it was mentioned in section 3.1.2, for a tipless  $\text{Si}_3\text{N}_4$ -cantilever with simple geometry, it is possible to estimate the resonance frequency via the theoretical and analytical solutions. Here, the same principle is applied to calculate the resonance frequency of silicon nanowires, as schematically illustrated in **Figure 58** (a), based on the following relation:

$$f_n = \frac{ra_n}{4\pi l^2} \sqrt{\frac{E}{d}} \quad (3-17)$$

Here,  $f_n$  stands for the resonance frequency of the silicon nanowire at the order of  $n$ .  $E$ ,  $d$  and  $l$  represent Young's elastic modulus, diameter and length of silicon nanowires, respectively. Here, the silicon nanowire density is  $2329 \text{ kg/cm}^3$  [225]. The value of  $a_n$  is given correspondingly in **Table 1**, in section 3.1.2. According to the mentioned relation, it is possible to plot a contour map, as it is shown in **Figure 63**. Based on this plot and the relation, it can be depicted that the resonance frequency of nanowires depends on their length more than on the diameter. Nevertheless, changing any of these parameters results in a different resonance frequency value.

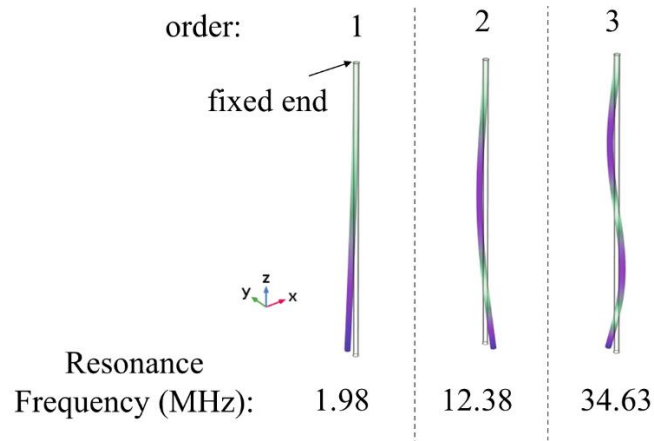


**Figure 63** Contour plot of the first order of the silicon nanowire resonance frequency. The silicon nanowire is a cylindrical-shaped beam with one fixed-end. Here,  $r_{NW}$ ,  $l_{NW}$  and  $f$  stand for the silicon nanowire radius, length and resonance frequency, respectively.

AFM cantilever resonance frequencies are commonly between 10 and 350 kHz. Specially designed fast-scanning probes have also been produced by various manufacturers (e.g., Olympus and Bruker). These probes have very high resonance frequencies even in the MHz range and these ultra-high frequency scanning probes enable very fast scanning compared to the conventional ones [226], [227]. However, working with ultra-high frequency probes requires a compatible scanning device with an optical beam deflection system with a sufficiently small focus spot to use small cantilevers. [228][229] It is likely for silicon nanowires to oscillate, while the corresponding cantilever resonates at a frequency close to the resonance frequency of the nanowire. Based on the theory, it is only possible to investigate the resonance frequency of cantilevers and nanowires separately and only the comparison of the resonance frequencies gives a hint on whether silicon nanowires oscillate, while the cantilever oscillates. If the resonance frequency of a silicon nanowire tip is nearly the same or even smaller than the resonance frequency of the corresponding cantilever, the silicon nanowire tip is prone to oscillation. Therefore, in this case, performing measurements is feasible only in contact mode. In order to study the vibrational behavior of a silicon nanowire probe, they are simulated and investigated in COMSOL Multiphysics software, which is discussed fully in the next section.

## II. Simulation Investigations for Silicon Nanowire Oscillations

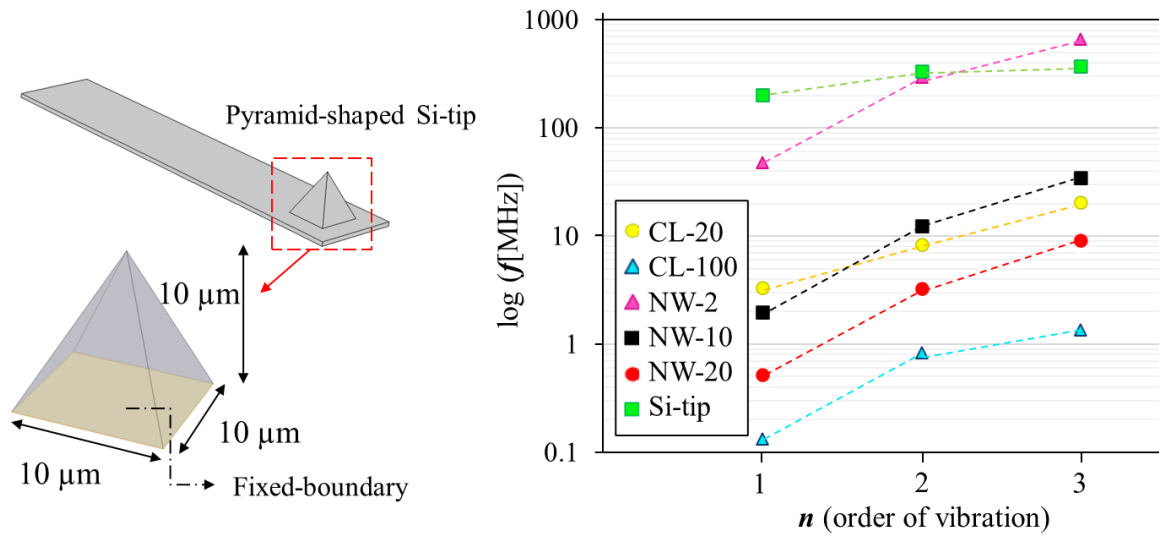
At first, silicon nanowire resonance frequencies and vibrational behavior are simulated in COMSOL multiphysics software 5.3a. In the simulation, solid mechanics and eigenfrequency are selected as the physics and study field, respectively. It is important to note that, in the eigenfrequency mode, it is possible to estimate only the resonance frequency and vibrational mode shapes. As mentioned in section 3.1.2, the resonance frequency and vibrational mode shapes of cantilevers were investigated in this mode. Here, similar simulations were conducted for silicon nanowires. Correspondingly, silicon nanowires are considered as a cylindrical-shaped beam with one fixed-end, as schematically illustrated in **Figure 58** (a). For instance, in **Figure 64**, the vibrational mode shapes of a silicon nanowire with a length of  $10\ \mu\text{m}$  and a diameter of  $160\ \text{nm}$  are shown for the first three orders of its resonance. Here, a resonance order represents the sequence of the resonance frequencies, so that the first order corresponds to the lowest resonance frequency. As silicon nanowires are considered here with a circular cross-section, the vibration shape is similar in different directions (e.g., in  $x$ - or  $y$ -directions) at each order of the resonance.



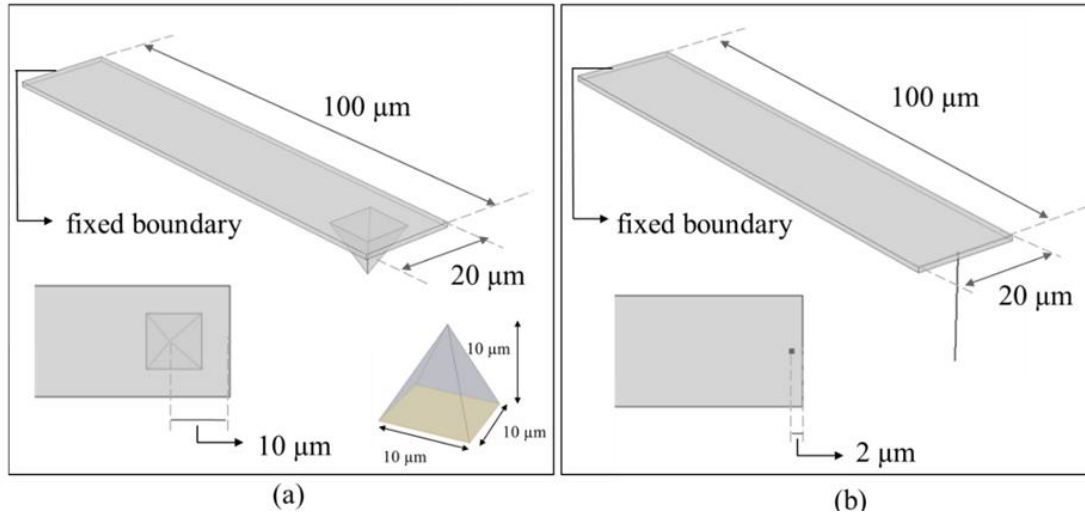
**Figure 64** Vibrational mode shapes of a cylindrical-shaped silicon nanowire with a diameter of  $160\ \text{nm}$  and a length of  $10\ \mu\text{m}$  at the first three resonance frequencies.

As discussed earlier, one of the approaches to understand whether silicon nanowires are at risk of vibration by the cantilever oscillations, is to simply compare their resonance frequencies. For instance, a relevant comparison is shown in **Figure 65** for the first three orders of resonance frequencies for a pyramidal-shaped silicon tip, schematically shown in **Figure 65** and indicated as Si-tip. The pyramidal silicon tip is considered with a baseplate being fixed, as shown in **Figure 65**. Furthermore, the resonance frequencies are simulated and plotted for a rectangular  $1\ \mu\text{m}$  thick tipless  $\text{Si}_3\text{N}_4$ -cantilever with a width of  $20\ \mu\text{m}$  and a length of  $20\ \mu\text{m}$  (denoted as CL-20), another rectangular  $1\ \mu\text{m}$  thick tipless  $\text{Si}_3\text{N}_4$ -cantilever with a width of  $20\ \mu\text{m}$  and a length of  $100\ \mu\text{m}$  (denoted as CL-100), a  $2\ \mu\text{m}$  long silicon nanowire with a diameter of  $160\ \text{nm}$  (NW-2), a  $10\ \mu\text{m}$  long silicon nanowire with a diameter of  $160\ \text{nm}$  (NW-10) and a  $20\ \mu\text{m}$  long silicon nanowire with a diameter of  $160\ \text{nm}$  (NW-20). Here, silicon nanowires and cantilevers are considered as a beam with one fixed

end. In this graph, for a better comparison, the logarithmic value of the resonance frequency is taken into account. As the graph depicts, the resonance frequency of the pyramidal silicon tip is quite large compared to the other resonance frequencies, confirming that it is unlikely for the pyramidal tip to oscillate. At the second resonance frequencies of “CL-100”, the “NW-20” is prone to oscillation, as the resonance frequency of the nanowire at its first order is lower than the resonance frequency of the cantilever at its second order. Therefore, for the cantilever “CL-20”, choosing a right tip is more critical. For further analysis, the investigated cantilever (CL-100), silicon tip and nanowire tips, whose resonance frequencies are shown in **Figure 65**, are simulated together in COMSOL, solid mechanics/eigenfrequency mode. In **Figure 66**, the schematic illustrations of a pyramidal silicon tip (a) and silicon nanowire tip (b) on a  $1\text{ }\mu\text{m}$  thick  $\text{Si}_3\text{N}_4$ -cantilever are shown, which are used for the simulation.

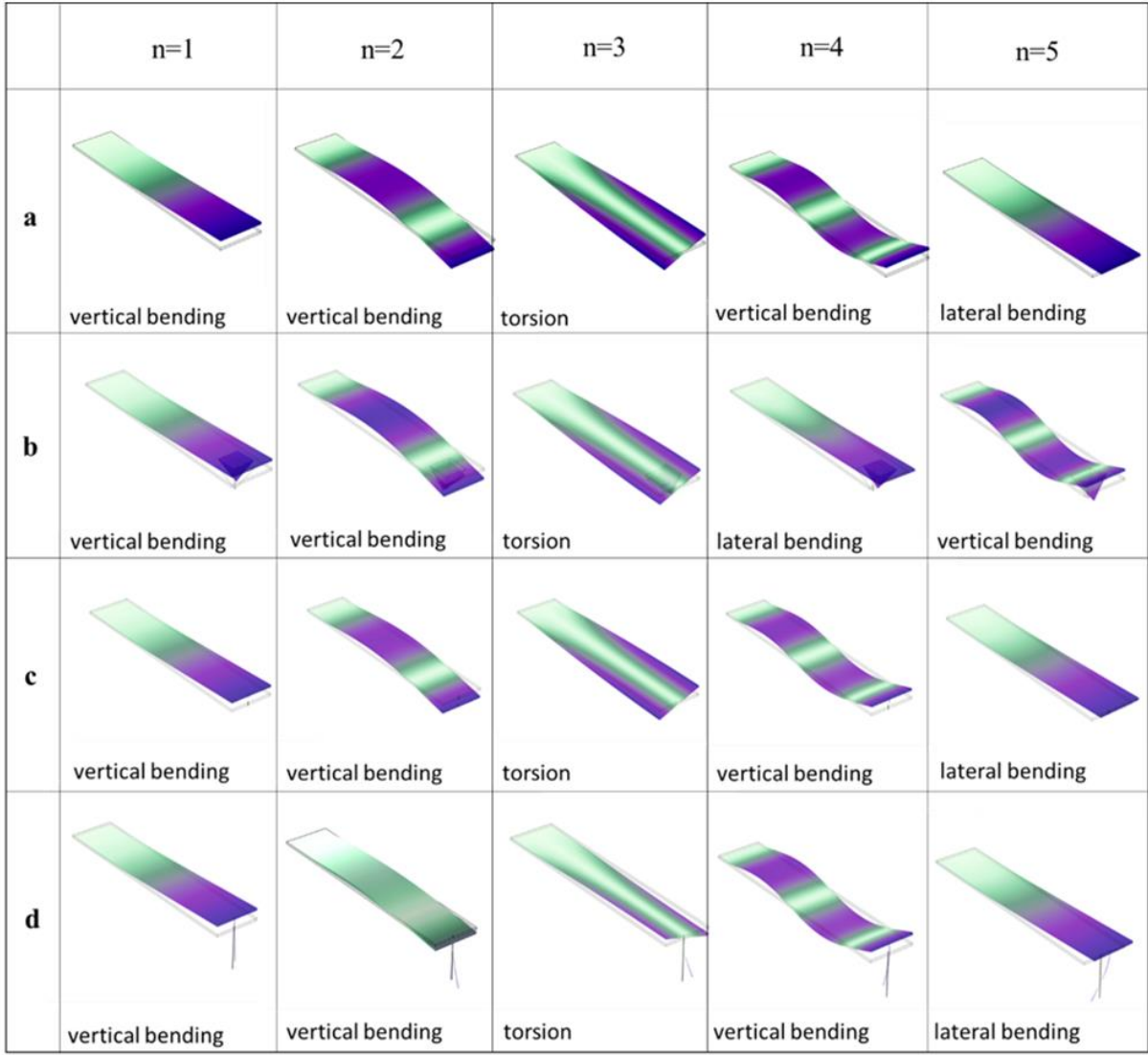


**Figure 65** (left) Schematic illustration of a pyramidal silicon tip with a fixed boundary at the baseplate and given geometry. (right) Logarithmic values of the resonance frequencies for a rectangular  $1\text{ }\mu\text{m}$  thick tipless  $\text{Si}_3\text{N}_4$ -cantilever with a width of  $20\text{ }\mu\text{m}$  and a length of  $20\text{ }\mu\text{m}$  (denoted as CL-20), a rectangular  $1\text{ }\mu\text{m}$  thick tipless  $\text{Si}_3\text{N}_4$ -cantilever with a width of  $20\text{ }\mu\text{m}$  and a length of  $100\text{ }\mu\text{m}$  (denoted as CL-100), a  $2\text{ }\mu\text{m}$  long silicon nanowire with a diameter of  $160\text{ nm}$  (NW-2), a  $10\text{ }\mu\text{m}$  long silicon nanowire with a diameter of  $160\text{ nm}$  (NW-10) and a  $20\text{ }\mu\text{m}$  long silicon nanowire with a diameter of  $160\text{ nm}$  (NW-20). Silicon nanowires and cantilevers are considered as a beam with one fixed end. A pyramidal silicon tip here is denoted as Si-tip and its fixed boundary is indicated in the schematic illustration on the left. Furthermore,  $f$  and  $n$  indicate the frequency and order of the resonance, respectively.

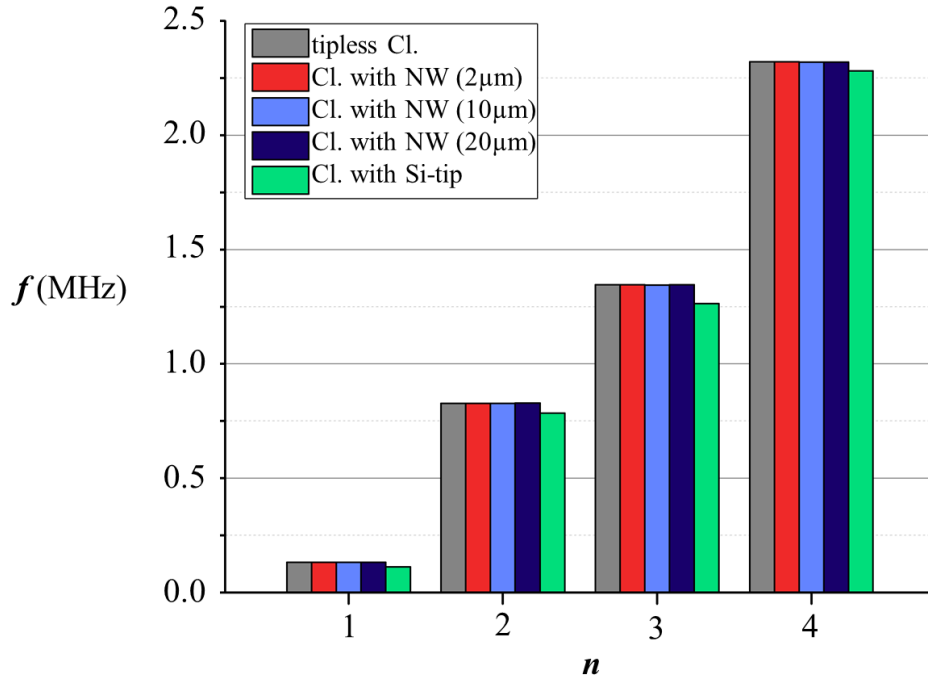


**Figure 66** Schematic illustrations of (a) Pyramidal silicon tip on a  $1\ \mu\text{m}$  thick  $\text{Si}_3\text{N}_4$ -cantilever and (b) A silicon nanowire tip ( $160\ \text{nm}$  in diameter) on a  $1\ \mu\text{m}$  thick  $\text{Si}_3\text{N}_4$ -cantilever, considered for COMOSL simulations.

As mentioned earlier, it is possible to obtain the resonance frequency and vibrational modes in the eigenfrequency mode. Therefore, in order to estimate the resonance frequency of scanning probes with silicon nanowires or a pyramidal silicon tip, they are simulated in the eigenfrequency mode. The applied geometries for the simulated probes are based on the schematic illustrations in **Figure 66**. The corresponding mode shapes are shown in **Figure 67** for the first five orders of the resonance. The mode shapes are accordingly categorized in three classes: vertical bending, lateral bending and the torsion movement. Depending on the type of measurements and applications in AFM, either of these modes is favored [230]. However, for the simple topography measurements, the vertical bending is required [230]. Therefore, for the rest of the investigations, only the vertical bending is considered, which can be found in the first, second and fourth order of the resonance for the tipless and silicon nanowire probes and the first, second and fifth order of the resonance for the pyramidal silicon probe. Besides the mode shapes, the resonance frequency of the mentioned probes is presented in the graph shown in **Figure 68**. According to the theory and due to the larger mass in a silicon pyramidal tip, the resonance frequency of the mentioned probe is slightly lower than the one of the tipless cantilever and silicon nanowire probes.

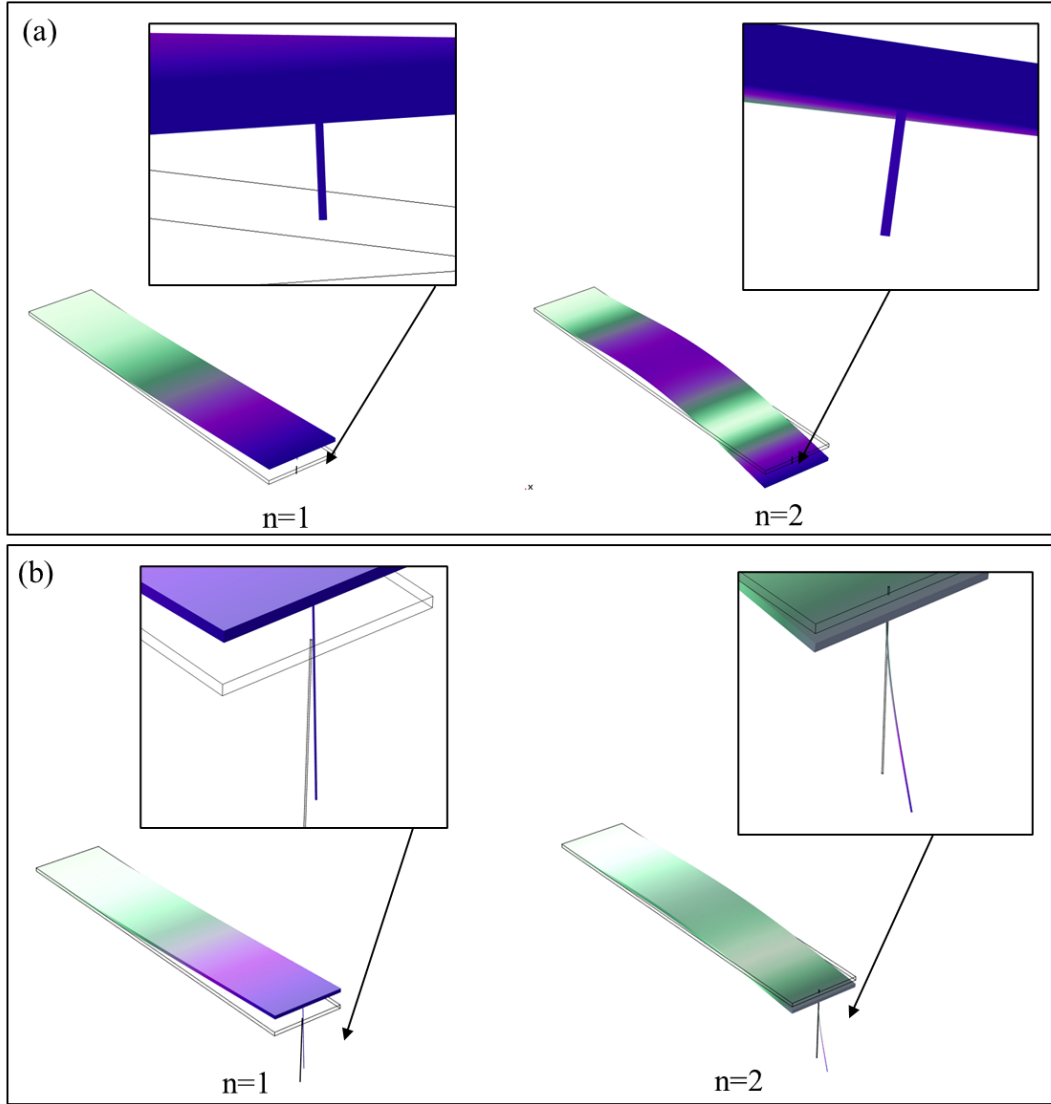


**Figure 67** Vibrational mode shapes for the first five orders of the resonance for; (a) a rectangular  $1\ \mu\text{m}$  thick tipless  $\text{Si}_3\text{N}_4$ -cantilever with a length of  $100\ \mu\text{m}$  and a width of  $20\ \mu\text{m}$ , (b) a pyramidal silicon tip (as illustrated in **Figure 65** on the tipless cantilever shown in (a)), (c) a  $20\ \mu\text{m}$  long silicon nanowire probe (as illustrated in **Figure 69** on the tipless cantilever shown in (a)), (d) a  $2\ \mu\text{m}$  long silicon nanowire probe (as illustrated in **Figure 69** on the tipless cantilever shown in (a)).



**Figure 68** The first four orders of resonance frequencies of a tipless  $\text{Si}_3\text{N}_4$ -cantilever, silicon nanowire probes and a pyramidal silicon tip, as schematically illustrated in **Figure 66**. Here, Cl. With NW stands for the cantilever with a silicon nanowire tip. The silicon nanowire length is shown in parentheses.

As mentioned before, a comparison of resonance frequency is shown in **Figure 65**, in order to estimate the silicon nanowire oscillation. Accordingly, the first resonance frequency of the silicon nanowire with a length of 20  $\mu\text{m}$  is lower than the second resonance frequency of the cantilever with a length of 100  $\mu\text{m}$ . This shows that the silicon nanowire most likely oscillates, while the cantilever resonates at its second order. The eigenfrequency mode provides some information about oscillations, including the resonance frequency and vibrational mode shapes, as presented in **Figure 67** and **Figure 68**. A closer view of vibrational modes of the silicon nanowire scanning probes composed of a cantilever with a length of 100  $\mu\text{m}$  and a silicon nanowire 2 and 20  $\mu\text{m}$  are shown in **Figure 69** (a) and (b), respectively. As it can be depicted, in probe (a), the silicon nanowire does not deform and instead remains straight at the first and second resonance frequency. On the other hand, the 20  $\mu\text{m}$  long silicon nanowire at the second order of the resonance, deforms and deflects from the straight line shown in the image. This confirms again a great likelihood for the 20  $\mu\text{m}$  long silicon nanowire to oscillate, unlike the 2  $\mu\text{m}$  long silicon nanowire. In eigenfrequency mode, it is not possible to derive to the displacement values, as the damping and excitation force can not be implemented into the simulation. This is the reason why no scale bar is used for the vibrational mode as the displacement or stress values are invalid. However, the main vibrational mode shape can be extracted.



**Figure 69** Vibrational mode shapes of a silicon nanowire probe (shown schematically in **Figure 66**) at first and second order of the resonance frequency with a silicon nanowire tip with a length of  $2\ \mu\text{m}$  (a) and  $20\ \mu\text{m}$  (b). Here,  $n$  stands for the order of the resonance.

As mentioned before, the displacement values can not be obtained in the eigenfrequency mode and for a better analysis, the displacement values are indeed quite useful, so as to know the vibration amplitude, not only for the cantilever but also the tip. For instance, if the nanowire oscillates, the displacement might not lead to a huge value and considerable disturbance in the measurements. Therefore, the displacement values and quality factors can provide useful information about the oscillation and its likelihood. One of the important factors for determining the oscillation displacement is damping. In a simple word, damping is defined as a dissipation in mechanical energy [231]. If the oscillation of the system is in a single well-defined mode, the energy lost ( $W$ ) per cycle is defined as a function of amplitude ( $a$ ) and frequency ( $\omega$ ). A simple definition of damping is defined as the energy lost per cycle compared to the peak potential energy stored within a cycle and denoted as  $V$ . The loss factor  $\eta$  is defined as [231]:

$$\eta = \frac{W}{2\pi V} \quad (3-18)$$



In finite element simulations, the equations of the motion in a matrix form can be written as [231]:

$$M\ddot{u} + C\dot{u} + Ku = f(t) \quad (3-19)$$

Here,  $M$ ,  $C$ ,  $K$ ,  $u$  and  $f$  are the mass, damping, stiffness, displacement vector, and force vector, respectively. The mass and stiffness matrices can be obtained given the geometry and basic material parameters, such as mass density and Young's modulus. The damping matrix can, however, be formed in many ways. One of the damping types that is used for the frequency-response analysis here is the loss factor. The damping ( $c$ ) is defined as follows [232]:

$$c = \frac{\eta K}{\omega} \quad (3-20)$$

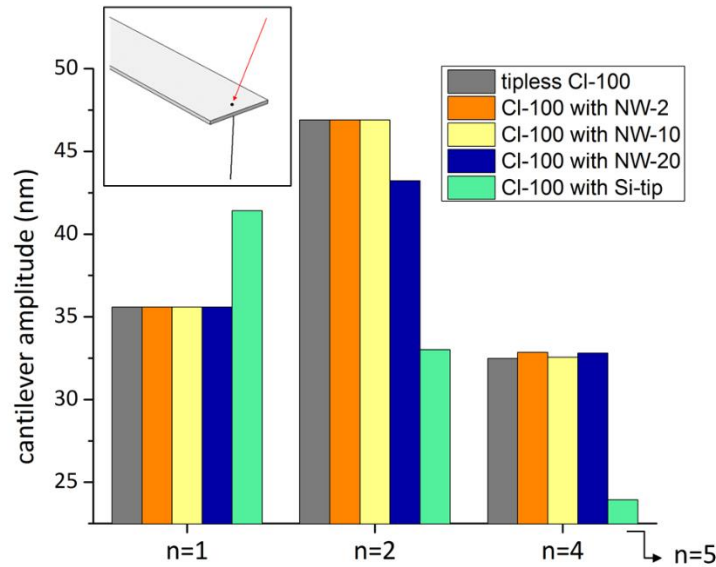
In the following analysis, the isotropic loss factor of silicon and silicon nitride were approximated and set as 0.0001 [233], [234]. In addition, an excitation force was required for activating the oscillations. The excitation force was applied in the  $z$ -direction, on both cantilever and tip, by activating the harmonic perturbation option. The corresponding values for the excitation forces are listed in **Table 5**, which are different for the different orders of the resonance. The values were set in a way that the amplitude of the resonance remains around 40-50 nm, which is used conventionally for the free oscillations in AFM measurements. Damping and excitation forces are the main features, which should be applied in the frequency-domain mode in order to investigate the displacement values at any frequency range.

**Table 5** Applied force on probes for the probe oscillation at their resonance frequencies in COMSOL structural mechanics, frequency-domain mode. Here,  $n$  and  $F$  represent the order of resonance and the corresponding applied load, respectively. Only for the pyramidal silicon tip, the fifth order is applied instead of the fourth.

<b>n</b>	<b>F [nN]</b>
1	0.01
2	1
4	10
5	10

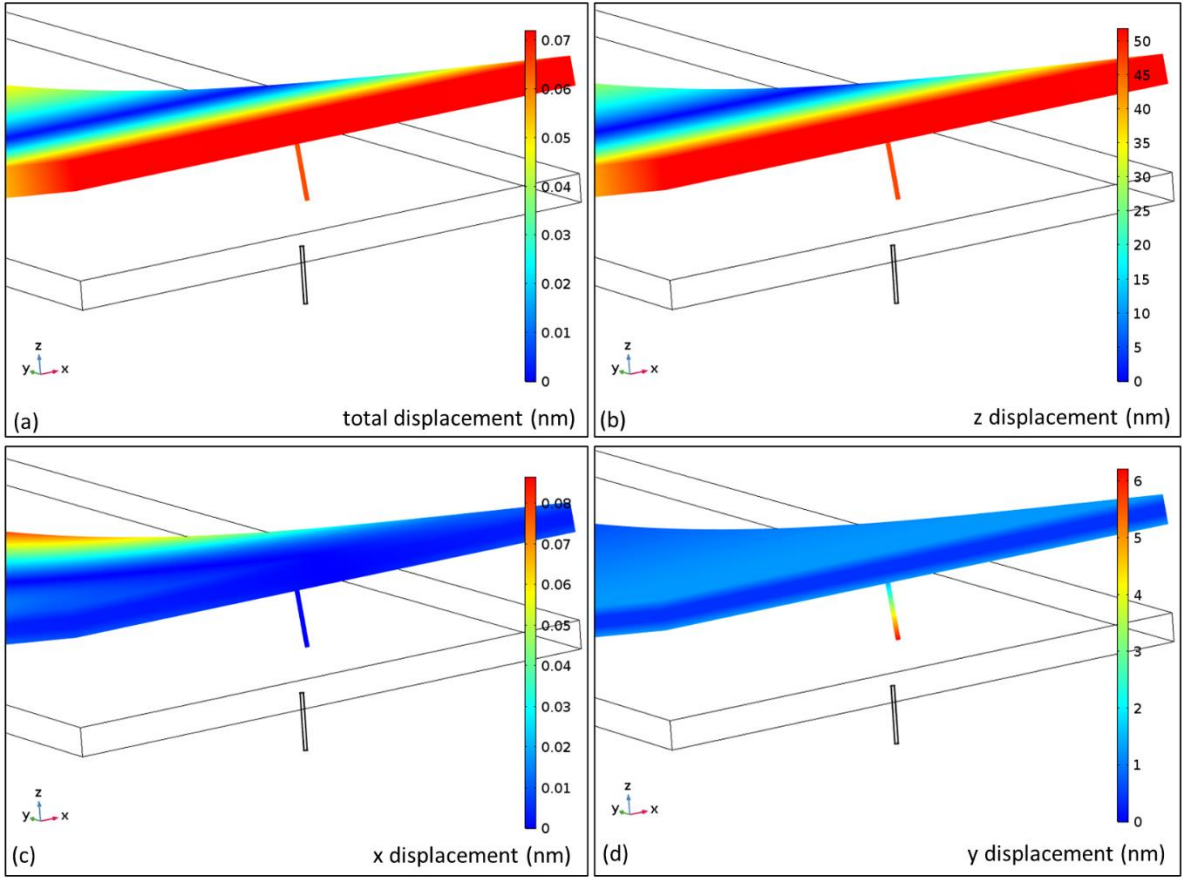
Based on the defined parameters, the simulations were conducted in the frequency-domain mode for the scanning probes shown in **Figure 66**. Correspondingly, the amplitudes of the vibration were investigated only for the resonance orders, for which the cantilever has only a vertical bending movement. Therefore, for the silicon pyramidal probe, the fifth order is compared to the fourth order of the silicon nanowire probes, based on the vibrational mode shapes shown in **Figure 67**. The amplitude of the vibrations is studied by considering only the vertical/ $z$ -direction movement on a point on the cantilever, in the width center. This point is distanced about 2  $\mu\text{m}$  from the edge of the cantilever (shown and indicated by the red arrow in **Figure 70**). With regard to the plotted data, the amplitude of the vibration for the pyramidal

silicon tip is lower than the one for the other types of the probes, as the pyramidal silicon tip has a considerable mass compared to the silicon nanowires. Therefore, a greater force is required to excite this probe for a similar amplitude value. Furthermore, the amplitude of the vibration for the tipless  $\text{Si}_3\text{N}_4$ - cantilever and the silicon nanowire is nearly the same, except for the second order of the resonance, at which the 20  $\mu\text{m}$  silicon nanowire probe has a lower amplitude. The occurrence of the silicon nanowire vibration and oscillation can be a reason for the lower amplitude value, as the excitation force applied on the mentioned probe causes not only the cantilever vibration, but also the nanowire resonance.

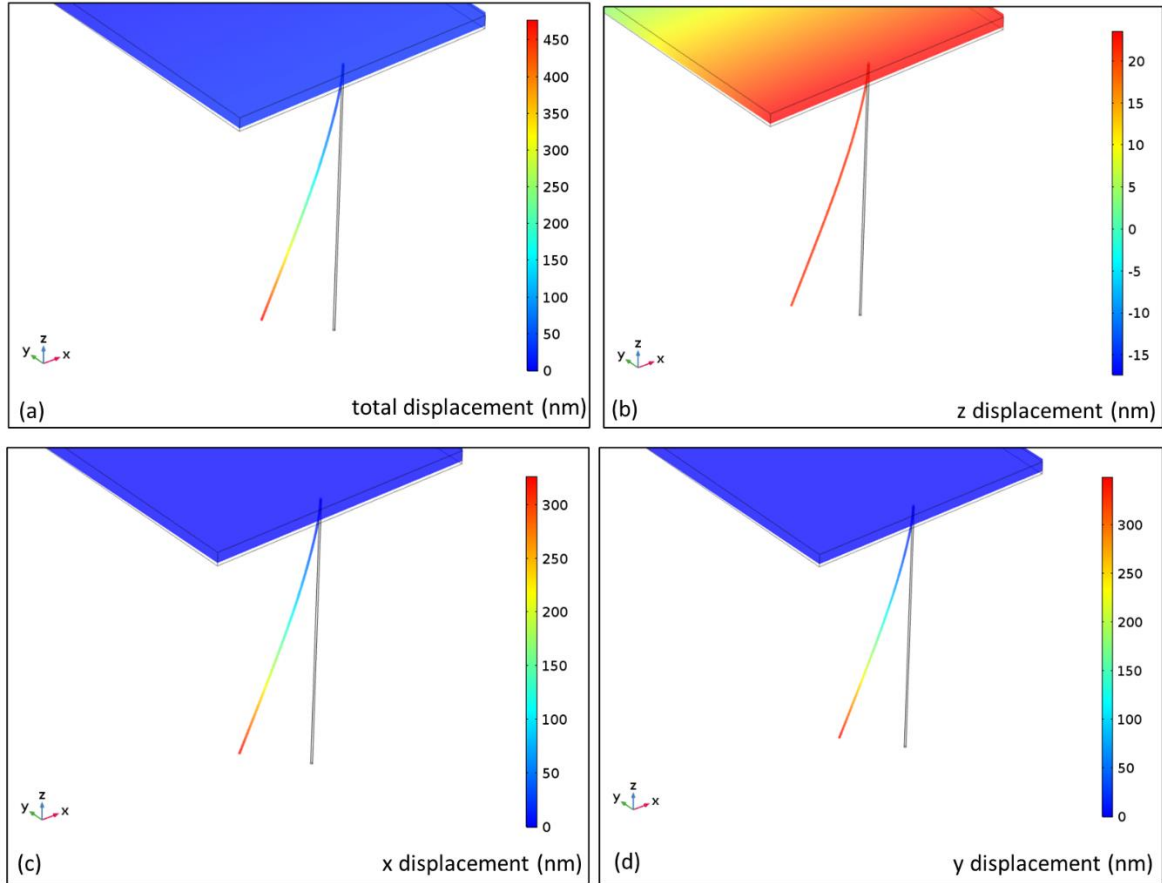


**Figure 70** *Vibration amplitudes for the probes shown in Figure 66 by considering the excitation force given in the Table 5 and vertical displacement of the point indicated in the schematic. The fifth order is considered only for the pyramidal silicon probe instead of the fourth due to the vertical bending.*

The frequency-domain mode can also provide a 3D map of total displacements or any displacement in  $x$ - or  $y$ - or  $z$ -direction. Previously, based on the mode shapes obtained in the eigenfrequency mode, it was shown that the 2  $\mu\text{m}$  long silicon nanowire is nearly straight at the resonance frequencies of the cantilever. On the other hand, the 20  $\mu\text{m}$  long silicon nanowire at the second resonance frequency of the cantilever deforms and apparently does not remain straight, indicating the nanowire vibration. For a better analysis, the mentioned probes were simulated in the frequency-domain mode and the corresponding 3D displacement contour at the second resonance frequency of the cantilevers are shown in Figure 71 and Figure 72. As depicted from the results in Figure 71, the 2  $\mu\text{m}$  long silicon nanowire has a slight movement of about 6 nm in  $y$ -direction. The displacement here is based on displacement from the initial position of the nanowire and cantilever. Therefore, the initial displacement here does not represent nanowire deformation. Therefore, it is very unlikely for the 2  $\mu\text{m}$  nanowire to be deformed at this resonance frequency, as the value is very small and can be attributed to the movement of the cantilever during oscillation. In contrast, the 20  $\mu\text{m}$  long silicon nanowire at the second resonance frequency of the cantilever shows a huge displacement in both  $x$ - and  $y$ -directions for about 350 nm. This can clearly show and confirm the vibration of the nanowire.

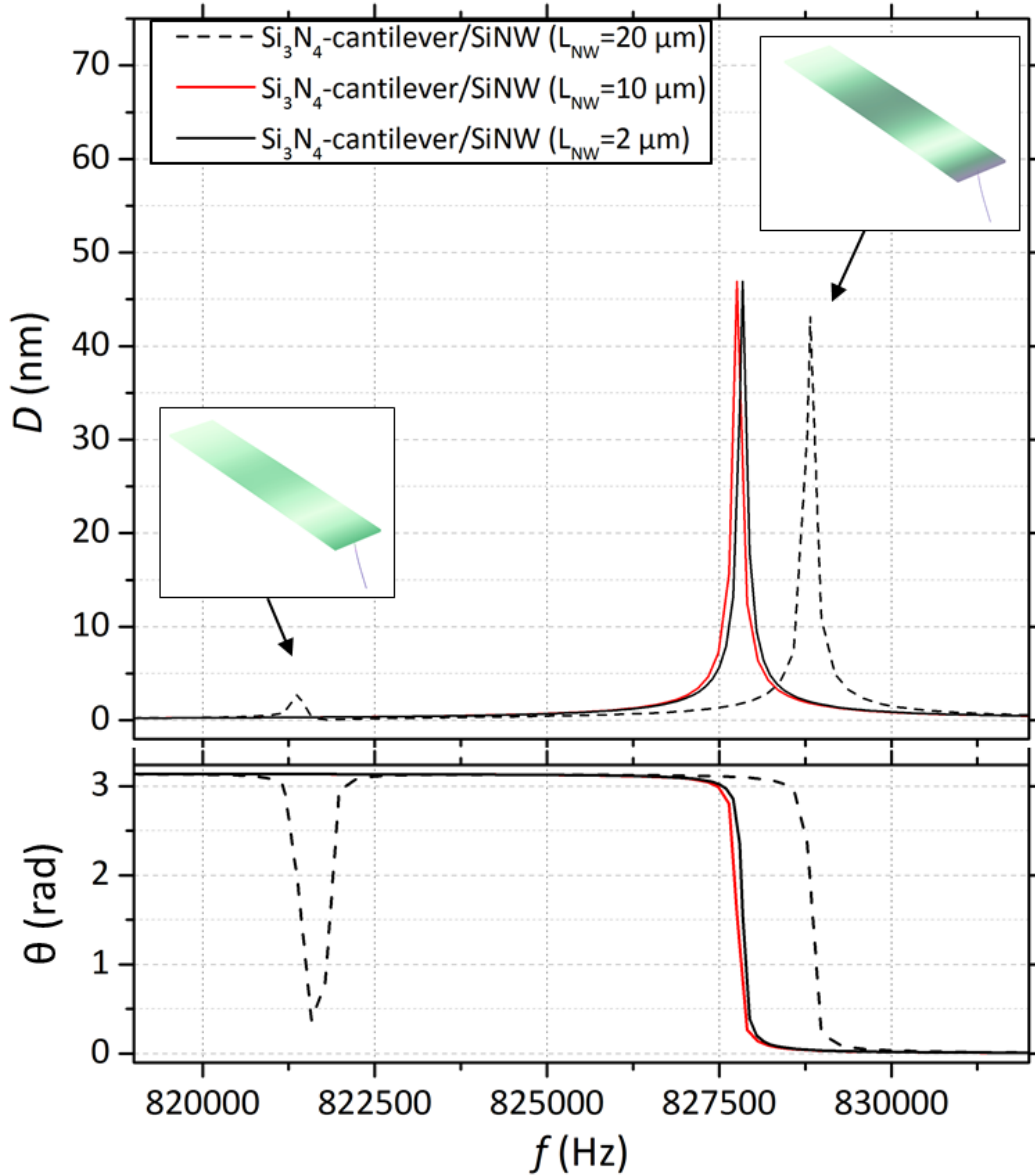


**Figure 71** (a) Total displacement, (b) Displacement in  $z$ -direction, (c) Displacement in  $x$ -direction and (d) Displacement in  $y$ -direction of a silicon nanowire probe shown in **Figure 69** (a) at the second resonance frequency of the cantilever, simulated in COMSOL multiphysics, structural mechanics, frequency-domain mode. The excitation force applied on the probe is 1 nN.



**Figure 72** (a) Total displacement, (b) Displacement in  $z$ -direction, (c) Displacement in  $x$ -direction and (d) Displacement in  $y$ -direction of a silicon nanowire probe shown in **Figure 69** (b) at the second resonance frequency of the cantilever, simulated in COMSOL multiphysics, structural mechanics, frequency-domain mode. The excitation force applied on the probe is 1 nN.

The vibrational amplitude of cantilevers can also be investigated for a frequency range close to the resonance frequency. Accordingly, in **Figure 73** the plotted vibrational amplitudes and phases versus a frequency range are presented. The range of the frequency is chosen in a way that the second resonance frequency is in the range. In **Figure 73**, the peak value represents the amplitude of the cantilever with the 2  $\mu\text{m}$  and 10  $\mu\text{m}$  long silicon nanowires at the resonance frequency of the cantilever, where the phase abruptly changes. On the other hand, there are two peaks observed for the 20  $\mu\text{m}$  silicon nanowire probe shown in **Figure 73**. The main peak represents the vibration at the second resonance frequency of the cantilever. However, the smaller peak (indicated by the red arrow) represents the nanowire vibration. Here, apparently, the nanowire vibration causes a slight vibration for the cantilever.



**Figure 73** Plotted cantilever amplitude and phase versus frequency range, including the second resonance frequency of the cantilever for the silicon nanowire probes schematically illustrated in **Figure 69**.  $L_{NW}$  stands for the silicon nanowire length.

Acquiring such plots is advantageous in order to investigate the quality factor of the vibrations, as well. The quality factor ( $Q$ ) of a cantilever probe indicates the energy dissipation capacity and the damping present in the system, which can be defined as [235]:

$$Q = \frac{f_r}{\Delta f} \quad (3-21)$$

Where,  $f_r$  is the resonance frequency,  $\Delta f$  is the resonance width or full width at half maximum (FWHM). In fact, the  $Q$  factor shows the qualitative behavior of a simple damped oscillator. The larger  $Q$ , the less an oscillator, is damped. [236] A system with a low quality factor ( $Q < 0.5$ ) is known as an overdamped system. [222] In this case, a system does not oscillate at all, but when displaced from its equilibrium steady-state, by returning it decays exponentially. [222] Underdamped systems with  $Q > 0.5$ , combine oscillation at

a frequency with a decay in the signal amplitude. [222] Accordingly, the  $Q$ -values were obtained for the resonances, shown in **Figure 73** and are listed in **Table 6**. FWHF values were acquired by a non-linear curve fitting function to the mentioned plots. The coefficient of determination ( $R^2$ ) was above 0.9. The applied equation for fitting is:

$$y = y_0 + Ae^{\frac{-(x-x_c)^2}{2w^2}} \quad (3- 22)$$

Here,  $x$  and  $y$  are the only variables.  $A$ ,  $x_c$  and  $w$  are constants and obtained by the fitting.

**Table 6** Obtained quality factors ( $Q$ ) for the silicon nanowire probe oscillation shown in **Figure 73**.

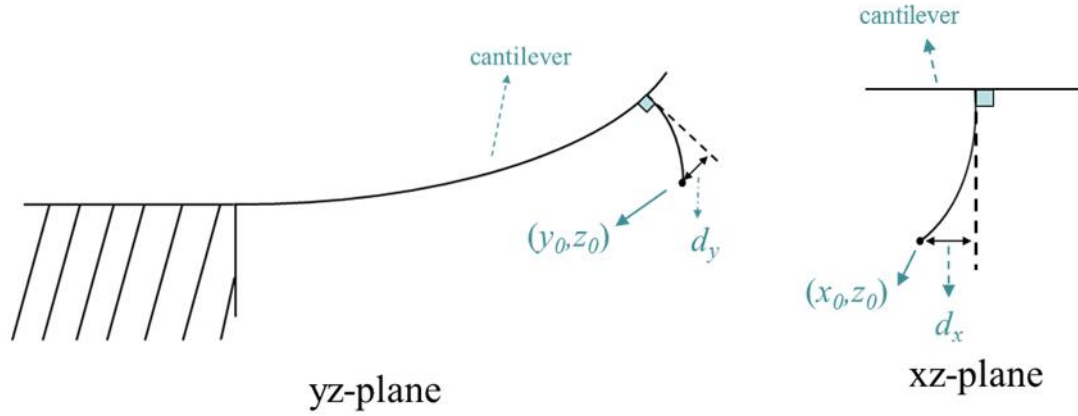
Type of SiNW tip	FWHM (Hz)	$f_r$ (Hz)	$Q$
SiNW 20 $\mu\text{m}$ / small peak	$215.8 \pm 21.8$	821392.4	$3805.7 \pm 383.9$
SiNW 20 $\mu\text{m}$ / main peak	$177.6 \pm 8.7$	828822.2	$4665.7 \pm 228.8$
SiNW 10 $\mu\text{m}$	$196.5 \pm 6.9$	827767.8	$4212.7 \pm 147.3$
SiNW 2 $\mu\text{m}$	$207.7 \pm 8.7$	827838.6	$3984.9 \pm 168.0$

As mentioned before, the acquired displacements from the simulation show the initial NW displacement, as illustrated in **Figure 74**. In order to investigate the NW displacement, regardless of the cantilever displacement, the coordinates of each point ( $x, y, z$ ) after displacement is calculated and the translation is performed as followed:

$$(x, y, z) \rightarrow (x + \Delta x, y + \Delta y, z + \Delta z) \quad (3- 23)$$

By considering the fact that the vibration of the cantilever has a vertical bending movement, for further analysis, the nanowire displacement is only considered in  $yz$ -plane. A normalized vector is subsequently defined near the nanowire position on the cantilever, which represents the nanowire shape in a straight form without any vibrations. The new coordinate for the point at the nanowire tip, as illustrated in **Figure 74**, is obtained similarly. Basically, the distance of this point from the normalized vector is investigated and indicated by the nanowire displacement in  $y$ -direction ( $d_y$ ). The distance ( $d$ ) of a point ( $y_0, z_0$ ) from a line ( $ay+bz+c=0$ ) is defined based on the following relation:

$$d_y = \frac{|a(y_0)+b(z_0)+c|}{\sqrt{a^2+b^2}} \quad (3- 24)$$



**Figure 74** Schematic illustrations of a cantilever and deformed silicon nanowire with a displacement at the tip in the  $yz$ - and  $xz$ -planes.  $(x_0, z_0)$  and  $(y_0, z_0)$  stand for the coordination of a point at the nanowire tip in the  $xz$ - and  $yz$ -planes, respectively. The displacement of the nanowire tip in the  $x$ - and  $y$ -directions is denoted as  $d_x$  and  $d_y$ , respectively.

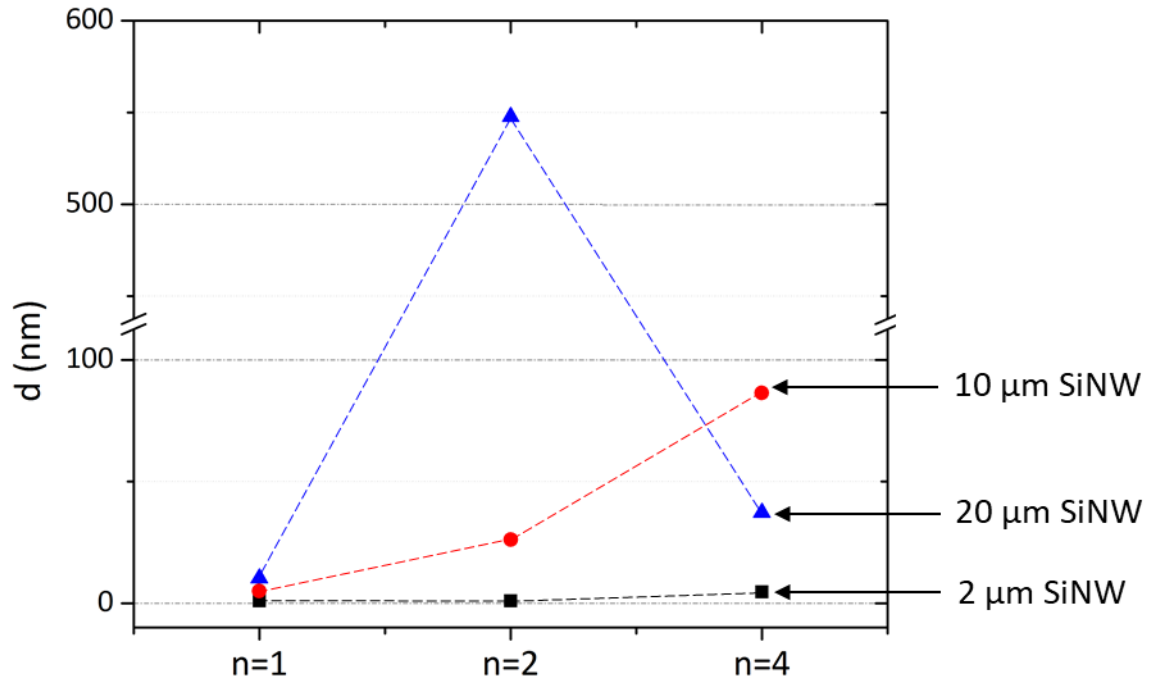
Similarly, the displacement in the  $x$ -direction ( $d_x$ ) was investigated by considering the distance ( $d_x$ ) of a point  $(x_0, z_0)$  from a line ( $dx+ez+f=0$ ), which is a normalized vector on the cantilever at the nanowire position in the  $xz$ -plane.  $d_x$  can be consequently investigated by the following relation:

$$d_x = \frac{|d(x_0)+e(z_0)+f|}{\sqrt{d^2+e^2}} \quad (3-25)$$

The total displacement was then obtained by the following relation:

$$d = \sqrt{d_x^2 + d_y^2} \quad (3-26)$$

Consequently, the amplitude of the vibration for the 2  $\mu\text{m}$ , 10  $\mu\text{m}$  and 20  $\mu\text{m}$  silicon nanowires were studied for the first, second and fourth resonance frequencies of the cantilever. The corresponding results are plotted in the graph of **Figure 75**. The displacement values for all silicon nanowire tips at the first order of the cantilever resonance are quite small and nearly the same. However, at the second order, the 20  $\mu\text{m}$  silicon nanowire has a large lateral displacement, which can cause severe distortions in the topography measurements. This large displacement can be attributed to the fact that the resonance frequency of the nanowire coincides with the second order of the cantilever resonance frequency. At the fourth order of the resonance, the 2  $\mu\text{m}$  silicon nanowire is the only tip with a lowest lateral displacement.



**Figure 75** Lateral displacement of a silicon nanowire tip (with a length of 2  $\mu\text{m}$ , 10  $\mu\text{m}$  and 20  $\mu\text{m}$ ) at first, second and fourth orders of the cantilever resonance.





## 4. Synthesis of Highly Ordered Silicon Nanowires

*Some parts of this section include materials and results which were published in the following paper:*

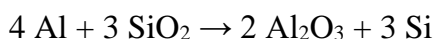
*A. Behroudj, D. Geiger, and S. Strehle, “Epitaxial Bottom-up Growth of Silicon Nanowires on Oxidized Silicon by Alloy-Catalyzed Gas-Phase Synthesis,” Nano Lett., vol. 19, no. 11, pp. 7895–7900, Nov. 2019. DOI: [10.1021/acs.nanolett.9b02950](https://doi.org/10.1021/acs.nanolett.9b02950) [1]*

*Adapted with permission from [1]. Copyright (2019) American Chemical Society.*

At the moment, the silicon nanowire orientation can not be controlled by the regrowth method. However, in the previous section, it was shown that the angle of silicon nanowires with respect to a scanning surface is very important and has a great impact on scanning quality and resolution. In this regard, there are methods, reported so far on how to modify the orientation of silicon nanowire tips. For instance, FIB is used to induce stress into synthesized silicon nanowires in order to modify the nanowire orientation [16]. Not only using FIB might affect silicon nanowire mechanical properties (by inducing stress), but also as mentioned earlier, these techniques are quite expensive, complex and indeed in contrast with the purpose of this work. Therefore, controlling nanowire orientations within the synthesis is more favored for the scope of this thesis. Synthesis of highly ordered silicon nanowires was realized first by top-down etching methods [237]. Despite the well-realized method, tuning and controlling silicon nanowire properties and particularly their sidewalls are found to be yet elaborate and challenging [237]. Later, epitaxial synthesis of silicon nanowires via bottom-up methods was introduced as a new approach to synthesize highly ordered silicon nanowires to overcome the limitations of top-down etching methods. The bottom-up growth approaches are favored on account of a facile process and great control over nanowire characteristics [23], [24]. Therefore, the epitaxial synthesis of silicon nanowires on cantilevers can be an alternative solution to the regrowth approach and can yield highly ordered silicon nanowire scanning tips for AFM applications. This section of the thesis focuses on a new approach using alloy catalysts for the epitaxial synthesis of silicon nanowires, properties of the nanowires, growth mechanism and conditions. So far, alloy catalysts were introduced for synthesis of silicon nanowires and creating abrupt Si/Ge heterojunctions (state of the art, section 1.1.1, II), but the epitaxial synthesis was not extensively studied and demonstrated. Although the epitaxial synthesis is targeted here to be employed as an alternative approach for the regrowth strategy to fabricate highly ordered silicon nanowire scanning probes, the epitaxial synthesis using the new approach could not be realized on scanning probes within the PhD course and is subject to the future study.

## 4.1. Epitaxial Synthesis of Silicon Nanowires Using Alloy Catalysts

Based on the bottom-up approach, silicon nanowires can be synthesized via the chemical vapor deposition (CVD) technique by using a metal catalyst such as Au, Al, Ag, Ni and many other metals. [23], [24] With this approach, epitaxial synthesis of silicon nanowires demands a certain pretreatment to remove the native oxide on silicon substrates, which is known to be the main hindering reason for the epitaxial synthesis [238]. Treating silicon substrates with HF (hydrofluoric acid), known as one of the most common wet chemical etchants for silicon oxide, leads to a hydrogen-terminated silicon surface. [239] However, the silicon surface reoxidizes within a few minutes under ambient conditions. This prevents any epitaxial growth, particularly if a non-high vacuum system is used for synthesis. [1] With this in mind, a new approach is introduced in this work by applying a substance that can react with an oxide layer, reduce it and provide pure silicon for epitaxial synthesis. [1] Simultaneously, this substance can endure the synthesis conditions. This simply eliminates the pretreatment step, required for the oxide removal and subsequently, its limitations. [1] For this purpose, here Al is used as a substance that is assumed to dissolve the oxide layer, as Al can react with silicon oxide based on the following reaction [240]:



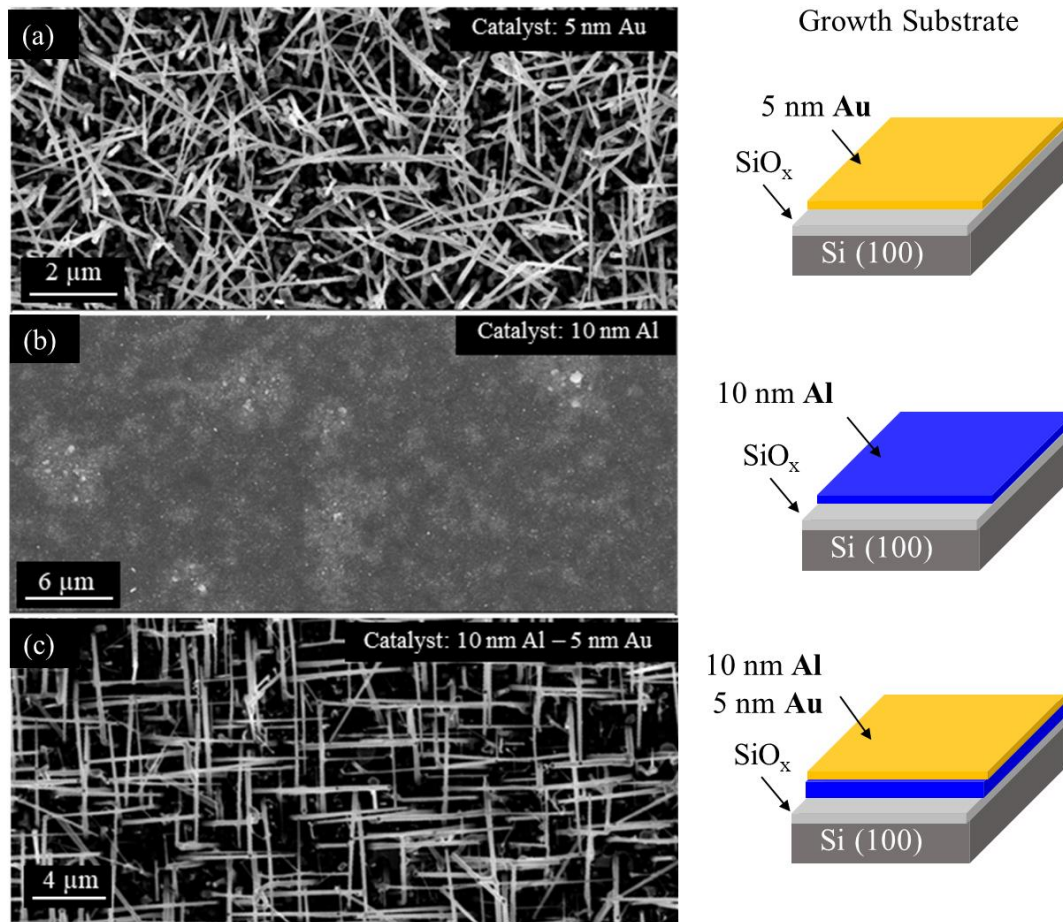
The temperature and the oxide quality significantly affect the kinetics of the reaction, particularly the activation energy. [241], [242] However, temperature above 500 °C should be high enough to initiate the reaction. [241], [242] The first synthesis of Al/Au-catalyzed silicon nanowires was carried out on single-crystalline silicon wafers having the crystallographic orientation (100) and covered by a native oxide layer (assumed to be around 1.5 nm thick). After cleaning the substrates (the cleaning procedure is described in Appendix section E), a thin Al film with a thin Au film on top was thermally evaporated on the substrates. The sample preparation procedure is described in Appendix section E and H. An Au layer on top can prevent the Al oxidation underneath. In the case of using one element as a catalyst, understanding the growth mechanism and consequently setting the growth conditions become quite simple, as the binary phase diagrams are available. However, no ternary phase diagram for Al-Au-Si is experimentally realized and only a pseudo-binary phase diagram of AlAu<sub>2</sub>-Si (with a eutectic temperature of about 487 °C) and Al<sub>2</sub>Au-Si (with a eutectic temperature of about 922 °C) is reported. [243] The synthesis conditions were consequently optimized at different growth temperatures, pressures using Al/Au-catalysts with different thicknesses (in the range of 2-20 nm), which are elaborated in the sections 4.2. The optimum growth parameters for the epitaxial synthesis with the highest density are listed in **Table 7**, using 10 nm Al and 5 nm Au. Afterward, for the sake of comparison, a sole 5 nm thick Au film and a sole 10 nm thick Al film were deposited on the substrates as well. Later, the as-prepared substrates were placed in the NWCVD tube.

The nanowires were subsequently synthesized under the optimized growth conditions demonstrated in **Table 7**.

**Table 7** *Optimized growth parameters for silicon nanowire synthesis using Al/Au-catalysts.*

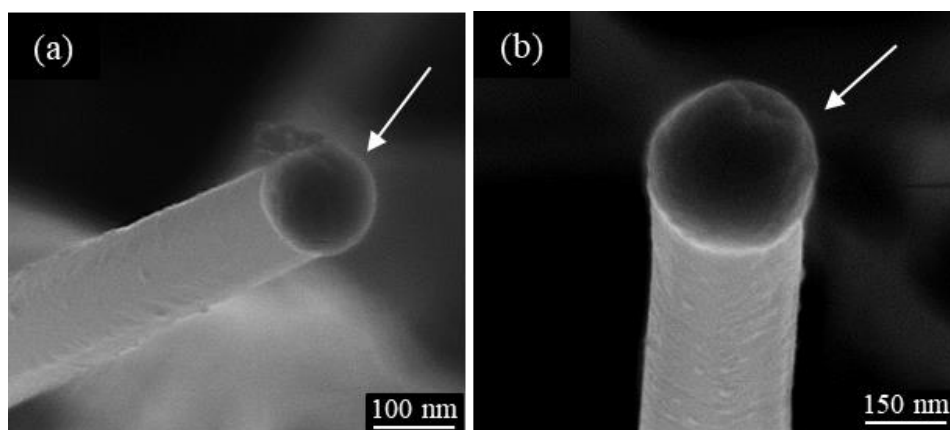
Growth Parameters	
Temperature	550 °C
H <sub>2</sub> flow	80 sccm
SiH <sub>4</sub> /He (2% SiH <sub>4</sub> in He) flow	20 sccm
Pressure	10 mbar
Time	60 minutes

The SEM images of the substrates after the synthesis are shown in **Figure 76**. As expected, Au-catalyzed silicon nanowires were grown with random orientations, due to the native oxide remaining on the silicon substrate (**Figure 76 (a)**). Epitaxial synthesis is hindered by the native oxide on the silicon substrate. [1] Furthermore, using only Al as a catalyst did not result in any silicon nanowire growth (**Figure 76 (b)**). Although the element Al is known as a catalyst for silicon nanowire synthesis [62], the synthesis is quite challenging, presumably due to the formation of Al<sub>2</sub>O<sub>3</sub>. [1] Ambient conditions or residual oxygen in the reaction chamber can also be reasons for the formation of Al<sub>2</sub>O<sub>3</sub>. [1] The formation of aluminum oxide was reported to restrain the nanowire growth. [61], [62] On the contrary, employing Al/Au-catalyst resulted in the highly ordered silicon nanowires, as shown in **Figure 76 (c)**. As the native silicon oxide is presumably reduced based on the reaction with Al, the silicon lattice becomes available for the epitaxial synthesis of silicon nanowires. [1]



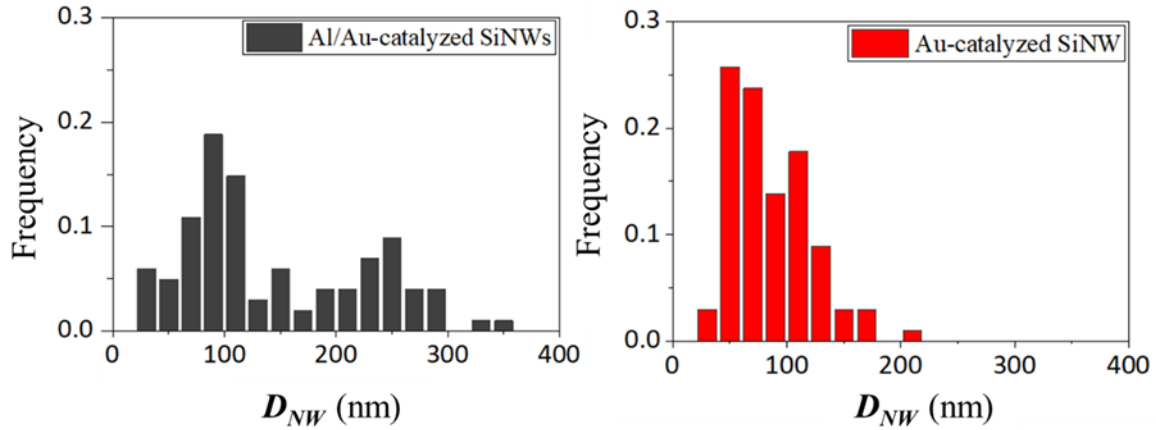
**Figure 76** (a) SEM image of top-view on silicon nanowires grown on Si (100) using 5 nm Au. The schematic illustration of the growth substrate is shown on the right. (b) SEM image of top-view on Si (100) coated by 10 nm Al, after the synthesis process. The schematic illustration of the growth substrate is shown on the right. (c) SEM image of top-view on silicon nanowires grown on Si (100) by using 10 nm Al and 5 nm Au. The schematic illustration of the growth substrate is shown on the right. (based on [1])

It is already known for the VLS mechanism that the catalyst particle remains at the tip of catalyzed silicon nanowires [23]. According to SEM images shown in **Figure 77**, both Au- and Al/Au catalyzed silicon nanowires have a catalytic particle at their tips, which is indicated by the white arrows.



**Figure 77** (a) SEM image of the catalyst particle at the tip of the Au-catalyzed silicon nanowire, indicated by the white arrow. (a) SEM image of the catalyst particle at the tip of the Al/Au-catalyzed silicon nanowire, indicated by the white arrow.

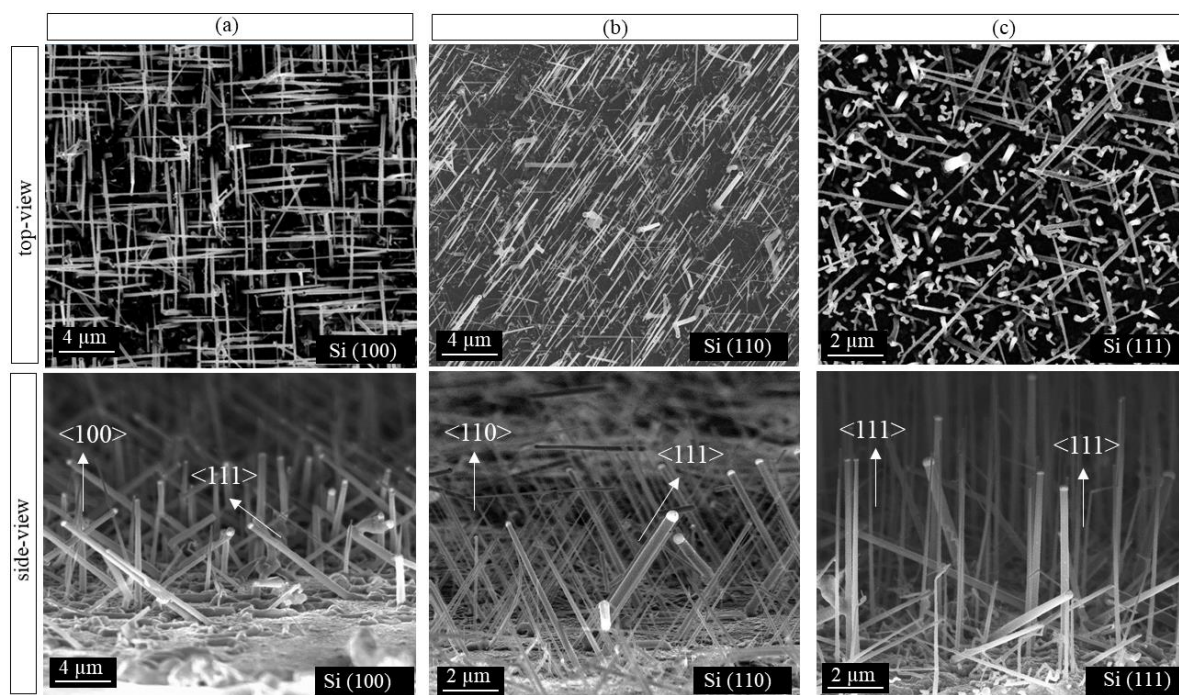
Even though both Al/Au- and Au-catalyzed silicon nanowires have the similarity of having the catalyst particles at their tips, these two types of nanowires appeared to have different diameter distributions. In order to compare their diameter distributions, diameters of the nanowires shown in SEM images of **Figure 76** were measured. Then, the corresponding histograms of the silicon nanowire diameters were plotted, as shown in **Figure 78**. The diameter distribution of Au-catalyzed silicon nanowires revealed a normal distribution with a maximum frequency in the range of 50 nm to 75 nm. On the other hand, the histogram of Al/Au-catalyzed silicon nanowires shows two peaks at 90 and 250 nm, showing a bimodal distribution. Unlike Al/Au- and Au-catalyzed silicon nanowires, the Au/Ga- and Au-catalyzed silicon nanowires reported by Lugstein et al. [76] appeared to have a different histogram. For Au-catalyzed silicon nanowires, synthesized at 550 °C, a broader dispersion of diameters was observed from 40 to 300 nm with the highest proportion between 60 to 100 nm, while for Au/Ga-catalyzed silicon nanowires, synthesized at 550 °C, a smaller range for nanowire diameter distribution is observed between 20 to 40 nm with the maximum proportion at 30 nm. In their report, it is mentioned that the different diameter distribution is presumably originated from the different dewetting behavior for the metal catalyst in the presence of Ga. Although the difference between the Al/Au- and Au-catalyzed silicon nanowires is found to be contrary to the aforementioned report, the assumption of dewetting behavior for Au-catalyst in the presence of Al may also be the reason for their different diameter distributions. [1] However, further elucidation in dewetting behavior is required in the future.



**Figure 78** Histograms of silicon nanowire diameters ( $D_{NW}$ ) synthesized using an Au-catalyst (red) and an Al/Au-catalyst (grey).

In order to substantiate the epitaxial synthesis, the Al/Au-catalyzed synthesis was carried out on silicon substrates with the crystal orientations of (110) and (111) as well. At first, 10 nm Al and 5 nm Au were deposited on the silicon substrates (100), (110) and (111). Then, nanowires were synthesized under the growth conditions mentioned in **Table 7**. The corresponding SEM images of the synthesized silicon nanowires on Si (100), (110) and (111) are shown in **Figure 79** (a), (b) and (c), respectively. Most of the Al/Au-catalyzed nanowires synthesized on the silicon (100) substrate have an angle of approximately  $55^\circ$  with the surface normal. As silicon nanowires grow preferentially in a  $\langle 111 \rangle$  direction, the angle between the silicon nanowire axis and normal surface should be  $54.7^\circ$  [23], [24], which is nearly the same as the angle observed in **Figure 79** (a). Similarly, the silicon nanowire synthesis on Si (111) substrates showed that the nanowires have the expected orientation with respect to the surface, as the majority of the nanowires are grown perpendicularly on the surface or have an angle of  $70.5^\circ$  with respect to the surface normal [23], [24]. The same inspection on silicon nanowires grown on Si (110) revealed that nanowires have an angle of  $35.3^\circ$  with the normal surface. Based on this observation, the alignment of Al/Au-catalyzed silicon nanowires with respect to the growth surface can simply confirm the epitaxial synthesis of silicon nanowires on the native oxide of silicon substrates. [1]



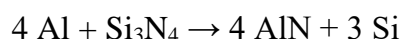


**Figure 79** (a) Top-view and side-view SEM images of synthesized silicon nanowires on Si (100) using 10 nm A and 5 nm Al. (b) Top-view and side-view SEM images of synthesized silicon nanowires on Si (110) using 10 nm A and 5 nm Al. (c) Top-view and side-view SEM images of synthesized silicon nanowires on Si (111) using 10 nm A and 5 nm Al. (Adapted with permission from [1]. Copyright (2019) American Chemical Society.)

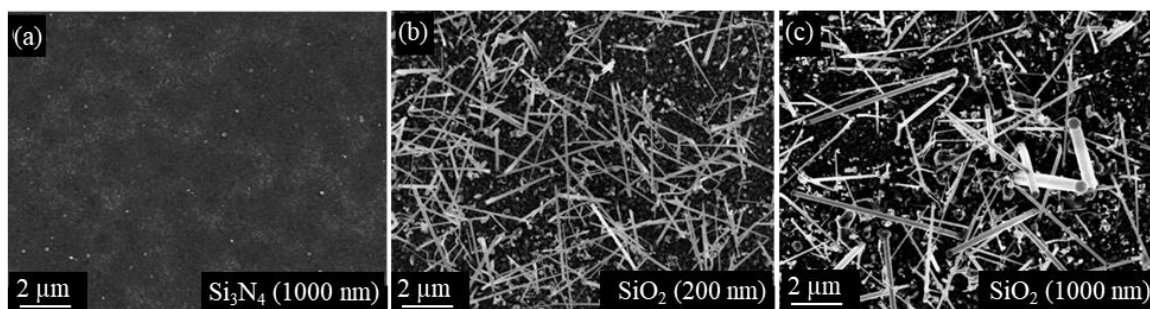


### 4.1.1. Synthesis of Al/Au-catalyzed Silicon Nanowires on Different Substrate Materials

Previously, the synthesis of Al/Au-catalyzed silicon nanowires was shown on single-crystalline silicon substrates. As expected, the epitaxial synthesis of nanowires takes place when the liquid catalyst is on the silicon lattice. Therefore, the epitaxy on amorphous surfaces cannot be expected, unless the first precipitated layer of silicon from the catalyst particle would create the basis for epitaxial growth. In this section, the synthesis is therefore verified on amorphous surfaces such as  $\text{Si}_3\text{N}_4$  and  $\text{SiO}_2$  surfaces. The substrates were basically single-crystalline silicon substrates (100) with different coatings; 1000 nm thick  $\text{Si}_3\text{N}_4$ , 1000 nm thick  $\text{SiO}_2$ , 200 nm thick  $\text{SiO}_2$  films. After evaporating 10 nm Al and 5 nm Au on the substrates, the as-prepared samples were then placed in the nanowire CVD tube. Then, the nanowires were synthesized under the growth conditions mentioned in **Table 7**. The Al/Au-catalyzed synthesis on 1000 nm thick  $\text{Si}_3\text{N}_4$ -film on Si (100), 200 nm and 1000 nm thick  $\text{SiO}_2$ -films on Si (100) are shown in **Figure 80** (a), (b) and (c), respectively. Accordingly, no silicon nanowires were synthesized on  $\text{Si}_3\text{N}_4$  surface. This can be due to the reaction that takes place between Al and  $\text{Si}_3\text{N}_4$ . The reaction is followed as [244], [245]:



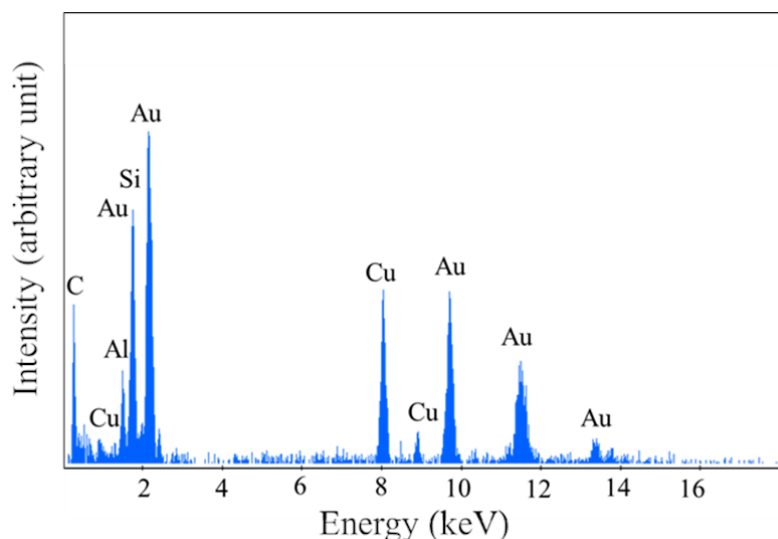
Most likely, due to the formation of AlN, the silicon nanowire synthesis is hindered. On the other hand, silicon nanowires can grow on  $\text{SiO}_2$  surfaces. However, no epitaxy is observed and silicon nanowires are grown with random orientations. Presumably, Al cannot reduce entirely  $\text{SiO}_2$  to Si, not even when the thickness of  $\text{SiO}_2$ -films is 200 nm. Therefore, silicon is not accessible for the epitaxial synthesis.



**Figure 80** SEM images of (a) Si (100) coated with 1000 nm thick  $\text{Si}_3\text{N}_4$  (b) Si (100) coated with 200 nm thick  $\text{SiO}_2$  (c) Si (100) coated with 1000 nm thick  $\text{SiO}_2$  after silicon nanowire synthesis using 10 nm Al and 5 nm Au as catalysts.

#### 4.1.2. TEM/EDX Analysis of Al/Au-catalyzed Silicon Nanowires

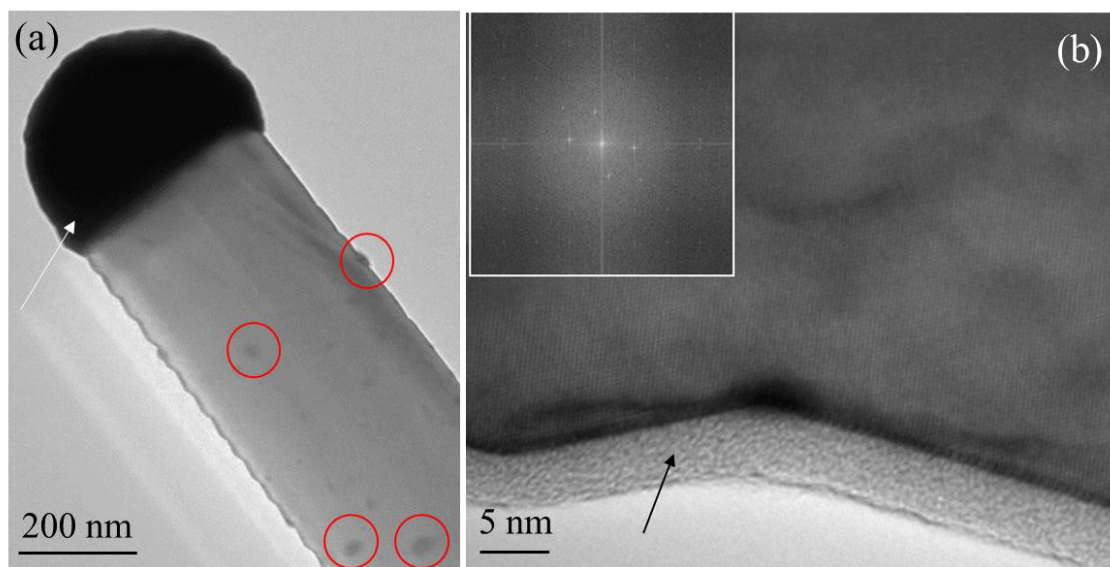
In order to study the crystal structure and catalyst composition of Al/Au-catalyzed silicon nanowires, high-resolution transmission electron microscopy (HRTEM) with energy dispersive X-ray (EDX) spectroscopy was utilized. Silicon nanowires were synthesized on Si (100) using 10 nm Al and 5 nm Au, under the growth conditions demonstrated in **Table 7**. For this purpose, silicon nanowires were transferred into a copper TEM grid with lacy carbon films. The detailed procedure for sample preparations is described in Appendix section **K**. The EDX investigation was then carried out on the catalyst particles for four silicon nanowires. The Al-Au composition appeared to be composed of  $39 \pm 5$  at. % Al and  $61 \pm 5$  at. % Au. [1] This composition can be approximately attributed to an intermetallic  $\text{AlAu}_2$ -phase, with a melting point of about  $620^\circ\text{C}$  [246]. Unfortunately, the silicon composition in the catalyst particle could not be investigated, as excluding the parasitic contributions from the silicon nanowires itself, was not possible. [1] An EDX graph on a catalyst particle is shown in **Figure 81**. In this graph, Cu and C elements correspond to the copper TEM grids and lacy carbon film. [1] In general, in order to understand the growth mechanism here, a ternary phase diagram of Al-Au-Si is required. However, a ternary phase diagram for these three elements has not yet been realized experimentally. Nevertheless, theoretical calculations were carried out for  $\text{AlAu}_2$ -Si, which showed a eutectic temperature at  $487^\circ\text{C}$ . [243] Hence, the synthesis of silicon nanowires at a temperature of  $550^\circ\text{C}$  is assumed to be based on a VLS mechanism. [1] Furthermore, as expected from the pseudo-binary phase diagram of  $\text{AlAu}_2$ -Si and other binary phase diagrams Al-Au, Al-Si and Au-Si, precipitation of a pure Si phase was also observed. [44], [246], [247]



**Figure 81** An EDX graph of Al/Au-synthesized silicon nanowire on the catalyst particle. (Adapted with permission from [1]. Copyright (2019) American Chemical Society.)

Based on the TEM and FFT images shown in **Figure 82**, Al/Au-catalyzed silicon nanowires are single-crystalline. Furthermore, the lattice plane distance in the silicon nanowire axis was measured and the average value was 0.31 nm (see Appendix, section **K**, **Figure-A 2**).

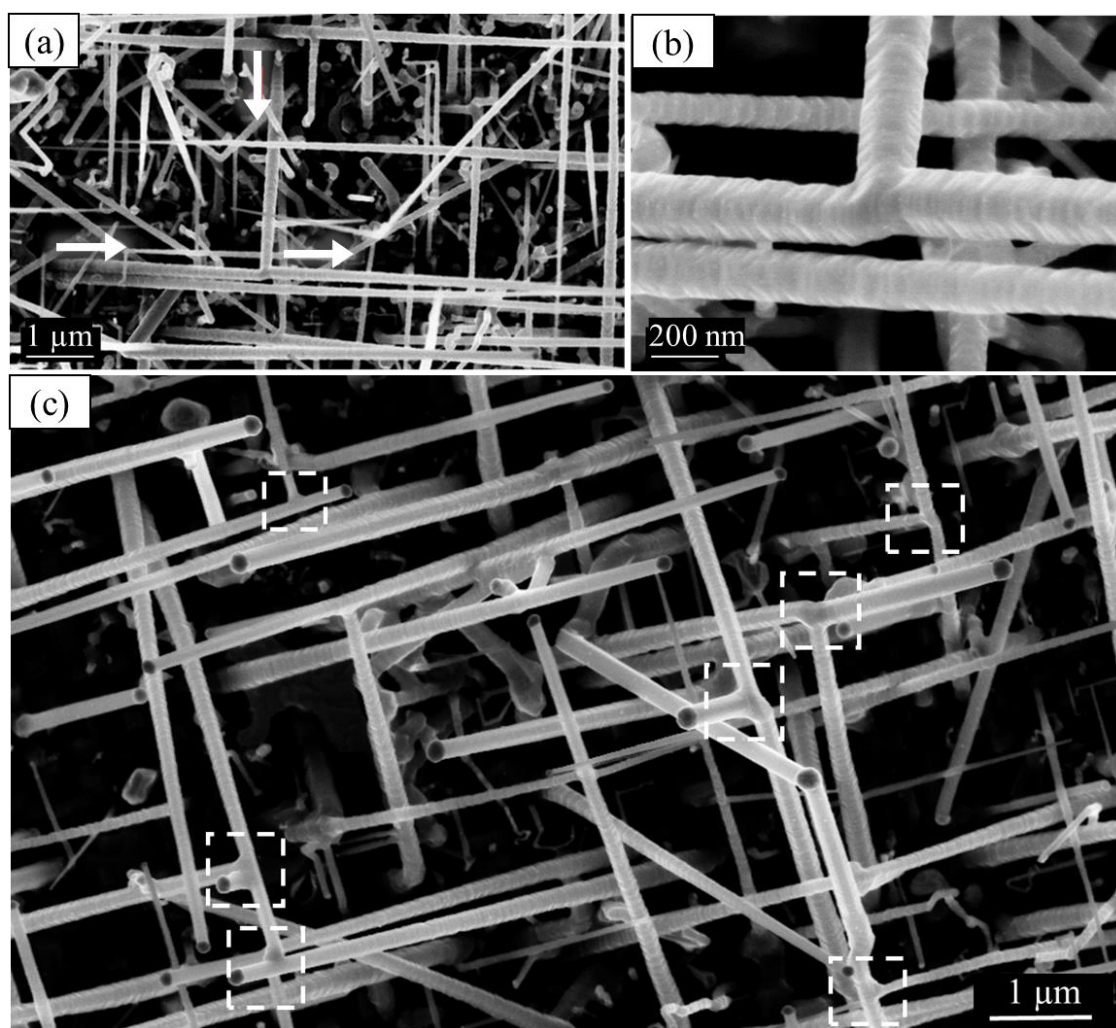
This observation can simply support the growth of silicon nanowires in the direction of  $\langle 111 \rangle$  [248]. Besides this, silicon nanowire side-surfaces appeared with a so-called saw-tooth faceting feature, which was observed for Au-catalyzed and Ag/Au-catalyzed silicon nanowires with the growth direction of  $\langle 111 \rangle$  as well [59], [78]. The other similarity of Al/Au-catalyzed silicon nanowires to Au-catalyzed ones is that the nanowires were decorated with catalyst particles on their stem, as they are indicated by the red circles in **Figure 82** (a). [1] For Au-catalyzed silicon nanowires, the catalyst migration at high temperature is the main reason for the formation of catalyst particles on the stem of the nanowires [249]. As expected, silicon nanowires are encapsulated by an amorphous native oxide layer. However, the thickness of this layer (4.3 nm) is higher than a typically observed native oxide layer, which is formed under the ambient conditions or during the cool-down after the silicon nanowire synthesis (1.5 nm). [1] Due to the oxygen residuals in the NWCVD tube and non-UHV (ultra-high vacuum) system, the oxidation might be further enhanced. [1] However, enhanced oxidation was not observed for Au-catalyzed silicon nanowires. Moreover, the formation of an amorphous silicon overcoating is also possible. [1] Silicon overcoating happens by the thermally cracking the  $\text{SiH}_4$  gas at elevated temperatures, for instance, at 550 °C.



**Figure 82** (a) HRTEM image of an Al/Au-catalyzed silicon nanowire. The white arrow and red circles indicate the catalytic part and the catalyst particles on the nanowire, respectively. (b) HRTEM image of an Au/Al-catalyzed silicon nanowire. The black arrow indicates the amorphous native oxide layer. The inset shows the fast Fourier Transform (FFT) image of the silicon nanowire, which indicates the single-crystal nature. (Adapted with permission from [1]. Copyright (2019) American Chemical Society.)

### 4.1.3. Network Formation

Some of the Al/Au-catalyzed silicon nanowires appeared to be merged and show a tendency for network formation. This characteristic can be observed in the SEM images shown in **Figure 83**. For instance, two silicon nanowires are merged and formed one silicon nanowire, whose direction is aligned with the epitaxial synthesis orientations. [1] Images in **Figure 83** (b) and (c) show a closer view of the merging area and density of the merging regions on a surface area, respectively. Such networks can be applied, for instance, for nanoscale sensors and applications, based on photon harvesting, as the photon absorption probability is considerably improved by suppressing the light reflections [249], [250]. The network formation mechanism here is seemingly different from the capillarity driven self-welding effect reported for silicon nanowires. [251]



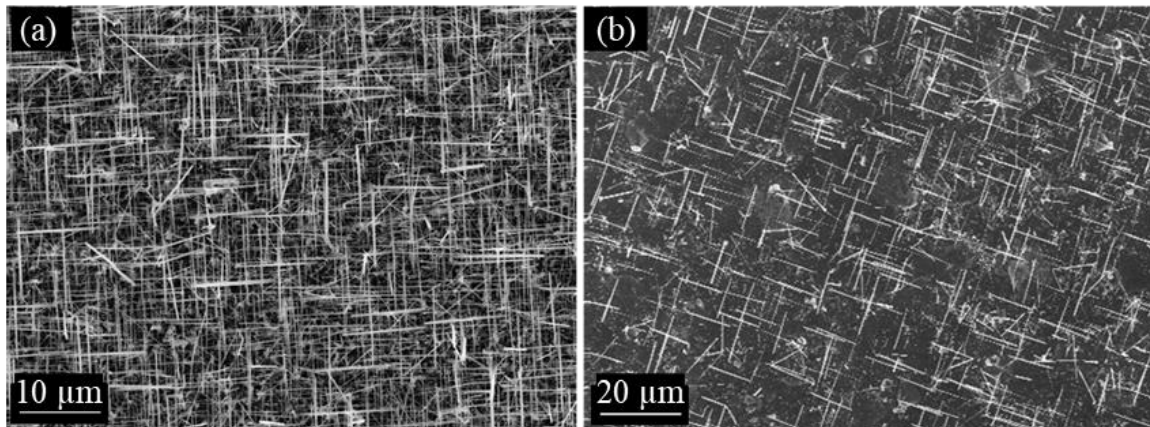
**Figure 83** Network formation in Al/Au-catalyzed silicon nanowires. (a) SEM image of Al/Au-catalyzed silicon nanowires merging into one silicon nanowire, as are indicated by the white arrows. (b) Closer view of merged silicon nanowires. (c) The dashed white squares indicate the merging areas. (Adapted with permission from [1]. Copyright (2019) American Chemical Society.)

## 4.2. Effect of Growth Conditions and Catalyst Thickness on Epitaxial Synthesis

In this section, the focus of the study is given to investigate the effects of growth conditions and catalysts thickness on the epitaxial synthesis, length and density of silicon nanowires.

### 4.2.1. Time Between Metal Deposition and Synthesis

Silicon nanowires are synthesized on silicon substrates using 10 nm Al and 5 nm Au. The Au-film as a top layer covers the Al-film. However, the 5 nm thick Au-film, which is evaporated in an electron-beam evaporator, is not a homogenous film and does not entirely and homogeneously cover the substrates and subsequently, the Al-film. Therefore, Al-film can be oxidized in the ambient condition, but not as fast as when only Al is exposed to the ambient condition. However, the time between the metal evaporation and growth has a remarkable effect on the oxidation of the Al layer and consequently, the density of silicon nanowires. For instance, **Figure 84** shows two samples prepared with Al and Au catalysts but with a different time interval between metal evaporation and synthesis. Correspondingly, the SEM image in **Figure 84** (a) shows Al/Au-catalyzed silicon nanowires, which were grown only after 4 hours of Al/Au evaporation on the growth-substrate and SEM image (b) shows silicon nanowires, which were grown after four days since the Al/Au evaporation on the growth-substrate. Both samples were stored in the same ambient condition before the synthesis. It can be clearly seen that the density of silicon nanowires noticeably drops, after keeping the metal-coated substrates 4 days in the ambient condition. Nevertheless, compared to the HF pretreatment, using the Au-film as a top layer is less self-limiting and the oxidation can be avoided/delayed even up to several weeks by proper sample storage, for instance, wrapping sample boxes with a Parafilm.

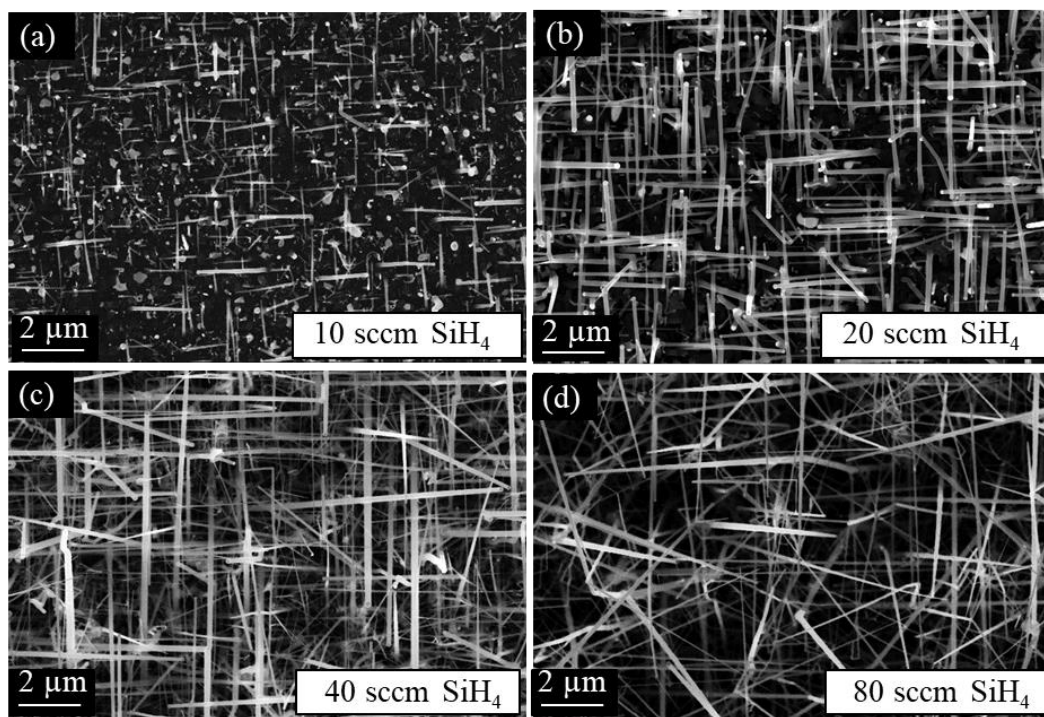


**Figure 84** SEM images of Al/Au-catalyzed silicon nanowires. The nanowires are synthesized (a) 4 hours and (b) 4 days after Al and Au evaporation and stored in the ambient condition.



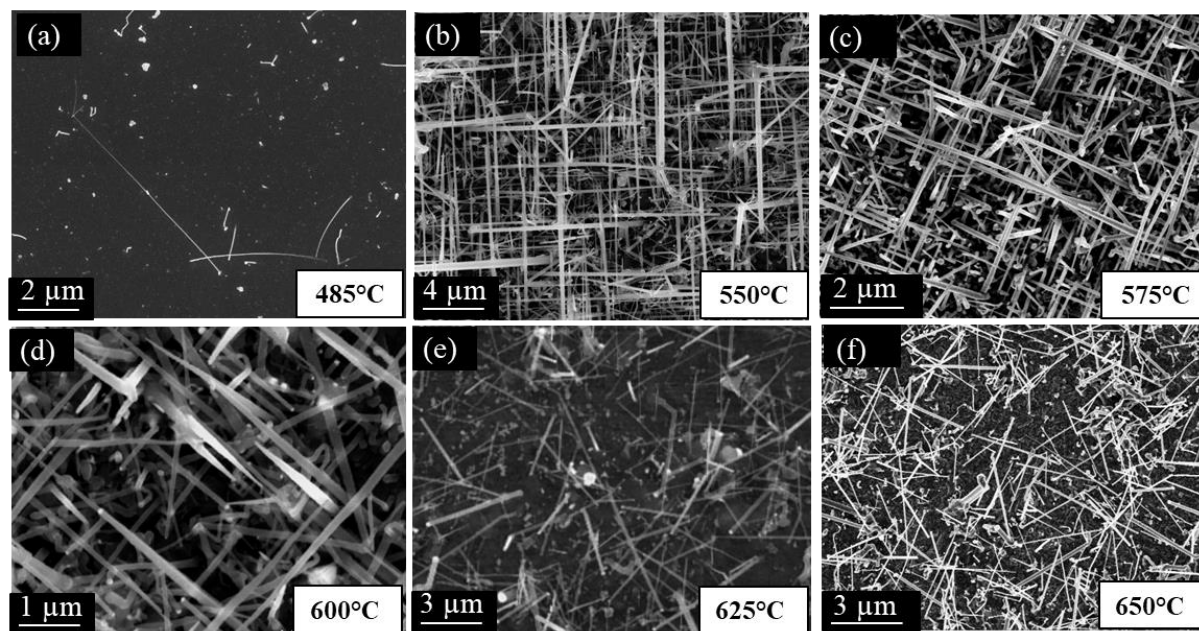
### 4.2.2. Temperature and Pressure Effects on Silicon Nanowire Epitaxial Synthesis Using Al/Au-Catalyst

In order to study the effect of growth conditions on the synthesis of Al/Au silicon nanowires, they were synthesized at different growth temperatures and different partial pressures of  $\text{SiH}_4/\text{He}$  (2%  $\text{SiH}_4$  in He). Silicon nanowires were synthesized at a growth temperature of 550 °C, in an atmosphere of  $\text{SiH}_4/\text{He}$  (2%  $\text{SiH}_4$  in He) and  $\text{H}_2$  with a total flow of 100 sccm, at a working pressure of 10 mbar for 1 hour. The synthesis was carried out in four series by changing the  $\text{SiH}_4/\text{He}$  (2%  $\text{SiH}_4$  in He) partial pressure or flow (for 10, 20, 40 and 80 sccm). The  $\text{H}_2$  flow was subsequently set in a way that the total flow of the gases was kept constant for 100 sccm. The corresponding SEM images of the synthesized silicon nanowires are shown in **Figure 85**. As it can be depicted from the images, the higher the partial pressure (or flow) of  $\text{SiH}_4/\text{He}$ , the longer are the synthesized silicon nanowires. [1] Basically, the epitaxial growth is observed by the lower partial pressure of  $\text{SiH}_4/\text{He}$  and it is hindered by  $\text{SiH}_4/\text{He}$  flow of 40 and more strongly by 80 sccm of  $\text{SiH}_4/\text{He}$ . Also, the number of nanowires decreased with 80 sccm flow of  $\text{SiH}_4/\text{He}$ . The reason can be that by thermal silicon overgrowth, the catalysts are covered by silicon layer and consequently, become deactivated. [1]



**Figure 85** (a) Synthesized silicon nanowires using 10 nm Al and 5 nm Au as catalysts and partial pressure of  $\text{SiH}_4/\text{He}$  for 1 mbar, at 550 °C. (b) Synthesized silicon nanowires using 10 nm Al and 5 nm Au as catalysts and partial pressure of  $\text{SiH}_4/\text{He}$  for 2 mbar, at 550 °C. (c) Synthesized silicon nanowires using 10 nm Al and 5 nm Au as catalysts and partial pressure of  $\text{SiH}_4/\text{He}$  for 4 mbar, at 550 °C. (d) Synthesized silicon nanowires using 10 nm Al and 5 nm Au as catalysts and partial pressure of  $\text{SiH}_4/\text{He}$  for 8 mbar, at 550 °C. (Adapted with permission from [1]. Copyright (2019) American Chemical Society.)

Similar to the pressure, in order to study the effect of the temperature on the growth, the synthesis was carried out using 80 sccm of  $H_2$  flow, 20 sccm of  $SiH_4/He$  (2%  $SiH_4$  in  $He$ ) flow and at a total pressure of 10 mbar and at different growth temperatures (485, 550, 575, 600, 625 and 650 °C). At 485 °C, almost a few nanowires were synthesized based on the SEM image of **Figure 86** (a). However, above 550 °C, silicon nanowires with a higher density were grown and notably, their epitaxial behavior is hindered by increasing the growth temperature. [1] Besides this, by increasing the temperature, the more tapering is observed for silicon nanowires. [1] All in all, increasing either partial pressure of  $SiH_4/He$  or the growth temperature can hinder the epitaxial synthesis. [1]

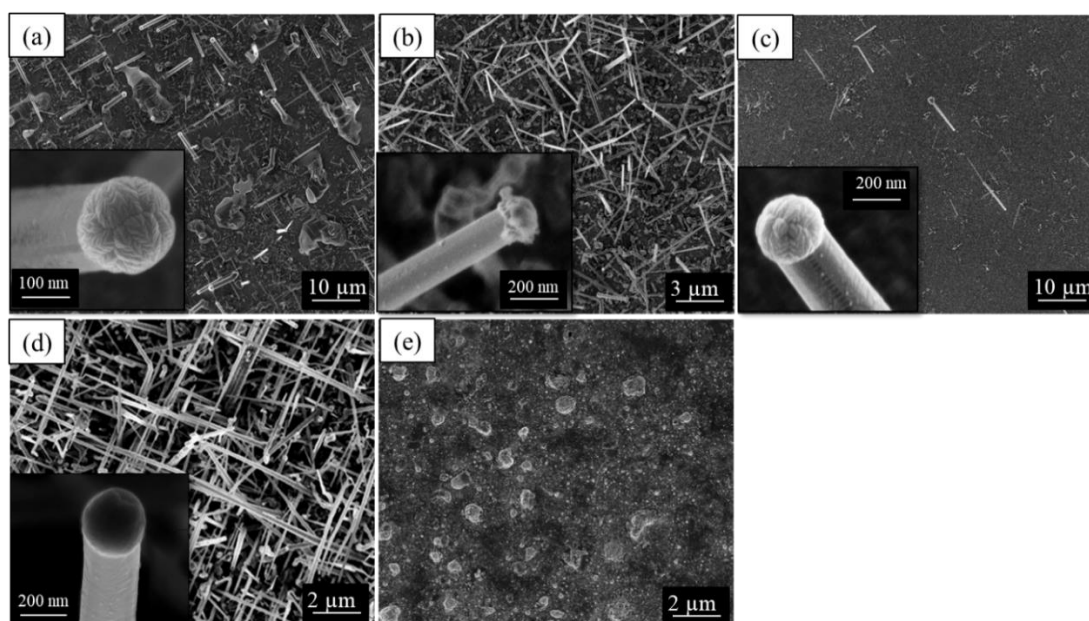


**Figure 86** Synthesized silicon nanowires using 10 nm Al and 5 nm Au as catalysts at growth temperatures of 485 °C (a), 550 °C (b), 575 °C (c), 600 °C (d), 625 °C (e) and 650 °C (f). (Adapted with permission from [1]. Copyright (2019) American Chemical Society.)

#### 4.2.3. Al and Au Thickness and Ratio Effects on Silicon Nanowire Epitaxial Synthesis

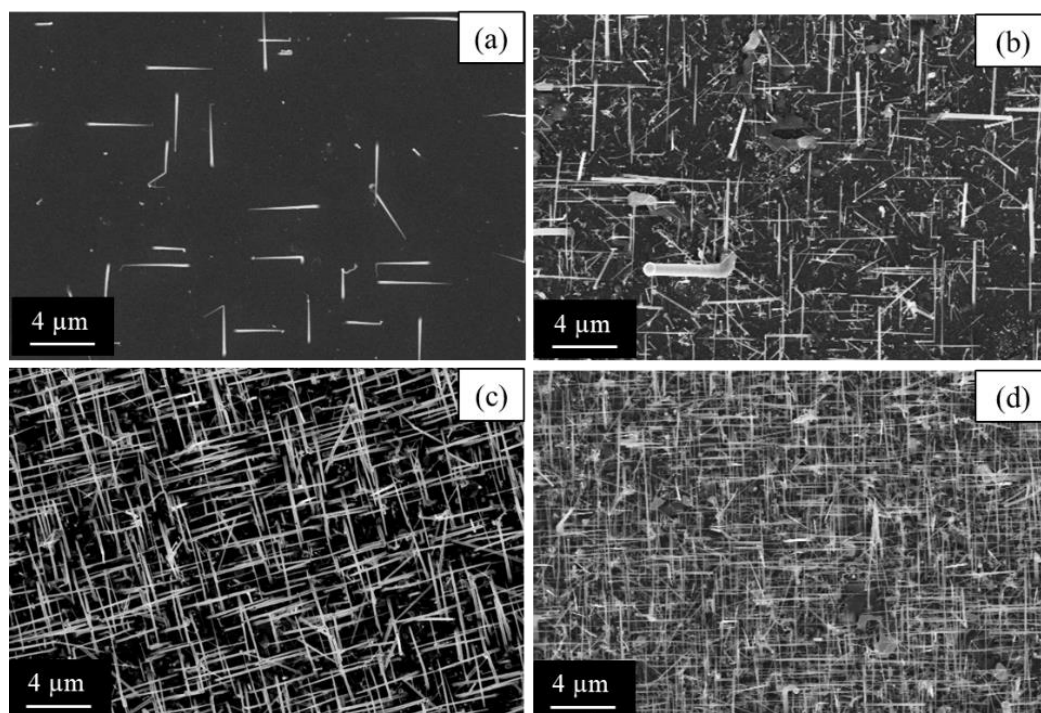
As it was already reported for Au-catalyzed silicon nanowires, the thickness of the Au-film, used as a catalyst, has an impact on the morphology, density and geometries of the synthesized nanowires [252], [253]. Here, not only Au but also Al is used as a catalyst and, to investigate their effects on the nanowire synthesis, different thicknesses of these two layers were used for silicon nanowire synthesis under two conditions, once by considering different Al:Au thickness ratios and in the latter case, different thicknesses of Al- and Au-films, but keeping the Al:Au ratio constant. [1] The synthesis was performed on silicon (100) substrates coated by an alloy catalyst, under the growth conditions demonstrated in **Table 7**. The SEM images in **Figure 87** show the condition, at which the different ratios of Al:Au are employed for the synthesis. The thickness of the Al and Au films varies between 5 to 20 nm and the Al:Au ratio was chosen for 1:4, 1:2, 1:1, 2:1 and 4:1 and the

corresponding SEM images of the synthesized silicon nanowires are shown in **Figure 87** (a), (b), (c), (d) and (e), respectively. Accordingly, the highest density of epitaxial silicon nanowires is observed, when the ratio of the Al:Au ratio is 2:1 and the thickness of the Al and Au is 10 nm and 5 nm, respectively. When the Al:Au ratio is 4:1, no nanowires were synthesized, as Al-layer was most likely oxidized and the formation of Aluminum oxide hindered the growth. Moreover, the catalyst particle morphology is affected by the different thicknesses of the Al and Au films. [1] On the other hand, for the different thickness of Al and Au, but with a constant Al:Au ratio for 2:1, the epitaxial behavior was clearly observed. The corresponding SEM images of the synthesized silicon nanowires using 4 nm Al - 2 nm Au, 8 nm Al - 4 nm Au, 10 nm Al - 5 nm Au and 20 nm Al - 10 nm Au are shown in **Figure 88** (a), (b), (c) and (d), respectively. As depicted from the images, the thicker catalyst layers resulted in a higher density and length of silicon nanowires. [1]



**Figure 87** Synthesized silicon nanowires at 550 °C, 10 mbar, 80 sccm  $H_2$  and 20 sccm  $SiH_4/He$ , using different Al and Au film thicknesses and different Al:Au ratios; (a) 5 nm Al - 20 nm Au (b) 5 nm Al - 10 nm Au (c) 5 nm Al - 5 nm Au (d) 10 nm Al - 5 nm Au (e) 20 nm Al - 5 nm Au. (Adapted with permission from [1]. Copyright (2019) American Chemical Society.)





**Figure 88** Synthesized silicon nanowires at 550 °C, 10 mbar, 80 sccm  $H_2$  and 20 sccm  $SiH_4/He$ , using different Al and Au film thicknesses and Al:Au for 2:1 (a) 4 nm Al - 2 nm Au (b) 8 nm Al - 4 nm Au (c) 10 nm Al - 5 nm Au (d) 20 nm Al - 10 nm Au. (Adapted with permission from [1]. Copyright (2019) American Chemical Society.)

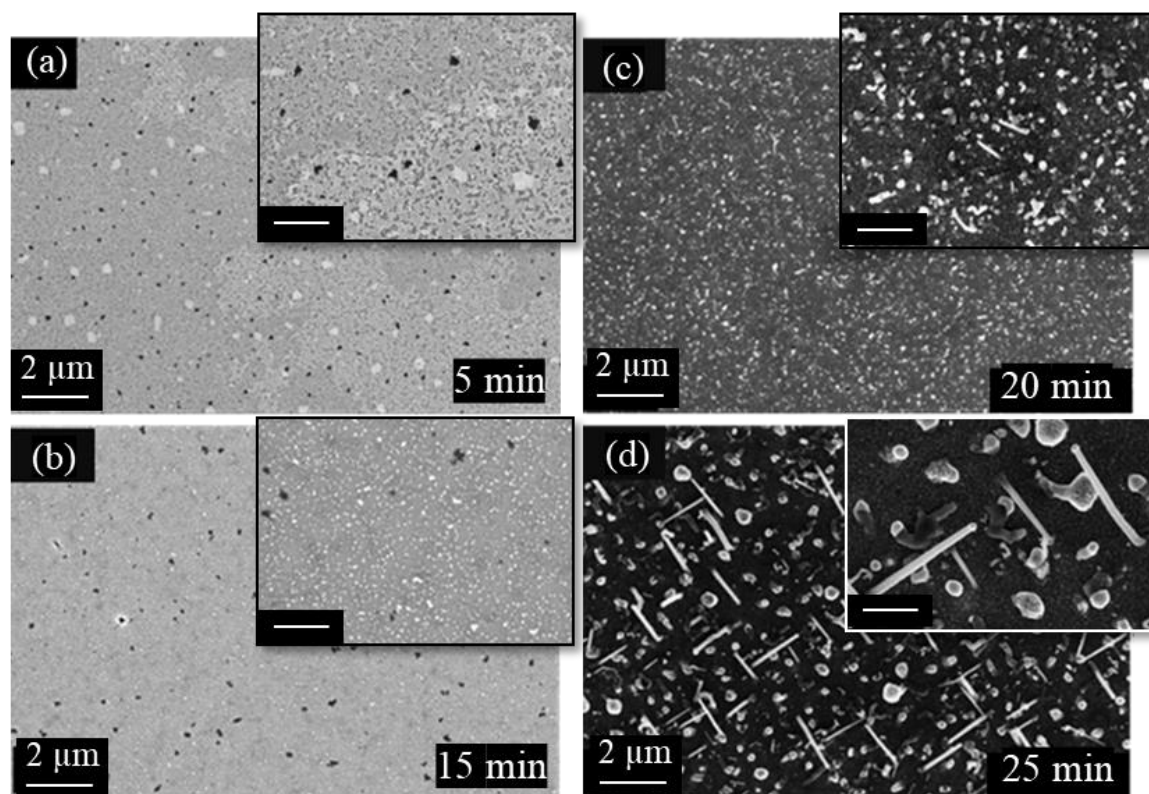
### 4.3. Nucleation Time, Growth Rate and Activation Energy

In principle, the synthesis time, which is set for the NWCVD reactor after reaching to the growth temperature, is composed of two main steps; nucleation time and the growth time after the nucleation. [14] In order to estimate the nucleation time for Al/Au-catalyzed silicon nanowires, they were synthesized under the growth conditions demonstrated in **Table 7**, but for 5, 15, 20 and 25 minutes. The catalysts here were 10 nm Al and 5 nm Au films, deposited on Si (100) substrates. The corresponding SEM images are shown in **Figure 89**. As depicted from the SEM images, the nucleation takes place approximately 15 minutes after that the synthesis is initiated and SiH<sub>4</sub> gas is inserted into the CVD reactor at the growth temperature. [1] It should be noted that this time can slightly vary for different diameters of silicon nanowires. [1]

As mentioned in the previous section, silicon nanowires were synthesized at different growth temperatures. Based on the SEM images, the length of the silicon nanowires, which were synthesized for one hour, was measured. Based on the assumption that the nucleation time for silicon nanowire synthesis at each growth temperatures is nearly 15 minutes, the growth rate of silicon nanowires was investigated using the following relation:

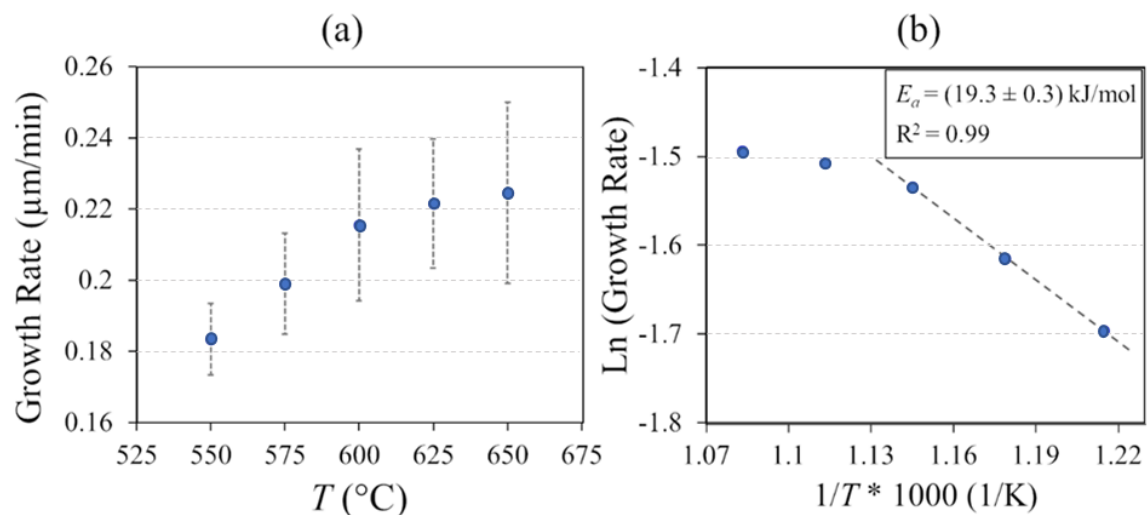
$$R = \frac{L_{NW}}{t_{synthesis} - t_{nucleation}} \quad (4-1)$$

Here,  $R$ ,  $L_{NW}$ ,  $t_{synthesis}$  and  $t_{nucleation}$  stand for the growth rate, nanowire length, synthesis time (here one hour) and nucleation time (here 15 minutes), respectively. The length of silicon nanowires with a diameter of 200-300 nm was measured. [1] Then, the growth rate of silicon nanowires with a diameter range of 200-300 nm was calculated and plotted against the growth temperature in the graph shown in **Figure 90** (a). Based on the graph, the silicon nanowire growth rate appeared to increase in the growth temperature range of 500-600 °C. [1] However, above this temperature, the growth rate seemed to reach a saturate. Presumably, above this temperature, the thermal silicon over deposition is activated and not the entire silicon supply (from SiH<sub>4</sub> gas) is used to grow silicon nanowires axially. [1] Hence, a so-called diffusion-limited growth can be assumed. In principle, the diffusion of silicon through the catalyst can be the main reason for limiting the growth rate. [1]



**Figure 89** Synthesis of Al/Au catalyzed silicon nanowires at a growth temperature of 550 °C, using  $\text{SiH}_4/\text{He}$  (2%  $\text{SiH}_4$  in He) and  $\text{H}_2$  gases, flowing with 20 sccm and 80 sccm, respectively, at a working pressure of 10 mbar for (a) 5 minutes, (b) 15 minutes, (c) 20 minutes and (d) 25 minutes. (Adapted with permission from [1]. Copyright (2019) American Chemical Society.)

The Arrhenius plot of the growth rates was accordingly plotted and shown in **Figure 90** (b). Subsequently, the activation energy was estimated from the Arrhenius plot by considering only the growth temperatures below 625 °C. [1] The reason for choosing the data from the first three growth temperatures is that they showed nearly a linear relationship, while the linear estimation for the data of the five growth temperatures resulted in a higher error value (as the growth rate above 625 °C reaches almost a plateau). [1] The slope in the Arrhenius plot (for the temperatures below 625 °C) yields an activation energy of  $19.3 \pm 0.3$  kJ/mol and  $R^2$  value for 0.99. [1] The estimated value for the activation energy is very close to the value reported for silicon nanowires using Au/Ag-catalysts with an activation energy of 24.1 kJ/mol [78]. However, the investigated activation energy is slightly lower than values in other reports, for instance, for Au-catalyzed silicon nanowires (with a diameter of 80 nm) with an activation energy of 79.5 kJ/mol [43], for silicon nanowires using Au/Ga-catalysts with a value of 59 kJ/mol [76], and for silicon nanowires using Au- and Pt-catalysts with a value of 130 kJ/mol and 80 kJ/mol, respectively [254]. It should be noted that the variation in the reported activation energy may also be originated from the different growth conditions, catalyst type and the silicon nanowire diameters. [1]



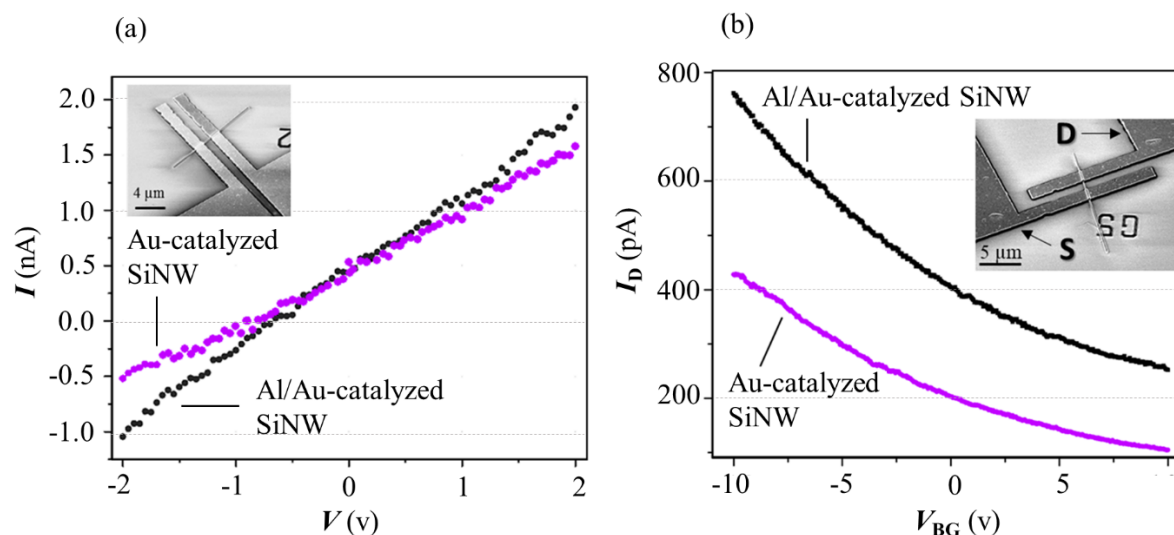
**Figure 90** (a) Investigated growth rates vs. growth temperature for Al/Au-catalyzed silicon nanowires, synthesized on Si (100) using 10 nm Al and 5 nm Au films. The growth rates here were calculated for the silicon nanowires with a diameter of 200-300 nm. (b) Arrhenius plot of the growth rates shown in (a). The indicated line for growth temperatures below 625  $^{\circ}\text{C}$  yielded an activation energy of  $19.3 \pm 0.3 \text{ kJ/mol}$ . (Adapted with permission from [1]. Copyright (2019) American Chemical Society.)

### 4.3. Electrical Properties of Al/Au-catalyzed Silicon Nanowires

As metal catalysts used for silicon nanowire synthesis can be incorporated in the silicon nanowires as an impurity and have an impurity energy level in the bandgap of the silicon nanowires, the electrical properties of the nanowires are consequently affected. [23] For instance, Al is known as a shallow p-dopant for silicon, whereas Au creates deep trap levels in the mid energy bandgap of silicon [23], [24], [255]. In this work, the electrical properties of silicon nanowires were studied and compared to Au-catalyzed silicon nanowires. Here, Au- and Al/Au-catalyzed silicon nanowires were synthesized on Si (100), under the growth conditions demonstrated in **Table 7**. The investigation was carried out on a single-silicon nanowire-device using Au- and Al/Au-catalyzed silicon nanowires. The procedure of the sample preparations is illustrated in section 2.1.3. The measurements were carried out on 15 silicon nanowire-devices of each type of nanowire. Examples of single-silicon nanowire-based devices are shown in SEM images in **Figure 91** (a) and (b). At first, the ohmic behavior and electrical resistance values were evaluated for each types of nanowires and two examples of the electrical ohmic behavior are shown in **Figure 91** (a) for each type of silicon nanowires. In the graph, there is a background current in the range of 1 nA or even smaller, which unfortunately could not be avoided in the measurements. [1] This is probably due to the internal potential in the setup itself. [1] As the graphs indicate and the other measurements revealed, the electrical resistance values are in the range of a few G $\Omega$  for both types of silicon nanowires with a diameter of approximately 120 nm and contact distance of 1.4  $\mu\text{m}$ . [1] The mean value of electrical resistance for Al/Au- and Au-catalyzed silicon nanowires are  $1.8 \pm 0.6 \text{ G}\Omega$  and  $2.9 \pm 2.0 \text{ G}\Omega$ , respectively. [1] The measurements indicated that the overall electrical properties of Au- and Al/Au-catalyzed nanowires are comparable. By considering the distance between the contacts on a nanowire (1.4  $\mu\text{m}$ ) and nanowire diameter of 120 nm, the resistivity of silicon nanowires using Al/Au- and Au-catalysts was calculated as  $1.4 \pm 0.5 \text{ k}\Omega\text{cm}$  and  $2.3 \pm 1.6 \text{ k}\Omega\text{cm}$ , respectively. [1] The resistivity values of both types of nanowires are very similar, and resistivity of Al/Au-catalyzed silicon nanowires are only slightly lower than the one from Au-catalyzed silicon nanowires. [1] This indicates that Al incorporation is not very significant. For a better analysis of the electrical resistivity of the nanowires, a four-probe measurement or TLM (transmission line measurements) analysis is generally considered to be a more valid investigation approach. However, within my doctoral research course, such electrode configurations and measurements could not be realized due to the short lengths of the synthesized silicon nanowires and limitations in nanofabrication (e.g. e-beam lithography).

Furthermore, silicon nanowires were investigated individually in a field-effect-transistor configuration. In the inset SEM image of the graph (b) in **Figure 91**, the source and drain contacts are indicated by **S** and **D**, respectively. A gate potential (from -10 V to 10 V) was applied from the backside of the sample. The corresponding back-gate potential is denoted as  $V_{\text{BG}}$ , while the electrical current between the source and drain was measured, by applying

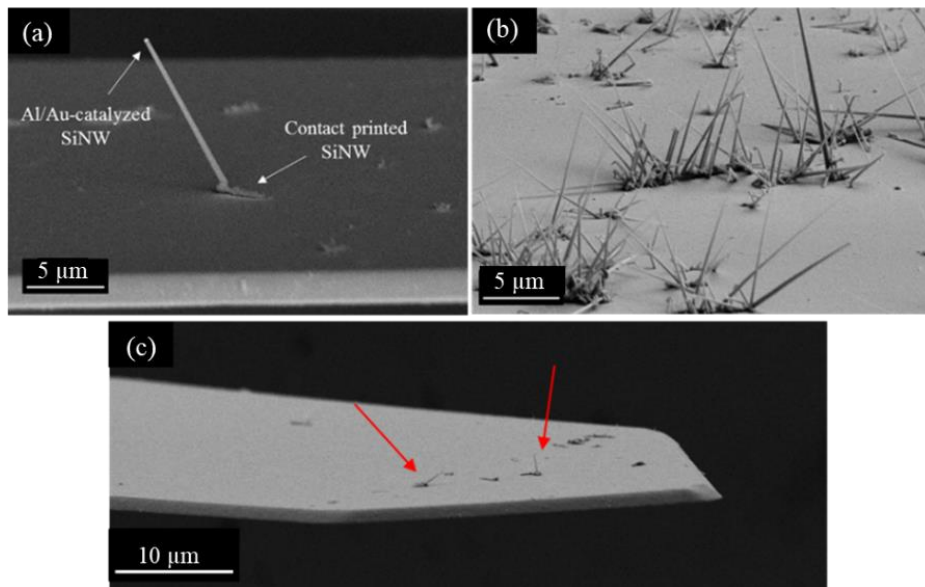
2 V potential between the source and drain. This measurement revealed that the overall back-gate response of the Au- and Al/Au-catalyzed silicon nanowires are similar, and a p-type behavior is observed for both types of nanowires. Using the observed p-type behavior and an assumed hole mobility of about  $450 \text{ cm}^2/\text{Vs}$  for silicon at room temperature [256], [257], yields a hole charge carrier concentration of about  $1.0 \times 10^{13}/\text{cm}^3$ . Nevertheless, the interpretation or the relation of the charge carrier concentration and impurity or dopant level for silicon nanowires are so far a complex topic, which requires future study and investigations.



**Figure 91** (a)  $IV$ -measurements for an Au-catalyzed silicon nanowire (pink dots) vs. an Al/Au-catalyzed silicon nanowire (black dots). (b) The measured  $I_D$  (drain-source current) for  $V_{BG}$  (back-gate voltage) varying from -10 V to +10 V, while the  $V_{DS}$  (drain-source voltage) is 2 V. The pink and black dots indicate respectively measurement results from an Au-catalyzed and Al/Au-catalyzed silicon nanowire. The inset images show SEM images of the nanowires with contact pads. Here, **S** and **D** stand for the source and drain, respectively. (Adapted with permission from [1]. Copyright (2019) American Chemical Society.)

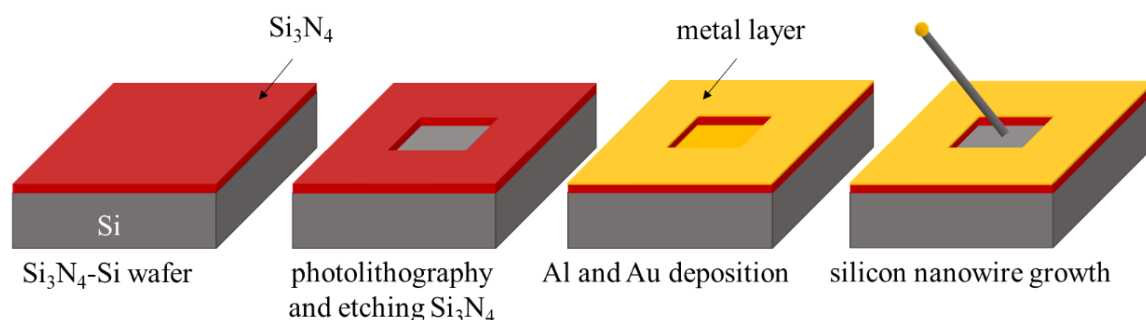
#### 4.4. Growth of a Single Al/Au-catalyzed Silicon Nanowire

Al/Au-catalyzed silicon nanowire integration into AFM probes as a scanning tip seems very intriguing. The main advantage of employing the Al/Au-catalyzed silicon nanowires is the epitaxial synthesis, as the nanowire orientation with respect to the cantilever surface has a significant impact on the topography scanning quality. Therefore, in order to exploit these nanowires for AFM applications, using single-crystalline substrate materials, like silicon-on-insulator substrates, is the main prerequisite. For instance,  $\text{Si}_3\text{N}_4$ -cantilevers can not provide the pre-condition for epitaxial synthesis, as they are made of an amorphous  $\text{Si}_3\text{N}_4$ -film [258]. Furthermore, as mentioned before, the synthesis of Al/Au-catalyzed silicon nanowires on  $\text{Si}_3\text{N}_4$ -substrates is not feasible, presumably due to the formation of AlN at the growth temperature. As  $\text{Si}_3\text{N}_4$  material suppresses the synthesis of the Al/Au-catalyzed silicon nanowires, they can be employed as a material to confine the growth area of silicon nanowires. Based on this principle, two methods are demonstrated here to confine the synthesis area. The first approach is based on contact printing silicon nanowires onto  $\text{Si}_3\text{N}_4$ -cantilevers. Basically, silicon nanowires are the confined silicon surface (only growth areas) on  $\text{Si}_3\text{N}_4$ -substrates. After metal catalyst evaporation and subsequently, the synthesis, silicon nanowires are grown on silicon nanowires, which are shown in the corresponding SEM images in **Figure 92**. The smaller the contact printed silicon nanowire, the higher is the probability of growing a single silicon nanowire. However, silicon nanowires have different facet side-walls [59], resulting in randomly oriented synthesized silicon nanowires using Al/Au-catalysts.



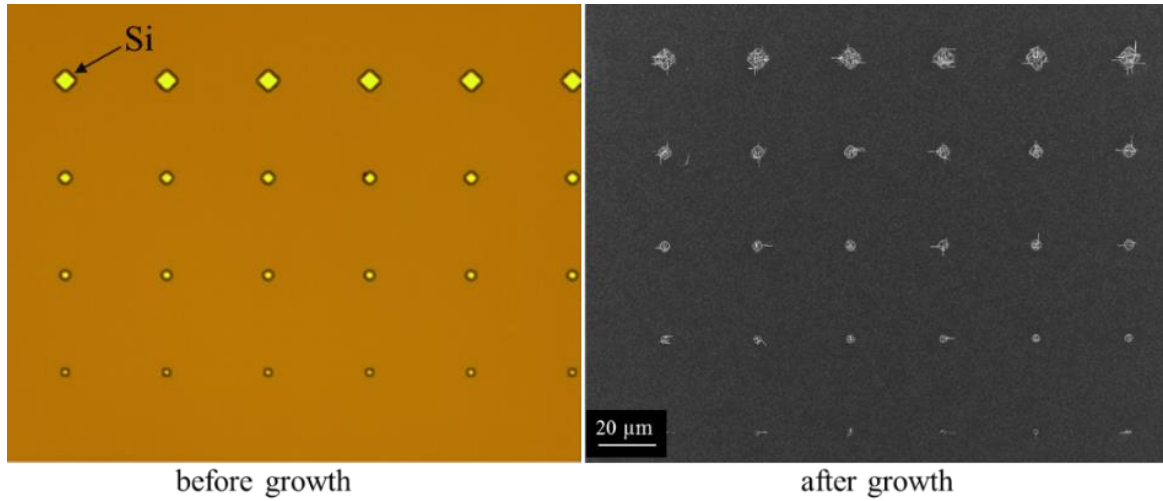
**Figure 92** (a) SEM image of an Al/Au-catalyzed silicon nanowire grown on a contact printed silicon nanowire on a  $\text{Si}_3\text{N}_4$ -cantilever. (b) SEM image of Al/Au-catalyzed silicon nanowires grown on contact printed silicon nanowires on a  $\text{Si}_3\text{N}_4$  surface. (c) SEM image of Al/Au-catalyzed silicon nanowires grown on contact printed silicon nanowires on a  $\text{Si}_3\text{N}_4$ -cantilever. The red arrows indicate the Al/Au-catalyzed silicon nanowires.

The second approach is applied to single-crystalline silicon substrates covered by a  $\text{Si}_3\text{N}_4$ -film. Basically, within one step photolithography, a small area of the  $\text{Si}_3\text{N}_4$ -film is etched, so that the silicon becomes accessible for the epitaxial synthesis. A schematic illustration of the fabrication steps is shown in **Figure 93**. Silicon nanowires grow only on the silicon regions and not on the  $\text{Si}_3\text{N}_4$  areas. For instance, **Figure 94** (a) shows a light microscope image of micro-etched areas (brighter areas in the image) on a  $\text{Si}_3\text{N}_4$ -film before the synthesis. Here, the silicon substrates have the crystal orientation of (100). After the synthesis, silicon nanowires grew only in the silicon regions, as it can be observed in the SEM image of **Figure 94** (b). The more confined are the silicon areas, the higher is the probability of growing a single silicon nanowire. **Figure 95** shows magnified views of the synthesized silicon nanowires in smaller areas. Here, the applied catalysts were 10 nm Al and 5 nm Au, and nearly 2  $\mu\text{m}$  large silicon areas could yield synthesis of a single silicon nanowire. As mentioned before, the catalyst thickness has a significant impact on the density of silicon nanowires and consequently, the confined silicon region required for the synthesis of a single silicon nanowire. Employing this approach on AFM probes requires the fabrication of silicon cantilevers, preferably (111) oriented, which are covered by a  $\text{Si}_3\text{N}_4$ -film. In this work, the fabrication of such cantilevers and integration of Al/Au-catalyzed silicon nanowires via the aforementioned method was not realized, as silicon (111) cantilevers are not readily available. Their fabrication procedure is based on using silicon-on-insulator wafers, which is different from the approach applied for the fabrication of  $\text{Si}_3\text{N}_4$ -cantilevers.

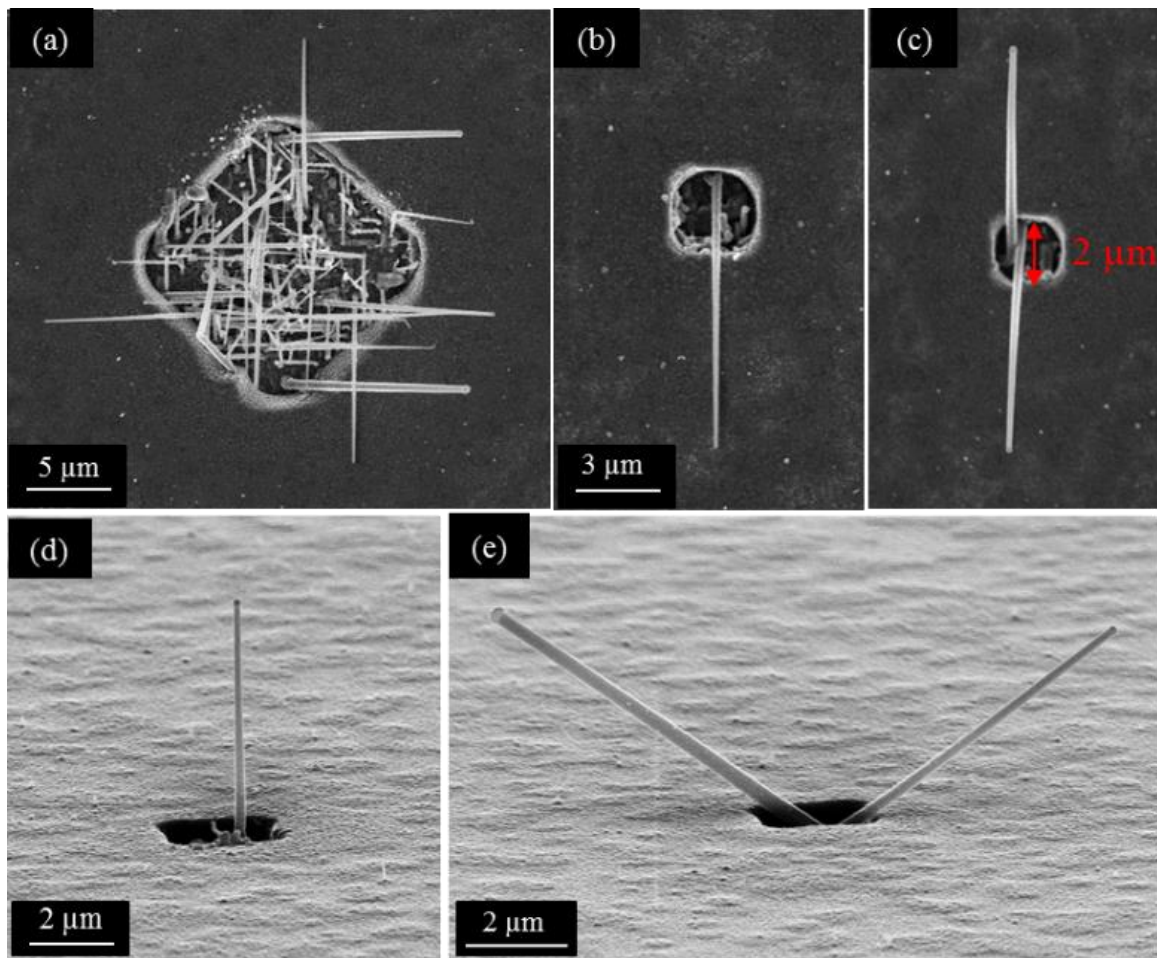


**Figure 93** Schematic illustrations of growing a localized single Al/Au-catalyzed silicon nanowire on Si (100) coated with 1  $\mu\text{m}$  thick  $\text{Si}_3\text{N}_4$ -film.





**Figure 94** (left) Light microscope image of a structured  $1\ \mu\text{m}$  thick  $\text{Si}_3\text{N}_4$ -film on Si (100) substrate. The yellow areas correspond to Si (100), on which  $\text{Si}_3\text{N}_4$  is removed. (right) SEM image of synthesized silicon nanowires using 10 nm Al and 5 nm Au deposited on the sample, shown in the left image.



**Figure 95** SEM images of Al/Au-catalyzed silicon nanowires on the substrate shown in **Figure 94**. (a), (b) and (c) show the top-views and (d) and (e) show the side-views of synthesized silicon nanowires.

# Summary

In this work, a new strategy was studied toward the low-cost fabrication of silicon nanowire scanning probes. The demonstrated fabrication procedure is composed of two main steps, including fabrication of  $\text{Si}_3\text{N}_4$  micro-cantilevers and regrowth of Au-catalyzed silicon nanowires. The regrowth approach is based on silicon nanowire contact printing and regrowing a silicon nanowire from the catalyst particle at the tip of the contact printed nanowires. In principle, this approach eliminates the fabrication step, required for confining the catalyst region, as the confined catalyst regions (catalyst particle at the tip of the nanowires) are readily provided after silicon nanowire contact printing.

By applying this method, silicon nanowire scanning probes were successfully fabricated. Then, the fabricated probes were analyzed and compared to a conventional AFM probe by testing them in AFM using reference samples. The fabricated probe functionality is overall comparable to the conventional AFM probes, even for the high aspect ratio measurement. The reason for not excelling at high aspect ratio measurement is mainly because of the lack of control over silicon nanowire orientations within the regrowth process. By considering this issue, a high reproducibility in fabricating (high aspect ratio) silicon nanowire probes could not yet be achieved.

In the next part of the thesis, the mechanical behaviors of silicon nanowire scanning tips, including softness and vibrational behavior, were studied by conducting finite element simulations. Based on the simulation analysis, it appeared that the overall softness of a scanning probe equipped with a silicon nanowire tip depends significantly on the nanowire geometry and the cantilever spring constant. Furthermore, the cantilever oscillations may cause vibrations in nanowire tips, depending on the cantilever resonance frequency and nanowire geometry. These analyses show that preferred characteristic in scanning probes can be simply achieved by altering the geometry of the nanowire or the cantilever while designing a silicon nanowire scanning probe.

As mentioned before, the orientation of silicon nanowire scanning tips has a significant impact on the scanning quality. Since the orientation of silicon nanowires via the regrowth method could not be controlled, the epitaxial synthesis of silicon nanowires was considered as an alternative approach for realizing silicon nanowire scanning tips. With this in mind, the last part of the thesis focused on the high-yield epitaxial synthesis of silicon nanowires. In this work, single-crystalline silicon nanowires were epitaxially synthesized in a bottom-up manner using Al/Au-catalysts. Al here is used for the *in-situ* removal of native silicon oxide, instead of pretreating substrates in HF. In addition, the electrical characteristics of the Al/Au-catalyzed silicon nanowires appeared similar to Au-catalyzed silicon nanowires.



# Outlook

Silicon nanowire regrowth optimization is one of the future work proposals in order to control the regrowth mode for the synthesis of a single silicon nanowire and enhance the overall reproducibility in the fabrication of silicon nanowire scanning probes. As the regrowth is based on both the synthesis and the contact printing process, the optimization of the entire process is divided in two sections:

- Realization of selective silicon nanowire contact printing, directly on cantilevers. (e.g. structuring catchers on cantilevers)
- Optimizing regrowth conditions (e.g. temperature and pressure) for growing a single silicon nanowire with well-controlled angles.

If a majority of silicon nanowires can be synthesized based on the kinking mechanism within the regrowth process, highly oriented silicon nanowire scanning tips can be fabricated with a high yield. Furthermore, realizing strategies for sharpening silicon nanowire scanning tips can be an alternative approach for enhancing the lateral resolution of nanowire tips, as similarly demonstrated in Appendix section N.

As Al/Au-catalyzed silicon nanowires were aimed to be integrated into scanning probes, realizing approaches for confining catalyst regions or designing a shadow mask on single-crystalline silicon (111) cantilevers can be a subject to future studies. Furthermore, to elucidate the role of Al in the synthesis of Al/Au-catalyzed silicon nanowires, further studies are required.



# Appendix

## A. Devices and Machines

**Table-A 1** *List of devices, machines and their models.*

Device Type	Brand and Model
Ultrasonication bath	Bandelin, Sonorex Digiplus HF-power: 120/480W
Plasma etcher	Plasmalab $\mu$ -etch
RIE (reactive ion etching)	Plasmalab System 100
Mask-aligner (photolithography) operating at 405 nm wavelength	Süss MJB4 (exposure density: 4 mW/cm <sup>2</sup> ) Süss MJB3 (exposure density: 3.6 mW/cm <sup>2</sup> )
Electron-beam lithography	Leica EBPG 5 HR
Electron beam evaporator with substrate heaters	Temescal FC 1800
Diamond plasma-enhanced CVD	ASTEX
Light microscope	Nikon Microphot-FXA
Confocal microscope	Keyence Corporation VK-9710
SEM (scanning electron microscope)	Zeiss Leo Gemini 1550 Hitachi S-4000
TEM (transmission electron microscope)	Philips CM 20 with LaB6 thermionic source at 200 kV
AFM	Bruker Bioscope Catalyst
Probe Station	Karl Süss PM5
Parameter analyzer	Keithley 4200-SCS

**Table-A 2** *List of components in the NWCVD reactor with their brands and model types.*

Device Type	Brand and Model
8-channel flow controller	MKS Instruments Inc., Typ 647C
Mass flow controller (MFC)	MKS Instruments Inc., Typ MF1
Capacitive manometer	MKS Instruments Inc., Typ Baratron
Pressure controller	MKS Instruments, Typ 651C
Butterfly valve	MKS Instruments, Typ 653B
Pirani manometer	InstruTech Inc., CVM201, (SuperBee)
Heater	Momentive Performance Materials Inc.
Oven	Carbolite EST 12/450

## B. Software

**Table-A 3** *List of software.*

Software Name	Purpose of Usage
Nanoscope Analysis 1.5	for analyzing AFM images
ImageJ	for processing SEM and TEM images
K-layout	for creating mask files for lithography processes
COMSOL Multiphysics 5.3 a	for simulating mechanical behaviors of silicon nanowires and AFM cantilevers

## C. Chemicals and Substrates

**Table-A 4** List of substrate materials and their applications in this work.

Substrate Materials	Purpose of Usage	Purchased from
Single-crystalline Si wafers with (100), (110) and (111) crystal orientations	as a substrate for silicon nanowire growth	MicroChemicals GmbH
380 $\mu\text{m}$ thick single-crystalline Si (100) wafers, with LPCVD 1 $\mu\text{m}$ thick $\text{Si}_3\text{N}_4$ coatings on both sides	for the fabrication of $\text{Si}_3\text{N}_4$ -cantilevers	MicroChemicals GmbH
Single-crystalline Si (100) wafers, highly boron-doped (with a resistivity ranging from 0.001 to 0.05 $\Omega\text{cm}$ ), with 200 nm thick $\text{SiO}_2$ coatings on both sides	for the fabrication of marker-fields	MicroChemicals GmbH
Copper TEM grids with lacy carbon films	for TEM/EDX analysis of silicon nanowires	PLANO GmbH
Silicon cantilevers with tip and without tip	for silicon nanowire contact printing and regrowth	- NanoAndMore GmbH - Bruker GmbH
AFM reference sample, composed of square-shaped structures with 10 $\mu\text{m}$ pitch and 180 nm height	AFM calibration and analysis of fabricated probes by performing AFM measurements on the reference samples	Bruker GmbH
AFM reference sample, composed of cylindrically shaped structures with 5 $\mu\text{m}$ pitch and 500 nm height	AFM calibration and analysis of fabricated probes by performing AFM measurements on the reference sample	Micro to Nano GmbH
Glass microscope slides	As a support-substrate for cantilevers for the contact printing process and also for fabricating silicon nanowire-based devices in FET (field-effect transistor) configuration with a back-gate potential	PLANO GmbH



**Table-A 5** List of chemicals and their applications in this work.

Chemicals	Purpose of Usage
Acetone	Cleaning process
Isopropyl alcohol (Isopropanol)	Cleaning process
Piranha solution (a mixture of sulfuric acid (H <sub>2</sub> SO <sub>4</sub> ) and hydrogen peroxide (H <sub>2</sub> O <sub>2</sub> ) with ratio of 2:1 for H <sub>2</sub> SO <sub>4</sub> :H <sub>2</sub> O <sub>2</sub> )	Cleaning process
N-Ethyl-2-pyrrolidon (NEP)	Cleaning process Resist removal Lift-off process
2% buffered Hydrofluoric acid (HF)	Silicon native oxide removal
Potassium iodide (KI)	Etching gold
Photoresist (AZ4214E)	for photolithography step
E-beam resists (PMMA 50 k)	for e-beam lithography step
AZ 726 MIF	Developing photoresists
Potassium Hydroxide (KOH)	Etching silicon
Crystalbond 509	for gluing cantilevers to glass slides
Conductive silver glue	As a back-gate for silicon nanowire FET devices
Ethanol	for silicon nanowire drop-casting

## D. Process Recipes

**Table-A 6** Etching recipes for Si<sub>3</sub>N<sub>4</sub>, SiO<sub>2</sub> and diamond in RIE.

Etching LPCVD Si <sub>3</sub> N <sub>4</sub> in RIE		Etching SiO <sub>2</sub> in RIE		Etching Diamond in RIE	
CF <sub>4</sub> flow	50 sccm	CF <sub>4</sub> flow	45 sccm	O <sub>2</sub> flow	50 sccm
				Ar flow	20 sccm
Power	600 W	Power	600 W	Power	600 W
Working pressure	40 mTorr	Working pressure	40 mTorr	Working pressure	40 mTorr
Etching rate	50 nm/min	Etching rate	25 nm/min	Etching rate	20 nm/min

**Table-A 7** Cleaning procedure in the plasma etcher ( $\mu$ -Etch).

cleaning substrate surface in the plasma etcher ( $\mu$ -Etch)			
O <sub>2</sub> flow	Working pressure	power	time
10 sccm	0.1 Torr	100 W	5 min

**Table-A 8** *Silicon nanowire synthesis in NWCVD.*

Silicon Nanowire Synthesis in NWCVD		
Step 1 (evacuating the tube)		
Pressure	0.08 mbar	
Time	10 min	
Step 2 (pre-conditioning)		
Ar flow	500 sccm	
time	5 min	
Step 3 (evacuating the tube)		
Ar flow	0 sccm	
Step 4 (increasing the oven temperature to the growth temperature)		
Recipes	Recipe 1	Recipe 2
Growth Temperature	550 °C	485 °C
Step 5 (pre-setting the growth parameters)		
Temperature	550 °C	485 °C
Ar flow	100 sccm	120 sccm
Pressure	10 mbar	75 mbar
Time	5 min	5 min
Step 6 (silicon nanowire growth)		
Temperature	550 °C	485 °C
H <sub>2</sub> flow	80 sccm	20 sccm
SiH <sub>4</sub> /He (2% SiH <sub>4</sub> in He) flow	20 sccm	100 sccm
Pressure	10 mbar	75 mbar
Time	60 min	20 min
Step 7 (cool down)		
Ar flow	500 sccm	500 sccm
H <sub>2</sub> flow	0 sccm	0 sccm
SiH <sub>4</sub> /He (2% SiH <sub>4</sub> in He) flow	0 sccm	0 sccm
time	5 min	5 min
Step 8 (cool down to room temperature and evacuation)		
Ar flow	0 sccm	0 sccm

**Table-A 9** *Photolithography recipe for AZ5214E (positive) on a Si<sub>3</sub>N<sub>4</sub> surface.*

<b>Photolithography for Positive AZ5214 E</b>	
<b>Spin Coating</b>	
Rotation speed	4000 rpm
Time	60 seconds
<b>Baking</b>	
Temperature	110 °C
Time	90 seconds
<b>Cooling Down</b>	
<b>Exposure</b>	
Using MJB4	33 s
Using MJB3	30 s
<b>Developing</b>	
AZ726 MIF	30-40 s
<b>Immersing in Water and Subsequently Drying</b>	

**Table-A 10** *Photolithography recipe for AZ5214E (negative) on a Si<sub>3</sub>N<sub>4</sub> surface.*

<b>Photolithography for Negative AZ5214 E</b>	
<b>Spin Coating</b>	
Rotation speed	4000 rpm
Time	60 seconds
<b>Baking</b>	
Temperature	110 °C
Time	90 seconds
<b>Cooling Down</b>	
<b>1<sup>st</sup> Exposure</b>	
Using MJB4	7.2 s
Using MJB3	8 s
<b>Baking</b>	
Temperature	120 °C
Time	60 seconds
<b>Flood Exposure</b>	
Using MJB4	38 s
Using MJB3	40 s
<b>Developing</b>	
AZ726 MIF	30-40 s
<b>Immersing in Water and Subsequently Drying</b>	

## E. Cleaning Procedure

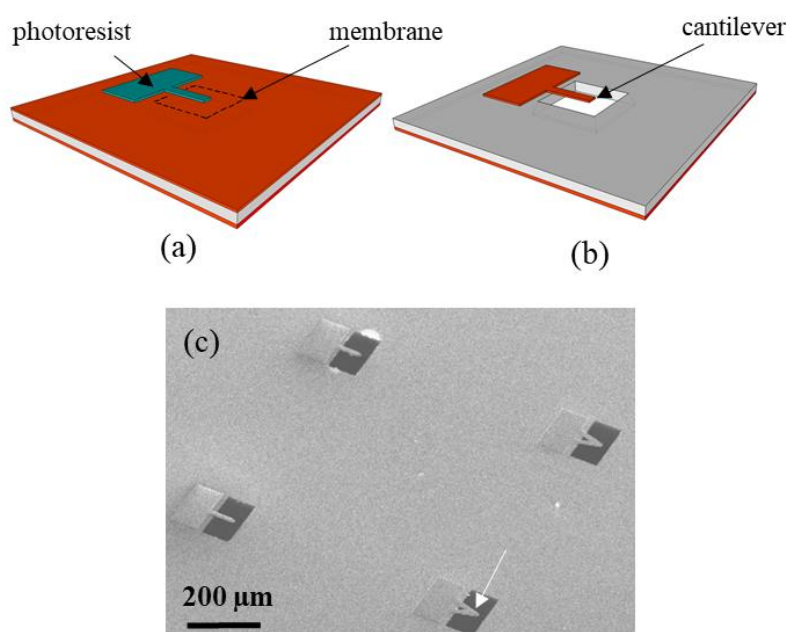
- Cutting samples with dicer (manually or using a dicing machine).
- Immersing samples in piranha solution for 60 seconds and subsequently, immersing in a baker with flowing water for 10 minutes. (This step is optional and only performed for substrates with a high amount of contaminations or with unknown storage conditions.)
- Immersing samples in NEP for 30-40 minutes at 100 °C. (This step is optional and only performed with substrates with a high amount of contaminations or with unknown storage conditions.)
- Immersing samples in Acetone for 5 minutes at room temperature in the ultrasonication bath using 50 % of the maximum power. (Fragile samples such as membranes and cantilevers were not placed in the ultrasonic bath.)
- Immersing samples in Isopropanol for 5 minutes at room temperature in the ultrasonication bath using 50 % of the maximum power. (Fragile samples such as membranes and cantilevers were not placed in the ultrasonic bath.)
- Drying samples on a hot plate or simply using a stream of gaseous nitrogen.
- Cleaning samples in the plasma etcher using O<sub>2</sub> (μ-Etch), as demonstrated in **Table-A 7**.

## F. Si<sub>3</sub>N<sub>4</sub>-Membrane Fabrication

- Performing the cleaning procedure (demonstrated in section E) for Si wafers, with Si<sub>3</sub>N<sub>4</sub> coatings on both sides.
- Spin-coating the photoresist (AZ5214 E) on one side of the substrates with a speed of 4000 rpm.
- Baking at 110 °C for 90 seconds.
- Repeating the two previous steps for the other side of the sample.
- UV-exposure in the mask aligner only one side of the substrate (**Table-A 9**).
- Developing the exposed photoresist in the developer (AZ726 MIF).
- Etching Si<sub>3</sub>N<sub>4</sub> in the unprotected areas in RIE using CF<sub>4</sub> (**Table-A 6**).
- Removing the photoresist by immersing the samples in Acetone and Isopropanol, each for 5 minutes.
- Etching silicon in 20% wt KOH (using water and isopropanol as solvents with ratio of 2:1) at 80 °C. The etching rate is almost 45 µm/hour.
- At last, rinsing the membranes in the water and subsequently, drying.

## G. Si<sub>3</sub>N<sub>4</sub>-Cantilever Fabrication

- Performing the cleaning procedure (demonstrated in section E) for Si<sub>3</sub>N<sub>4</sub>-membranes.
- Gluing the Si<sub>3</sub>N<sub>4</sub>-membranes to glass slides using the crystal bond on a hot plate at 50 °C. (As membranes are fragile, the vacuum holder of the spin-coating device can break and damage the membranes.)
- Spin-coating the photoresist (AZ5214 E) on one side of the substrates with a speed of 4000 rpm.
- Baking at 110 °C for 90 seconds.
- UV-exposure in the mask aligner (**Table-A 9**).
- Developing the exposed photoresist in the developer (AZ726 MIF).
- Etching Si<sub>3</sub>N<sub>4</sub> in the unprotected areas in RIE using CF<sub>4</sub> (**Table-A 6**).
- Removing the photoresist by immersing the samples in Acetone and Isopropanol, each for 5 minutes.



**Figure-A 1** (a) Schematic illustration of a patterned photoresist with a cantilever shape after the photolithography step on a square-shaped Si<sub>3</sub>N<sub>4</sub>-membrane. (b) Schematic illustration of a fabricated cantilever after etching Si<sub>3</sub>N<sub>4</sub> in CF<sub>4</sub> and plasma and subsequent photoresist removal. (c) SEM image of fabricated Si<sub>3</sub>N<sub>4</sub>-cantilevers on membranes. The white arrow indicates one of the fabricated cantilevers.

## H. Silicon Nanowire Growth

- Cleaning procedure (demonstrated in section E) for silicon substrates (100), (110) and (111). The substrates are cut in the size of 1.5 cm  $\times$  0.3 cm.
- Evaporating Au and Al with different thickness (ranging from 2 nm to 20 nm).
- Storage: in case of Al, they are stored in a sample box wrapped by a parafilm
- Placing them in NWCVD and performing synthesis (**Table-A 8**).
- Taking out the samples after synthesis and cooling the temperature to 250 °C or below.

## I. Silicon Nanowire Contact Printing

- Cleaning procedure (demonstrated in section E) for receiving substrates.
- Silicon nanowire contact printing. The following table shows the contact printing parameters (velocity and force) applied for each sample types. Each parameter has a range, in which performing contact printing can be carried out safely on samples. Unfortunately, due to low accuracy in calibrating force and uneven surfaces, particularly for cantilevers glued on glass slides, the values can vary slightly. The silicon nanowires are synthesized based on the recipe 1 demonstrated in **Table-A 8**.

**Table-A 11** *List of contact printing parameter (velocity and force) ranges for Si<sub>3</sub>N<sub>4</sub>- and Si-cantilevers, membranes and bulk substrates.*

Sample Type	Velocity (mm/s)	Force (N)
Si <sub>3</sub> N <sub>4</sub> -cantilevers without tip	1-2	0.75-1
Membranes	1.5-2	0.5-1
Si and Si <sub>3</sub> N <sub>4</sub> substrates	0.5-2	0.5-2
Si-cantilevers with tip	0.5-1.5	0.75-1
Si-cantilevers without tip	0.5-1	1-2

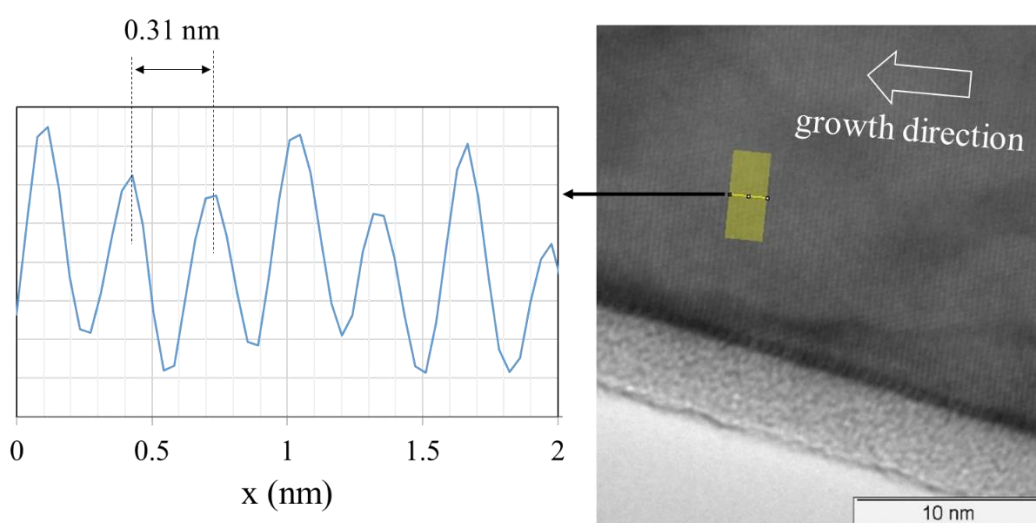


## J. Fabricating Metal Pads for Silicon Nanowires (Electrical Measurements)

- Cleaning procedure (demonstrated in section E) on silicon (100) with SiO<sub>2</sub> coatings on both sides.
- Covering one side of the wafers by spin-coating AZ5214E with a rotation speed of 4000 rpm and subsequently, baking for 1 min at 110 °C (**Table-A 9**).
- Etching SiO<sub>2</sub> from the unprotected side of the wafers using CF<sub>4</sub> in RIE (**Table-A 6**).
- Performing cleaning procedure on the samples.
- Fabrication of marker fields using PMMA resists, e-beam lithography and subsequent lift-off process. The evaporated metals for marker fields are 5 nm Ti and 45 nm Au films.
- Transferring silicon nanowires on the growth substrate into a small bottle (1.5 ml).
- Filling the bottle with Ethanol and placing the enclosed bottle in the ultrasonic bath for 3-4 seconds with 20 % of the maximum power.
- Casting a drop of Ethanol with the suspended nanowires with a pipette on the sample with marker field structures and subsequently, letting the solvent evaporate. If necessary, repeating this step, in order to reach an adequate density of nanowires.
- Creating metal contacts structures in K-layout based on optical images of the nanowires on the marker-field.
- Spin-coating the samples with PMMA 50 k ohm resist with a rotation speed of 2000 rpm for 1 minute. Then, baking the samples at 180 °C for 5 minutes. After cooling back to room temperature, repeating the same procedure on the sample using PMMA k 4%.
- After lithography and development, removing the native oxide of the silicon nanowires using 2 % HF for 10 seconds. Subsequently, evaporating metal contacts composed of 20 nm Ti, 300 nm Al and 80 nm Au.
- Performing the lift-off process by immersing the samples in Acetone (10 to 20 minutes) and Isopropanol (5 minutes).

## K. TEM Investigations and Sample Preparations

- Transferring silicon nanowires on the growth substrate into a small bottle (1.5 ml).
- Filling the bottle with Ethanol and placing the enclosed bottle in the ultrasonic bath for 3-4 seconds with 20 % of the maximum power.
- Casting a drop of Ethanol with the suspended nanowires with a pipette on copper TEM grids with lacy carbon films and subsequently, letting the solvent evaporate. If necessary, repeating this step, in order to reach an adequate density of nanowires.



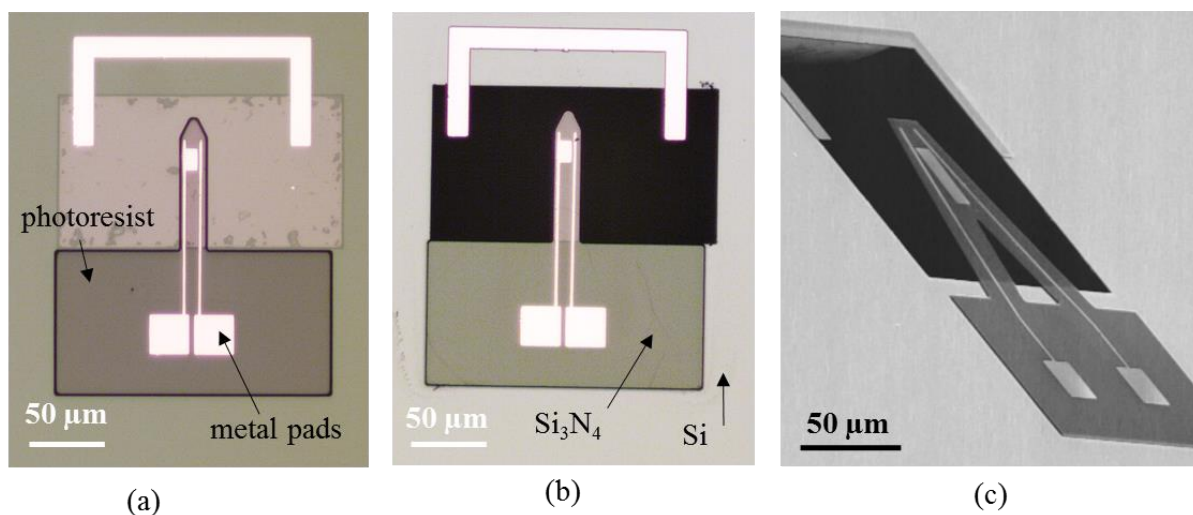
**Figure-A 2** Lattice plane distance measurements of a HRTEM image of an Al/Au-catalyzed silicon nanowire using ImageJ software. The graph corresponds to a highlighted region in the HRTEM image.

**Table-A 12** Atomic composition of Al and Au in the catalyst particles of Al/Au-catalyzed silicon nanowires. (Reprinted with permission from [1]. Copyright (2019) American Chemical Society.)

	Al [at.%]	Au [at.%]
Sample 1	37.8	62.2
Sample 2	45.9	54.1
Sample 3	36.0	64.0
Sample 4	36.2	63.8

## **L. Lift-off Process on Si<sub>3</sub>N<sub>4</sub>-Membranes and Fabricating Metal Structures on Si<sub>3</sub>N<sub>4</sub>-Cantilevers**

- Performing the cleaning procedure (demonstrated in section **E**) for Si<sub>3</sub>N<sub>4</sub>-membranes.
- Gluing Si<sub>3</sub>N<sub>4</sub>-membranes to glass slides using a crystal bond on a hot plate at 50 °C. (As membranes are fragile, the vacuum holder of the spin-coating device can break and damage membranes.)
- Spin-coating the photoresist (AZ5214 E) on one side of substrates with a rotation speed of 4000 rpm.
- Baking at 110 °C for 90 seconds.
- UV-exposure in the mask aligner using quartz masks (**Table-A 10**).
- Baking at 120 °C for 1 minute.
- Flood exposure in the mask aligner.
- Developing the photoresist in the developer.
- Evaporating 100 nm Al on the samples.
- Immersing the samples in NEP at 100°C for 20 minutes. Then immersing it in the acetone and isopropanol each for 5 minutes at room temperature.
- Cantilever fabrication (as demonstrated in section **G**). An example is shown in **Figure-A 3**.



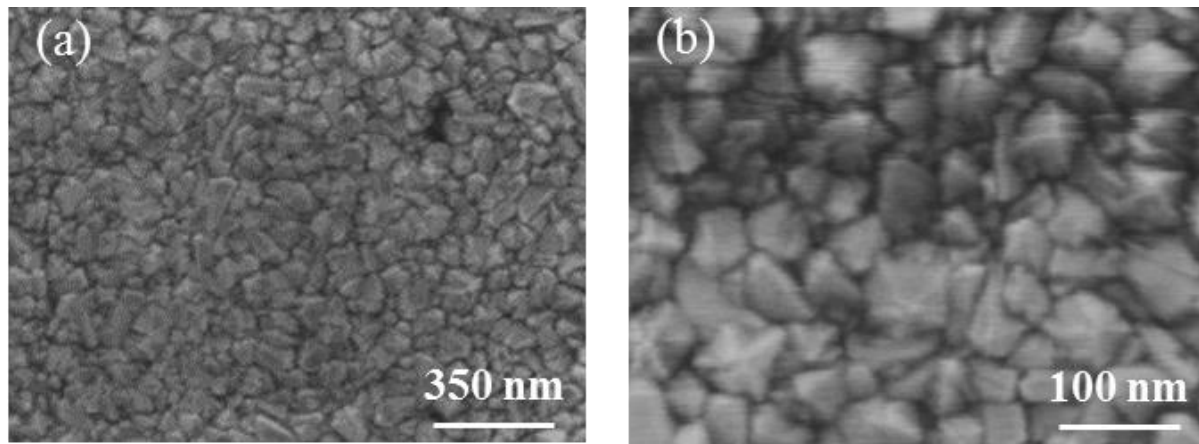
**Figure-A 3** (a) A light microscope image of fabricated metal pads (100 nm Al) on a  $\text{Si}_3\text{N}_4$ -membrane and a patterned photoresist. (b) The fabricated cantilever with the metal pads after etching  $\text{Si}_3\text{N}_4$  and removing the photoresist. (c) SEM image of a fabricated V-shaped  $\text{Si}_3\text{N}_4$ -cantilever with metal pads.

## **M. Fabricating Diamond Coated Si<sub>3</sub>N<sub>4</sub>-Membranes and Cantilevers**

Modification of fabricated Si<sub>3</sub>N<sub>4</sub>-cantilever geometries might not always provide a wide range of resonance frequencies and spring constants. For instance, in a case of Si<sub>3</sub>N<sub>4</sub>-cantilevers, spring constants are in the range of 0.1 N/m to nearly 1 N/m with a reasonable size and geometry which is compatible with AFM measurements. In order to achieve a higher spring constant, introducing a thin film on Si<sub>3</sub>N<sub>4</sub>-cantilevers, particularly with a higher Young's elastic modulus can be a solution. Here, for this purpose, nano-crystalline diamond film synthesis was realized on fabricated Si<sub>3</sub>N<sub>4</sub>-membranes. Afterward, the cantilever fabrication was followed, as demonstrated in section G.

### **M.1. Diamond Synthesis on Si<sub>3</sub>N<sub>4</sub>-Membranes**

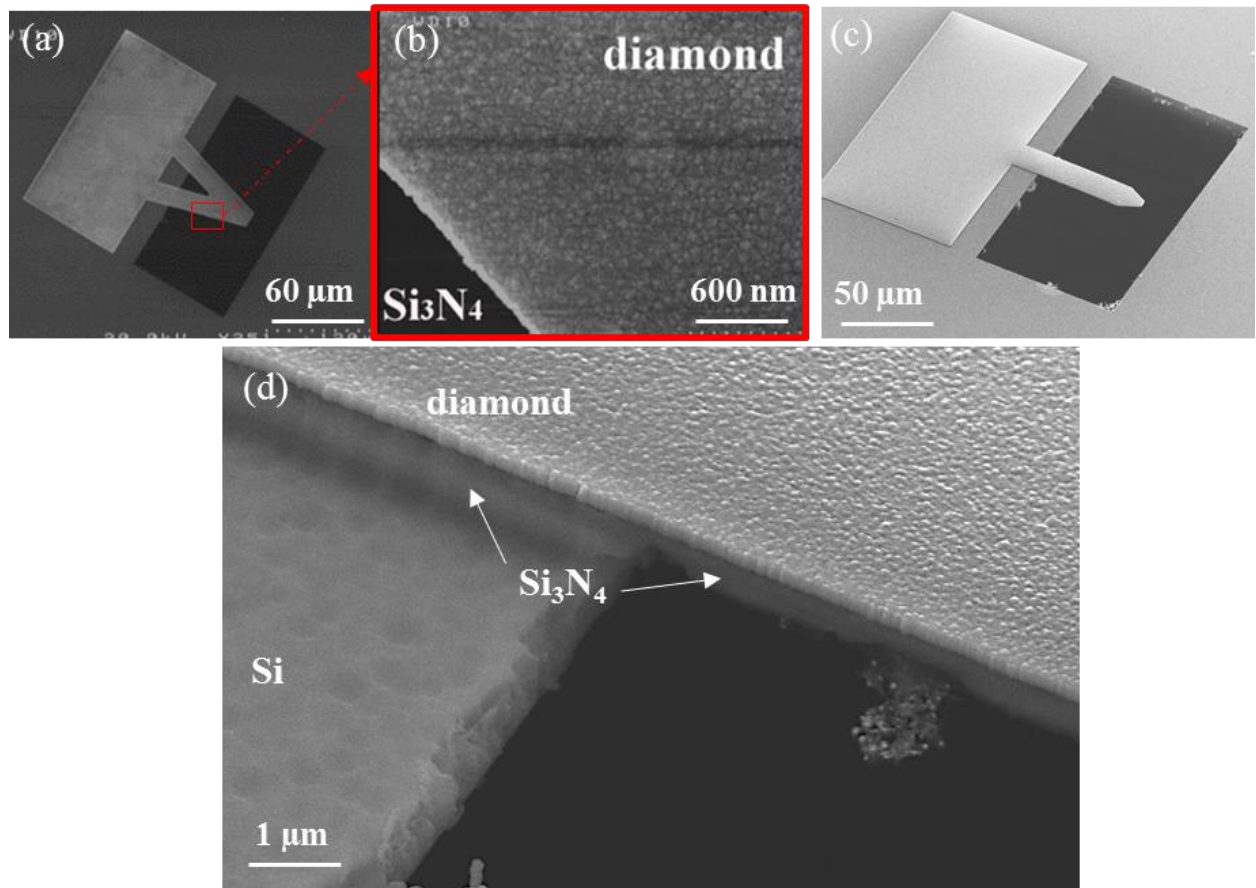
Prior to the diamond synthesis, diamond nucleation is an essential prerequisite. There are different methods for this purpose. Here, a diamond seeding solution was applied [259]. The seed solution is commercially available, which is basically a colloidal solution of diamond particles with a size of 4-5 nm in DI (deionized) water. The seeding was carried out via spin-coating the seed solution on the Si<sub>3</sub>N<sub>4</sub>-membrane surface. Before starting the rotation, the sample surface was covered by the solution using a pipette for 1 minute. Then, spin-coating was carried out, starting with 65 rpm rotation speed for 1 minute. Then, it was followed by the rotation speed of 2000 rpm for 1 min and at last, 4000 rpm for 30 seconds. After the seeding step, a thin film of nanocrystalline diamond was synthesized on the fabricated Si<sub>3</sub>N<sub>4</sub>-membranes in a plasma-enhanced CVD device (ASTEX). For the synthesis, the flow of CH<sub>4</sub> and H<sub>2</sub> gases were set respectively 3 sccm and 200 sccm at a gas pressure of 0.3 Torr with a plasma power of 1000 W for 60 minutes. The growth temperature was kept constant at 750 °C during the entire growth process. After the growth, it was observed that membranes are not bent or deformed. This simply indicates that the stress in the diamond film does not cause an issue for the mechanical stability of the membranes. So, they remained nearly flat, which makes them again suitable for further microfabrication steps. Furthermore, the diamond film after the synthesis was observed in SEM (**Figure-A 4**). According to the SEM investigations, the synthesized diamond films are quite homogenous on the sample with sufficient coverage. The crystal grains of diamonds are in the range of 20-100 nm.



**Figure-A 4** (a) Diamond film synthesized on a  $\text{Si}_3\text{N}_4$ -membrane. (b) Grains of the diamond film synthesized on a  $\text{Si}_3\text{N}_4$ -membrane.

## M.2. Cantilever Fabrication on Diamond Coated $\text{Si}_3\text{N}_4$ -Membranes

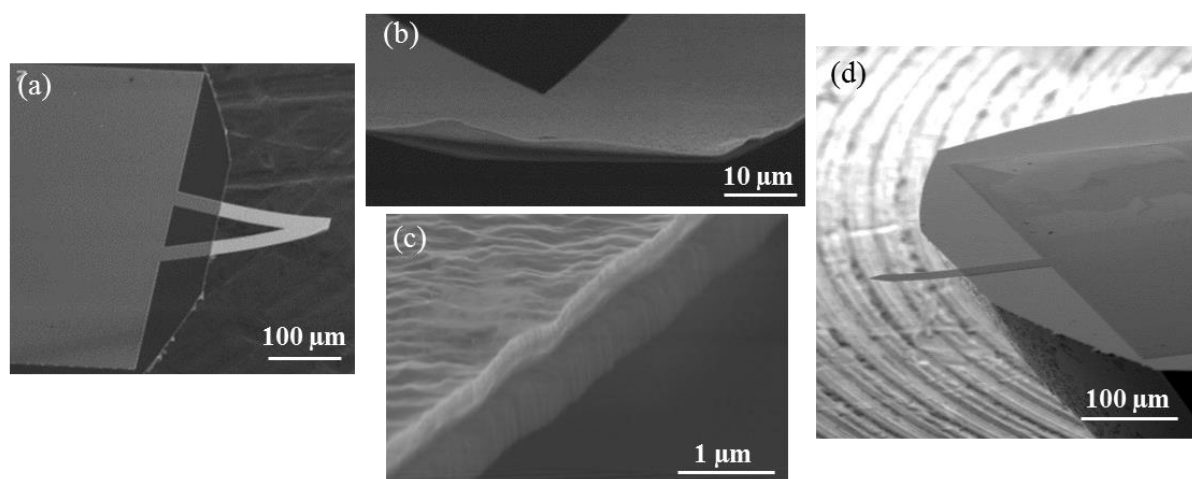
The cantilever fabrication on the diamond coated  $\text{Si}_3\text{N}_4$ -membranes were followed similarly to the fabrication procedure of  $\text{Si}_3\text{N}_4$ -cantilevers. However, dry etching the diamond film is only doable with  $\text{O}_2$  gas in a reactive ion etching (RIE) device [260]. For this purpose, using photoresists as an etching mask will no longer be effective as  $\text{O}_2$  can simply etch photoresists. Therefore, it is required to use a material which cannot be etched by  $\text{O}_2$  and can be simply removable. Usually, metals for this purpose would be a proper alternative [261]. Cantilevers were fabricated with and also without  $\text{Si}_3\text{N}_4$ -films. Fabricating cantilevers composed of  $\text{Si}_3\text{N}_4$  and diamond films was carried out, as it was described in section G for the  $\text{Si}_3\text{N}_4$ -cantilever fabrication. However, one step is added to define the metal mask on the membrane areas. The metal area is the same as the cantilever area. Here, a 135 nm thick Al film was used as a metal mask. After metal deposition and performing the lift-off process, the diamond film was etched using  $\text{O}_2$ , Ar and plasma for 30 minutes with an etching rate of 20 nm/min. Before etching  $\text{Si}_3\text{N}_4$ , the Al mask was removed to measure the diamond film thickness, which was established to be 600-610 nm (using a profilometer (Bruker's Dektak)). The SEM images of the selectively etched diamond film on  $\text{Si}_3\text{N}_4$  are shown in **Figure-A 5**. Subsequently, the second etching step was carried out using  $\text{CF}_4$  gas in RIE. At the end of the fabrication processes, the Al mask was removed in KOH. The final fabricated cantilever was composed of 1  $\mu\text{m}$  thick  $\text{Si}_3\text{N}_4$  and 600 nm nanocrystalline diamond films.



**Figure-A 5** (a) and (b) SEM images of a synthesized and patterned diamond film on a  $\text{Si}_3\text{N}_4$ -membrane. (c) and (d) SEM images of fabricated  $\text{Si}_3\text{N}_4$ -cantilevers coated with a diamond film after etching  $\text{Si}_3\text{N}_4$ .

### M.3. Diamond Cantilever Fabrication

In this section, the fabrication of a diamond cantilever is demonstrated. This part is also very similar to the conventional cantilever fabrication procedure in this work. However, the only difference is that the  $\text{Si}_3\text{N}_4$ -film is etched from the backside of the membrane using  $\text{CF}_4$  and plasma. So only the diamond membrane remained at the end. Later, the cantilever area was defined using an Al-hard mask. Then, the cantilever is fabricated by etching diamond in  $\text{O}_2$  and plasma. The Al layer was subsequently removed in KOH. However, in some cases, the Al-mask could not be fully removed in KOH (see **Figure-A 6** (a), (b) and (c)). This might be due to the formation of  $\text{Al}_2\text{O}_3$  after being in the atmosphere condition or during the etching process with  $\text{O}_2$ . Nevertheless, the fabricated cantilevers with and without  $\text{Si}_3\text{N}_4$ -films are nearly straight, indicating the low stress in the diamond film. The Young's elastic modulus of the diamond film was investigated to be  $666 \pm 202$  GPa using the static beam bending method in AFM, as demonstrated in section 3.1.1. The uncertainty in the results could arise from variation in the thickness of the diamond film. All in all, the higher Young's elastic modulus in the diamond film can enhance the spring constant of fabricated  $\text{Si}_3\text{N}_4$ -cantilevers.

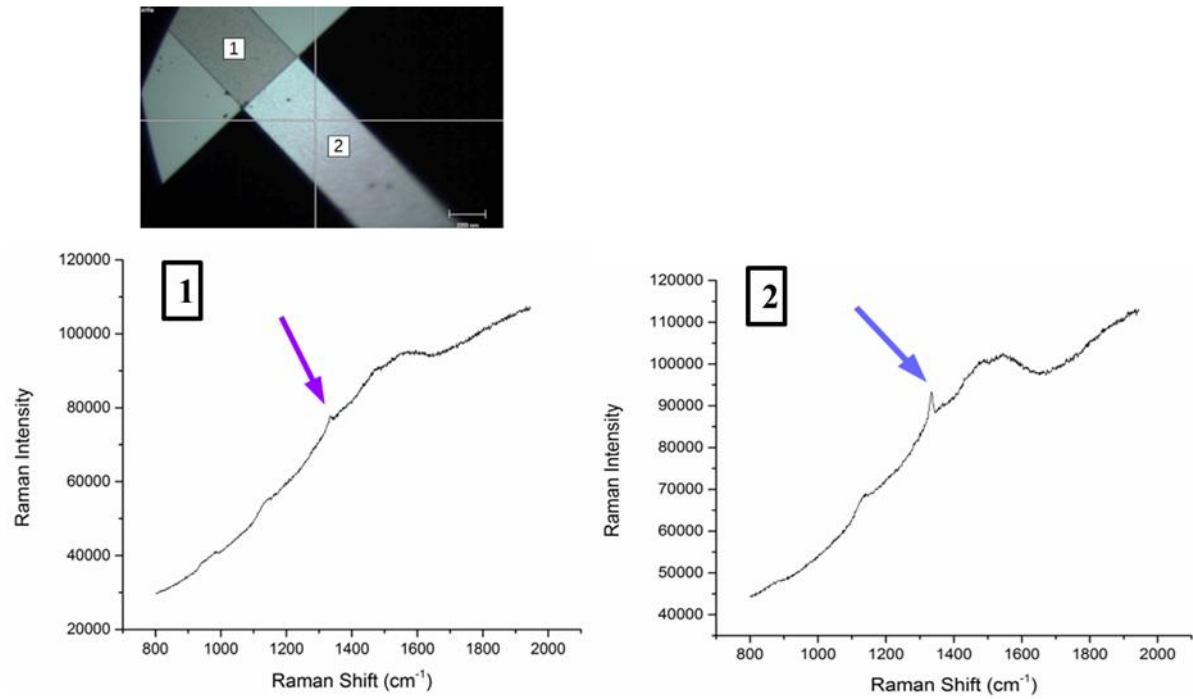


**Figure-A 6** (a), (c) and (b) SEM images of a fabricated diamond cantilever after the Al mask removal. However, in this case, the Al layer could not be fully etched in the process and it is slightly detached from the cantilever. (d) SEM image of a fabricated diamond cantilever after the Al mask removal. In this case, the Al mask was fully removed.

#### M.4. Raman Investigations

After the diamond synthesis and cantilever fabrication, a Raman measurement was performed to assure the diamond characteristic of the film. This measurement was carried out on the diamond cantilever using a 514.5 nm laser radiation, as shown in **Figure-A 7**. Two spots on the cantilevers were selected for this investigation; one spot is on the diamond film on the bulk area of Si-Si<sub>3</sub>N<sub>4</sub> (position 1) and the other spot is on the diamond cantilever (position 2) where no Si-Si<sub>3</sub>N<sub>4</sub> is underneath. The two spots are indicated in the optical image of the cantilever shown in **Figure-A 7**. Basically, diamond exhibits one vibration peak at 1333 cm<sup>-1</sup> in the Raman spectrum [262]. This peak is detected in both spectra taken from both positions 1 and 2 shown in **Figure-A 7** and indicated by the blue arrow. However, the intensity of this peak from the spectra on the cantilever area (position 2) is higher than the area where the diamond layer is on Si-Si<sub>3</sub>N<sub>4</sub> (position 1). The CVD diamond film is composed of non-diamond forms as well. The non-diamond carbon can correspond to the graphite or amorphous carbons. Pure graphite in the Raman spectra appears at the 1580 cm<sup>-1</sup>. However, for the small crystal sizes of graphite, the sharp peak of graphite becomes a broader band of G-band at around 1357 cm<sup>-1</sup> and a disordered peak (D-band) at ~1350 cm<sup>-1</sup> [263]. An asymmetric hump observed in the region of 1000-1600 cm<sup>-1</sup> represents amorphous carbon [264]. This effect is observed clearly in the obtained Raman spectra. The peaks at 1135 cm<sup>-1</sup> and 1457 cm<sup>-1</sup> are assigned to the C-C and C-H vibration modes [265], [266].

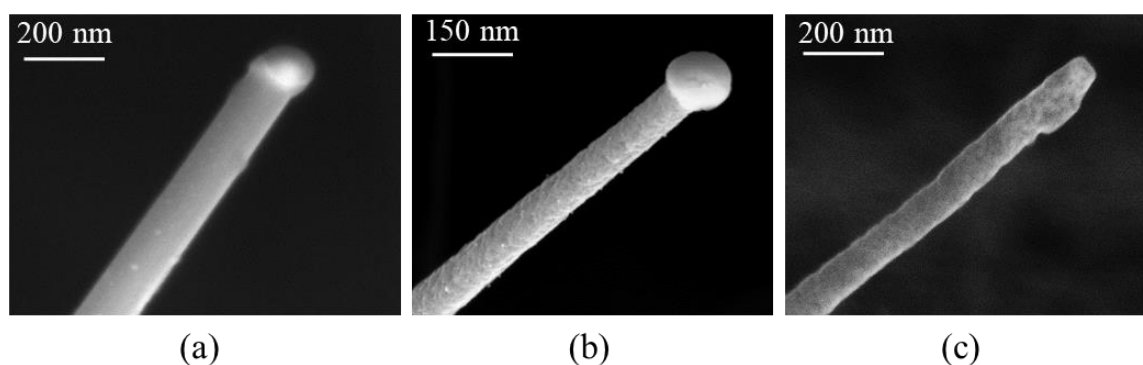




**Figure-A 7** Raman measurements on the fabricated diamond cantilever. The position 1 corresponds to a spot on the diamond film on the bulk area (on Si-Si<sub>3</sub>N<sub>4</sub>) and position 2 is on the diamond cantilever.

## N. Etching Silicon Nanowires

The diameter of silicon nanowires can be modified by a post-treatment process yielding a smaller diameter for silicon nanowires. This is beneficial for achieving high resolution scanning images and adjusting the tip softness. The lateral resolution of the silicon nanowire tips can be simply enhanced by performing a dry etching step in RIE using  $\text{CF}_4$  gas (**Table-A 6**). Within this process, silicon nanowires are radially and partially etched, resulting in a smaller diameter for silicon nanowires (**Figure-A 8** (a) and (b)). The catalytic metal (Au) particle at the silicon nanowire tip can be later removed by potassium iodide (KI) (**Figure-A 8** (c)).



**Figure-A 8** Silicon nanowire before (a), after (b) etching by  $\text{CF}_4$  and plasma for 1 minute; the diameter decreased for about 60 nm after etching and after Au removal (c).

**Table-A 13** *Electrical resistance values for Al/Au- and Au-catalyzed silicon nanowires with a diameter of approximately 120 nm and contact distance of about 1.4  $\mu\text{m}$ . (Reprinted with permission from [1]. Copyright (2019) American Chemical Society.)*

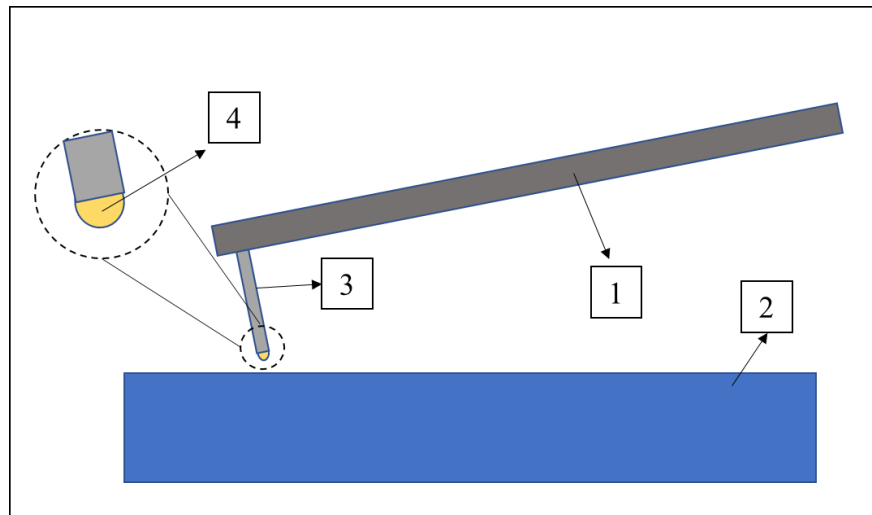
Resistance for Al/Au-catalyzed Silicon Nanowires ( $\text{G}\Omega$ )	Resistance for Au- catalyzed Silicon Nanowires ( $\text{G}\Omega$ )
0.89	4.97
0.73	6.60
1.54	1.89
1.69	1.62
1.15	1.29
1.42	1.70
1.69	2.58
1.85	5.15
3.29	6.11
1.68	4.75
1.81	1.60
2.25	2.29
2.52	0.69
1.61	0.75
2.28	1.73

## O. Simulation Parameters and Conditions

### O.1. Silicon Nanowire Softness

**Table-A 14** *Physics and study of the simulation for the silicon nanowire softness.*

<b>Physics</b>	solid mechanics
<b>Study</b>	stationary



**Figure-A 9** *Schematic illustration of the silicon nanowire probe considered for COMSOL simulations.*

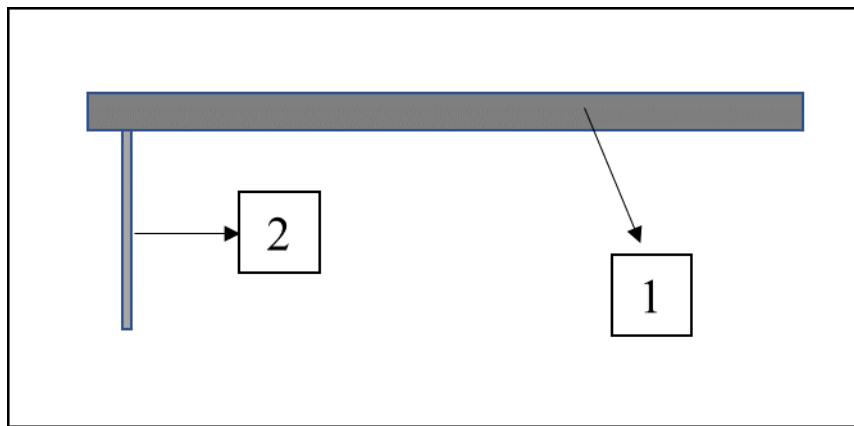
**Table-A 15** *Simulation parameters. The item numbers are indicated in the schematic illustration of **Figure-A 9**.*

Item number	1	2	3	4
<b>Material</b>	silicon nitride (Si <sub>3</sub> N <sub>4</sub> )	silicon (Si)	single crystal, isotropic silicon (Si)	gold (Au)
<b>Young's modulus (<i>E</i>)</b>	250 GPa	190 GPa	170 GPa	70 GPa
<b>Poisson's ratio (<i>ν</i>)</b>	0.23	0.17	0.28	0.44
<b>Density (<i>d</i>)</b>	3100 kg/cm <sup>3</sup>	2329 kg/cm <sup>3</sup>	2329 kg/cm <sup>3</sup>	19300 kg/cm <sup>3</sup>

## O.2. Silicon Nanowire Oscillation

**Table-A 16** *Physics and study of the simulation for silicon nanowire oscillation.*

<b>Physics</b>	solid mechanics
<b>Study</b>	eigenfrequency (to find resonance frequency)
	frequency-domain (to find displacement at different frequencies)



**Figure-A 10** *Schematic illustration of the silicon nanowire probe considered for COMSOL simulations.*

**Table-A 17** *Simulation parameters. The item numbers are indicated in the schematic illustration of Figure-A 10.*

Item number	1	2
<b>Material</b>	silicon nitride ( $\text{Si}_3\text{N}_4$ )	single crystal, isotropic silicon (Si)
<b>Young's modulus (<math>E</math>)</b>	204.4 GPa	170 GPa
<b>Poisson's ratio (<math>\nu</math>)</b>	0.23	0.28
<b>Density (<math>d</math>)</b>	3100 kg/cm <sup>3</sup>	2329 kg/cm <sup>3</sup>
<b>Loss factor (<math>\eta</math>)</b>	0.0001	0.0001

# Table of Abbreviations

<b>AFM</b>	Atomic Force Microscopy
<b>Al</b>	Aluminum
<b>Au</b>	Gold
<b>C</b>	Carbon
<b>CP</b>	Contact Printed (Silicon Nanowire)
<b>Cu</b>	Copper
<b>CVD</b>	Chemical Vapor Deposition
<b>EDX</b>	Energy-Dispersive X-ray Analysis
<b>FET</b>	Field-Effect Transistor
<b>FFT</b>	Fast Fourier Transform
<b>FIB</b>	Focused Ion Beam
<b>HF</b>	Hydrofluoric Acid
<b>HRTEM</b>	High Resolution Transmission Electron Microscopy
<b>LPCVD</b>	Low Pressure Chemical Vapor Deposition
<b>NWCVD</b>	Nanowire Chemical Vapor Deposition Reactor
<b>PMMA</b>	Poly(Methyl Methacrylate)
<b>RIE</b>	Reactive Ion Etching
<b>SEM</b>	Scanning Electron Microscopy
<b>Si</b>	Silicon
<b>SiNW</b>	Silicon Nanowire
<b>SPM</b>	Scanning Probe Microscopy
<b>TEM</b>	Transmission Electron Microscopy
<b>UHV</b>	Ultra-high vacuum
<b>VLS</b>	Vapor Liquid Solid



# References

- [1] A. Behroudj, D. Geiger, and S. Strehle, “Epitaxial Bottom-up Growth of Silicon Nanowires on Oxidized Silicon by Alloy-Catalyzed Gas-Phase Synthesis,” *Nano Lett.*, vol. 19, no. 11, pp. 7895–7900, Nov. 2019.
- [2] Y. Cui, C. M. Lieber, and M. G. Bawendi, “Functional nanoscale electronic devices assembled using silicon nanowire building blocks,” *Sci.*, vol. 291, no. 5505, pp. 851–3, Feb. 2001.
- [3] R. S. Wagner and W. C. Ellis, “Vapor-Liquid-Solid Mechanism of Single Crystal Growth,” *Appl. Phys. Lett.*, vol. 4, no. 5, pp. 89–90, Mar. 1964.
- [4] J.-Y. Jung, Z. Guo, S.-W. Jee, H.-D. Um, K.-T. Park, and J.-H. Lee, “A strong antireflective solar cell prepared by tapering silicon nanowires,” *Opt. Express*, vol. 18, no. S3, p. A286, Sep. 2010.
- [5] A. Najar *et al.*, “Effective antireflection properties of porous silicon nanowires for photovoltaic applications,” in *2013 Saudi International Electronics, Communications and Photonics Conference*, 2013, pp. 1–4.
- [6] S. M. Thalluri *et al.*, “Highly-ordered silicon nanowire arrays for photoelectrochemical hydrogen evolution: an investigation on the effect of wire diameter, length and inter-wire spacing,” *Sustain. Energy Fuels*, vol. 2, no. 5, pp. 978–982, May 2018.
- [7] J. Zhu *et al.*, “Optical Absorption Enhancement in Amorphous Silicon Nanowire and Nanocone Arrays,” *Nano Lett.*, vol. 9, no. 1, pp. 279–282, Jan. 2009.
- [8] S. T. Jäger and S. Strehle, “Design parameters for enhanced photon absorption in vertically aligned silicon nanowire arrays,” *Nanoscale Res. Lett.*, vol. 9, no. 1, p. 511, Sep. 2014.
- [9] N. Hibst, P. Knittel, J. Biskupek, C. Kranz, B. Mizaikoff, and S. Strehle, “The mechanisms of platinum-catalyzed silicon nanowire growth,” *Semicond. Sci. Technol.*, vol. 31, no. 2, p. 025005, Feb. 2016.
- [10] D. S. Engstrom *et al.*, “High Throughput Nanofabrication of Silicon Nanowire and Carbon Nanotube Tips on AFM Probes by Stencil-Deposited Catalysts,” *Nano Lett.*, vol. 11, no. 4, pp. 1568–1574, Apr. 2011.
- [11] K.-I. Chen, B.-R. Li, and Y.-T. Chen, “Silicon nanowire field-effect transistor-based biosensors for biomedical diagnosis and cellular recording investigation,” *Nano Today*, vol. 6, no. 2, pp. 131–154, Apr. 2011.
- [12] M. Kwiat, S. Cohen, A. Pevzner, and F. Patolsky, “Large-scale ordered 1D-nanomaterials arrays: Assembly or not?,” *Nano Today*, vol. 8, no. 6, pp. 677–694, Dec. 2013.
- [13] A. Solanki and H. Um, “Top-Down Etching of Si Nanowires,” *Semicond.*



- Semimetals*, vol. 98, pp. 71–149, Jan. 2018.
- [14] H. Schmid *et al.*, “Patterned epitaxial vapor-liquid-solid growth of silicon nanowires on Si(111) using silane,” *J. Appl. Phys.*, vol. 103, no. 2, p. 024304, Jan. 2008.
  - [15] D. Roßkopf and S. Strehle, “Surface-controlled contact printing for nanowire device fabrication on a large scale,” *Nanotechnology*, vol. 27, no. 18, p. 185301, May 2016.
  - [16] P. Knittel, N. Hibst, B. Mizaikoff, S. Strehle, and C. Kranz, “Focused ion beam-assisted fabrication of soft high-aspect ratio silicon nanowire atomic force microscopy probes,” *Ultramicroscopy*, vol. 179, pp. 24–32, Aug. 2017.
  - [17] N. Jalili and K. Laxminarayana, “A review of atomic force microscopy imaging systems: application to molecular metrology and biological sciences,” *Mechatronics*, vol. 14, no. 8, pp. 907–945, Oct. 2004.
  - [18] C. L. Cheung, J. H. Hafner, and C. M. Lieber, “Carbon nanotube atomic force microscopy tips: direct growth by chemical vapor deposition and application to high-resolution imaging,” *Proc. Natl. Acad. Sci. U. S. A.*, vol. 97, no. 8, pp. 3809–13, Apr. 2000.
  - [19] A. B. H. Tay and J. T. L. Thong, “Fabrication of super-sharp nanowire atomic force microscope probes using a field emission induced growth technique,” 2004.
  - [20] T. Mikolajick *et al.*, “Silicon nanowires - a versatile technology platform,” *Phys. status solidi - Rapid Res. Lett.*, vol. 7, no. 10, pp. 793–799, Oct. 2013.
  - [21] M. T. Björk, J. Knoch, H. Schmid, H. Riel, and W. Riess, “Silicon nanowire tunneling field-effect transistors,” *Appl. Phys. Lett.*, vol. 92, no. 19, p. 193504, May 2008.
  - [22] N. Singh *et al.*, “Ultra-Narrow Silicon Nanowire Gate-All-Around CMOS Devices: Impact of Diameter, Channel-Oriented and Low Temperature on Device Performance,” in *2006 International Electron Devices Meeting*, 2006, pp. 1–4.
  - [23] V. Schmidt, J. V. Wittemann, and U. Gösele, “Growth, Thermodynamics, and Electrical Properties of Silicon Nanowires <sup>†</sup>,” *Chem. Rev.*, vol. 110, no. 1, pp. 361–388, Jan. 2010.
  - [24] V. Schmidt, J. V. Wittemann, S. Senz, and U. Gösele, “Silicon Nanowires: A Review on Aspects of their Growth and their Electrical Properties,” *Adv. Mater.*, vol. 21, no. 25–26, pp. 2681–2702, Jul. 2009.
  - [25] Z. Huang, N. Geyer, P. Werner, J. de Boor, and U. Gösele, “Metal-Assisted Chemical Etching of Silicon: A Review,” *Adv. Mater.*, vol. 23, no. 2, pp. 285–308, Jan. 2011.
  - [26] Z. Huang, H. Fang, and J. Zhu, “Fabrication of Silicon Nanowire Arrays with Controlled Diameter, Length, and Density,” *Adv. Mater.*, vol. 19, no. 5, pp. 744–748, Mar. 2007.
  - [27] P. Hashemi, L. Gomez, and J. L. Hoyt, “Gate-all-around n-MOSFETs with uniaxial tensile strain-induced performance enhancement scalable to sub-10-nm nanowire diameter,” *IEEE*, vol. 30.4, pp. 401–403, 2009.
  - [28] S. S. Walavalkar, C. E. Hofmann, A. P. Homyk, M. D. Henry, H. A. Atwater, and

- A. Scherer, "Tunable Visible and Near-IR Emission from Sub-10 nm Etched Single-Crystal Si Nanopillars," *Nano Lett.*, vol. 10, no. 11, pp. 4423–4428, Nov. 2010.
- [29] R. G. Hobbs, N. Petkov, and J. D. Holmes, "Semiconductor Nanowire Fabrication by Bottom-Up and Top-Down Paradigms," *Chem. Mater.*, vol. 24, no. 11, pp. 1975–1991, Jun. 2012.
- [30] J. Nakamura, K. Higuchi, and K. Maenaka, "Vertical Si nanowire with ultra-high-aspect-ratio by combined top-down processing technique," *Microsyst. Technol.*, vol. 19, no. 3, pp. 433–438, Mar. 2013.
- [31] B. M. Kayes, M. A. Filler, M. C. Putnam, M. D. Kelzenberg, N. S. Lewis, and H. A. Atwater, "Growth of vertically aligned Si wire arrays over large areas ( $>1\text{cm}^2$ ) with Au and Cu catalysts," *Appl. Phys. Lett.*, vol. 91, no. 10, p. 103110, Sep. 2007.
- [32] Y. Wang, V. Schmidt, S. Senz, and U. Gösele, "Epitaxial growth of silicon nanowires using an aluminium catalyst," *Nat. Nanotechnol.*, vol. 1, no. 3, pp. 186–189, Dec. 2006.
- [33] I. Lombardi, A. I. Hochbaum, P. Yang, C. Carraro, and R. Maboudian, "Synthesis of High Density, Size-Controlled Si Nanowire Arrays via Porous Anodic Alumina Mask," *Chem. Mater.*, vol. 18, no. 4, pp. 988–991, Feb. 2006.
- [34] V. A. Nebol'sin, A. A. Shchetin, A. A. Dolgachev, and V. V. Korneeva, "Effect of the Nature of the Metal Solvent on the Vapor-Liquid-Solid Growth Rate of Silicon Whiskers," *Inorg. Mater.*, vol. 41, no. 12, pp. 1256–1259, Dec. 2005.
- [35] L. Schubert *et al.*, "Silicon nanowhiskers grown on  $\langle 111 \rangle$  Si substrates by molecular-beam epitaxy," *Appl. Phys. Lett.*, vol. 84, no. 24, pp. 4968–4970, Jun. 2004.
- [36] N. Zakharov, P. Werner, L. Sokolov, and U. Gösele, "Growth of Si whiskers by MBE: Mechanism and peculiarities," *Phys. E Low-dimensional Syst. Nanostructures*, vol. 37, no. 1–2, pp. 148–152, Mar. 2007.
- [37] N. D. Zakharov, P. Werner, G. Gerth, L. Schubert, L. Sokolov, and U. Gösele, "Growth phenomena of Si and Si/Ge nanowires on Si (1 1 1) by molecular beam epitaxy," *J. Cryst. Growth*, vol. 290, no. 1, pp. 6–10, Apr. 2006.
- [38] B. Fuhrmann, H. S. Leipner, H.-R. Höche, L. Schubert, P. Werner, and U. Gösele, "Ordered Arrays of Silicon Nanowires Produced by Nanosphere Lithography and Molecular Beam Epitaxy," *Nano Lett.*, vol. 5, no. 12, pp. 2524–2527, Dec. 2005.
- [39] P. Werner, N. D. Zakharov, G. Gerth, L. Schubert, and U. Gösele, "On the formation of Si nanowires by molecular beam epitaxy," *Int. J. Mater. Res.*, vol. 97, no. 7, pp. 1008–1015, Jul. 2006.
- [40] A. M. Morales and C. M. Lieber, "A Laser Ablation Method for the Synthesis of Crystalline Semiconductor Nanowires," *Science (80-. )*, vol. 279, no. 5348, pp. 208–211, Jan. 1998.
- [41] M. . Farnaam and D. . Olander, "The surface chemistry of the thermal cracking of silane on silicon (111)," *Surf. Sci.*, vol. 145, no. 2–3, pp. 390–406, Oct. 1984.

- [42] S. T. Picraux, S. A. Dayeh, P. Manandhar, D. E. Perea, and S. G. Choi, "Silicon and germanium nanowires: Growth, properties, and integration," *JOM*, vol. 62, no. 4, pp. 35–43, Apr. 2010.
- [43] H. Schmid *et al.*, "Patterned epitaxial vapor-liquid-solid growth of silicon nanowires on Si(111) using silane," *J. Appl. Phys.*, vol. 103, no. 2, p. 024304, Jan. 2008.
- [44] H. Okamoto and T. B. Massalski, "The Au–Si (Gold-Silicon) system," *Bull. Alloy Phase Diagrams*, vol. 4, no. 2, pp. 190–198, Sep. 1983.
- [45] W. Lu and C. M. Lieber, "Semiconductor nanowires," *J. Phys. D. Appl. Phys.*, vol. 39, no. 21, pp. R387–R406, Nov. 2006.
- [46] C. O'Regan, S. Biswas, N. Petkov, and J. D. Holmes, "Recent advances in the growth of germanium nanowires: synthesis, growth dynamics and morphology control," *J. Mater. Chem. C*, vol. 2, no. 1, pp. 14–33, Nov. 2014.
- [47] F. Zhuge *et al.*, "Fundamental Strategy for Creating VLS Grown  $\text{TiO}_2$  Single Crystalline Nanowires," *J. Phys. Chem. C*, vol. 116, no. 45, pp. 24367–24372, Nov. 2012.
- [48] V. Purushothaman, V. Ramakrishnan, and K. Jeganathan, "Interplay of VLS and VS growth mechanism for GaN nanowires by a self-catalytic approach," *RSC Adv.*, vol. 2, no. 11, p. 4802, May 2012.
- [49] Y. Wang *et al.*, "Use of Phosphine as an n-Type Dopant Source for Vapor–Liquid–Solid Growth of Silicon Nanowires," *Nano Lett.*, vol. 5, no. 11, pp. 2139–2143, Nov. 2005.
- [50] K. K. Lew *et al.*, "Structural and electrical properties of trimethylboron-doped silicon nanowires," *Appl. Phys. Lett.*, vol. 85, no. 15, pp. 3101–3103, Oct. 2004.
- [51] M. T. Björk, J. Knoch, H. Schmid, H. Riel, and W. Riess, "Silicon nanowire tunneling field-effect transistors," *Appl. Phys. Lett.*, vol. 92, no. 19, p. 193504, May 2008.
- [52] K.-K. Lew and J. M. Redwing, "Growth characteristics of silicon nanowires synthesized by vapor–liquid–solid growth in nanoporous alumina templates," *J. Cryst. Growth*, vol. 254, no. 1–2, pp. 14–22, Jun. 2003.
- [53] Y. Wu, Y. Cui, L. Huynh, C. J. Barrelet, D. C. Bell, and C. M. Lieber, "Controlled Growth and Structures of Molecular-Scale Silicon Nanowires," *Nano Lett.*, vol. 4, no. 3, pp. 433–436, Mar. 2004.
- [54] V. Schmidt, S. Senz, and U. Gösele, "Diameter-Dependent Growth Direction of Epitaxial Silicon Nanowires," *Nano Lett.*, vol. 5, no. 5, pp. 931–935, May 2005.
- [55] R.-Q. Zhang, Y. Lifshitz, and S.-T. Lee, "Oxide-Assisted Growth of Semiconducting Nanowires," *Adv. Mater.*, vol. 15, no. 78, pp. 635–640, Apr. 2003.
- [56] C.-P. Li, C.-S. Lee, X.-L. Ma, N. Wang, R.-Q. Zhang, and S.-T. Lee, "Growth Direction and Cross-Sectional Study of Silicon Nanowires," *Adv. Mater.*, vol. 15, no. 78, pp. 607–609, Apr. 2003.
- [57] S. Ge, K. Jiang, X. Lu, Y. Chen, R. Wang, and S. Fan, "Orientation-Controlled

- Growth of Single-Crystal Silicon-Nanowire Arrays,” *Adv. Mater.*, vol. 17, no. 1, pp. 56–61, Jan. 2005.
- [58] E. I. Givargizov, “Fundamental aspects of VLS growth,” *J. Cryst. Growth*, vol. 31, pp. 20–30, Dec. 1975.
- [59] F. M. Ross, J. Tersoff, and M. C. Reuter, “Sawtooth Faceting in Silicon Nanowires,” *Phys. Rev. Lett.*, vol. 95, no. 14, p. 146104, Sep. 2005.
- [60] J. V. Wittemann, W. Münchgesang, S. Senz, and V. Schmidt, “Silver catalyzed ultrathin silicon nanowires grown by low-temperature chemical-vapor-deposition,” *J. Appl. Phys.*, vol. 107, no. 9, p. 096105, May 2010.
- [61] S. J. Whang, S. J. Lee, W. F. Yang, B. J. Cho, Y. F. Liew, and D. L. Kwong, “Complementary Metal-Oxide-Semiconductor Compatible Al-Catalyzed Silicon Nanowires,” *Electrochem. Solid-State Lett.*, vol. 10, no. 6, p. E11, Jun. 2007.
- [62] M. F. Hainey, X. Zhang, K. Wang, and J. M. Redwing, “Aluminum-Catalyzed Growth of Silicon Nanowires in High-Energy Growth Directions,” *ACS Appl. Nano Mater.*, vol. 1, no. 10, pp. 5493–5499, Oct. 2018.
- [63] Y. Osada, H. Nakayama, M. Shindo, T. Odaka, and Y. Ogata, “Growth and Structure of Silicon Fibers,” *J. Electrochem. Soc.*, vol. 126, no. 1, p. 31, Jan. 1979.
- [64] V. A. Nebol’sin, A. A. Shchetinin, A. A. Dolgachev, and V. V. Korneeva, “Effect of the Nature of the Metal Solvent on the Vapor-Liquid-Solid Growth Rate of Silicon Whiskers,” *Inorg. Mater.*, vol. 41, no. 12, pp. 1256–1259, Dec. 2005.
- [65] C.-Y. Wen, M. C. Reuter, J. Tersoff, E. A. Stach, and F. M. Ross, “Structure, Growth Kinetics, and Ledge Flow during Vapor–Solid–Solid Growth of Copper-Catalyzed Silicon Nanowires,” *Nano Lett.*, vol. 10, no. 2, pp. 514–519, Feb. 2010.
- [66] M. K. Sunkara, S. Sharma, R. Miranda, G. Lian, and E. C. Dickey, “Bulk synthesis of silicon nanowires using a low-temperature vapor–liquid–solid method,” *Appl. Phys. Lett.*, vol. 79, no. 10, pp. 1546–1548, Sep. 2001.
- [67] S. Conesa-Boj *et al.*, “Defect Formation in Ga-Catalyzed Silicon Nanowires,” *Cryst. Growth Des.*, vol. 10, no. 4, pp. 1534–1543, Apr. 2010.
- [68] E. C. Garnett, W. Liang, and P. Yang, “Growth and Electrical Characteristics of Platinum-Nanoparticle-Catalyzed Silicon Nanowires,” *Adv. Mater.*, vol. 19, no. 19, pp. 2946–2950, Oct. 2007.
- [69] N. Hibst, P. Knittel, C. Kranz, B. Mizaikoff, and S. Strehle, “Beam-deposited platinum as versatile catalyst for bottom-up silicon nanowire synthesis,” *Appl. Phys. Lett.*, vol. 105, no. 15, p. 153110, Oct. 2014.
- [70] G. A. Bootsma and H. J. Gassen, “A quantitative study on the growth of silicon whiskers from silane and germanium whiskers from germane,” *J. Cryst. Growth*, vol. 10, no. 3, pp. 223–234, Aug. 1971.
- [71] J. L. Murray and A. J. McAlister, “The Al-Si (Aluminum-Silicon) system,” *Bull. Alloy Phase Diagrams*, vol. 5, no. 1, pp. 74–84, Feb. 1984.
- [72] S. M. Sze and S. M., *Physics of semiconductor devices*. 1981.

- [73] A. A. Shchetinin, V. A. Nebol'sin, O. D. Kozenkov, A. F. Tatarenkov, and A. I. N. E. P. Dunaev, "Distribution coefficient of the initiating impurity and its influence on the electrical resistivity of filamentary silicon crystals," *Inorg. Mater.*, vol. 27, pp. 1137–1139, 1991.
- [74] J. E. Allen *et al.*, "High-resolution detection of Au catalyst atoms in Si nanowires," *Nat. Nanotechnol.*, vol. 3, no. 3, pp. 168–173, Mar. 2008.
- [75] G. Majni and G. Ottaviani, "Large-area uniform growth of  $\langle 100 \rangle$  Si through Al film by solid epitaxy," *Appl. Phys. Lett.*, vol. 31, no. 2, pp. 125–126, Jul. 1977.
- [76] A. Lugstein, M. Steinmair, Y. J. Hyun, E. Bertagnolli, and P. Pongratz, "Ga/Au alloy catalyst for single crystal silicon-nanowire epitaxy," *Appl. Phys. Lett.*, vol. 90, no. 2, p. 023109, Jan. 2007.
- [77] D. E. Perea, N. Li, R. M. Dickerson, A. Misra, and S. T. Picraux, "Controlling Heterojunction Abruptness in VLS-Grown Semiconductor Nanowires via in situ Catalyst Alloying," *Nano Lett.*, vol. 11, no. 8, pp. 3117–3122, Aug. 2011.
- [78] Y.-C. Chou, C.-Y. Wen, M. C. Reuter, D. Su, E. A. Stach, and F. M. Ross, "Controlling the Growth of Si/Ge Nanowires and Heterojunctions Using Silver–Gold Alloy Catalysts," *ACS Nano*, vol. 6, no. 7, pp. 6407–6415, Jul. 2012.
- [79] C.-Y. Wen *et al.*, "Formation of compositionally abrupt axial heterojunctions in silicon-germanium nanowires," *Science*, vol. 326, no. 5957, pp. 1247–50, Nov. 2009.
- [80] Z. Yu *et al.*, "Bi-Sn alloy catalyst for simultaneous morphology and doping control of silicon nanowires in radial junction solar cells," *Appl. Phys. Lett.*, vol. 107, no. 16, p. 163105, Oct. 2015.
- [81] J. L. Gole, J. D. Stout, W. L. Rauch, and Z. L. Wang, "Direct synthesis of silicon nanowires, silica nanospheres, and wire-like nanosphere agglomerates," *Appl. Phys. Lett.*, vol. 76, no. 17, pp. 2346–2348, Apr. 2000.
- [82] B.-S. Kim *et al.*, "Catalyst-free Growth of Single-Crystal Silicon and Germanium Nanowires," *Nano Lett.*, vol. 9, no. 2, pp. 864–869, Feb. 2009.
- [83] G. Gundiah, F. L. Deepak, A. Govindaraj, and C. N. R. Rao, "Carbon-assisted synthesis of silicon nanowires," *Chem. Phys. Lett.*, vol. 381, no. 5–6, pp. 579–583, Nov. 2003.
- [84] S. D. Hutagalung, K. A. Yaacob, and A. F. A. Aziz, "Oxide-assisted growth of silicon nanowires by carbothermal evaporation," *Appl. Surf. Sci.*, vol. 254, no. 2, pp. 633–637, Nov. 2007.
- [85] T. Ishiyama, S. Morishima, Y. Ishii, and M. Fukuda, "Synthesis of silicon nanowires by metal-catalyst-free process," in *14th IEEE International Conference on Nanotechnology*, 2014, pp. 466–469.
- [86] B.-S. Kim *et al.*, "Catalyst-free Growth of Single-Crystal Silicon and Germanium Nanowires," *Nano Lett.*, vol. 9, no. 2, pp. 864–869, Feb. 2009.
- [87] P. Rai-Choudhury, *Handbook of Microlithography, Micromachining, and*

- Microfabrication. Volume 1: Microlithography*. SPIE PRESS, 1997.
- [88] M. Nilsen, F. Port, M. Roos, K.-E. Gottschalk, and S. Strehle, “Facile modification of freestanding silicon nitride microcantilever beams by dry film photoresist lithography,” *J. Micromechanics Microengineering*, vol. 29, no. 2, p. 025014, Feb. 2019.
  - [89] T. Mårtensson, P. Carlberg, M. Borgström, L. Montelius, W. Seifert, and L. Samuelson, “Nanowire Arrays Defined by Nanoimprint Lithography,” *Nano Lett.*, vol. 4, no. 4, pp. 699–702, Apr. 2004.
  - [90] H. J. Fan, P. Werner, and M. Zacharias, “Semiconductor Nanowires: From Self-Organization to Patterned Growth,” *Small*, vol. 2, no. 6, pp. 700–717, Jun. 2006.
  - [91] H. Chik, J. Liang, S. G. Cloutier, N. Kouklin, and J. M. Xu, “Periodic array of uniform ZnO nanorods by second-order self-assembly,” *Appl. Phys. Lett.*, vol. 84, no. 17, pp. 3376–3378, Apr. 2004.
  - [92] Z. H. Wu, X. Y. Mei, D. Kim, M. Blumin, and H. E. Ruda, “Growth of Au-catalyzed ordered GaAs nanowire arrays by molecular-beam epitaxy,” *Appl. Phys. Lett.*, vol. 81, no. 27, pp. 5177–5179, Dec. 2002.
  - [93] D. Grogg, C. Santschi, M. A. F. van den Boogaart, J. Brugger, V. Pott, and A. M. Ionescu, “Nanostencil-based Lithography for Silicon Nanowires Fabrication.” 2005.
  - [94] B. J. Ohlsson, M. T. Björk, M. H. Magnusson, K. Deppert, L. Samuelson, and L. R. Wallenberg, “Size-, shape-, and position-controlled GaAs nano-whiskers,” *Appl. Phys. Lett.*, vol. 79, no. 20, pp. 3335–3337, Nov. 2001.
  - [95] L. Cao, D. N. Barsic, A. R. Guichard, and M. L. Brongersma, “Plasmon-Assisted Local Temperature Control to Pattern Individual Semiconductor Nanowires and Carbon Nanotubes,” *Nano Lett.*, vol. 7, no. 11, pp. 3523–3527, Nov. 2007.
  - [96] O. Englander, D. Christensen, and L. Lin, “Local synthesis of silicon nanowires and carbon nanotubes on microbridges,” *Appl. Phys. Lett.*, vol. 82, no. 26, pp. 4797–4799, Jun. 2003.
  - [97] S. Ryu, E. Kim, D. J. Hwang, and C. P. Grigoropoulos, “Selective and directed growth of silicon nanowires by tip-enhanced local electric field,” *Appl. Phys. A*, vol. 121, no. 1, pp. 255–260, Oct. 2015.
  - [98] K. M. Ryan, A. Mastroianni, K. A. Stancil, H. Liu, and A. P. Alivisatos, “Electric-Field-Assisted Assembly of Perpendicularly Oriented Nanorod Superlattices,” *Nano Lett.*, vol. 6, no. 7, pp. 1479–1482, Jul. 2006.
  - [99] C. H. Lee, D. R. Kim, and X. Zheng, “Orientation-Controlled Alignment of Axially Modulated pn Silicon Nanowires,” *Nano Lett.*, vol. 10, no. 12, pp. 5116–5122, Dec. 2010.
  - [100] R. Yerushalmi, Z. A. Jacobson, J. C. Ho, Z. Fan, and A. Javey, “Large scale, highly ordered assembly of nanowire parallel arrays by differential roll printing,” *Appl. Phys. Lett.*, vol. 91, no. 20, p. 203104, Nov. 2007.
  - [101] A. Javey, Nam, R. S. Friedman, H. Yan, and C. M. Lieber, “Layer-by-Layer

- Assembly of Nanowires for Three-Dimensional, Multifunctional Electronics,” *Nano Lett.*, vol. 7, no. 3, pp. 773–777, Mar. 2007.
- [102] Z. Fan *et al.*, “Wafer-Scale Assembly of Highly Ordered Semiconductor Nanowire Arrays by Contact Printing,” *Nano Lett.*, vol. 8, no. 1, pp. 20–25, Jan. 2008.
- [103] K. Takei *et al.*, “Nanowire active-matrix circuitry for low-voltage macroscale artificial skin,” *Nat. Mater.*, vol. 9, no. 10, pp. 821–826, Oct. 2010.
- [104] J. Yao, H. Yan, and C. M. Lieber, “A nanoscale combing technique for the large-scale assembly of highly aligned nanowires,” *Nat. Nanotechnol.*, vol. 8, no. 5, pp. 329–335, May 2013.
- [105] C. García Núñez, F. Liu, W. T. Navaraj, A. Christou, D. Shakthivel, and R. Dahiya, “Heterogeneous integration of contact-printed semiconductor nanowires for high-performance devices on large areas,” *Microsystems Nanoeng.*, vol. 4, no. 1, p. 22, Dec. 2018.
- [106] G. K. Binnig, “Atomic force microscope and method for imaging surfaces with atomic resolution,” 4724318, 09-Feb-1988.
- [107] G. Binnig, C. F. Quate, and C. Gerber, “Atomic Force Microscope,” *Phys. Rev. Lett.*, vol. 56, no. 9, pp. 930–933, Mar. 1986.
- [108] R. García and R. Pérez, “Dynamic atomic force microscopy methods,” *Surf. Sci. Rep.*, vol. 47, no. 6–8, pp. 197–301, Sep. 2002.
- [109] F. J. Giessibl, “Advances in atomic force microscopy,” *Rev. Mod. Phys.*, vol. 75, no. 3, pp. 949–983, Jul. 2003.
- [110] Y. Seo and W. Jhe, “Atomic force microscopy and spectroscopy,” *Reports Prog. Phys.*, vol. 71, no. 1, p. 016101, Jan. 2008.
- [111] G. Meyer and N. M. Amer, “Simultaneous measurement of lateral and normal forces with an optical-beam-deflection atomic force microscope,” *Appl. Phys. Lett.*, vol. 57, no. 20, pp. 2089–2091, Nov. 1990.
- [112] D. Rugar, H. J. Mamin, and P. Guethner, “Improved fiber-optic interferometer for atomic force microscopy,” *Appl. Phys. Lett.*, vol. 55, no. 25, pp. 2588–2590, Dec. 1989.
- [113] M. Tortonese, R. C. Barrett, and C. F. Quate, “Atomic resolution with an atomic force microscope using piezoresistive detection,” *Appl. Phys. Lett.*, vol. 62, no. 8, pp. 834–836, Feb. 1993.
- [114] C. Kittel, *Introduction to solid state physics*. Wiley, 2005.
- [115] Y. Martin, C. C. Williams, and H. K. Wickramasinghe, “Atomic force microscope—force mapping and profiling on a sub 100-Å scale,” *J. Appl. Phys.*, vol. 61, no. 10, pp. 4723–4729, May 1987.
- [116] J. P. Cleveland, B. Anczykowski, A. E. Schmid, and V. B. Elings, “Energy dissipation in tapping-mode atomic force microscopy,” *Appl. Phys. Lett.*, vol. 72, no. 20, pp. 2613–2615, May 1998.

- 
- [117] A. Rosa-Zeiser, E. Weilandt, S. Hild, and O. Marti, "The simultaneous measurement of elastic, electrostatic and adhesive properties by scanning force microscopy: pulsed-force mode operation," *Meas. Sci. Technol.*, vol. 8, no. 11, pp. 1333–1338, Nov. 1997.
- [118] F. Gaboriaud, B. S. Parcha, M. L. Gee, J. A. Holden, and R. A. Strugnell, "Spatially resolved force spectroscopy of bacterial surfaces using force-volume imaging," *Colloids Surfaces B Biointerfaces*, vol. 62, no. 2, pp. 206–213, Apr. 2008.
- [119] I. Medalsy, U. Hensen, and D. J. Muller, "Imaging and Quantifying Chemical and Physical Properties of Native Proteins at Molecular Resolution by Force-Volume AFM," *Angew. Chemie Int. Ed.*, vol. 50, no. 50, pp. 12103–12108, Dec. 2011.
- [120] B. Pittenger, N. Erina, and C. Su, "Mechanical Property Mapping at the Nanoscale Using PeakForce QNM Scanning Probe Technique," 2014, pp. 31–51.
- [121] T. Boland and B. D. Ratner, "Direct measurement of hydrogen bonding in DNA nucleotide bases by atomic force microscopy," *Proc. Natl. Acad. Sci. U. S. A.*, vol. 92, no. 12, pp. 5297–301, Jun. 1995.
- [122] H. G. Hansma *et al.*, "Recent advances in atomic force microscopy of DNA," *Scanning*, vol. 15, no. 5, pp. 296–299, 1993.
- [123] G. Lee, L. Chrisey, and R. Colton, "Direct measurement of the forces between complementary strands of DNA," *Science (80-. )*, vol. 266, no. 5186, pp. 771–773, Nov. 1994.
- [124] S. B. Smith, Y. Cui, and C. Bustamante, "Overstretching B-DNA: The Elastic Response of Individual Double-Stranded and Single-Stranded DNA Molecules," *Science (80-. )*, vol. 271, no. 5250, pp. 795–799, Feb. 1996.
- [125] T. R. Strick, J.-F. Allemand, D. Bensimon, A. Bensimon, and V. Croquette, "The Elasticity of a Single Supercoiled DNA Molecule," *Science (80-. )*, vol. 271, no. 5257, pp. 1835–1837, Mar. 1996.
- [126] M. Ludwig *et al.*, "AFM, a tool for single-molecule experiments," *Appl. Phys. A Mater. Sci. Process.*, vol. 68, no. 2, pp. 173–176, Feb. 1999.
- [127] P. E. Marszalek, A. F. Oberhauser, Y.-P. Pang, and J. M. Fernandez, "Polysaccharide elasticity governed by chair–boat transitions of the glucopyranose ring," *Nature*, vol. 396, no. 6712, pp. 661–664, Dec. 1998.
- [128] M. Rief, M. Gautel, F. Oesterhelt, J. M. Fernandez, and H. E. Gaub, "Reversible Unfolding of Individual Titin Immunoglobulin Domains by AFM," *Science (80-. )*, vol. 276, no. 5315, pp. 1109–1112, May 1997.
- [129] M. Rief, J. M. Fernandez, and H. E. Gaub, "Elastically Coupled Two-Level Systems as a Model for Biopolymer Extensibility," *Phys. Rev. Lett.*, vol. 81, no. 21, pp. 4764–4767, Nov. 1998.
- [130] P. E. Marszalek, Y. P. Pang, H. Li, J. El Yazal, A. F. Oberhauser, and J. M. Fernandez, "Atomic levers control pyranose ring conformations," *Proc. Natl. Acad. Sci. U. S. A.*, vol. 96, no. 14, pp. 7894–8, Jul. 1999.



- [131] K. Nakajima *et al.*, “Nano-palpatation AFM and its quantitative mechanical property mapping,” *Microscopy*, vol. 63, no. 3, pp. 193–208, Jun. 2014.
- [132] A. Caron, “Quantitative Hardness Measurement by Instrumented AFM-indentation,” *J. Vis. Exp.*, no. 117, 2016.
- [133] R. Ferencz, J. Sanchez, B. Blümich, and W. Herrmann, “AFM nanoindentation to determine Young’s modulus for different EPDM elastomers,” *Polym. Test.*, vol. 31, no. 3, pp. 425–432, May 2012.
- [134] M. Toader, H. Fiedler, S. Hermann, S. E. Schulz, T. Gessner, and M. Hietschold, “Conductive AFM for CNT characterization,” *Nanoscale Res. Lett.*, vol. 8, no. 1, p. 24, Jan. 2013.
- [135] J. Alvarez *et al.*, “Conductive-probe atomic force microscopy characterization of silicon nanowire,” *Nanoscale Res. Lett.*, vol. 6, no. 1, p. 110, Dec. 2011.
- [136] M. Lanza, *Conductive atomic force microscopy: applications in nanomaterials*. Wiley-VCH, 2017.
- [137] A. J. Bard, F. R. F. Fan, J. Kwak, and O. Lev, “Scanning electrochemical microscopy. Introduction and principles,” *Anal. Chem.*, vol. 61, no. 2, pp. 132–138, Jan. 1989.
- [138] A. N. Patel and C. Kranz, “(Multi)functional Atomic Force Microscopy Imaging,” *Annu. Rev. Anal. Chem.*, vol. 11, no. 1, pp. 329–350, Jun. 2018.
- [139] D. Polcari, P. Dauphin-Ducharme, and J. Mauzeroll, “Scanning Electrochemical Microscopy: A Comprehensive Review of Experimental Parameters from 1989 to 2015,” *Chem. Rev.*, vol. 116, no. 22, pp. 13234–13278, Nov. 2016.
- [140] J. Shirakashi, K. Matsumoto, N. Miura, and M. Konagai, “Single-Electron Transistors (SETs) with Nb/Nb Oxide System Fabricated by Atomic Force Microscope (AFM) Nano-Oxidation Process,” *Jpn. J. Appl. Phys.*, vol. 36, no. Part 2, No. 9A/B, pp. L1257–L1260, Sep. 1997.
- [141] P. M. Campbell, E. S. Snow, and P. J. McMarr, “AFM-based fabrication of Si nanostructures,” *Phys. B Condens. Matter*, vol. 227, no. 1–4, pp. 315–317, Sep. 1996.
- [142] E. S. Snow and P. M. Campbell, “Fabrication of Si nanostructures with an atomic force microscope,” *Appl. Phys. Lett.*, vol. 64, no. 15, pp. 1932–1934, Apr. 1994.
- [143] H. Sugimura, T. Uchida, N. Kitamura, and H. Masuhara, “Scanning tunneling microscope tip-induced anodization of titanium: Characterization of the modified surface and application to the metal resist process for nanolithography,” *J. Vac. Sci. Technol. B Microelectron. Nanom. Struct.*, vol. 12, no. 5, p. 2884, Sep. 1994.
- [144] S. Sasa, T. Ikeda, M. Akahori, A. Kajiuchi, and M. Inoue, “Novel Nanofabrication Process for InAs/AlGaSb Heterostructures Utilizing Atomic Force Microscope Oxidation,” *Jpn. J. Appl. Phys.*, vol. 38, no. Part 1, No. 2B, pp. 1064–1066, Feb. 1999.
- [145] Y. Okada, S. Amano, M. Kawabe, B. N. Shimbo, and J. S. Harris, “Nanoscale

- oxidation of GaAs-based semiconductors using atomic force microscope,” *J. Appl. Phys.*, vol. 83, no. 4, pp. 1844–1847, Feb. 1998.
- [146] K. Matsumoto, “Room temperature operated single electron transistor made by STM/AFM nano-oxidation process,” *Phys. B Condens. Matter*, vol. 227, no. 1–4, pp. 92–94, Sep. 1996.
- [147] S. Sasa, S. Yodogawa, A. Ohya, and M. Inoue, “A Single-Electron Transistor Produced by Nanoscale Oxidation of InAs,” *Jpn. J. Appl. Phys.*, vol. 40, no. Part 1, No. 3B, pp. 2026–2028, Mar. 2001.
- [148] B. Huang, M. Bates, and X. Zhuang, “Super-Resolution Fluorescence Microscopy,” *Annu. Rev. Biochem.*, vol. 78, no. 1, pp. 993–1016, Jun. 2009.
- [149] M. F. Garcia-Parajo, “Optical antennas focus in on biology,” *Nat. Photonics*, vol. 2, no. 4, pp. 201–203, Apr. 2008.
- [150] T. Schmid, B.-S. Yeo, G. Leong, J. Stadler, and R. Zenobi, “Performing tip-enhanced Raman spectroscopy in liquids,” *J. Raman Spectrosc.*, vol. 40, no. 10, pp. 1392–1399, Oct. 2009.
- [151] A. Nakata, T. Nomoto, T. Toyota, and M. Fujinami, “Tip-enhanced Raman Spectroscopy of Lipid Bilayers in Water with an Alumina- and Silver-coated Tungsten Tip,” *Anal. Sci.*, vol. 29, no. 9, pp. 865–869, Sep. 2013.
- [152] G. Haugstad, *Atomic force microscopy : understanding basic modes and advanced applications*. .
- [153] B. Voigtländer, “Technical Aspects of Scanning Probe Microscopy,” 2015, pp. 31–63.
- [154] S. C. Tan, H. Zhao, and C. V. Thompson, “Fabrication of high aspect ratio AFM probes with different materials inspired by TEM ‘lift-out’ method,” *J. Vac. Sci. Technol. B, Nanotechnol. Microelectron. Mater. Process. Meas. Phenom.*, vol. 34, no. 5, p. 051805, Sep. 2016.
- [155] D. P. Burt, N. R. Wilson, J. M. R. Weaver, P. S. Dobson, and J. V. Macpherson, “Nanowire Probes for High Resolution Combined Scanning Electrochemical Microscopy – Atomic Force Microscopy,” 2005.
- [156] A. Boisen, O. Hansen, and S. Bouwstra, “AFM probes with directly fabricated tips,” *J. Micromechanics Microengineering*, vol. 6, no. 1, pp. 58–62, Mar. 1996.
- [157] A. Slattery, C. Shearer, J. Shapter, J. Quinton, and C. Gibson, “Solution Based Methods for the Fabrication of Carbon Nanotube Modified Atomic Force Microscopy Probes,” *Nanomaterials*, vol. 7, no. 11, p. 346, Oct. 2017.
- [158] H. Dai, J. H. Hafner, A. G. Rinzler, D. T. Colbert, and R. E. Smalley, “Nanotubes as nanoprobe in scanning probe microscopy,” *Nature*, vol. 384, no. 6605, pp. 147–150, Nov. 1996.
- [159] \* Liwei Chen, Chin Li Cheung, and Paul D. Ashby, and C. M. Lieber, “Single-Walled Carbon Nanotube AFM Probes: Optimal Imaging Resolution of Nanoclusters and Biomolecules in Ambient and Fluid Environments,” 2004.

- [160] H. Nishijima, S. Akita, and Y. Nakayama, “Novel Process for Fabricating Nanodevices Consisting of Carbon Nanotubes,” *Jpn. J. Appl. Phys.*, vol. 38, no. Part 1, No. 12B, pp. 7247–7252, Dec. 1999.
- [161] K. Carlson *et al.*, “A carbon nanofibre scanning probe assembled using an electrothermal microgripper,” *Nanotechnology*, vol. 18, no. 34, p. 345501, Aug. 2007.
- [162] C. V Nguyen, Q. Ye, and M. Meyyappan, “Carbon nanotube tips for scanning probe microscopy: fabrication and high aspect ratio nanometrology,” *Meas. Sci. Technol.*, vol. 16, no. 11, pp. 2138–2146, Nov. 2005.
- [163] X. Ma *et al.*, “Sharp-Tip Silver Nanowires Mounted on Cantilevers for High-Aspect-Ratio High-Resolution Imaging,” *Nano Lett.*, vol. 16, no. 11, pp. 6896–6902, Nov. 2016.
- [164] S. H. Christiansen *et al.*, “Signal enhancement in nano-Raman spectroscopy by gold caps on silicon nanowires obtained by vapour–liquid–solid growth,” *Nanotechnology*, vol. 18, no. 3, p. 035503, Jan. 2007.
- [165] S. T. Jäger, “Herstellung und Untersuchung von Silizium-Nanodrahten fuer Solarzellen und andere optische Anwendungen,” Ulm University, 2015.
- [166] C. S. and B. O. Bede Pittenger, Natalia Erina, “Quantitative Mechanical Property Mapping at the Nanoscale with PeakForce QNM | Microscopy and Analysis,” *Bruker Appl.*, 2011. [Online]. Available: [https://www.bruker.com/fileadmin/user\\_upload/8-PDF-Docs/SurfaceAnalysis/AFM/ApplicationNotes/AN128-RevB0-Quantitative\\_Mechanical\\_Property\\_Mapping\\_at\\_the\\_Nanoscale\\_with\\_PeakForceQNM-AppNote.pdf](https://www.bruker.com/fileadmin/user_upload/8-PDF-Docs/SurfaceAnalysis/AFM/ApplicationNotes/AN128-RevB0-Quantitative_Mechanical_Property_Mapping_at_the_Nanoscale_with_PeakForceQNM-AppNote.pdf). [Accessed: 09-Jul-2018].
- [167] J. H. Hafner, C. L. Cheung, A. T. Woolley, and C. M. Lieber, “Structural and functional imaging with carbon nanotube AFM probes,” *Prog. Biophys. Mol. Biol.*, vol. 77, no. 1, pp. 73–110, 2001.
- [168] Q. Ye, A. M. Cassell, H. Liu, K. J. Chao, J. Han, and M. Meyyappan, “Large-scale fabrication of carbon nanotube probe tips for atomic force microscopy critical dimension imaging applications,” *Nano Lett.*, vol. 4, no. 7, pp. 1301–1308, Jul. 2004.
- [169] M. Radmacher, M. Fritz, and P. K. Hansma, “Imaging soft samples with the atomic force microscope: gelatin in water and propanol,” *Biophys. J.*, vol. 69, no. 1, pp. 264–270, Jul. 1995.
- [170] K. K. M. Sweers, K. O. van der Werf, M. L. Bennink, and V. Subramaniam, “Spatially resolved frequency-dependent elasticity measured with pulsed force microscopy and nanoindentation,” *Nanoscale*, vol. 4, no. 6, p. 2072, Mar. 2012.
- [171] H. Kim *et al.*, “Tensile properties of millimeter-long multi-walled carbon nanotubes,” *Sci. Rep.*, vol. 7, no. 1, p. 9512, Dec. 2017.
- [172] J. Li, J. Xie, W. Xue, and D. Wu, “Fabrication of cantilever with self-sharpening nano-silicon-tip for AFM applications,” *Microsyst. Technol.*, vol. 19, no. 2, pp. 285–290, Feb. 2013.
- [173] Q. Yu, G. Qin, C. Darne, C. Cai, W. Wosik, and S.-S. Pei, “Fabrication of short and

- thin silicon cantilevers for AFM with SOI wafers,” *Sensors Actuators A Phys.*, vol. 126, no. 2, pp. 369–374, Feb. 2006.
- [174] P. J. Holmes and P. Handler, “The Electrochemistry of Semiconductors,” *J. Electrochem. Soc.*, vol. 109, no. 8, p. 228C, Aug. 1962.
- [175] H. Seidel, L. Csepregi, A. Heuberger, and H. Baumgärtel, “Anisotropic Etching of Crystalline Silicon in Alkaline Solutions,” *J. Electrochem. Soc.*, vol. 137, no. 11, p. 3612, Nov. 1990.
- [176] O. Powell and H. B. Harrison, “Anisotropic etching of {100} and {110} planes in (100) silicon,” *J. Micromechanics Microengineering*, vol. 11, no. 3, pp. 217–220, May 2001.
- [177] R. J. (Raymond J. Roark, W. C. (Warren C. Young, R. G. (Richard G. Budynas, and A. M. Sadegh, *Roark’s formulas for stress and strain*. McGraw-Hill, 2012.
- [178] S. C. Minne, S. R. Manalis, and C. F. Quate, “Parallel atomic force microscopy using cantilevers with integrated piezoresistive sensors and integrated piezoelectric actuators,” *Appl. Phys. Lett.*, vol. 67, p. 3918, 1995.
- [179] H. J. Quenzer, U. Drechsler, A. Sebastian, S. Marauska, B. Wagner, and M. Despont, “Fabrication of conducting AFM cantilevers with AlN-based piezoelectric actuators,” in *Procedia Engineering*, 2011, vol. 25, pp. 665–668.
- [180] P. Hess, “The mechanical properties of various chemical vapor deposition diamond structures compared to the ideal single crystal,” *Journal of Applied Physics*, vol. 111, no. 5. 01-Mar-2012.
- [181] R. L. Edwards, G. Coles, and W. N. Sharpe, “Comparison of tensile and bulge tests for thin-film silicon nitride,” *Exp. Mech.*, vol. 44, no. 1, pp. 49–54, Feb. 2004.
- [182] L. Kiesewetter, J.-M. Zhang, D. Houdeau, and A. Steckenborn, “Determination of Young’s moduli of micromechanical thin films using the resonance method,” *Sensors Actuators A Phys.*, vol. 35, no. 2, pp. 153–159, Dec. 1992.
- [183] T. Yoshioka, T. Ando, M. Shikida, and K. Sato, “Tensile testing of SiO<sub>2</sub> and Si<sub>3</sub>N<sub>4</sub> films carried out on a silicon chip,” *Sensors Actuators A Phys.*, vol. 82, no. 1–3, pp. 291–296, May 2000.
- [184] T. F. Retajczyk and A. K. Sinha, “Elastic stiffness and thermal expansion coefficients of various refractory silicides and silicon nitride films,” *Thin Solid Films*, vol. 70, no. 2, pp. 241–247, Aug. 1980.
- [185] C. Serre, P. Gorostiza, A. Pérez-Rodríguez, F. Sanz, and J. R. Morante, “Measurement of micromechanical properties of polysilicon microstructures with an atomic force microscope,” *Sensors Actuators A Phys.*, vol. 67, no. 1–3, pp. 215–219, May 1998.
- [186] C. Serre, A. Pérez-Rodríguez, J. R. Morante, P. Gorostiza, and J. Esteve, “Determination of micromechanical properties of thin films by beam bending measurements with an atomic force microscope,” *Sensors Actuators A Phys.*, vol. 74, no. 1–3, pp. 134–138, Apr. 1999.

- [187] E. Obermeier, "Mechanical and Thermophysical Properties of Thin Film Materials for MemS: Techniques and Devices," *MRS Online Proc. Libr. Arch.*, vol. 444, 1996.
- [188] D. Sarid, *Scanning force microscopy : with applications to electric, magnetic, and atomic forces*. Oxford University Press, 1994.
- [189] A. Khan, J. Philip, and P. Hess, "Young's modulus of silicon nitride used in scanning force microscope cantilevers," *J. Appl. Phys.*, vol. 95, no. 4, pp. 1667–1672, Feb. 2004.
- [190] H. Guo and A. Lal, "Characterization of micromachined silicon nitride membrane using resonant ultrasound spectroscopy," *Proc. IEEE Ultrason. Symp.*, vol. 2, pp. 863–866, 2001.
- [191] T. Y. Zhang, Y. J. Su, C. F. Qian, M. H. Zhao, and L. Q. Chen, "Microbridge testing of silicon nitride thin films deposited on silicon wafers," *Acta Mater.*, vol. 48, no. 11, pp. 2843–2857, Jun. 2000.
- [192] "The Euler-Bernoulli and Timoshenko Theories," in *Beam Structures*, Chichester, UK: John Wiley & Sons, Ltd, 2011, pp. 9–22.
- [193] T. Iwinski and B. G. Neal, *Theory of Beams : the Application of the Laplace Transformation Method to Engineering Problems*. Elsevier Science, 1967.
- [194] R. Huszank, L. Csedreki, Z. Kertész, and Z. Török, "Determination of the density of silicon–nitride thin films by ion-beam analytical techniques (RBS, PIXE, STIM)," *J. Radioanal. Nucl. Chem.*, vol. 307, no. 1, pp. 341–346, Jan. 2016.
- [195] A. Markwitz, H. Baumann, E. F. Krimmel, K. Bethge, and P. Misaelides, "Characterisation of thin sputtered silicon nitride films by NRA, ERDA, RBS and SEM," *Fresenius. J. Anal. Chem.*, vol. 346, no. 1–3, pp. 177–180, Jan. 1993.
- [196] T. Kawashima *et al.*, "Control of Surface Migration of Gold Particles on Si Nanowires," *Nano Lett.*, vol. 8, no. 1, pp. 362–368, Jan. 2008.
- [197] R. S. Wagner and C. J. Ooherty, "Mechanism of Branching and Kinking during VLS Crystal Growth," *J. Electrochem. Soc.*, vol. 115, no. 1, p. 93, Jan. 1968.
- [198] J. Westwater, D. P. Gosain, S. Tomiya, S. Usui, and H. Ruda, "Growth of silicon nanowires via gold/silane vapor–liquid–solid reaction," *J. Vac. Sci. Technol. B Microelectron. Nanom. Struct.*, vol. 15, no. 3, p. 554, May 1997.
- [199] Z. He, H. T. Nguyen, L. Duc Toan, and D. Pribat, "A detailed study of kinking in indium-catalyzed silicon nanowires," *CrystEngComm*, vol. 17, no. 33, pp. 6286–6296, Aug. 2015.
- [200] "Introduction to Microfabrication, 2nd Edition | Wiley." [Online]. Available: <https://www.wiley.com/en-us/Introduction+to+Microfabrication%2C+2nd+Edition-p-9780470749838>. [Accessed: 04-Nov-2019].
- [201] H. Schmid *et al.*, "Patterned epitaxial vapor-liquid-solid growth of silicon nanowires on Si(111) using silane," *J. Appl. Phys.*, vol. 103, no. 2, p. 024304, Jan. 2008.
- [202] Z. Cui, *Micro-nanofabrication : technologies and applications / Zheng Cui.* -

- Version details - Trove*. Beijing: Higher Education Press, 2005.
- [203] H. S. Dow, W. S. Kim, and J. W. Lee, “Thermal and electrical properties of silicon nitride substrates,” *AIP Adv.*, vol. 7, no. 9, p. 095022, Sep. 2017.
- [204] J. Cognard, “Adhesion to gold: A review,” *Gold Bull.*, vol. 17, no. 4, pp. 131–139, Dec. 1984.
- [205] B. Voigtländer, “Technical Aspects of Atomic Force Microscopy (AFM),” 2015, pp. 157–175.
- [206] F. Golek, P. Mazur, Z. Ryszka, and S. Zuber, “AFM image artifacts,” *Appl. Surf. Sci.*, vol. 304, pp. 11–19, Jun. 2014.
- [207] J. I. Paredes, A. Martinez-Alonso, and J. M. D. Tascon, “Adhesion artefacts in atomic force microscopy imaging,” *J. Microsc.*, vol. 200, no. 2, pp. 109–113, Nov. 2000.
- [208] B. N. J. Persson, O. Albohr, U. Tartaglino, A. I. Volokitin, and E. Tosatti, “On the nature of surface roughness with application to contact mechanics, sealing, rubber friction and adhesion,” *J. Phys. Condens. Matter*, vol. 17, no. 1, pp. R1–R62, Jan. 2005.
- [209] T. D. B. Jacobs, T. Junge, and L. Pastewka, “Quantitative characterization of surface topography using spectral analysis,” *Surf. Topogr. Metrol. Prop.*, vol. 5, no. 1, p. 013001, Jan. 2017.
- [210] E. Sidick, “Power spectral density specification and analysis of large optical surfaces,” 2009, vol. 7390, p. 73900L.
- [211] A. Duparré, J. Ferre-Borrull, S. Gliech, G. Notni, J. Steinert, and J. M. Bennett, “Surface characterization techniques for determining the root-mean-square roughness and power spectral densities of optical components,” *Appl. Opt.*, vol. 41, no. 1, p. 154, Jan. 2002.
- [212] M. A. Hopcroft, W. D. Nix, and T. W. Kenny, “What is the Young’s Modulus of Silicon?,” *J. Microelectromechanical Syst.*, vol. 19, no. 2, pp. 229–238, Apr. 2010.
- [213] A. Furmanchuk, O. Isayev, T. C. Dinadayalane, D. Leszczynska, and J. Leszczynski, “Mechanical properties of silicon nanowires,” *Wiley Interdiscip. Rev. Comput. Mol. Sci.*, vol. 2, no. 6, pp. 817–828, Nov. 2012.
- [214] Y. Zhu, F. Xu, Q. Qin, W. Y. Fung, and W. Lu, “Mechanical Properties of Vapor–Liquid–Solid Synthesized Silicon Nanowires,” *Nano Lett.*, vol. 9, no. 11, pp. 3934–3939, Nov. 2009.
- [215] H. Sadeghian *et al.*, “Characterizing size-dependent effective elastic modulus of silicon nanocantilevers using electrostatic pull-in instability,” *Appl. Phys. Lett.*, vol. 94, no. 22, p. 221903, Jun. 2009.
- [216] B. Lee and R. E. Rudd, “First-principles calculation of mechanical properties of Si(001) nanowires and comparison to nanomechanical theory,” *Phys. Rev. B*, vol. 75, no. 19, p. 195328, May 2007.
- [217] Y. E. Yaish, Y. Calahorra, O. Shtempluck, and V. Kotchetkov, “Three-point bending

- analysis of doubly clamped silicon nanowire beams; Young's modulus, initial stress, and crystal orientation," *J. Appl. Phys.*, vol. 117, no. 16, p. 164311, Apr. 2015.
- [218] M. J. Gordon, T. Baron, F. Dhalluin, P. Gentile, and P. Ferret, "Size Effects in Mechanical Deformation and Fracture of Cantilevered Silicon Nanowires," *Nano Lett.*, vol. 9, no. 2, pp. 525–529, Feb. 2009.
- [219] A. Heidelberg *et al.*, "A generalized description of the elastic properties of nanowires," *Nano Lett.*, vol. 6, no. 6, pp. 1101–1106, Jun. 2006.
- [220] Y. Hwangbo, J. M. Park, W. L. Brown, J. H. Goo, H. J. Lee, and S. Hyun, "Effect of deposition conditions on thermo-mechanical properties of free standing silicon-rich silicon nitride thin film," *Microelectron. Eng.*, vol. 95, pp. 34–41, Jul. 2012.
- [221] B. Voigtländer, "Scanning Probe Microscopy Designs," 2015, pp. 65–76.
- [222] B. Voigtländer, *Scanning Probe Microscopy*. Berlin, Heidelberg: Springer Berlin Heidelberg, 2015.
- [223] B. Pittenger, N. Erina, and C. Su, "Quantitative mechanical property mapping at the nanoscale with PeakForce QNM," *Bruker Appl.*, 2010.
- [224] J. Körner, "A highly sensitive co-resonant cantilever sensor for materials research: Application to nanomaterial characterization," *J. Mater. Res.*, vol. 33, no. 17, pp. 2504–2514, Sep. 2018.
- [225] I. Henins, "Precision density measurement of silicon," *J. Res. Natl. Bur. Stand. Sect. A Phys. Chem.*, vol. 68A, no. 5, p. 529, Sep. 1964.
- [226] G. E. Fantner *et al.*, "Components for high speed atomic force microscopy," *Ultramicroscopy*, vol. 106, no. 8–9, pp. 881–887, Jun. 2006.
- [227] A. D. Slattey, A. J. Blanch, J. S. Quinton, and C. T. Gibson, "Efficient attachment of carbon nanotubes to conventional and high-frequency AFM probes enhanced by electron beam processes," *Nanotechnology*, vol. 24, no. 23, p. 235705, Jun. 2013.
- [228] A. P. Nievergelt, J. D. Adams, P. D. Odermatt, and G. E. Fantner, "High-frequency multimodal atomic force microscopy," *Beilstein J. Nanotechnol.*, vol. 5, pp. 2459–67, 2014.
- [229] G. E. Fantner, R. J. Barbero, D. S. Gray, and A. M. Belcher, "Kinetics of antimicrobial peptide activity measured on individual bacterial cells using high-speed atomic force microscopy," *Nat. Nanotechnol.*, vol. 5, no. 4, pp. 280–285, Apr. 2010.
- [230] A. Raman, J. Melcher, and R. Tung, "Cantilever dynamics in atomic force microscopy," *Nano Today*, vol. 3, no. 1–2, pp. 20–27, Feb. 2008.
- [231] S. H. Crandall, "The role of damping in vibration theory," *J. Sound Vib.*, vol. 11, no. 1, pp. 3-IN1, Jan. 1970.
- [232] M. Martínez Rodríguez, "Analysis of structural damping," 2006.
- [233] "Properties: A Background to Silicon and its Applications." [Online]. Available: <https://www.azom.com/properties.aspx?ArticleID=599>. [Accessed: 08-Jun-2019].

- [234] “Properties: Silicon Nitride (Si<sub>3</sub>N<sub>4</sub>) Properties and Applications.” [Online]. Available: <https://www.azom.com/properties.aspx?ArticleID=53>. [Accessed: 08-Jun-2019].
- [235] A. Perez-Cruz, A. Dominguez-Gonzalez, I. Stiharu, and R. A. Osornio-Rios, “Optimization of Q-factor of AFM cantilevers using genetic algorithms,” *Ultramicroscopy*, vol. 115, pp. 61–67, Apr. 2012.
- [236] A. Varol, I. Gunev, B. Orun, and C. Basdogan, “Numerical simulation of nano scanning in intermittent-contact mode AFM under  $Q$  control,” *Nanotechnology*, vol. 19, no. 7, p. 075503, Feb. 2008.
- [237] Y.-J. Hung, S.-L. Lee, B. J. Thibeault, and L. A. Coldren, “Fabrication of Highly Ordered Silicon Nanowire Arrays With Controllable Sidewall Profiles for Achieving Low-Surface Reflection,” *IEEE J. Sel. Top. Quantum Electron.*, vol. 17, no. 4, pp. 869–877, Jul. 2011.
- [238] S. Kim, D. J. Hill, C. W. Pinion, J. D. Christesen, J. R. McBride, and J. F. Cahoon, “Designing Morphology in Epitaxial Silicon Nanowires: The Role of Gold, Surface Chemistry, and Phosphorus Doping,” *ACS Nano*, vol. 11, no. 5, pp. 4453–4462, May 2017.
- [239] J. D. Plummer, *Silicon VLSI technology: fundamentals, practice and modeling*. Dorling Kindersley, 2009.
- [240] F. Dadabhai, F. Gaspari, S. Zukotynski, and C. Bland, “Reduction of silicon dioxide by aluminum in metal–oxide–semiconductor structures,” *J. Appl. Phys.*, vol. 80, no. 11, p. 6505, Jun. 1998.
- [241] W. Xu and S. Zukotynski, “Failure of Al-SiO<sub>2</sub>-Si MOS Capacitors at High Temperatures,” *J. Electrochem. Soc.*, vol. 140, no. 7, p. 2063, Jul. 1993.
- [242] R. B. Godfrey and M. A. Green, “High-temperature lifetesting of Al/SiO<sub>x</sub>/p-Si contacts for MIS solar cells,” *Appl. Phys. Lett.*, vol. 34, no. 12, pp. 860–861, Jun. 1979.
- [243] M. Hoch, “The ternary system aluminum-gold-silicon,” *J. Alloys Compd.*, vol. 220, no. 1–2, pp. 27–31, Apr. 1995.
- [244] X. S. Ning, T. Okamoto, Y. Miyamoto, A. Koreeda, and K. Suganuma, “Reaction chemistry at joined interfaces between silicon nitride and aluminium,” *J. Mater. Sci.*, vol. 26, no. 15, pp. 4142–4149, Aug. 1991.
- [245] X. S. Ning, K. Suganuma, M. Morita, and T. Okamoto, “Interfacial reaction between silicon nitride and aluminium,” *Philos. Mag. Lett.*, vol. 55, no. 3, pp. 93–97, Mar. 1987.
- [246] J. L. Murray, H. Okamoto, and T. B. Massalski, “The Al–Au (Aluminum-gold) system,” *Bull. Alloy Phase Diagrams*, vol. 8, no. 1, pp. 20–30, Feb. 1987.
- [247] J. L. Murray and A. J. McAlister, “The Al–Si (Aluminum-Silicon) system,” *Bull. Alloy Phase Diagrams*, vol. 5, no. 1, pp. 74–84, Feb. 1984.
- [248] C. A. and E. of the L. V. III/17A-22A-41A1b, “Silicon (Si), lattice parameter,



- thermal expansion,” in *Group IV Elements, IV-IV and III-V Compounds. Part b - Electronic, Transport, Optical and Other Properties*, Berlin/Heidelberg: Springer-Verlag, pp. 1–17.
- [249] M. J. Bierman and S. Jin, “Potential applications of hierarchical branching nanowires in solar energy conversion,” *Energy Environ. Sci.*, vol. 2, no. 10, p. 1050, Sep. 2009.
- [250] D. Wang, F. Qian, C. Yang, Z. Zhong, and C. M. Lieber, “Rational Growth of Branched and Hyperbranched Nanowire Structures,” *Nano Lett.*, vol. 4, no. 5, pp. 871–874, 2004.
- [251] T. A. Celano *et al.*, “Capillarity-Driven Welding of Semiconductor Nanowires for Crystalline and Electrically Ohmic Junctions,” *Nano Lett.*, vol. 16, no. 8, pp. 5241–5246, Aug. 2016.
- [252] S. Sharma, T. I. Kamins, and R. S. Williams, “Synthesis of thin silicon nanowires using gold-catalyzed chemical vapor deposition,” *Appl. Phys. A*, vol. 80, no. 6, pp. 1225–1229, Mar. 2005.
- [253] C.-Y. Meng, B.-L. Shih, and S.-C. Lee, “Silicon nanowires synthesized by vapor–liquid–solid growth on excimer laser annealed thin gold film,” *J. Nanoparticle Res.*, vol. 9, no. 4, pp. 657–660, May 2007.
- [254] H. Jeong, T. E. Park, H. K. Seong, M. Kim, U. Kim, and H. J. Choi, “Growth kinetics of silicon nanowires by platinum assisted vapour–liquid–solid mechanism,” *Chem. Phys. Lett.*, vol. 467, no. 4–6, pp. 331–334, Jan. 2009.
- [255] S. M. Sze and K. K. Ng, *Physics of semiconductor devices*. Wiley-Interscience, 2007.
- [256] C. Jacoboni, C. Canali, G. Ottaviani, and A. Alberigi Quaranta, “A review of some charge transport properties of silicon,” *Solid State Electron.*, vol. 20, no. 2, pp. 77–89, Feb. 1977.
- [257] J. M. Dorkel and P. Leturcq, “Carrier mobilities in silicon semi-empirically related to temperature, doping and injection level,” *Solid State Electron.*, vol. 24, no. 9, pp. 821–825, Sep. 1981.
- [258] B. C. Joshi, G. Eranna, D. P. Runthala, B. B. Dixit, O. P. Wadhawan, and P. D. Vyas, “LPCVD and PECVD silicon nitride for microelectronics technology,” *IJEMS Vol.07(5-6) [October-December 2000]*, vol. 7, no. 5–6, pp. 303–309, 2000.
- [259] H. Liu and D. S. Dandy, “Studies on nucleation process in diamond CVD: an overview of recent developments,” *Diam. Relat. Mater.*, vol. 4, no. 10, pp. 1173–1188, Sep. 1995.
- [260] G. S. Sandhu and W. K. Chu, “Reactive ion etching of diamond,” *Appl. Phys. Lett.*, vol. 55, no. 5, pp. 437–438, Jul. 1989.
- [261] D. T. Tran, C. Fansler, T. A. Grotjohn, D. K. Reinhard, and J. Asmussen, “Investigation of mask selectivities and diamond etching using microwave plasma-assisted etching,” *Diam. Relat. Mater.*, vol. 19, no. 7–9, pp. 778–782, Jul. 2010.
- [262] M. Mohr, L. Daccache, S. Horvat, K. Brühne, T. Jacob, and H.-J. Fecht, “Influence of grain boundaries on elasticity and thermal conductivity of nanocrystalline

- diamond films,” *Acta Mater.*, vol. 122, pp. 92–98, Jan. 2017.
- [263] A. C. Ferrari *et al.*, “Density,  $sp^3$  fraction, and cross-sectional structure of amorphous carbon films determined by x-ray reflectivity and electron energy-loss spectroscopy,” *Phys. Rev. B*, vol. 62, no. 16, pp. 11089–11103, Oct. 2000.
- [264] M. Yoshikawa, G. Katagiri, H. Ishida, A. Ishitani, and T. Akamatsu, “Raman spectra of diamondlike amorphous carbon films,” *Solid State Commun.*, vol. 66, no. 11, pp. 1177–1180, Jun. 1988.
- [265] A. C. Ferrari and J. Robertson, “Origin of the  $1150\text{ cm}^{-1}$  Raman mode in nanocrystalline diamond,” *Phys. Rev. B*, vol. 63, no. 12, p. 121405, Mar. 2001.
- [266] F. Klauser, D. Steinmüller-Nethl, R. Kaindl, E. Bertel, and N. Memmel, “Raman Studies of Nano- and Ultra-nanocrystalline Diamond Films Grown by Hot-Filament CVD,” *Chem. Vap. Depos.*, vol. 16, no. 4–6, pp. 127–135, Jun. 2010.



# Author Publications

## *Journal articles*

- A. Behroudj, D. Geiger, and S. Strehle, “Epitaxial Bottom-up Growth of Silicon Nanowires on Oxidized Silicon by Alloy-Catalyzed Gas-Phase Synthesis,” *Nano Lett.*, vol. 19, no. 11, pp. 7895–7900, Nov. 2019.
- M. Mohr, A. Behroudj, N. Wiora, M. Mertens, K. Brühne and H-J. Fecht, “Fabrication and Characterization of a Hybrid Silicon and Nanocrystalline Diamond Membrane Pressure Sensor”, *Quantum Matter*, vol. 6, no. 1, pp.41-44 (2017).

## *Conference Proceeding Papers*

- A. Pasquarelli, A. Moeinian, A. Behroudj, M. Nilsen, M. Roos, A.B. Udoy, and S. Strehle, “Integration Technologies for the Assembly of Silicon Nanowire Devices” IEEE 4th International Forum on Research and Technology for Society and Industry (RTSI) 2018.
- A. Behroudj and S. Strehle, “Transfer of Nanocrystalline Diamond Films Grown by Chemical Vapor Deposition for Sensors and Other Applications”, Micro-Nano-Integration; 6. GMM-Workshop 2016.

## *Conference Contributions*

- A. D. Dashtestani, A. Behroudj, A. Moeinian, W. Ahmad, and S. Strehle: *Exploring Alternative Catalysts for the Bottom-up Synthesis of Silicon Nanowires*, MRS fall meeting 2018, Boston, USA.
- M. Nilsen, A. Behroudj and S. Strehle: *Direct nanowire integration onto microcantilever beams by dry photoresist film lithography (talk)*, the 44th International Conference on Micro and Nanoengineering (MNE) 2018, Copenhagen, Denmark.
- M. M. Roos, T. Huffert, A. Moeinian, A. Behroudj and S. Strehle: *Integration of kinked silicon nanowires in polymeric scanning probes for biomedical applications (poster)*, the 44th International Conference on Micro and Nanoengineering (MNE) 2018, Copenhagen, Denmark.
- A. Behroudj and S. Strehle: *Epitaxial Growth of Silicon Nanowires on Native Silicon Oxide by Aluminum/Gold-catalyzed Vapor-Liquid-Solid Synthesis (talk)*, E-MRS fall meeting 2018, Warsaw, Poland.
- A. Pasquarelli, A. Moeinian, A. Behroudj, M. Nilsen, M. M. Roos, A. Udoy and S. Strehle: *Integration technologies for the assembly of silicon nanowire devices (talk)*,

IEEE 4th International Forum on Research and Technology for Society and Industry (RTSI) 2018, Palermo, Italy.

- M. M. Roos, A. Behroudj, M. Nilsen and S. Strehle: *Integration von „bottom-up“-gewachsenen Silizium-Nanodrähten in Rastersonden für „lab-on-a-tip“-Sensorik (poster)*, Mikrosystemtechnik VDI 2017, Munich, Germany.
- M. Nilsen, A. Behroudj and S. Strehle: *Customization of Pre-fabricated AFM cantilevers by Conventional Photolithography using Dry Photoresist Films (poster)*, the 44th International Conference on Micro and Nanoengineering (MNE) 2017, Braga, Portugal.
- M. Nilsen, A. Behroudj and S. Strehle: *Aligned Assembly of Nanowires on Flexible Membranes and Cantilevers by Contact Printing*, E-MRS spring meeting 2017, Strasbourg, France.
- A. Behroudj, M. Nilsen and S. Strehle: *Bottom-up Regrowth of Silicon Nanowires for Advanced 3D Nanoscale Probes (talk)*, E-MRS spring meeting 2017, Strasbourg, France.
- A. Behroudj and S. Strehle: *Transfer of Nanocrystalline Diamond Films Grown Directly on  $Si_3N_4$ -Membranes for Sensors and Other Applications (poster)*, 6. GMM-Workshop Mikro-Nano-Integration 2016, Duisburg, Germany.
- M. Mohr, A. Behroudj, N. Wiora, M. Mertens, K. Brühne and H. –J. Fecht: *Fabrication and Characterization of a Nanocrystalline Diamond Membrane Pressure Sensor (poster)*, Hasselt Diamond Workshop 2015 – SBDD XX, Hasselt, Belgium.
- S. Chitsaz, A. Behroudj and M. Montazer: *Investigation of Simultaneous Desizing and Antimicrobial Process on Cellulose Goods by Synthesis Nano-Silver from Silver Nitrate (poster)*, NANOSMAT 2012, Prague, Czech Republic.

# Curriculum Vitae

The contents of this page have been removed for data privacy protection reasons.